Universitat Autònoma de Barcelona

The Sun as a laboratory of particle physics

Núria Vinyoles Vergés

The Sun as a laboratory of particle physics

Núria Vinyoles Vergés
Institut de Ciències de l'Espai (ICE, CSIC/IEEC)

Advisor: Aldo Serenelli
Tutor: Lluís Font Guiteras

Universitat Autònoma de Barcelona
Departament de Física

A thesis submitted for the degree of
Doctor of Philosophy in Physics

Bellaterra, April 2017

Abstract

The Sun is by far the most studied and best-known star. The solar structure, revealed by helioseismology and solar neutrinos, is well determined, and accurate solar models give information about the past, present and the future of the Sun. These solar models, or Standard Solar Models (SSM), are useful for describing the solar interior, and at the same time provide a deeper knowledge on other disciplines, such as stellar structure and evolution, particle physics and even non-standard particle physics. In fact, the large density of the solar core, its temperature and sheer size allow studying physics in environments that are hard to reproduce in earth-based experiments. Consequently, the Sun is a powerful laboratory to test non-standard particle physics. In particular, the Sun offers very interesting possibilities for studying weakly interacting light particles that arise from extensions of the Standard Model of particles to address some of the most pressing open questions in fundamental physics, such as the nature of dark matter.

The main goal of this thesis is to use solar models to study the impact of different types of weakly interacting particles on the solar structure. Then, based on the structural changes they produce, the goal is to set the most restrictive bounds to properties of these particles using solar data from helioseismology and neutrinos.

In order to pursue this goal, it is important to have realistic solar models that reproduce, as best as possible, the available observations. Motivated by this fact, this thesis presents a new generation of SSMs that includes recent updates on some important nuclear reaction rates and a more consistent treatment of the equation of state. Models also include updated errors computed using Monte-Carlo simulations and a novel and flexible treatment of opacity uncertainties based on opacity kernels, required in the light of recent theoretical and experimental works on radiative opacity. In fact, radiative opacities are proposed as one of the possible solutions to the *solar abundance problem*, that is the conflict between helioseismic predictions from the models and observations when new a releases of solar composition are used to construct the SSM, in contrast to the good agreement obtained with the older compositions based on more simplistic one-dimensional model atmospheres. Therefore, to have an understanding of the current status of the radiative opacities and the corresponding uncertainties is important. For that reason, an exhaustive study of the available radiative opacity tables is presented in this thesis in the context of SSMs.

Current uncertainties in the solar composition and opacities can be overcome for studies of particle physics that do not depend on a detailed knowledge of the solar interior composition. For this purpose, the Best Fit Model, a solar model that better reproduces the observations using realistic evolutionary inputs, is introduced.

Finally, a new statistical analysis that combines helioseismology and solar neutrino observations (the ^{8}B and ^{7}Be fluxes) is presented, and it is used to place upper limits to the properties of non standard weakly interacting particles, and in particular, to axions, hidden photons and minicharged particles. This statistical analysis is based on the Best Fit Model and it includes theoretical and observational errors, accounts for tensions between input parameters of solar models and can be easily extended to include other observational constraints. For the fist time, constraints on the properties of these particles are placed by using a method that combines both helioseismology and solar neutrino observations. Additionally, the fact that Best Fit Models are the basis of the statistical analysis results in more robust bounds independent on the *solar abundance problem.* The bounds obtained are: for the axion-photon coupling constant $g_{10} < 4.1$ at 3 C.L., for the product of the kinetic mixing and mass of hidden photons, $\chi m < 1.8 \cdot 10^{-12}$ eV at 3 C.L and for the chage of the minicharged particles, $\epsilon = 2.2 \cdot 10^{-14}$ at 2 CL for $m_f = 0 - 25$ eV. For all the cases, the results are the most restrictive solar bounds, being a factor of 2 better for axions and hidden photons. Moreover, the results obtained for hidden photons and minicharged particles are globally the most restrictive bounds.

Resum

El Sol és, amb diferència, l'estrella més estudiada i coneguda. L'estructura solar, revelada gràcies a l'heliosismologia i els neutrins solars, està ben determinada i els models solars donen informació sobre el passat, el present i el futur del Sol. Aquests models solars, o Models Estàndard Solars, són útils a l'hora de descriure l'interior solar, i a la vegada proporcionen un ample coneixement cap a altres disciplines, com per exemple, l'estudi de l'estructura i evolució estelar, la física de partícules i fins i tot, la física de partícules fora del model estàndard. De fet, les altes densitats a l'interior solar, la temperatura i el gran tamany del Sol permeten estudiar processos físics en unes condicions que són molt difícils de reproduir en experiments terrestres. Com a conseqüència, el Sol és un potent laboratori per examinar física de partícules fora del model estàndard. En particular, el Sol ofereix possibilitats molt interessants per estudiar partícules lleugeres, que interaccionen feblement i que sorgeixen d'extensions del model estàndard de partícules, per poder respondre algunes de les preguntes sense resposta de la física fonamental, com per exemple, la natura de la matèria fosca.

L'objectiu principal d'aquesta tesi és estudiar l'impacte que diferents partícules lleugeres que intereccionen feblement, produeixen a l'estructura solar fent servir models solars. Aleshores, a partir d'aquests canvis estructurals que produeixen les partícules, l'objectiu és establir els límits més restrictius possibles en las propietats de les partícules estudiades, utilitzant la informació donada per l'heliosismologia i els neutrins solars.

Per poder assolir aquest objectiu, és important tenir models solars que reprodueixin de la manera més realista possible, les observacions solars. Amb aquesta motivació, aquesta tesi presenta una nova generació de Models Estàndards solars que inclouen actualitzacions recents d'algunes de les velocitats de reacció nuclears més importants i un tractament més consistent de l'equació d'estat. A més a més, aquests models també inclouen errors actualitzats que han estat calculats utilitzant diferents simulacions

de Monte-Carlo i també contenen un innovador i flexible tractament de les incerteses en les opacitats basat en kernels (o nuclis) de les opacitats. De fet, les opacitats radiatives són una de les possibles solucions al *problema de les abundàncies solars*, que és el conflicte entre les prediccions heliosísmiques dels models i les observacions quan noves publicacions de composicions solars són utilitzades per calcular els models solars, en contrast amb el bon acord que s'obté quan s'utilitzen les composicions solars més antigues i basades en models d'atmosferes més simples. Per tant, és important entendre la situació actual de les opacitats radiatives i les seves incerteses associades. Amb aquest propòsit, en aquesta tesi es presenta un estudi exhaustiu per a totes les opacitats radiatives disponibles.

Les incerteses actuals en la composició solar i les opacitats poden ser pal·liades per estudis de física de partícules que no depenen del coneixement detallat de la composició solar interna. Amb aquest propòsit, es presenta el model més ben ajustat, un model que reprodueix les observacions solars de la millor manera possible utilitzant paràmetres inicials d'evolució realistes.

Finalment, en aquesta tesi es presenta un nou mètode estadístic que combina l'heliosismologia i les observacions dels neutrins solars que és utilitzat per establir límits superiors a les propietats de les partícules que no són estàndards i que interactuen feblement amb la matèria. En particular, les partícules estudiades són els axions, els fotons obscurs i les partícules minicarregades. Aquest mètode estadístic està basat en el model més ben ajustat i inclou errors teòrics i observacionals, també té en compte les tensions entre paràmetres d'entrada del model solar i està adaptat perquè noves observacions puguin ser introduïdes sense dificultat. Per primer cop, s'han establert restriccions en les propietats d'aquestes partícules utilitzant un mètode que combina totes les observacions solars, l'heliosismologia i els neutrins solars. A més a més, el fet que el model més ben ajustat sigui la base del mètode estadístic, fa que els resultats siguin sòlids i independents del *problema de les abundàncies solars*. Els límits obtinguts són: per la constant d'acoblament axió-fotó, $g_{10} < 4.1$ a 3 C.L., pel producte entre la constant de mescla cinètica i la massa del fotó obscur, $\chi m < 1.8 \cdot 10^{-12}$ eV a 3 C.L i per la càrrega de la partícula minicarregada, $\epsilon = 2.2 \cdot 10^{-14}$ a 2 CL per masses en el rang de $m_f = 0 - 25$ eV. Per tots els casos, els results són els més restrictius que s'han obtingut fins ara utilitzant el Sol, essent un factor 2 millors que els anteriors pels casos dels axions i els fotons obscurs. A més a més, els resultats obtinguts pels fotons obscurs i per les partícules minicarregades són més restrictius que qualsevol dels límits establerts prèviament.

Acknowledgements

First of all, I would like to thank Aldo for his supervision, his dedication, for everything he has taught me and for having his office open at anytime. Thanks for all the help and for always giving me support with my decisions.

I also want to thank Margarita and Jordi for opening me the doors of the institute and giving me this opportunity. Also to the rest of the people who is and have been part of the research group.

Thanks also to all the people who have helped me during the way, specially to Francesco Villante, to Josep for all the priceless help with computer topics and for everything he has taught me, and to all the administration staff, who made everything easier.

To Georg Raffelt and Javier Redondo, for giving me the opportunity to be part of the astroparticle group in the Max Planck for Physics in Münich during some months. Also thanks to all the people of the group who made me feel like home and specially to Hendrik, for our collaborations and for all the help he gives me even from another continent.

Also, a very special thank to all the people in the institute with whom I shared the best moments during these years, in the old building, in the new one, during the lunch, in the office, during all these things and activities that we have done together and for all the support that we have given to each other. Everything has been easier surrounded by all of you.

Finally I would like to thank all my friends and family, specially my parents, my sister Txell and Padu, for being always by my side.

List of Publications

The publications related to the topics of the thesis are:

- (Vinyoles et al., 2015) N. Vinyoles, A. Serenelli, F. Villante, S. Basu, J. Redondo and J. Isern, *New axion and hidden photon constraints from a solar data global fit*, *JCAP* **1510** (2015) 015, doi: 10.1088/1475-7516/2015/10/015
- (Vinyoles and Vogel, 2016) N. Vinyoles and H. Vogel *Minicharged Particles from the Sun: A Cutting-Edge Bound*, *JCAP* **1603** (2016) 002, doi: 10.1088/1475-7516/2016/03/002
- (Vinyoles et al., 2017) N. Vinyoles, A. M. Serenelli, F.L.Villante, S.Basu, J. Bergström, M.C. Gonzalez-Garcia, M. Maltoni, C. Peña-Garay, N. Song *A new generation of Solar Standard Models*, *APJ* **835** (2015) 202, doi: 10.3847/1538-4357/835/2/202

The following publications are currently in preparation:

- N. Song, N. Vinyoles, J. Bergström, M.C. Gonzalez-Garcia, C. Peña-Garay, A. Serenelli, F. L. Villante, *What can we learn from the Sun?: A solar neutrino and composition combined analysis* (2017, in preparation)
- N. Vinyoles, A. Serenelli, F.L Villante *State-of-the-art of radiative opacities in SSMs* (2017, in preparation)

Other works published during the period of the thesis, but not related to its topic are:

- (Vinyoles and Serenelli, 2016) N. Vinyoles, A. Serenelli *A sensitivity study of s-process: the impact of uncertainties from nuclear reaction rates*, *JPhCS* **665** (2016) 012028, doi: 10.1088/1742-6596/665/1/012028

- (Camisassa et al., 2016) M.E. Camisassa, L.G.Althaus, A.H. Córsico, N. Vinyoles, A.M.Serenelli, M.M. Bertolami, E. García-Berro and J. Isern *The effect of* ^{22}*Ne in the evolution and pulsation properties of solar metallicity white dwarfs*, *ApJ* **823** (2016) 158, doi: 10.3847/0004-637X/823/2/158

Acronyms list

A11	Adelberger et al., 2011
B16	Barcelona 2016 - Updated SSMs
BFM	Best Fit Model
$\mathrm{BFM_G}$	Best Fit Model - GS98
$\mathrm{BFM_A}$	Best Fit Model - AGSS09met
`GARSTEC`	GARching STEllar Code
HP	Hidden Photon
MCP	Minicharged Particles
SFII	Solar Fusion II SSMs (from Serenelli et al., 2011)
SM	Standard Model
SSM	Solar Standard Model
WIMP	Weakly Interacting Massive Particle
WISP	Weakly Interacting Light Particle

Contents

Abstract i

Resum iii

Acknowledgments vi

List of Publications viii

Acronyms list xi

1 Introduction 1

1.1 Basics on stellar structure and evolution 1
  1.1.1 Stellar structure and evolution equations 2
  1.1.2 Constitutive physics 7
  1.1.3 Modelling stars 8
1.2 The Sun 9
  1.2.1 Main properties and characteristics 9
  1.2.2 Solar Standard Models 12
  1.2.3 Evolution of the Sun 13
  1.2.4 Solar neutrino fluxes 15
  1.2.5 Helioseismology 17
  1.2.6 Agreement of the observations with SSMs 24
1.3 Physics Beyond the Standard Model of Particles 26
  1.3.1 Weakly Interacting Light particles 26
  1.3.2 Astrophysical constraints on WISPs 27
  1.3.3 Experiments and detectors 30

2 A new generation of Standard Solar Models 33

2.1 Main characteristics and updates . . . 35

2.1.1 Composition . . . 35

2.1.2 Nuclear Rates . . . 37

2.1.3 Equation of State . . . 41

2.1.4 Input parameters . . . 43

2.2 Treatment of model uncertainties . . . 43

2.2.1 Diffusion . . . 44

2.2.2 Radiative opacities . . . 44

2.3 Results . . . 52

2.3.1 Helioseismology . . . 53

2.3.2 Neutrino fluxes . . . 58

2.3.3 Global analysis . . . 63

2.4 Errors in SSMs . . . 64

2.4.1 Monte Carlo Simulations . . . 64

2.4.2 Dominant error sources . . . 70

2.5 Summary and Conclusions . . . 74

3 State-of-the-art of radiative opacities in SSMs 79

3.1 Opacity tables . . . 79

3.2 The pull approach . . . 82

3.3 SSMs with different opacity tables . . . 83

3.3.1 Helioseismology . . . 83

3.3.2 Neutrino Fluxes . . . 92

3.3.3 Global results . . . 95

3.4 Summary and conclusions . . . 97

4 The Best Fit Model 101

4.1 Statistical method . . . 102

4.2 Observables . . . 103

4.3 Power-laws . . . 103

4.3.1 Opacities . . . 104

4.4 The Best fit model . . . 107

4.4.1 Linear approximation . . . 107

4.4.2 Solar calibration . . . 107

4.5 Results . . . 108

4.5.1 Minimization . . . 108

4.5.2 Best Fit Models . . . 114
4.6 Summary and conclusions . . . 118

5 Constraints on exotic particles using solar models 121
5.1 Cases of study . . . 122
5.1.1 Axions . . . 122
5.1.2 Hidden photons . . . 123
5.1.3 Minicharged particles . . . 124
5.2 Models and data . . . 125
5.2.1 Models with Axions . . . 125
5.2.2 Models with hidden photons . . . 126
5.2.3 Models with minicharged particles . . . 127
5.3 Observations . . . 128
5.4 Statistical Method . . . 128
5.5 Results . . . 130
5.5.1 Energy distribution . . . 130
5.5.2 Solar neutrinos and convective envelope properties . . . 133
5.5.3 Solar sound speed profile . . . 141
5.5.4 Global results . . . 144
5.6 Discussion . . . 153
5.7 Summary and conclusions . . . 157

6 Summary and conclusions 159
6.1 Results . . . 159
6.2 Future work . . . 163

A Power-laws 165

Bibliography 168

Chapter 1

Introduction

This chapter contains a review of the main ingredients necessary for this thesis. In the first section basics on stellar structure and modeling stars are presented. In the following section, the case of study of this thesis, the Sun, is discussed starting with a description of the main characteristics and properties, following with the solar models and finishing with its main observations. Finally, in the last section there is an introduction of non-standard weakly interacting particles and how stars, and the Sun in particular, can be used to study their properties.

1.1 Basics on stellar structure and evolution

In order to understand how a star evolves and its corresponding characteristics is important to have a good knowledge of its internal structure and how it changes with time. Therefore, first of all, a set of equations describing the structure of the stars has to be determined. These equations define the structure of the stars and the main processes taking place, but the details will depend on the physical details of stellar matter and the different processes, and for that reason, a detailed knowledge of these ingredients (constitutive physics or microphysics) is indispensable. In the following sections, the basic structure and evolution equations and some details about the constitutive physics considered are presented. This part is finished by describing some notions of stellar modeling and the main characteristics of the code used in this thesis.

For a deep description of the topic the reader is referred to the following books and reviews (Clayton, 1984; Kippenhahn et al., 2012) but the basics of it is detailed in the following sections.

1.1.1 Stellar structure and evolution equations

The main ingredient of stellar models are the set of equations that describe the structure of the star. These equations are the mass conservation, hydrostatic equilibrium, energy conservation equation and the equation of the energy transport. The main approximations used to derive the structure equations presented in the following sections are spherical symmetry, meaning that no rotation or strong magnetic fields are considered and that the only forces acting over a mass element are the pressure and the gravity. Therefore, the derivation of the structure equations is done by using a Lagrangian approach and the mass as the independent variable.

$$\frac{\partial r}{\partial m} = \frac{1}{4\pi r^2 \rho} \tag{1.1a}$$

$$\frac{\partial P}{\partial m} = -\frac{Gm}{4\pi r^4 \rho} \tag{1.1b}$$

$$\frac{\partial l}{\partial m} = \epsilon_g + \epsilon_n - \epsilon_\nu \tag{1.1c}$$

$$\frac{\partial T}{\partial m} = \frac{GmT}{4\pi r^4 P}\nabla, \qquad \nabla = \left(\frac{\partial \ln T}{\partial \ln P}\right) \tag{1.1d}$$

Mass conservation: (Equation 1.1a) Assuming the lagrangian description, to any mass element the value Δm contained in the corresponding shell is fixed, implying that there is no mass flow through the shell. Therefore, the radius is adjusted when there are changes on the density.

Hydrostatic equilibrium: (Equation 1.1b) The hydrostatic equilibrium equation is a particular case of the equation of conservation of the momentum. Therefore, if the star is not in hydrostatic equilibrium and is experiencing accelerated radial motions, an extra term should be added to Equation 1.1b obtaining the equation of motion (Equation 1.2).

$$\frac{\partial P}{\partial m} = -\frac{Gm}{4\pi r^4 \rho} - \frac{1}{4\pi r^2}\frac{\partial^2 r}{\partial t^2} \tag{1.2}$$

This extra term can be neglected if the star is evolving slower than τ_{hydr}, that is the time that the star reacts to a perturbation of the equilibrium. Evolution timescales are very long in the major evolutionary phases of the star when compared with the hydrostatic timescale, and then, any perturbation is relaxed very quickly into equilibrium. Therefore, in this approximation, the mass element cannot be accelerated meaning that the forces acting to a mass element have to compensate each other. Assuming the approximations described at the beginning, the only acting forces are the gravity and the pressure and Equation 1.1b represents these equilibrium between the forces. From this equation and assuming an ideal gas it is possible to obtain the *Virial theorem*, useful to relate the internal and gravitational energy of a star (see Equation 1.3).

$$2E_i = -E_g \tag{1.3}$$

Conservation of energy: (Equation 1.1c) This equation defines the energy per second passing through a sphere of radius $l(r)$ for a given element of mass. The different contributions to the energy are the ϵ_{nuc} term, related to the energy released through the nuclear reactions and the gravitational energy term, ϵ_g, that accounts for the exchange of mechanical work and heat with the neighboring layers when, for example, there is expansion (negative term) or contraction (positive) in a given mass shell. The last term ϵ_ν accounts for the energy carried away by neutrinos resulting from nuclear reactions and from thermal plasma processes, this term is always negative.

Energy transport: (Equation 1.1d) This last equation is the energy transport equation. The energy radiated of the star trough its surface comes from the energy released in its central region, and therefore, is necessary to describe the energy transport mechanisms. This transport is possible due to the temperature gradient of the star and the three existing mechanisms are radiation, convection and conduction. Each of the mechanisms define a different temperature gradient ∇. The particular cases and the stability criteria used to determine which transport dominates are discussed in the following section.

1.1.1.1 Energy transport

Radiative transport Radiative transport consists of photons carrying energy away while are absorbed and re-emitted by the stellar matter performing a random walk. In the interior of a star like the Sun, stellar matter is very opaque to radiation because the mean free path of a photon (Equation 1.4) is much smaller than the solar radius, $l_{ph} << R_\odot$. The mean free path of a photon is defined as,

$$l_{ph} = \frac{1}{\kappa\rho} \tag{1.4}$$

where κ is the mean absorption coefficient (opacity) of the radiation. Therefore, due to the opaqueness of the stellar matter is possible to approximate the radiative transport as a diffusion problem.

By considering the equations of diffusive flux ($\mathbf{j} = -D\nabla_n$ with $D = \frac{1}{3}vl_{ph}$), combined with the energy density of radiation ($U = aT^4$) it is possible to obtain an expression for the flux of radiative energy,

$$F = -\frac{4ac}{3}\frac{T^3}{\kappa\rho}\frac{\partial T}{\partial r}. \tag{1.5}$$

After replacing the flux for the local luminosity $l = 4\pi r^2 F$ and transforming to the variable m, the expression of radiative transport is finally obtained,

$$\frac{\partial T}{\partial m} = -\frac{3}{64\pi^2 ac}\frac{\kappa l_{ph}}{r^4 T^3}. \tag{1.6}$$

Therefore, when the energy transport is radiative, ∇ is replaced by ∇_{rad} in Equation 1.1d,

$$\nabla_{rad} = \frac{3}{16\pi acG}\frac{\kappa l P}{mT^4}, \tag{1.7}$$

where κ is the opacity of the stellar matter averaged over ν (see Section 1.1.2.1 for details).

Convective transport Convective transport consists in the exchange of energy between hotter and cooler regions through the rising and sinking of macroscopic mass elements. The determination of ∇ for this case is typically done by using the mixing length theory. The mixing length theory is a 1-D treatment of the convection and its basic assumption is that one bubble travels a characteristic distance and then dissolves. This distance is determined by the mixing length parameter (α_{MLT}) that scales this distance as follows:

$$l = \alpha_{\mathrm{MLT}} Hp, \tag{1.8}$$

where Hp is the pressure scale height. The final temperature gradient is determined by the thermodynamic conditions of the stellar matter and the value of the mixing length parameter used. The α_{MLT} parameter cannot be determined using physical principles and its value is often determined by calibrating solar models (see Section 1.2.2) with final values in the range of 1.5-2.5.

Stability criteria The criteria to determine the energy transport in a given region is whether the considered layer is stable under small perturbations and therefore, the energy transport is radiative or if it presents instabilities and consequently, convection takes place.

Considering homogeneous chemical composition, the criteria to determine the stability on a given region is described by the *Schwarzchild criterion*;

$$\nabla_{rad} < \nabla_{ad}, \qquad \nabla_{ad} = \left(\frac{\partial \ln T}{\partial \ln P}\right)_s \approx \left(\frac{P}{T}\frac{\mathrm{d}T}{\mathrm{d}P}\right)_s = \frac{P\delta}{T\rho c_P} \tag{1.9}$$

where ∇_{rad} expression can be found in Equation 1.7 and $\delta = -\left(\frac{\partial \ln \rho}{\partial \ln T}\right)$.

Therefore, by reading the expressions of ∇_{rad} and ∇_{ad} is possible to understand under which conditions the transport is going to be radiative or convective. For example, high energy fluxes would produce instability because radiation would not be enough to transport all the energy, that is the case at the interior of high mass stars as a consequence of the large temperature gradient due to the high sensitivity of the nuclear reactions to temperature. Another situation that can make radiation ineffective is when opacities are very large, and then, the photons are absorbed too often making the radiative transport very inefficient. This is the case of intermediate and low-mass stars that have a convective envelope.

1.1.1.2 Chemical composition

Finally, an important equation to define the structure's evolution of a star is the evolution of the chemical composition with time. Changes on the chemical composition modify the energy generation through nuclear reactions, the absortion properties of the radiation and basically the thermodynamics properties of the stellar matter. Therefore, Equation 1.10 determines the time evolution of the chemical composition, that will determine the evolution of the star.

$$\frac{\partial X_i}{\partial t} = \frac{m_i}{\rho}\left[\sum_i r_{ji} - \sum_k r_{ik}\right] \tag{1.10}$$

where i corresponds to each individual nuclear specie considered in the evolution code, r_{ji} the reaction rate that produces the element i and r_{ik} the reaction rate that destroys the element i. This equation is valid in a radiative region without microscopic diffusion or any extra mixing process. If microscopic diffusion is considered, an extra term should be included as described later on in this section.

For the convective region is possible to assume that the mixing of the elements is instantaneous due to the fact that the convective motion is much faster than the changes on the composition due to nuclear reactions, and therefore, the composition in the convective region is homogeneous. Then, the chemical evolution on the convective region can be described as follows:

$$\frac{\partial \bar{X}_i}{\partial t} = \frac{1}{m_2 - m_1} \cdot \left(\int_{m_1}^{m_2} \frac{\partial X_i}{\partial t} dm + \frac{\partial m_2}{\partial t}(X_{i2} - \bar{X}_i) - \frac{\partial m_1}{\partial t}(X_{i1} - \bar{X}_i) \right), \qquad (1.11)$$

where m_1 and m_2 are the mass at the boundaries of the convective region, X_{i1} X_{i2} the abundances at these two points and $\bar{X}_i$ is the value of the composition inside the convective region. The first term on the brackets corresponds to changes on the chemical composition (X_i) due to nuclear reactions in the convective region and the next two terms are the changes due to variations of the composition at m_1 and m_2.

Microscopic diffusion Microscopic diffusion is the mechanism that allows the mixing of chemical elements through thermal, pressure or chemical gradients in the star. If microscopic diffusion is considered an extra term should be added to Equation 1.10 to accound for this extra mixing.

For example, in Thoul et al. (1994) and similarly in Bahcall and Loeb (1990), they describe this extra term as:

$$\frac{\partial X_i}{\partial t} = -\frac{\partial}{\partial m}[4\pi r^2 X_i T^{5/2} \xi_i] \qquad (1.12)$$

where ξ_i is a function of the diffusion velocity ω_i of the different species i an can be expressed as $\xi_i = \frac{\omega_i \rho}{T^{5/2}}$. This function can be formulated using analytic fits as function of the pressure, temperature and chemical gradients:

$$\xi_i = 4\pi r^2 \rho \left(A_P(i)\frac{\partial \ln p}{\partial r} + A_T(i)\frac{\partial \ln T}{\partial r} + \sum_{k \neq e, He^4} A_k(i)\frac{\partial \ln C_i}{\partial r} \right) \qquad (1.13)$$

In Equation 1.13 the first term accounts for pressure diffusion (gravitational settling), the second to thermal diffusion and the third is the chemical diffusion component. The coefficients A_P, A_T and A_k are calculated in Thoul et al. (1994).

Other extra mixing processes, such as overshooting, effects of rotation, thermohaling mixing, semiconvection, radiative levitation or other mixing processes (see Pinsonneault (1997) for a review about non standard mixing processes in stars) could be considered and their effects added to Equation 1.10 .

1.1.2 Constitutive physics

In the previous section, the set of differential equations (Equation 1.1) that describe the structure of a star spherically symmetric and in hydrostatic equilibrium have been presented together with the equation of the chemical evolution (Equation 1.10). In order to solve this system, the functions contained in these equations that describe the properties of the stellar material have to be determined. These can be separated in three main groups: radiative opacities, equation of state and nuclear reactions.

1.1.2.1 Opacities

The radiative energy transport expression depends on the opacities of the stellar material, that at the same time depend on the pressure, temperature, chemical composition and the frequency of the radiation, $\kappa_\nu = \kappa_\nu(P, T, X_i)$. Once κ_ν is obtained through atomic calculations, the mean over all frequencies is required to obtain the complete equation for the radiative transport. This averaged mean is the *Rosseland opacity* and can be expressed the following way,

$$\frac{1}{\kappa_{ross}} = \frac{\pi}{acT^3} \int_0^\infty \frac{1}{\kappa_\nu} \frac{\partial B(\nu, T)}{\partial T} d\nu, \tag{1.14}$$

where a is the radiation density constant and $B(\nu, T)$ is the Planck function for the intensity of black-body radiation.

There are not valid approximations for the radiative opacities that work at all the different regions of the star, therefore, when solving the differential equations, the *Rosseland mean* values are taken from different pre-computed numerical tables for a given chemical composition and tabulated for T and ρ. The most used opacities tables in stellar codes are OPAL (Iglesias and Rogers, 1996) and OP (Badnell et al., 2005). To calculate these opacities tables the atomic absorption cross section as function of the photon frequency have to be calculated through theoretical calculations for all the processes involved. The basic processes that contribute to the opacity are, electron scattering, free-free transitions, bound-free transitions, bound-bound transitions, the negative hydrogen Ion, molecular opacities for low temperatures and the contribution of the electron conduction to final opacities (see Clayton, 1984 and Kippenhahn et al., 2012 for details of these processes). Depending on the stellar matter conditions, each of these processes will dominate at different regions of the star.

1.1.2.2 Equation of State

The equation of state (EoS) provides the relation between different properties of the stellar matter, as the relation of the density with the temperature, pressure and chemical composition ($\rho = \rho(T, P, X_i)$). It also relates the thermodynamical properties of the gas as $\delta = \delta(T, P, X_i)$, $\nabla_{ad} = \nabla_{ad}(T, P, X_i)$ and $C_P = C_P(T, P, X_i)$, this last being the specific heat at constant pressure $C_P = \left(\frac{\partial Q}{\partial T}\right)_P$. In a similar way than the opacity tables, the EoS is calculated a priori in different tables with a given composition that contain the tabulated thermodynamic properties as function of T and ρ. Some examples of the most used EoS tables are, OPAL (Rogers and Nayfonov, 2002a), MHD (Hummer and Mihalas, 1988) or FreeEOS (Cassisi et al., 2003).

1.1.2.3 Nuclear reactions

In order to solve the set of differential equations is necessary to determine the energy production through nuclear burning $\epsilon_{nuc} = \epsilon_{nuc}(T, P, X_i)$ and the thermonuclear reactions rates $r_{jk} = r_{jk}(T, P, X_i)$ to calculate the chemical evolution of the star. Both need the determination of the cross sections of the different reactions and the most typically used are taken from the NACRE compilation (Angulo et al., 1999) or from Solar Fusion II (Adelberger et al., 2011) complemented by the more recent updates (see Chapter 2 for details about these updates). Details about the thermonuclear reactions and the corresponding calculation of cross sections and reactions rates can be found in Clayton (1984). Finally, to complete the energy conservation equation the energy lost by the neutrinos $\epsilon_\nu = \epsilon_\nu(T, P, X_i)$ have to be determined. This is done through the neutrino emission rates from the different thermal processes as detailed in Munakata et al. (1985) and Haft et al. (1994) and from thermonuclear reactions in Bahcall (1989).

1.1.3 Modelling stars

To solve the structure of the star during its evolution, there are not analytic solutions for the set of differential equations (Equation 1.1-1.10) and numerical solutions are required. Different numerical programs have been used to solve the differential structure equations for stars, being the code presented in Kippenhahn et al. (1967) one of the first used. In the next section the main characteristics of GARSTEC, the code used in this thesis, are described.

1.1.3.1 GARSTEC

GARching STEllar Code (`GARSTEC`) (Weiss and Schlattl, 2008) is a one dimensional hydrostatic code that does not include the effects of rotation. GARSTEC uses the Henyey-scheme (Henyey et al., 1964) to solve the four differential equations (Equation 1.1) and the chemical evolution equation (Equation 1.10). This code is used to follow the evolution of low-mass stars and to perform solar models. The main characteristics and physical details are as follows. Mass loss, if required, is treated according the Reimers formula (Reimers, 1975). The atmosphere is a plane-parallel grey Eddington fitted to the stellar interior at $\tau = 2/3$. Alternatively the Krishna-Swamy $T - \tau$ relation (Krishna Swamy, 1966) can also be used. Convection is described using the mixing length theory as described in Section 1.1.1.1 and it allows the possibility to include overshooting as described in Freytag et al. (1996). Atomic diffusion is included for 13 elements from hydrogen to iron and is treated as described in Section 1.1.1.2 and using the coefficients from Thoul et al. (1994). As explained in Section 1.1.2, the radiative opacities and equation of state are interpolated from precomputed tables. By default, the code uses OPAL opacity tables, OPAL-EoS and the nuclear rates are taken from the NACRE compilation. The particular details of the physics used to compute the models presented later on in this thesis are specified for each particular case.

1.2 The Sun

The Sun is a main-sequence star that has already burnt half of its initial hydrogen mainly through pp chain. The transport at the interior of the Sun is radiative while at the outer region ($r/R_\odot > 0.713$) the energy is transported by convection. In the following sections the main properties and characteristics of the Sun are presented, followed by one of the main ingredients of the thesis, the Standard Solar Models, complemented with a brief review of the Sun's evolution up to the present age. Finally, there is a brief review of the main observables that give information of the solar interior: solar neutrinos and helioseismology. The agreement (and disagreement) of SSMs with the different observations is discussed in the last section.

1.2.1 Main properties and characteristics

1.2.1.1 Mass

$\mathrm{M}_\odot = 1.98892(1 \pm 0.00013) \cdot 10^{33}$ g: The mass can be determined with high accuracy from planetary motion. With the known solar system distances and the third Kepler law the product $GM_\odot$ can be obtained. With the laboratory determination of the constant $G = (6.67259 \pm 0.00085) \cdot 10^{-11}$ m^3 kg^{-1} s^{-2} (Cohen and Taylor, 1987; Luther and Towler, 1982) the mass of the Sun can be determined.

1.2.1.2 Radius

$R_\odot = 6.9598(1 \pm 0.0001) \cdot 10^{10}$ cm: The determination of the solar radius is done by using the apparent diameter of the solar disk and solar distance, and the value that is generally used for solar modeling is taken from Allen (1973). Brown and Christensen-Dalsgaard (1998) also used these method resulting in a smaller value for the solar radius. Different works have used alternative methods to measure the solar radius. Works as Schou et al. (1997) and Antia (1998) use f-modes, that are surface modes (see Section 1.2.5), to provide an independent measure of the solar radius using the observations from Michelson Doppler Imager (MDI) on board of SOHO (Scherrer et al., 1995). The resulting radius from this method differs from the first one about ~ 0.3 Mm. These discrepancies come from the theoretical definition of the radius ($\tau_{ross} = 2/3$) and the observation of the extended solar disk (see Haberreiter et al. 2008 for details).

1.2.1.3 Luminosity

$L_\odot = 3.8418(1 \pm 0.004) \cdot 10^{33}$ erg s^{-1}: The solar luminosity is determined by using the total solar irradiance observed from different space satellites and ground experiments. The total solar irradiance is averaged over the variation from the solar cycle using the observations done during the 21 and 22 solar cycles. The variation obtained is about 0.1%. See Bahcall et al. (1995) and Fröhlich and Lean (1998) for more details.

1.2.1.4 Age

$\tau_\odot = 4.57(1 \pm 0.0044)$ Gyr: The solar age is determined from the meteorites by using radioactive dating and combined with models of the formation of the solar system. The accuracy of the age depends on the measured abundances, the initial abundances and the decay constants considered. Details about it can be found in the appendix of Bahcall et al. (1995).

1.2.1.5 Solar Composition

The solar surface composition is a fundamental constraint in the construction of solar models (see Section 1.2.2). The solar composition can be determined by analyzing the solar spectra and obtaining photospheric abundances or alternatively, by measuring primordial solar abundances in pristine meteorites, the so-called CI chondrites.

Photospheric abundances The solar composition can be inferred from the solar spectra by using models of solar atmosphere, radiative transfer and line formation combined with detailed atomic and molecular data. Then, abundances can be derived by using the equivalent width (or line strength) that is the product of the element abundance and the oscillation strength or by comparing the theoretical spectra from the models with observed spectra. The spectral lines are measured relative to the continuum, and the intensity of which is dominated by the H^- opacity. Therefore, the final abundances of the different elements are relative to the hydrogen abundances and typically expressed as:

$$\log(\epsilon_i) = \log \frac{N_i}{N_H} + 12, \tag{1.15}$$

where N_i is the atomic density number of the i element and N_H of the hydrogen. In the following paragraphs some basic notions about the main ingredients used to construct a syntetic spectra are summarized.

Atmosphere's model To have realistic atmosphere models is a requirement to obtain the chemical composition of the Sun and it is a previous step before modeling the spectral line formation. Usually, 1-D atmosphere models (e.g. Gustafsson et al., 2008) were used, where time-independence and hydrostatic equilibrium were assumed and in some cases, mixing length theory was used to describe convection. More recently, new models for the atmosphere have been used to simulate the synthetic spectra by performing 3D, time-dependent, radiation hydrodynamics simulations of the stellar near-surface convection (e.g. Asplund, 2005; Dravins and Nordlund, 1990; Nordlund et al., 2009). These models resulted in a good reproduction of the solar atmosphere when compared with observations of granulation, limb darkening or center to limb intensity variations among others.

Line spectra formation Using the computed model atmosphere and detailed line data from atomic and molecular data, it is possible to model how the spectrum is formed by studying the atomic level populations. Traditionally, LTE was assumed for all the cases and the atomic level populations were calculated by using Boltzman and Saha distribution. Lately, deviations from LTE (non-LTE) were taken into account by simultaneously solving the rate equations for all relevant levels and species together with the radiative transfer equation (see Asplund et al., 2009 for more details).

Different photospheric solar abundances compilations have been released. One of these is GS98 (Grevesse and Sauval, 1998), a solar compilation based on 1-D atmosphere modeling and LTE approximation for all the cases. Later on, a new solar composition, AGSS09 (Asplund et al., 2009 and updated later in Grevesse et al., 2015; Scott et al., 2015a,b) was released presenting new values for the photospheric abundances, obtaining lower values for the metallicity, specially for the C,N,O and Ne elements reaching values up to 30-40% lower than GS98. These changes were due to the use of 3D models for the atmosphere, the extension to NLTE regim when possible, the new and more complete atomic and molecular data available and the more accurate line selection. For example, Grevesse et al. (2010) discuss that the absorption line used to infer the abundance oxygen in GS98 was blended and therefore, the abundance overestimated, partially explaining the lower values for the oxygen. Other works have inferred the solar composition by using the most newest models and data, as it is the case for CO5BOLD Caffau et al. (2011). Their final values for the volatiles elements lay in between the AGSS09 and GS98. Grevesse et al. (2010) claims that these differences are mainly coming from the different line selection procedures and from the different atomic data used.

Meteoritic abundances Through mass spectroscopy of CI chrondrites, it is possible to obtain solar abundance with high accuracy. Basically, CI chrondrites are meteorites that at the time of formation were not heated enough to reach melting temperatures and thus, their composition reflects the solar system composition. Using meteorites it is possible to extract abundances only for refractories, i.e. elements with high condensation temperature and therefore, abundances of volatile elements such as (H ,C, N, O or Ne) are taken from photospheric values. As H abundances cannot be extracted from meteorites, the meteoritic abundances are calculated relative to Si and its photospheric abundance is used to scale the meteorites abundances with the photospheric ones. The most frequently meteoritic abundances used are taken from Lodders et al. (2009).

1.2.2 Solar Standard Models

Standard Solar Models (SSMs) are a snapshot in the evolution of a $1\,\mathrm{M}_\odot$ star, calibrated to match present-day surface properties of the Sun. In this models, two basic assumptions are that the Sun was initially chemically homogeneous and that at all moments during its evolution up to the present solar age $\tau_\odot = 4.57\,\mathrm{Gyr}$ mass loss is negligible. The calibration is done by adjusting the mixing length parameter (α_{MLT})

and the initial helium and metal mass fractions ($\mathrm{Y}_{\mathrm{ini}}$ and $\mathrm{Z}_{\mathrm{ini}}$ respectively) in order to satisfy the constraints imposed by the present-day solar luminosity $\mathrm{L}_{\odot}$, radius $\mathrm{R}_{\odot}$, and surface metal to hydrogen abundance ratio $(\mathrm{Z/X})_{\odot}$. The choice of $(\mathrm{Z/X})_{\odot}$ is critical because it essentially determines the distribution of metals in the entire solar structure and it has been the subject of much discussion over recent years in the context of the *solar abundance problem* (see Section 1.2.6.1).

Apart from the study of the structure and properties of the Sun, SSMs have been and still are a key ingredient to study topics as stellar evolution, neutrino and particle physics and to test non-standard physics and theories. Related to stellar evolution, the calibration of SSMs have been used to determine the value of α_{MLT} used to construct stellar models, to study the metal evolution of the galaxy and predict the metallicity of other stars or to test non standard evolution as extra mixing processes. Related to neutrino physics, the SSMs have been essential to discover that the neutrinos produced in the Sun are not massless and the neutrino flavor oscillations related with what is called the *solar neutrino problem* (Ahmad et al., 2002). Nowadays, SSMs are used to study the electron neutrino survival and the determination of the CNO fluxes (Bellini et al., 2014a; Maltoni and Smirnov, 2016). Finally, the Sun and SSMs have been used to study non-standard physics such as the presence of exotic particles (see Section 1.3 and Chapter 5 for details).

1.2.3 Evolution of the Sun

In this section the evolutionary history of the Sun until the present age is summarized together with some details about its current status that can be understood using Solar Standard Models. Nowadays, the Sun is burning hydrogen and producing helium through the fusion of four protons to produce one ^{4}He nucleus. There are two main chains of reactions by which the hydrogen fusion can be complete, pp-chain and the CNO cycle (see Figure 1.1). These two mechanisms can take place simultaneously but each of them will be more efficient depending on the stellar temperature (see Clayton, 1984 for details). In general, the hydrogen burning through pp-chain dominates over CNO at stars with low masses (lower temperatures) while at higher masses (high temperatures) it can be neglected in front of CNO cycle. This is due to the dependence of each of the chains to the temperatures $\epsilon_{pp} \sim T^5$ and $\epsilon_{CNO} \sim T^{20}$. Due to the temperatures reached in the Sun, the pp-chain dominates (99%) over the CNO cycle (1%). The details on the reactions that take place in the pp-chain and CNO cycle can be found in Figure 1.1.

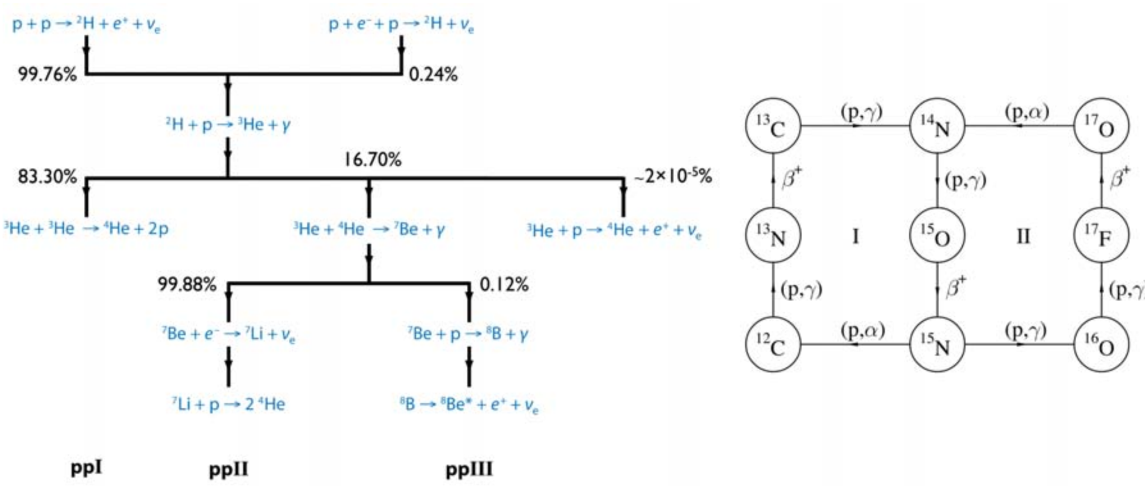

Figure 1.1: *Left panel*: Proton-proton nuclear reaction chain with its three branches. *Right panel:* CNO cycle. *Credit: Figure 2 from* Adelberger et al. *(2011)*

The Sun is set as initially homogeneous with the initial surface composition determined by $(Z/X)_\odot$ that is dependent on the solar composition used and will define the distribution of the different elements in the Sun. The evolution of the Sun starts at the pre-main sequence stage, where the Sun is contracting. Before the temperature necessary to burn hydrogen in equilibrium through the pp-chain is reached, ^{12}C burns into ^{14}N through the CNO-cycles reactions, although that cannot be complete becase the slow reaction rate of $(^{14}\mathrm{N}(\mathrm{p},\gamma)^{15}\mathrm{O})$. The energy released through this processes will stop the contraction and, at the same time, the first reactions of the pp chain transform H into ^{3}He. The energy released is concentrated in the center and therefore, due to large energy flux, the Sun will develop a convective core at the same time that the first reactions of the *pp* chain start becoming important. After the ^{12}C is exhausted, the hydrogen burning in equilibrium through *pp* chain is the main energy source of the star, the ^{3}He is destroyed and the convective core disappears. This situation is reached at the age of $\sim$ 120 Myr and from there, the evolution continues with the much slower nuclear timescales until the solar present age when it reaches the observed solar properties ($L_\odot$, $R_\odot$ and $(Z/X)_\odot$).

In Figure 1.2, the evolution of different element abundances profiles are represented as function of the solar mass. In the left panel, the hydrogen and helium profiles are plotted for 4 different solar ages. The first one, in black, is a model still in the pre-main sequence phase, as it can be identified by the flat profiles of H (solid lines) and He (dashed lines) showing that no nuclear burning takes place. For the other models, the Sun is already in the main-sequence phase, and the burning of H

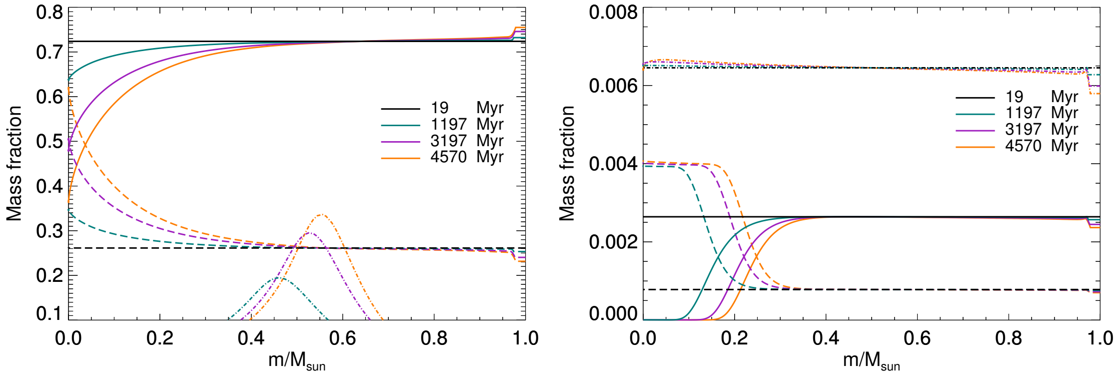

Figure 1.2: Element abundances profile evolution. *Left panel*: Hydrogen (solid lines), Helium-4 (dashed lines) and Helium-3 x 100 (dash-dotted lines). *Right panel*: Carbon-12 (solid lines), Nitrogen-14 (dashed lines) and Oxygen-16 (dashed-solid lines). From a solar model using AGSS09met composition and including diffusion.

into He can be clearly identified. Is also possible to see the effects of diffusion, with the abrupt change for the convective envelope and with the smooth profiles of the hydrogen and helium. Another extra feature worth to mention is the shape of ^{3}He abundance (dash-dotted lines and multiplied by a factor 100), at $m \sim 0.5 - 0.6 M_\odot$ related to the burning of ^{3}He in equilibrium with the pp-chain (for outer regions the ^{3}He is burnt to create ^{4}He through pp-chain while at the outer regions the temperature is to low to form it). In the left panel of Figure 1.2 the effects of the CNO cycle are presented. It is possible to see how the ^{12}C is burnt into ^{14}N, until the first one is exhausted, mainly before the start of the main sequence phase. By following the evolution of these elements it is also possible to notice the effects of the mentioned slow rate of the $^{14}\mathrm{N}(\mathrm{p}, \gamma)^{15}\mathrm{O}$ reaction that does not allow to close the CNO-cycle and therefore, the abundance of oxygen is almost constant along the different evolutionary stages represented.

Finally, in Figure 1.3, the radius, temperature, density and nuclear energy profiles evolution as a function of the solar mass are presented for 4 different ages. It is possible to see the big changes from the pre-main sequence (black color) to the main sequence stages, mainly from the low density and temperature profile and the low nuclear energy generation. Once the main-sequence phase is reached, the properties change much slower due to the low nuclear timescale for steady hydrogen burning.

1.2.4 Solar neutrino fluxes

Neutrinos in the Sun are produced by some of the thermonuclear reactions from pp chain and CNO cycle (see Figure 1.1). These reactions are the β-decay, inverse

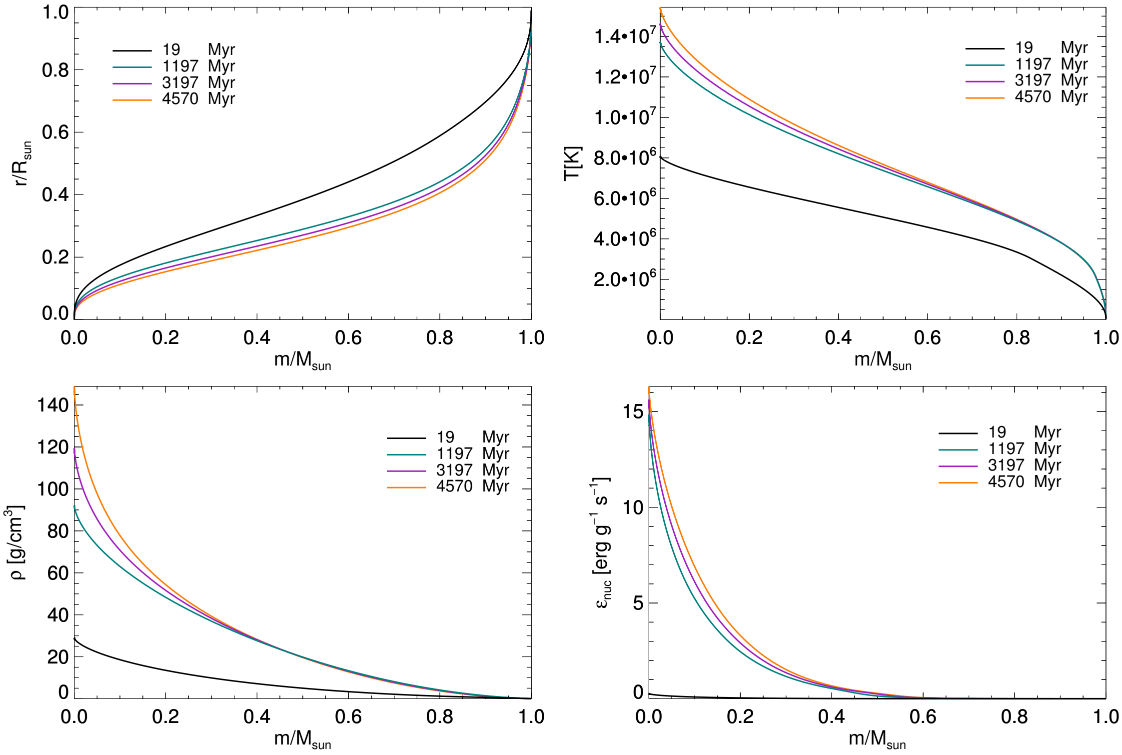

Figure 1.3: Evolution of the solar radius (left-top panel), the temperature (right-top panel), the density (left-bottom panel) and the nuclear energy (right-bottom panel) as a function of the solar mass for 4 different ages. These plots are done by using the data from a solar model using AGSS09met composition.

β-decay and electron captures. As neutrinos leave the Sun unimpeded, measuring the flux of solar neutrinos in the Earth gives very valuable information of the solar interior. For a solar model calibrated to match the present properties of the Sun, the resulting solar fluxes depend on the central temperature approximately ass $\phi \propto T_C^m$ where the exponent m is different for each of the neutrino fluxes. This is useful to predict how the solar fluxes change with variations of the central temperature of the Sun. The solar neutrino fluxes produced in the Sun are listed in Table 1.1 with the corresponding thermonuclear reaction from which they are produced and the exponent m that describes the dependence with the central temperature. The exponents are taken from Bahcall and Ulmer (1996).

99% of the energy generation is produced through pp-chain from which 99.76% is produced through the pp-reaction ($\mathrm{p} + \mathrm{p} \rightarrow {}^2\mathrm{H} + e^+ + \nu_e$). Therefore, assuming the luminosity constraint (nuclear fusion is responsible for the observed solar luminosity Bahcall (2002)), the pp-reaction reaction rate is constrained by the observed solar luminosity.

Neutrino flux	Reaction	Chain	Exponent
$\Phi(\mathrm{pp})$	$\mathrm{p}+\mathrm{p}\rightarrow {}^{2}\mathrm{H}+e^{+}+\nu_e$	ppI, ppII, ppIII	-1.1
$\Phi(\mathrm{pep})$	$\mathrm{p}+e^{-}+\mathrm{p}\rightarrow {}^{2}\mathrm{H}+\nu_e$	ppI, ppII, ppIII	-2.4
$\Phi(\mathrm{hep})$	${}^{3}\mathrm{He}+\mathrm{p}\rightarrow {}^{4}\mathrm{He}+e^{+}+\nu_e$	pp	-
$\Phi({}^{7}\mathrm{Be})$	${}^{7}\mathrm{Be}+e^{-}\rightarrow {}^{7}\mathrm{Li}+\nu_e$	ppII	10
$\Phi({}^{8}\mathrm{B})$	${}^{8}\mathrm{B}\rightarrow {}^{8}\mathrm{Be}^{*}+e^{+}+\nu_e$	ppIII	24
$\Phi({}^{13}\mathrm{N})$	${}^{13}\mathrm{N}\rightarrow {}^{13}\mathrm{C}+e^{+}+\nu_e$	CNOI	24.4
$\Phi({}^{15}\mathrm{O})$	${}^{15}\mathrm{O}\rightarrow {}^{15}\mathrm{N}+e^{+}+\nu_e$	CNOI	27.1
$\Phi({}^{17}\mathrm{F})$	${}^{17}\mathrm{F}\rightarrow {}^{17}\mathrm{O}+e^{+}+\nu_e$	CNOII	27.8

Table 1.1: Reactions from which solar neutrino are produced. The solar neutrinos are summarized in the first column, with the corresponding reaction in the second column and the chain or cycle in the third one. In the last column the exponent m that describes the dependence with the central temperature $\phi \propto T^m$ taken from Bahcall and Ulmer (1996).

As the CN cycle is residual in the Sun (1%) the CN neutrino fluxes depend on the solar interior conditions dominated by the pp-chain. Also, the CN cycle depends on the metallicity of the Sun, specially on C and N due to the catalytic effect that these abundances have on (p,γ) and (p,α). Then, the CN neutrino fluxes can give information about the temperature and interior conditions of the Sun as well as of the metallicity.

With the goal of understanding the solar interior and structure, different experiments have been designed to detect these solar neutrinos on the Earth. Some examples of the solar experiments are Chlorine (Cleveland et al., 1998), Gallex (Hampel et al., 1999), SAGE (Abdurashitov et al., 1999), Kamiokande (Fukuda et al., 1996), SuperKamiokande (Fukuda et al., 2001), SNO (Aharmim et al., 2013) and Borexino (Bellini et al., 2014b). Using the latest data of neutrino experiments, (Bergström et al., 2016) determined the most recent values for the solar neutrino fluxes using purely experimental data and therefore, obtaining results independent from the models. The reader is referred to (Bahcall, 1989) and (Haxton et al., 2013) for a detailed review of solar neutrinos and experiments.

1.2.5 Helioseismology

The Sun surface oscillates with small amplitude as consequence of the propagation of waves at its interior. Basically, *helioseismology* is the study of these observed surface oscillations to extract information about the solar interior. Essentially, the oscillations observed in the Sun are excited in the outer convective region and depending on the restoring force of the propagating wave, they can be classified the following way: p-modes are the acoustic modes for which the pressure is the restoring force, g-modes or gravity modes when the gravity acts as restoring force and f-modes that are surface g-modes and depend essentially on the surface gravity of the star. The oscillation modes can be identified with three numbers, the degree l, the azimuthal order m (where $m = 0$ if no rotation is considered) and the radial order n. This last represent the number of nodes in the radial direction and by convention, it has positive values assigned for p-modes, negative for g-modes and $n = 0$ for f-modes (see Basu 2016; Christensen-Dalsgaard 2002 for reviews on helioseismology).

In the next sections, the basic of solar oscillations are summarized, followed by a brief description of the available observations. Then, the inversion techniques, that basically extract information of the solar interior by using the observed frequencies are introduced. Finally, a brief review of the most relevant information from the interior of the Sun extracted from the observation is presented.

1.2.5.1 Basics on oscillations

In order to relate the properties of the Sun with the observed oscillation frequency some basics on solar oscillations are necessary. First, the equations of hydrodynamics for a fluid (continuity equation, equation of motion, energy equation and the equation of state) are defined assuming static equilibrium and spherical symmetry. Then, because of the very small amplitudes of the oscillations, a small lineal perturbation is added close to the equilibrium. This perturbation is described as a small displacement $\delta\mathbf{r}$ and it is added to all the characteristic quantities of the Sun (P, ρ, T, S, ϵ, ϕ) the following way:

$$p(r) = p_0(r) + p'(r,t) \qquad p(r) = p'(r)Y_{lm}(\theta,\phi)e^{i\omega t}, \tag{1.16}$$

where $p'(r)$ represents the changes with radius while the other term considers the evolution with time.

The solar oscillations can be treated adiabatically and then it is possible to solve the equations and find as solutions the frequencies with which the Sun oscillates. In order to understand the oscillations and the corresponding behavior, the equations can be reduced to second order by using some other approximations, as the Cowling approximation (neglects gravitational perturbations) and the plane-parallel layer under constant gravity (that neglects derivatives of g and r). By defining a new variable $X(r) = c^2\rho^{1/2}\nabla\delta\mathbf{r}$ (where $c^2 = \Gamma_1\frac{P}{\rho}$ is the sound speed) is possible to simplify the system of equations into the following expression:

$$\frac{d^2X(r)}{dr^2} + \frac{\omega_{eff}}{c^2}X(r) = 0 \qquad \omega_{eff} = S_l^2\left(\frac{N_0^2}{\omega^2} - 1\right) + \omega^2 - \omega_c^2 \tag{1.17}$$

where S_l and N^2 are the Lamb frequency and the Brünt-Väisala frequency that are, respectively, the acoustic and gravitational characteristic frequencies. These frequencies define the region where the different modes propagates or the regions where the waves are evanescent. ω_c is the cut-off acoustic frequency that determines the outer turning points of the oscillatory waves.

The expressions of these characteristic frequencies are:

$$\omega_c^2 = \frac{c_0^2}{4H^2}\left(1 - 2\frac{dH}{dr}\right) \qquad H^{-1} = -\frac{d\ln\rho}{dr} \tag{1.18}$$

$$N^2(r) = \frac{Gm(r)}{r}\left(\frac{1}{\Gamma_1}\frac{d\log p(r)}{dr} - \frac{d\log\rho(r)}{dr}\right) \tag{1.19}$$

$$S_l^2 = \frac{l(l+1)c^2}{r^2} \tag{1.20}$$

The general solution of Equation 1.17 can be expressed as: $X(r) = Ae^{i\frac{\omega_{eff}}{c^2}r} + Be^{-i\frac{\omega_{eff}}{c^2}r}$ were A and B are complex constants. There are two different kind of solutions, the ones with $\omega_{eff}^2 > 0$, resulting to an oscillatory behavior or $\omega_{eff}^2 < 0$ where the result is an evanescent wave (exponential grow or decay). The points where $\omega_{eff} = 0$ represent the internal turning points. Then, by means of Equation 1.17, it is possible to define different regions in the Sun:

1. $|\omega| > |N|$ and $|\omega| > S_l$: oscillates as a pressure wave (p-modes)
2. $|\omega| < |N|$ and $|\omega| < S_l$: oscillates as a gravity wave (g-mode)
3. $|N| < |\omega| < S_l$: exponential solution, evanescent wave
4. $|N| > |\omega| > S_l$: exponential solution, evanescent wave

In Figure 1.4 the Lamb (for different angular degree values) and the Brünt-Väisala frequency are plotted for the solar case as well as the propagation regions of a pressure and a gravity wave. Each mode is trapped in a different region, and therefore it gives information about different regions of the Sun. Low order p-modes reach deeper regions while high order modes are trapped in the surface. Both high and low order p-modes can be observed and identified in detail for the solar case.

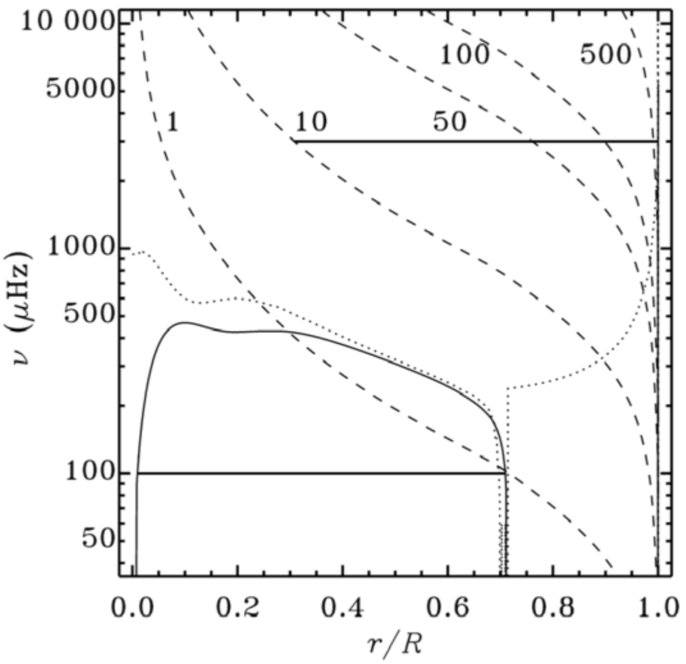

Figure 1.4: Characteristic Brünt-Vaisäla frequency (solid line) and Lamb frequency (dashed line) for different values of l along the solar profile. The horizontal lines represent the propagation regions for a g-mode and a p-mode. *Credit: Fig. 5 from Christensen-Dalsgaard (2002).*

It is clear the importance of g-modes to have observations of the most central part of the Sun. Lowest order p-modes have the turning point at $r/R_\odot \sim 0.1$ and $l = 0$ modes give few information about it, therefore, the observation of p-modes will not give information about the central region of the star so g-modes would give very valuable information of this region. The difficulty is that on the convective region, g-modes are damped and therefore their observation is not possible at this moment (see Section 1.2.5.2).

For a complete and detailed derivation of the oscillations equations the reader is referred to (Aerts et al., 2010; Christensen-Dalsgaard, 2002; Gough, 1993).

1.2.5.2 Observations

Basically, the determination of frequencies of solar oscillations is done by measuring the line-of-sight velocity through the observed Doppler shift of lines in the solar spectrum. There are two different ways to observe the Sun. The first one is to observe the Sun with high spatial resolution images of the spectrum intensity, that allows to measure the detailed frequencies of oscillations of high-order degree. The other method is what is called Sun-as-a-star, where the intensity of the disk is averaged and frequencies of low-degree modes oscillation are obtained.

Different observatories are devoted to detecting and analyzing the solar oscillations. On one hand, there are the ground observatories as for example, BiSON (Birmingham Solar Oscillation Network, (Elsworth et al., 1991)) or IRIS (International Research on the Interior of the Sun, (Fossat, 1991)) that observe the Sun-as-a-star or the GONG (Global Oscillation Network Group, (Harvey et al., 1996)) network that performs spatially resolved velocity observations. In order to have uninterrupted observations of the Sun, each of these ground experiment consists in a network of stations. Then there are the space observations, that are performed by different experiments on board of SOHO (Solar and Heliospheric Observatory, (Domingo et al., 1995)), as MDI (Michelson Doppler Imager, (Scherrer et al., 1995)), VIRGO (Variability of solar Irradiance and Gravity Oscillations, (Fröhlich et al., 1995)) and GOLF (Global Oscillations at Low Frequencies, (Gabriel et al., 1995)), and by HMI (Heliospheric and Magnetic Imager, (Scherrer et al., 2012; Schou et al., 2012)) on board of SDO (Solar Dynamics Observatory, (Pesnell et al., 2012)). As an example of some of the observations, results from MDI are shown in Figure 1.5 where the color corresponds to the power spectra. The color red corresponds to the maximum power and each of the ridges corresponds to a different radial order n for different p-modes.

The detection of solar gravity modes is difficult because their small surface amplitudes. However, some works claim that observations done with GOLF show features compatible with the solar g-modes predictions giving the hint that new and future experiments might be able to detect these g-modes (García, 2010; García et al., 2007)). Nowadays, this result is still controversial and not accepted for all the community as it is discussed in Appourchaux et al. (2010).

1.2.5.3 Inversion techniques

Once the observed frequencies of the Sun are available, the goal is to extract information about the solar structure. To do so, an inverse approach is used to derive the solar structure, the basic idea of it is to adjust the structure of a reference model to match the observed frequencies. The basics on inversion techniques are summarized below, but details about the mathematical derivation of the equations and the discussion of different techniques can be found in different reviews as Gough and Thompson (1991), Christensen-Dalsgaard (2002) or Basu (2016) and references therein.

The variational principle can be used to linearize the perturbed equation of motion around a known solar model obtaining the following expression:

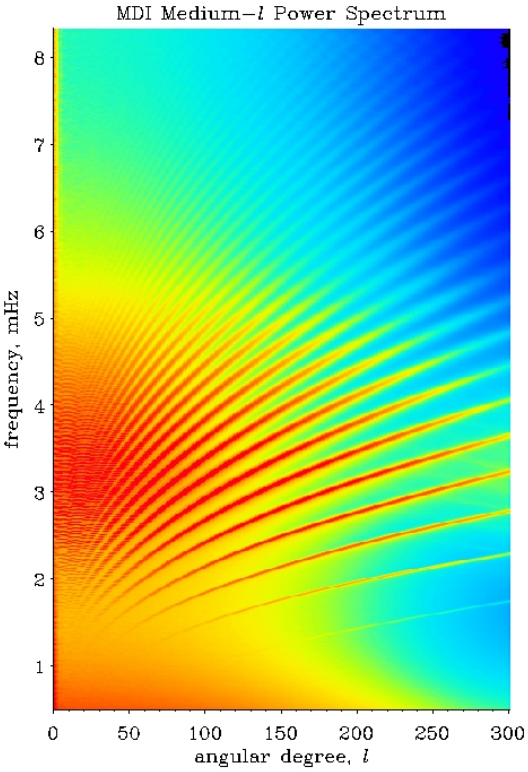

Figure 1.5: Power spectrum from MDI. The ridges of maximum power spectrum determine the modes and the oscillatory frequencies p-waves in the Sun. *This image is courtesy of SOHO/MDI consortium. SOHO is a project of international cooperation between ESA and NASA.*

$$\frac{\delta\nu_{nl}}{\nu_{nl}} = \int_0^R \mathcal{K}^{nl}_{c^2,\rho}(r)\frac{\delta_r c^2}{c^2}(r)\mathrm{d}r + \int_0^R \mathcal{K}^{nl}_{\rho,c^2}(r)\frac{\delta_r \rho}{\rho}(r)\mathrm{d}r + \frac{F(\nu_{nl})}{E_{nl}} \tag{1.21}$$

where $\frac{\delta\nu_{nl}}{\nu_{nl}}$ is the difference between the observed frequencies and the frequencies from the models and $\frac{\delta_r c^2}{c^2}$ and $\frac{\delta_r \rho}{\rho}$ are the model and solar differences of the sound speed and density profiles and are the unknown quantities to be extracted. $\mathcal{K}^{nl}_{c^2,\rho}$ and $\mathcal{K}^{nl}_{\rho,c^2}$ are the averaged kernels calculated from the reference models and basically are functions that give information of the changes on the frequencies in response to changes in the sound speed and density profiles. The last term $\frac{F(\nu_{nl})}{E_{nl}}$ accounts for the so-called *surface effects* that are the discrepancies of the observed frequencies with the model ones caused by problems on modeling the solar atmosphere (see (Christensen-Dalsgaard and Thompson, 1997; Kjeldsen et al., 2008) for details). It is possible to obtain information of (Γ_1, ρ) instead of (c^2, ρ) taking into account that $c^2 = \Gamma_1 P/\rho$. There are several (non-trivial) techniques to invert Equation 1.21 and obtain information about the solar structure, and some of these techniques are reviewed in Basu (2016).

1.2.5.4 Structure information

From the observed frequencies of the Sun and using the corresponding solar inversions, different relevant information about the interior solar structure can be obtained. In the following sections, the most relevant information for this thesis is briefly described.

Sound speed profile: The information that can be obtained from the inversions is $\delta c^2/c^2 = (c^2_\odot - c^2_{mod})/c^2_{mod}$. It is directly related to the thermal stratification of the solar interior ($c^2 = \Gamma_1 P/\rho \propto T/\mu$ for an ideal gas) and it gives very valuable information about all the solar profile but the deeper interior.

Surface Helium ($\mathrm{Y_S}$): The partial ionization of the helium, particularly HeII, produces a depression on Γ_1, and the measure of the depth of this dip on the Γ_1 is used to determine the helium abundance in the surface. See Basu and Antia (2004) and Basu (2016) for details on the procedure. The solar value is $\mathrm{Y_S} = 0.2485 \pm 0.0034$ (Basu, 2016).

Radius of the convective envelope ($\mathrm{R_{CZ}}$): It is the place where the radiative temperature gradient equals the adiabatic value, and thus, it is the boundary where the transition between the radiative and the convective transport takes place. Then, the corresponding change from the radiative temperature gradient to the convective one will lead to measurable changes on the sound speed profile of models with different $\mathrm{R_{CZ}}$. Therefore, these changes on the sound speed can be used to derive the solar location of the boundary of the convective envelope. In Basu et al. (1997) they found a value of $\mathrm{R_{CZ}} = (0.713 \pm 0.001)\mathrm{R}_\odot$.

Frequency separation ratios In general, the model oscillation frequencies are affected by *surface effects* and the inaccurate modeling of the surface layers. Thus, it is useful to have some observable that are independent of this surface region. In Roxburgh and Vorontsov (2003) they show that a given combination of frequencies, the ratio between different small frequency separations and large frequency separations, is independent of the structure of the outer layers and therefore, they give direct information of the solar core. The small frequency separation is sensitive to the solar core and can be expressed as:

$$\delta\nu_{n,l} = \nu_{n,l} - \nu_{n-1,l+2} \approx -(4l+6)\frac{\Delta\nu_{n,l}}{4\pi^2\nu_{n,l}}\int_0^R \frac{\mathrm{d}c}{\mathrm{d}r}\frac{\mathrm{d}r}{c}, \tag{1.22}$$

where $\Delta\nu_{n,l} = \nu_{n+1,l} - \nu_{n,l}$ is the large frequency separation and it is determined by the time that the sound travel from the center to the surface and therefore is affected by the surface effects. Therefore, the ratio of the small to large frequency separation will get rid of the dependence on the surface layers. Both quantities can be easily extracted from the frequency power spectrum. As presented in Roxburgh and Vorontsov (2003), different ratios combinations can be used to study the solar interior as r_{02} and r_{13}. The expressions of these ratios are:

$$r_{02}(n) = \frac{d_{02}(n)}{\Delta_1(n)} = \frac{\nu_{n,0} - \nu_{n-1,2}}{\nu_{n,1} - \nu_{n-1,1}} \tag{1.23}$$

$$r_{13}(n) = \frac{d_{13}(n)}{\Delta_0(n+1)} = \frac{\nu_{n,1} - \nu_{n-1,3}}{\nu_{n+1,0} - \nu_{n,0}} \tag{1.24}$$

1.2.6 Agreement of the observations with SSMs

Once the SSMs and the solar observations have been presented, it is important to analize the agreement of these models with the current observations. One example is the *solar neutrino problem*, that is how was called the discrepancy that existed between the observed solar neutrino fluxes and the predicted ones by the solar models, about a factor three higher. This could not be explained until neutrino flavor oscillations were introduced. Basically, the Sun only produces electron neutrinos and the neutrino experiments were only able to detect this flavor. What was discovered then is that during neutrino propagation their flavor could change converting them into muon and tau neutrinos explaining the deficit of detections (Ahmad et al., 2002). That shown the importance of Standard Solar Models, and how for this case, they were essential to discover the non-massless nature of neutrinos and their flavor oscillations. Nowadays, the conflict between observations and SSMs is related to the determination of the solar composition. Basically, the *solar abundance problem* is the disagreement of the SSMs with the helioseismological observations when the most recent determination solar abundances are used to construct the solar models (Bahcall et al., 2005; Basu and Antia, 2004; Bergemann and Serenelli, 2014; Serenelli et al., 2009). This is discussed it together with the corresponding possible solutions in the next section.

1.2.6.1 Solar Abundance Problem

As it has already been mentioned in Section 1.2.2, the choice of $(Z/X)_\odot$ is crucial and depends on the choice of the solar composition. One frequently adopted solar photospheric composition is that provided by Grevesse and collaborators (hereafter GS98) Grevesse and Sauval (1998), based on 1-D solar atmosphere models, from which $(Z/X)_\odot = 0.0229$. SSMs based on GS98 composition are in good agreement with helioseismic observables and solar neutrino fluxes determinations. A more recent compilation of the solar photospheric abundances has been provided by Asplund and collaborators Asplund et al. (2009) (hereafter AGSS09). It is based on a more accurate analysis with new 3-D hydrodynamical models of the solar atmosphere that reproduces very well the observed solar atmosphere properties. As a result of these and other improvements in atomic data, line blending or the assumption of NLTE in solar spectroscopic analysis, they obtain a much lower surface metallicity $(Z/X)_\odot = 0.0178$, mainly due to the lower values of the volatiles (C, N, O and Ne) that leads to SSMs in strong disagreement with the solar structure inferred from helioseismology.

Possible solutions to the *solar abundance problem* can be related to the spectral analysis or to the construction of the SSMs. About the first one, uncertainties on the atmosphere modeling or on the spectroscopic techniques could lead to the discrepancies observed, although it is unlikely due to the more sophisticated methods and synthetic spectra used for the most recent compilations. On the other hand, the solution could be related to solar models, either for some missing ingredient or to changes on the used input parameter. Lately, the focus have been on the radiative opacities used to compute the SSMs. In Christensen-Dalsgaard et al. (2009), and more recently in Villante et al. (2014), it was pointed out that current seismic and neutrino observables are only sensitive to the actual opacity profile that defines the temperature stratification of the Sun. The opacity profile is determined by a set of radiative opacity calculations (eg. OP Badnell et al. 2005, OPAL Iglesias and Rogers 1996) and the solar composition (eg. GS98 or AGSS09). While it is not possible to separate these two contributions, the solar opacity profile is well constrained by helioseismic and solar neutrino experiments Villante et al. (2014). Therefore, changes on the adopted radiative opacities could bring the agreement back to the level reached when the old composition was used. Some other possibilities studied have been the inclusion of non standard ingredients to the solar models as enhanced diffusion (Guzik et al., 2005), accretion of metal poor material (Castro et al., 2007; Guzik and Mussack, 2010; Serenelli et al., 2011), early mass loss and convective overshooting (Guzik and Mussack, 2010), extra dynamical processes as internal rotation or magnetic fields

(Turck-Chièze et al., 2010) or asymmetric dark matter (Vincent et al., 2015, 2016). Some of these works have provided at least partial solutions to the *solar abundance problem*. Finally, it is important to consider that the problem could be partially coming from the solar abundances (as the abundances of Caffau et al. 2011, with $Z_S = 0.02046$, seem to indicate) and from some ingredient of the solar models that should be revised or included.

1.3 Physics Beyond the Standard Model of Particles

The Standard Model of Particles (SM) is not a complete theory, and extensions are necessary to address some of the most pressing open questions in fundamental physics. Among others, some of these are: nature of dark matter, matter-antimatter asymmetry in the Universe, origin of neutrino masses, strong CP-violation problem. In order to solve these problems, physics beyond the SM is needed and the existence of new particles and/or non-standard properties of known particles are generally invoked. In particular, the existence of weakly interacting particles beyond the standard model or the existence of standard particles with non-standard properties can modify the internal structure of the stars and its evolution in different ways. For example, weakly interacting massive particles (WIMPs), too massive to be created inside stars, can be accreted from the dark matter halo of the Milky Way and contribute to the transport of energy inside stars Spergel and Press (1985); Taoso et al. (2010); Vincent and Scott (2014) and, in the case of self-annihilating particles act as a localized energy source. Weakly interacting light particles (WISPs), on the other hand, can be thermally produced in the stellar interiors and can easily escape due to their large mean free path and act as energy sinks. The increased rate of energy-loss then changes the internal structure of stars and also modifies evolutionary timescales. This thesis is focused in the second kind of particles, the weakly interacting light particles. In this chapter, these particles are introduced and the basics on how stars can be used to give constraints on their properties are presented. Finally the main instruments and experiments devoted to detect these kind of particles are reviewed.

1.3.1 Weakly Interacting Light particles

Some examples of predicted WISPs are axions (and Axion Like Particles (ALPs)), hidden photons, minicharged particles or chamaleons. Summarizing it here, *axions* are very light pseudoscalar particles introduced to solve the CP problem that can couple with photons or electrons (Peccei and Quinn, 1977) and could account for most of dark matter; *hidden photons* are vector bosons that couple weakly via kinetic mixing with the standard photons (Candelas et al., 1985); *minicharged particles* are fermions with an unquantized (and small) fraction of the electron charge (Holdom, 1986a,b); *chamaleons* are scalar particles that couple with ordinary matter with forces much weaker than gravity and they are motivated by the existence of dark energy (Khoury and Weltman, 2004a,b). Further details about the particles studied in this thesis can be found later on in Section 5.1 and in Jaeckel and Ringwald (2010).

1.3.2 Astrophysical constraints on WISPs

Stellar physics, while far from being a closed subject, is a mature discipline and it provides an accurate understanding of the internal structure of stars and their evolution. The sheer mass and size, the extreme conditions reigning in stellar interiors and, in many cases, the extremely long lifetimes that allow to *integrate* small effects over a very long time make stars appealing as laboratories for particle physics under conditions not reproducible anywhere else (see Raffelt, 1996 for a detailed review).

1.3.2.1 Energy-loss argument

WISPs leave unimpeded from the star efficiently carrying away energy from the stellar interior. Therefore, an exotic energy term should be included in Equation 1.1c with negative contribution to it,

$$\frac{\partial l}{\partial m} = \epsilon_g + \epsilon_n - \epsilon_\nu - \epsilon_{WISP}, \tag{1.25}$$

where the detailed formulation of ϵ_{WISP} depend on the nature of the particle being studied (see Chapter 5 for details).

The impact of this extra term in degenerate objects such as white dwarfs is straightforward, directly contributing to the cooling and thus, accelerating it. For non-degenerate scenarios where nuclear reactions still take place the impact is different. If an extra energy-loss channel is introduced, according to the virial theorem (see Equation 1.3), the star contracts rising the temperature in the interior that produces an acceleration of the nuclear reactions. This follows until the increase of nuclear reaction can compensate the energy loss and the gravothermal equilibrium state is recovered. Therefore, the evolution of the star is accelerated, its lifetime shortened and the structure modified when compared with the standard scenario (Frieman et al., 1987; Raffelt, 1996).

1.3.2.2 Astrophysical sites

The production rate of each particle depends differently on stellar conditions. Consequently, the impact of different particles on stellar structure will depend on the class of stars and on the evolutionary state. Several works have given constraints on the properties of the weakly interacting light particles using different stellar objects. In this section, the main astrophysical sites used to constraint particle physics and some concrete examples are reviewed.

Globular clusters Globular clusters are groups of stars that are gravitationally bound and were supposedly formed at the same time from the same molecular cloud. Therefore, its color-magnitude diagram will represent an isochrone with stars with the same age and metallicity but different masses. Consequently, this color-magnitude diagram can be tested to study deviations from the standard stellar evolution due to the presence of exotic particles. One of the useful features for constraining extra energy loss terms is the tip of the red giant, that is the maximum luminosity reached by the red giants of a given mass before the helium core is ignited. The luminosity of the RGB-tip depends on the mass of the degenerate helium core. If an extra energy-loss term is included, this will contribute in cooling the core and delaying the ignition of helium. That will result in a larger helium core due to the hydrogen burning shell on top of the core, that consequently will rise the luminosity of the RGB tip. The RGB-tip observed from the color-magnitude has been used to place constraints to the electron-axion coupling constant and to the magnetic moment of the neutrino among other cases (Raffelt, 1990; Raffelt and Weiss, 1995; Viaux et al., 2013). Also, the presence of energy-loss rate on the horizontal branch (HB) stars, that are stars burning helium in non-degenerate conditions, will shorten their life due to the *energy-loss argument*. Therefore, the ratio of RGB stars compared with the HB stars will be higher if non-standard particles are present. This ratio can be calculated using the color-magnitude diagram and counting the number of stars in each of the evolutionary stages. This has been used to constrain the axion-photon coupling constant or properties of the hidden photons (An et al., 2013; Ayala et al., 2014; Raffelt and Dearborn, 1988; Redondo and Raffelt, 2013).

Intermediate mass-stars When an intermediate mass-star ($\sim 5M_{\odot} - 12M_{\odot}$) start burning helium in non-degenerate conditions its effective temperature increases towards the blue region of the Hertzsprung-Rusell (HR) to go back to lower effective temperatures after the helium core burning phase is finished. These changes on the

HR diagram is are called *blue loops.* The presence of an extra-energy loss term during the helium-core burning phase can make this blue loop disappear due to an extra cooling, thus contradicting the presence of stars in this evolutionary phase, typically known as Cepheids stars (Friedland et al., 2013).

White dwarfs The anomalous cooling induced by the extra energy-loss would shorten the cooling timescale of white dwarfs (WD) affecting their luminosity function (LF). Basically, LF is defined as the number of white dwarfs per cubic parsec as function of unit luminosity and it gives information about the cooling processes of these objects, including the contribution of hypothetical exotic particles (Dreiner et al., 2013; Isern et al., 2008; Miller Bertolami et al., 2014; Raffelt, 1986). Alternatively, the study of the pulsation properties of variable WDs can also be used as test of non-standard energy losses. The secular drift of the period of g-modes is related to the cooling process of the WD, and therefore, the presence of non-standard particles would increase this drift (Córsico et al., 2012; Isern et al., 1992, 2010).

Neutron stars After they formation, neutron stars cool rapidly via neutrino emission. If additional energy losses are present, the cooling rate will be enhanced. By assuming that the extra energy loss cannot exceed the neutrino energy emission an upper limit on the axion mas can be placed (Keller and Sedrakian, 2013; Umeda et al., 1997). This upper limit can also be determined by observing deviations of surface cooling in real time (Leinson, 2014).

SN1987A Supernova SN1987A is an observed supernova where the extra cooling of the proto-neutron core would shorten the neutrino pulse (Mayle et al., 1988, 1989; Raffelt and Seckel, 1988; Turner, 1988) and the hypothetical production of axions could produce a prompt gamma ray signal (Payez et al., 2015; Turner, 1988).

The Sun The proximity and the availability of a large amount of observations and detailed solar models make the Sun a key object to study the effect of different kind of particles although their interior conditions are not as extreme as other objects. This is the case study in this thesis and in Chapter 5, the results when using all the information available of the Sun (solar neutrino fluxes and helioseismology) to constraint the properties of different particles are presented. A review of the main constraints placed using the Sun can be found in Chapter 5.

1.3.3 Experiments and detectors

Different experiments and detectors have been designed to detect WISPs or restrict the parameter space of the different particles. Some of these experiments are briefly described in this section.

One of the most relevant examples are helioscopes (Sikivie, 1983), experiments dedicated to detect WISPs produced in the Sun, the case study of this thesis. Helioscopes are detectors pointing toward the Sun with a magnetic field to convert axions into detectable X-rays. Due to the conditions of the solar interior, a lot of interactions are expected and a large axions flux predicted, making this experiment very powerful to detect axions and non-standard particles. Some examples of helioscopes are SUMICO (Moriyama et al., 1998) and CAST, one of the most sensitive helioscope currently working (Zioutas et al., 2005), that for example, placed the most restrictive limit for the coupling constant for photon-axion (Andriamonje et al., 2007). Looking at the future, there is IAXO, a new generation of helioscope that is expected to be at least one order of magnitude more sensitive than CAST (Irastorza et al., 2012). Another example are the laser experiments. They can be alternatively called *light shining through walls* and the basis of them are that a laser beam goes through a magnetic field that converts a fraction of the photons to axions with the same photon energy. Then, a wall blocks the photons but the axions can cross it unimpeded entering to the re-conversion region where another magnetic field converts the axions back to photons (van Bibber et al., 1987). Microwave cavities (or haloscopes) aim to detect dark matter axions by converting them into photons using a microwave cavity with an strong magnetic field. This conversion would take place when the cavity frequency matches the axion mass. Some examples are the ADMX (Asztalos et al., 2001) and CARRICK II (Tada et al., 1999) experiments. A future experiment aiming to detect dark matter (DM) axions without having to scan over the different possible frequencies are the dish antennas. The basic concept of this experiment is to focus the electromagnetic radiation emitted by conducting surfaces when excited by cold DM into a detector. The large size of the antennas could compensate the lack of resonance present in the microwave cavity experiment (Horns et al., 2013). Experiments designed to detect dark matter in the form of WIMPs have also been adapted to search for axions, being the Large Underground Xenon experiment (LUX) (Akerib et al., 2017) one example.

The previous paragraph is focused on experiments used in the search of axions, but they can also be used for other particles as hidden photons or minicharged particles. For these cases, the concept of the experiment is the same but the magnetic fields for the conversion-re-conversion are not used. There are also other experiments exclusively designed to detect exotic light particles as hidden photons or minicharged particles. One of them is the helioscope SHIPS Schwarz (2012), experiments designed to detect light dark matter through atomic ionization as XENON10 (Angle et al., 2011) or experiments designed at future beam collider facilities (see Essig et al., 2013 for more details). In this section, some of the most relevant experiments have been reviewed, but the reader is referred to the reviews of Essig et al. (2013) and Jaeckel and Ringwald (2010) for further information about searches on weakly interacting light particles.

Chapter 2

A new generation of Standard Solar Models

The origin of Standard Solar Models (SSMs) is related to the need of having solar neutrino fluxes predictions in order to explore the possibilities of solar neutrino experiments. Combined with the development of new numerical techniques, the first SSMs were developed (e.g. Bahcall et al., 1963; Sears, 1964). Later on, and still motivated by the determination of the neutrino fluxes and by the improvements in the inputs of the models as nuclear reaction rates or radiative opacities, several new models were released, as for example, Bahcall and Ulrich (1988) and Turck-Chieze et al. (1988). The use of helioseismic data was crucial for the solar models and, as an addition of predictions for the solar fluxes, new models started computing frequencies from models in order to compare them with the available observations, (e.g. Christensen-Dalsgaard and Gough, 1980, Bahcall and Ulrich, 1988). By the same time, solar models made a new big step by including diffusion as a standard ingredient obtaining better agreement with observations (Cox et al., 1989, Christensen-Dalsgaard et al., 1993). During the following years and until nowadays, the Standard Solar Models have been constantly updated with new releases of the input physics. Some examples of Standard Solar Models most widely used are: Bahcall and Pinsonneault (1992), Christensen-Dalsgaard et al. (1996), Bahcall et al. (2001) (used to solve the *solar neutrino problem*) or Serenelli et al. (2011) among other models.

In the present, and as it has been presented in Chapter 1, the *solar abundance problem* is one of the main topics that the current generation of SSMs is trying to give a solution on. During the recent years, the focus has been placed on new calculations of these radiative opacities and how the results could go on the direction of mitigating the *solar abundance problem.* Some examples of this efforts are the updated calculations by the Opacity Project (Badnell et al., 2005), followed by OPAS

(Blancard et al., 2012; Mondet et al., 2015), STAR (Krief et al., 2016b) and a new version of OPLIB, the opacities from Los Alamos (Colgan et al., 2016)[1]. Apart from the new releases of theoretical radiative opacitities, Bailey et al. (2015) have presented the first ever measurement of opacity under conditions close to those at the bottom of the solar convective envelope. While the experiment has been carried out only for iron, their conclusion is that all theoretical calculations predict a too low Rosseland mean opacity, at a level of $7 \pm 4\%$, for the temperature and density combinations realized in the experiment. Krief et al. (2016a) have casted additional doubts in the accuracy of currently available opacity calculations after showing that the approximations done in the modelling of line broadening have a critical impact on the final Rosseland mean opacity.

In parallel to work on radiative opacities, there have been new determinations (with respect to the last SSMs released Serenelli et al. (2011)) of important nuclear reaction rates affecting energy and neutrino production in the Sun. These updates introduce differences in model expectations for neutrino fluxes comparable to current experimental uncertainties of the well determined $\Phi(^7\mathrm{Be})$ and $\Phi(^8\mathrm{B})$ fluxes. Additionally, development in `GARSTEC` (Section 1.1.3) allows now the implementation of an equation of state obtained for a mixture of elements that is consistent with the solar composition adopted in the calculation of the SSM.

Motivated by the developments just described, in this chapter a new generation of SSMs that includes updates to the microscopic input physics of the models and revised model errors calculated using a new set of Monte Carlo simulations following the work presented in Bahcall et al. (2006) is presented. Also, in the light of the new results in radiative opacities, the previous treatment of opacity uncertainties in solar model predictions is improved. The implementation of a new flexible scheme based on opacity kernels (Tripathy and Christensen-Dalsgaard, 1998) allows to test the impact of any opacity error function without the need to perform lengthy calculations of large sets of solar models. In addition to presenting the models, an exhaustive comparison of SSMs based on alternative compositions against different ensembles of solar observables have been carried out. The hypothesis that radiative opacities can offer a solution to the solar abundance problem is also tested.

Some of the main results and conclusions of this chapter have been published in Vinyoles et al. (2017).

---

[1] These opacities tables are exhaustively tested and discussed in Chapter 3

2.1 Main characteristics and updates

In Serenelli et al. (2011) a generation of SSMs was computed using the nuclear reaction rates recommended in the Solar Fusion II paper (Adelberger et al., 2011; hereafter A11). For simplicity, they are referred as the SFII SSMs. Here a new generation of SSMs, Barcelona 2016 or B16 for short, is presented. B16 models share with the SFII models much of the physics. As for SFII SSMs, models have been calculated using `GARSTEC`. Physics included in the models, unless stated otherwise, is as follows. Atomic opacities are from OP Badnell et al. (2005) and are complemented at low temperatures with molecular opacities from Ferguson et al. (2005). Microscopic diffusion of helium and metals is followed according to the method of Thoul et al. (1994). Convection is treated according to the mixing length theory and the atmosphere is a grey Krishna-Swamy model (Krishna Swamy, 1966). Screening is treated by using Salpeter's formulation of weak screening Salpeter (1954). For more details about SSMs calibrations and physics included in the models see Serenelli et al. (2011) and Serenelli (2016).

However, B16-SSMs include updates in some nuclear reaction rates and, most notably, a new treatment of uncertainties due to radiative opacities. In the following sections there is a description of the main ingredients and updates of the new generation of SSMs related to composition, nuclear rates, equation of state and the treatment of errors.

2.1.1 Composition

As described in Section 1.2.1.5, solar photospheric (surface) abundances of almost all metals can be determined from spectroscopy. In the context of solar models, the only relevant exceptions are Ne and Ar, the latter with a much lesser influence, that have to be determined by other, more indirect, methods (see Asplund et al. 2009 for details). For refractories, however, meteorites offer a very valuable alternative method (see e.g. Lodders et al. 2009) and, in fact, elemental abundances determined from meteorites have been historically more robust than spectroscopic ones.

In Asplund et al. (2009) some differences existed between photospheric and meteoritic abundances for some refractory elements. In particular, photospheric Fe and Ca were 0.05 dex higher than their meteoritic counterparts, while for Mg the difference was 0.07 dex. In a recent series of papers Grevesse et al. (2015); Scott et al. (2015a,b) (for short, AGSS15) have updated previous results from AGSS09 for all but the CNO elements (and Ne, as its abundance is linked to that of O). Interestingly, the photospheric abundances of the discrepant elements just mentioned have shifted towards meteoritic values and with the new AGSS15 recommended photospheric values the differences above are now 0.02 dex for Fe, 0.03 dex for Ca and 0.06 dex for Mg.

In the past, the robustness of meteoritic abundances have made them the preferred choice as source of solar abundances. Recent changes in the AGSS15 photospheric values compared to AGSS09 give added strength to this preference. Then, in building the B16-SSMs, the sets of solar abundances used are always composed by meteoritic values for refractory elements and photospheric values for volatile elements. Both scales are tied together by forcing a rigid translation of the meteoritic scale such that the meteoritic abundance of Si matches the photospheric value (see Section 1.2.1.5). The photospheric abundance of Si in AGSS15 remained unchanged from AGSS09. For this reason, the discussion above on the choice of a combined photospheric and meteoritic solar mixture, and the fact that unfortunately AGSS15 does not include a revision of CNO abundances, does not lead to any changes with respect to the AGSS09 based set of solar abundances.

In Caffau et al. (2011) they find values for C, N and O in between the ones of GS98 and AGSS09 by also using 3D-RHD models for the atmosphere. By complementing the photospheric abundances with the ones presented in Lodders et al. (2009) and taking the meteoritic values for the refrectories also from Lodders et al. (2009), the CO5BOLD solar mixture is obtained with a metallicity that lays in between of the considered GS98 and AGSS09 solar mixtures.

Given that the preferred choice are the meteoritic abundances and that AGSS15met is exactly the same than AGSS09met, the two central sets of solar abundances from which SSM are presented are the same employed in Serenelli et al. (2011), GS98 and AGSS09met representing high and low solar metallicity respectively. As CO5BOLD composition lays right in between of these both composition, as well as the corresponding SSMs results, the final choice is to present GS98 and AGSS09met compositions as upper and lower limits.

In Section 1.2.1.5 the differences between the solar mixtures described above have been briefly summarized, their main characteristics can be found in the following list and the main element abundances and the corresponding errors can be found in Table 2.1.

- **GS98**: Photospheric (volatiles) + meteoritic (refractories) abundances from Grevesse and Sauval (1998). The metal-to-hydrogen ratio used for the calibration is $(Z/X)_\odot = 0.02293$,

Element	GS98	CO5BOLD	AGSS09met	AGSS09ph	AGSS15ph
C	8.52 ± 0.06	8.50 ± 0.06	8.43 ± 0.05	8.43 ± 0.05	8.43 ± 0.05
N	7.92 ± 0.06	7.86 ± 0.12	7.83 ± 0.05	7.83 ± 0.05	7.83 ± 0.05
O	8.83 ± 0.06	8.76 ± 0.07	8.69 ± 0.05	8.69 ± 0.05	8.69 ± 0.05
Ne	8.08 ± 0.06	8.05 ± 0.10	7.93 ± 0.10	7.93 ± 0.10	7.93 ± 0.10
Mg	7.58 ± 0.01	7.54 ± 0.06	7.53 ± 0.01	7.60 ± 0.04	7.59 ± 0.04
Si	7.56 ± 0.01	7.52 ± 0.01	7.51 ± 0.01	7.51 ± 0.03	7.51 ± 0.03
S	7.20 ± 0.06	7.16 ± 0.02	7.15 ± 0.02	7.12 ± 0.03	7.12 ± 0.03
Ar	6.40 ± 0.06	6.50 ± 0.10	6.40 ± 0.13	6.40 ± 0.13	6.40 ± 0.13
Fe	7.50 ± 0.01	7.46 ± 0.08	7.45 ± 0.01	7.50 ± 0.04	7.47 ± 0.04
$(Z/X)_\odot$	0.02292	0.02046	0.01780	0.01813	0.01797

Table 2.1: Abundances of the GS98 (Grevesse and Sauval (1998)), AGSS09ph and AGSS09met (Asplund et al. (2009)), COBOLD (Caffau et al. (2011), Lodders et al. (2009)) and AGSS15ph (Grevesse et al. (2015); Scott et al. (2015a,b)) solar mixtures given as $\log \epsilon_i \equiv \log N_i/N_H + 12$.

- **CO5BOLD**: Photospheric abundances from Caffau et al. (2011), complemented by Lodders et al. (2009) and using the meteoritic abundances from Lodders et al. (2009) $(Z/X)_\odot = 0.02046$.
- **AGSS09met**: Photospheric (volatiles) + meteoritic (refractories) abundances from Asplund et al. (2009). The metal-to-hydrogen ratio used for the calibration is $(Z/X)_\odot = 0.01781$.
- **AGSS09ph**: Photospheric (volatiles) abundances from Asplund et al. (2009). The metal-to-hydrogen ratio used for the calibration is $(Z/X)_\odot = 0.01813$.
- **AGSS15ph**: Photospheric (volatiles) abundances from Grevesse et al. (2015); Scott et al. (2015a,b) and CNO from Asplund et al. (2009). The metal-to-hydrogen ratio used for the calibration is $(Z/X)_\odot = 0.01797$.

2.1.2 Nuclear Rates

The most relevant changes in the B16 SSMs compared to SFII models arise from updates in the nuclear reaction rates. As usual, the astrophysical S-factor $S(E)$ is expressed as a Taylor series around $E = 0$ (Equation 2.1, see also Adelberger et al. 2011)

$$S(E) = S(0) + S'(0) \cdot E + \frac{1}{2}S''(0) \cdot E^2 + \mathcal{O}(E^3). \tag{2.1}$$

	$S(0)$	Uncert. %	$\Delta S(0)/S(0)$	Ref.
S_{11}	$4.03 \cdot 10^{-25}$	1	$0.5\%^{\dagger}$	1,2,3
S_{17}	$2.13 \cdot 10^{-5}$	4.7	+2.4%	4
S_{114}	$1.59 \cdot 10^{-3}$	7.5	-4.2%	5

Table 2.2: Astrophysical S-factors (in units of MeV b) and uncertainties updated in this work. Fractional changes with respect to A11 are also included. $^{\dagger}S_{11}(0)$ underestimates the actual increase in $S_{11}(E)$ that is dominated by changes in higher orders in the Taylor expansion (see text). (1) Marcucci et al. (2013), (2) Tognelli et al. (2015), (3) Acharya et al. (2016), (4) Zhang et al. (2015), (5) Marta et al. (2011).

Updates in the reaction rates are generally introduced as changes in $S(0)$ and, eventually, the first and higher order derivatives. New $S(0)$ values and errors are summarized in Table 2.2 together with the fractional changes in $S(0)$ with respect to A11. Rates not listed in Table 2.2 are taken from A11 and remain unchanged with respect to the SFII SSMs.

Details about the updated rates are specified in the following sections.

2.1.2.1 $\mathbf{p(p, e^{+}\nu_e)d}$

$S_{11}(E)$ has been recalculated in Marcucci et al. (2013) by using chiral effective field theory framework, including the P-wave contribution that had been previously neglected. In addition, they provide fits to $S(E)$ using the Taylor expansion (Equation 2.1). For the leading order they obtain $S_{11}(0) = (4.03 \pm 0.006) \cdot 10^{-25}$ MeV b. This is 0.5% higher and with a much smaller error than the recommended value in A11. More recently, and also using chiral effective field theory, Acharya et al. (2016) determined $S_{11}(E)$, resulting in $S_{11}(0) = 4.047^{+0.024}_{-0.032} \cdot 10^{-25}$ MeV b. This is in very good agreement with Marcucci et al. (2013) result. Acharya et al. (2016) have performed a more thorough assessment of uncertainty sources leading to an estimated error of 0.7%, much closer to the 1% uncertainty which was obtained by A11. Based on the larger error estimate by Acharya et al. (2016) and the difference in the central values for $S_{11}(0)$ and higher order derivatives between both works, it is preferred to make a conservative choice and a 1% uncertainty for the p+p reaction rate is adopted.

The evaluation of $S(E)$ presented by Marcucci et al. (2013) allows a full integration of the p+p rate, avoiding the Taylor expansion. Moreover, Tognelli et al. (2015) provide a routine[2] to directly compute the p+p rate that is used to implement this rate in `GARSTEC`. In Figure 2.1, the ratio between the newly adopted (Marcucci et al.,

---

[2] `http://astro.df.unipi.it/stellar-models/pprate/`

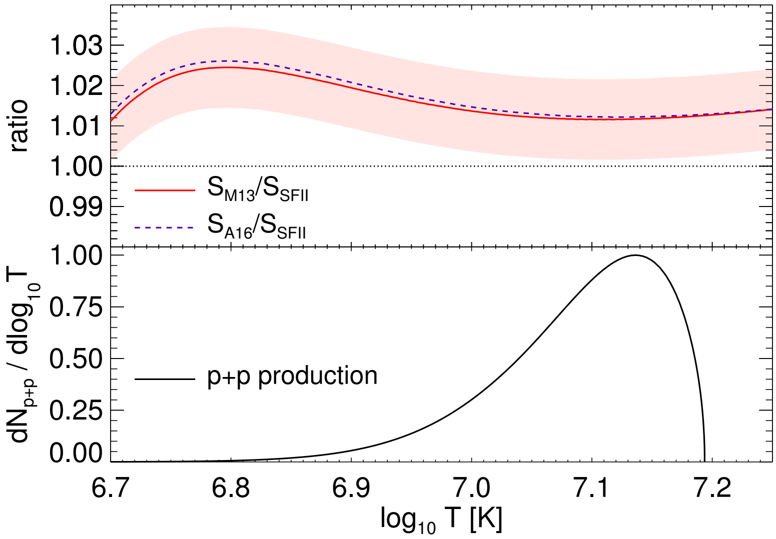

Figure 2.1: Top panel: ratio of p+p reaction rates as a function of temperature between Marcucci et al. (2013) and A11 (red solid line) and between Acharya et al. (2016) and A11 (purple dashed line). The band is the conservative 1σ uncertainty (1%). Bottom panel: number of p+p reactions produced per $\delta \log T$ interval as a function of temperature in SSMs (arbitrary units).

2013) and the older A11 reaction rates are plotted as a function of temperature For comparison, the rate inferred from Acharya et al. (2016) is also shown. The comparison with the A11 rate shows a larger variation than the 0.5% difference quoted for $S_{11}(0)$ that is due to changes in the first and the higher order derivatives, as well as to the different integration methods to compute the rate. The solid black line in the plot shows the distribution of p+p reactions in the Sun and illustrates that for solar conditions the average difference in the rates is of order 1.3%.

2.1.2.2 ^{7}Be(p, γ)^{8}B

A11 recommends $S_{17}(0) = (2.08 \pm 0.07 \pm 0.14) \cdot 10^{-5}\,\mathrm{MeV\,b}$, where the first error term comes from uncertainties in the different experimental results and the second one from considering different theoretical models employed for the low-energy extrapolation of the rate. Zhang et al. (2015) present a new low-energy extrapolation based on Halo Effective Field Theory, which allows for a continuous parametric evaluation of all low-energy models. Marginalization over the family of continuous parameters then amounts to marginalizing the results over the different low-energy models. They obtain $S_{17}(0) = (2.13 \pm 0.07) \cdot 10^{-5}\,\mathrm{MeV\,b}$, with an uncertainty that equals that of the experimental uncertainty as given above. In A11, this error source was inflated to accommodate systematic differences seen among different experimental results (see in particular their Appendix on Treating Uncertainties). This problem was not found by Zhang et al. (2015) in their analysis. While the different findings by A11 and Zhang et al. (2015) regarding inconsistency in the nuclear data need further study, in order to err on the safe side, an intermediate error between those from Zhang et al. (2015) is adopted. Therefore, $S_{17}(0) = (2.13 \pm 0.1) \cdot 10^{-5}$ MeV b is adopted and the derivatives are updated by using the recommended values of Zhang et al. (2015).

2.1.2.3 $^{14}\mathrm{N}(\mathrm{p},\gamma)^{15}\mathrm{O}$

Marta et al. (2011) present new cross-section data for this reaction obtained at the Laboratory for Underground Nuclear Astrophysics (LUNA) experiment. With the new data and using R-matrix analysis they recommend a new value for the ground-state capture of $S_{GS}(0) = (0.20 \pm 0.05) \cdot 10^{-3}$ MeV b, down from the previously recommended value of $0.27 \cdot 10^{-3}$ MeV b (A11). Combined with other transitions (see Table XI in that work) this leads to $S_{114}(0) = (1.59 \cdot 10^{-3})$ MeV b, about 4% lower than the previous A11 recommended value. The derivatives and the errors remain unchanged.

2.1.2.4 $^{3}\mathrm{He}(^{4}\mathrm{He},\gamma)^{7}\mathrm{Be}$

deBoer et al. (2014) combine *recent* (post 2004) experimental results including those in A11 but also newer data at medium and higher energies, from 300 up to 3500 keV (see references in their work). They perform a global R-matrix fit to determine the extrapolated $S_{34}(0)$ value and a Monte Carlo analysis of the R-matrix fit to determine the uncertainties in the rate. This is a very different approach to that used in A11, where microscopic models were used to determine $S_{34}(0)$ for four independent datasets and then combined statistically to provide a final result for $S_{34}(0)$. The final value reported by deBoer et al. (2014) is $S_{34}(0) = (5.42 \pm 0.23) \cdot 10^{-4}$ MeV b. The central value is $\sim 3\%$ lower than the previous A11 recommended value. It should be pointed out that this value is systematically lower than three out of the four results used in A11 and very similar to the fourth one. The underlying reasons for these differences are not discussed in deBoer et al. (2014).

More recently, Iliadis et al. (2016) have performed a global Bayesian estimation of S_{34} using the same data as in A11, but extended up to 1.6 MeV instead of 1 MeV, and found $S_{34}(0) = (5.72 \pm 0.12) \cdot 10^{-4}$ MeV b. This is 2% higher than A11 and almost 6% larger than deBoer et al. (2014). The use of larger energy ranges in deBoer et al. (2014) and Iliadis et al. (2016) compared to what is required for an accurate determination of $S_{34}(E)$ in the energy range required for solar neutrino calculations (see A11) makes one wary of the impact that derivatives of $S(E)$ could have on the expansion.

Given the reasons above, and that deBoer et al. (2014) and Iliadis et al. (2016) results bracket that from A11, the latter is the final preferred choice in B16 SSMs. However, it is important to take into account that a reduction in $S_{34}(0)$ such as that claimed by deBoer et al. (2014) would have an impact in the comparison between solar neutrino data and SSMs built with the GS98 or AGSS09met compositions for the $\Phi(^{8}\mathrm{B})$ and $\Phi(^{7}\mathrm{Be})$ fluxes. These alternative results are further discussed in Section 2.3.

2.1.3 Equation of State

SFII models used the equation of state (EoS) by OPAL Rogers and Nayfonov (2002b) in its 2005 version. This EoS has one slight disadvantage: the mixture of metals includes only C, N, O and Ne and their relative abundances are hardwired in the tables provided and cannot be modified. This does not represent an obstacle in using the OPAL EoS which has been, in fact, the most widely used EoS for solar models. However, it is desirable that the EoS offers consistency with the metal mixture used in the calibration of the solar model.

FreeEOS, the EoS developed by A. Irwin (Cassisi et al., 2003), allows overcoming this difficulty. The source codes are freely available[3] and although the running time is too long to allow *inline* implementation of the EoS during solar model calculations, precomputed tables with any desired solar composition can be computed in advanced.

Due to its flexibility FreeEOS is adopted as the standard EoS for the B16 SSMs. For the first time, EoS tables calculated consistently for each of the compositions used (GS98 and AGSS09met) are used in the solar calibrations. This is a qualitative step forward although quantitatively differences in the predicted solar properties by use of consistent EoS tables are small and have minimal impact in the production of solar neutrinos or helioseismic diagnostics used in this work. Figure 2.2 shows the differences between models with the same composition but using EoS tables computed for GS98 and AGSS09met mixtures.

For the sound speed and the density profile these differences are very small compared with the model errors but some notable effects can be found for the Γ_1 case. The use of EoS tables using different solar mixtures lead to differences in Γ_1 of the

---

[3] `http://freeeos.sourceforge.net/`

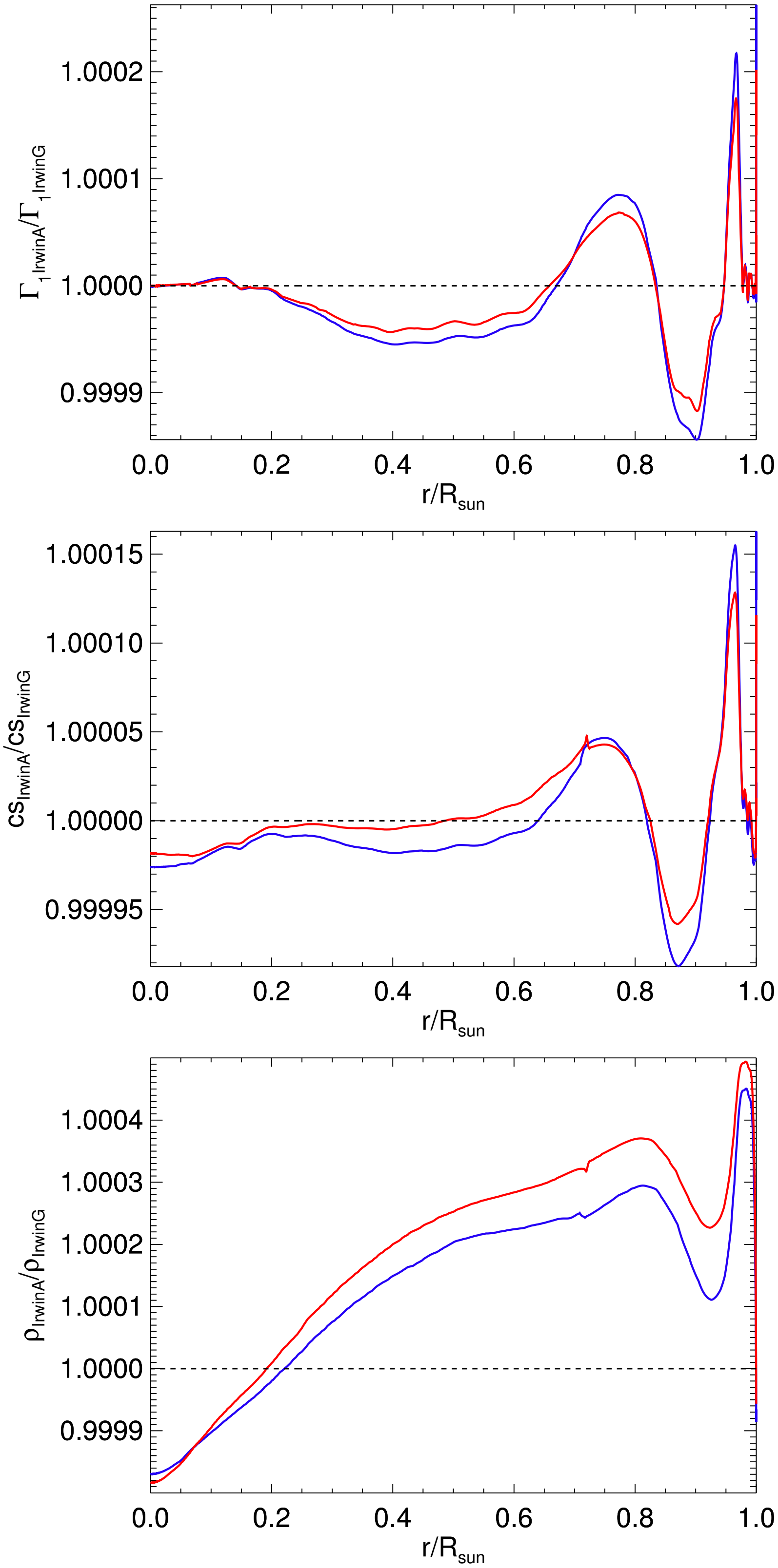

Figure 2.2: Relative differences between models calibrated with Irwin EoS calculated using different compositions (GS98 or AGSS09met). The results are presented for GS98 (blue) and AGSS09met (red). The quantities presented are: Top panel: Γ_1, Middle panel: Sound speed, Bottom panel: Density profiles

Qnt.	Central value	σ (%)	Ref.
$p(p, e^+\nu_e)d$	$4.03 \cdot 10^{-25}$	1.0	1
$^3He(^3He, 2p)^4He$	5.21 MeV b	5.2	2
$^3He(^4He, \gamma)^7Be$	$5.6 \cdot 10^{-4}$ MeV b	5.2	2
$^3He(p, e^+\nu_e)^4He$	$8.6 \cdot 10^{-20}$ MeV b	30.2	2
$^7Be(e^-, \nu_e)^7Li$	Eq (40) SFII	2.0	2
$^7Be(p, \gamma)^8B$	$2.13 \cdot 10^{-5}$	4.7	3
$^{14}N(p, \gamma)^{15}O$	$1.59 \cdot 10^{-3}$	7.5	4
$^{16}O(p, \gamma)^{17}F$	$1.06 \cdot 10^{-2}$ MeV b	7.6	2
$\tau_\odot$	$4.57 \cdot 10^9$ yr	0.44	5
diffusion	1.0	15.0	5
$L_\odot$	$3.8418 \cdot 10^{33}$ erg s^{-1}	0.4	5

Table 2.3: Central values for the main input parameters and the corresponding standard deviation. (1) Marcucci et al. (2013), (2) A11, (3) Zhang et al. (2015), (4) Marta et al. (2011) (5) Bahcall et al. (2006).

order of 2×10^{-4} in the region $r/R_\odot > 0.7$. This is comparable to results shown in Lin et al. (2007) using a different EoS, and it is about two times larger than the error in the helioseismic determination of Γ_1. These differences are important in the context of abundance determinations from EoS features such as the depression of the adiabatic index Γ_1 (see e.g. Lin et al., 2007; Vorontsov et al., 2013).

2.1.4 Input parameters

To summarize, Table 2.3 shows the input parameters used to calculate this new generation of standard solar models with the corresponding error considered including the updated nuclear rates with respect to the previous SSMs.

2.2 Treatment of model uncertainties

Within the framework defined by SSMs, the treatment of model uncertainties is generally simple. Most of the input physics in the models can be characterized by simple numbers such as the astrophysical factors or the surface abundance of a given element, as discussed in previous section. Table 2.1 and Table 2.3 list the uncertainties adopted for each of the input quantities that allow such simple parametrizations.

The choice of uncertainties for the microscopic diffusion and for radiative opacities are not as simple and they are discussed more deeply in Section 2.2.1 and Section 2.2.2 respectively.

2.2.1 Diffusion

The adopted uncertainty for the microscopic diffusion coefficients deserves a special comment, as the coefficients cannot be obtained experimentally. The quoted 15% uncertainty, the same used in previous SSM calculations (see Serenelli et al., 2011), is based on the results presented in Thoul et al. (1994), where the complete solution of the multiflow Burgers equations was initially presented in the context of SSMs. As discussed in that work, the uncertainty in the diffusion coefficients comes from the calculation of the Coulomb collision integrals. The comparison of their results with equivalent calculations available in the literature (Proffitt and Michaud, 1991) yielded a $< 15\%$ difference in the diffusion coefficients for all relevant elements in the solar interior. The adopted 15% uncertainty (1σ) is therefore conservative in more than one aspect: it is based on the difference between calculations (to use 1σ as half the difference between calculations would be equally well defined), and it reflects the largest difference between different calculations for all the solar interior and all relevant chemical elements. Later works showed that inclusion of radiative levitation, for instance (Turcotte et al., 1998), or quantum corrections to the collision integrals (Schlattl and Salaris, 2003), have very minor effects in solar model calculations which are well within the adopted uncertainties.

2.2.2 Radiative opacities

A fundamentally important physical ingredient in solar models that cannot be quantified by just one parameter is the radiative opacity, which is a complicated function of temperature (T), density (ρ) and chemical composition (X_i) of the solar plasma. The magnitude and functional form of its uncertainty is currently not well constrained in available opacity calculations. As a result, representation of the uncertainty in radiative opacity by a single parameter (Serenelli et al., 2013) or by taking the difference between two alternative sets of opacity calculations (Bahcall et al., 2006; Villante et al., 2014) are strong simplifications, at best. Here, the choice is to use a general and flexible approach based on opacity kernels originally developed by Tripathy and Christensen-Dalsgaard (1998) and later on by Villante (2010), which is described in the next section. These opacity kernels will provide a very flexible method to study how different opacity uncertainty functions affect the outputs of the SSMs.

2.2.2.1 Opacity kernels

The opacity kernels are functions that contain the response in a physical quantity of the solar model to small perturbations in the input physics. These opacity kernels can then be used to evaluate the contribution of opacity to the uncertainties of the solar properties. The calculation of them has been done following the procedure first presented in Tripathy and Christensen-Dalsgaard (1998).

First, it is assumed that in the region of the parameter-space (ρ, T, Xi) which describes the solar plasma during the Sun evolution, the variation of the opacity can be approximately described as a function of the temperature only, i.e. the modified opacity table $\kappa(\rho, T, X_i)$ is related to the reference opacity table $\bar{\kappa}(\rho, T, X_i)$ by:

$$\kappa(\rho, T, X_i) = [1 + \delta\kappa(T)]\ \bar{\kappa}(\rho, T, X_i), \tag{2.2}$$

where $\delta\kappa(T)$ is an arbitrary function. If the changes of opacity are small enough, i.e. $\delta\kappa(T) \ll 1$,the model responds linearly to these perturbations and the fractional variation of a generic observable Q can be expressed as:

$$\delta Q = \int \frac{dT}{T} K_Q(T)\delta\kappa(T). \tag{2.3}$$

In the above equation, the kernel $K_Q(T)$ describes the response of the considered quantity to changes of the opacity at a given temperature.

The goal is to obtain these kernels and to use them in order to study the effects produced by arbitrary opacity changes. To do so, it is necessary to determine the response of SSMs when opacity is changed in a thin shell whose position is determined by the temperature. This narrow perturbation is ideally represented as delta function:

$$\delta\kappa(T) = C\delta(\ln T - \ln T_0). \tag{2.4}$$

In numerical calculations, the δ-function is approximated by a gaussian, i.e.:

$$\delta\kappa(T) = \frac{C}{\sqrt{2\pi}\sigma} \exp\left[-\frac{(\ln T - \ln T_0)^2}{2\sigma^2}\right], \tag{2.5}$$

where a $\sigma \ll 1$ is required so that the opacity variations are sufficiently localized and $C/\sigma \ll \sqrt{2\pi}$ in order to avoid non linear effects. The choice is $\sigma = 0.03$ and $C = 0.004$. A set of SSMs has been calculated with opacity perturbations located in the temperature range $\log_{10} T_0 = 6.3 - 7.2$, where radiative transport takes place and thus, the uncertainties of the radiative opacities play an important role. Finally, the opacity kernels are calculated by using the outputs of these models and normalizing the obtained variations δQ according to:

$$K_Q(T_0) = \frac{\delta Q}{C} \tag{2.6}$$

as it is prescribed by Equation 2.3.

In Figure 2.3, the kernels are plotted as function of the temperature for the different relevant outputs of the system while in Figure 2.4 the kernels of the different frequency separation ratios (r_{02} and r_{13}) are presented. In the top panel of Figure 2.3, the kernels of different points of the sound speed profile are shown. Variations of the opacity in a shell of a given temperature produce a sharp perturbation of the sound speed at the same location of the opacity perturbation but also a modification of opposite sign all over the solar profile. This is related to the high correlation of the sound speed given by the fact that the models are forced to converge to the solar radius. The shape of the opacity kernel for the sound speed profile, that presents a peak with positive values at the region of the perturbation and negative values at the rest of the profile, will imply that, if a constant perturbation along the temperature is assumed for the opacity, the integrated effects will cancel out. Therefore, a constant value for the opacity uncertainty along the solar profile will not produce any effect on the sound speed profile as it is discussed later on in the chapter and in Villante (2010).

In the middle panel, the opacity kernels for the different neutrino fluxes are plotted. Basically, the kernels Φ(pp) and Φ(pep) are very small because the p+p reaction rate have to be roughly constant in order to reproduce the solar luminosity. That will affect the abundances of helium and hydrogen that will have to be reduced or enhanced in order to compensate the changes of the temperature due to the opacity perturbations at the center of the Sun. The effects on the other neutrino fluxes are a direct consequence of changes on the temperature in the corresponding production regions.

In the bottom panel, the kernels of the helium and metal abundances (initial and surface) and the results for $\mathrm{R_{CZ}}$ and α_{MLT} are presented. As mentioned in the previous paragraph, the dependence of the $\mathrm{Y_{ini}}$ and $\mathrm{Y_S}$ on the opacity is related to the fact that the total energy produced trough the p+p reaction have to be nearly constant. Changes on the opacity directly affect the radius where the transition between radiative and convective region occurs ($\mathrm{R_{CZ}}$) as it is represented by the sharp peak. The observed dependence of $\mathrm{R_{CZ}}$ on opacity changes in the center of the Sun is related to the fact that changes on the center affects the complete sound speed profile affecting the position of $\mathrm{R_{CZ}}$. The dependence of α_{MLT} to opacity changes is required to obtain the correct solar radius for a perturbed model.

To test the opacities at the solar core is important in order to understand how opacities changes at this region can affect helioseismology and neutrino fluxes. As it has been discussed previously in Section 1.2.5, the separation frequency ratios are useful to test the conditions of the solar core, where the sound speed cannot provide information. Therefore, the opacity kernels for different small separation ratios have been calculated for the first time to understand how they are affected by opacity perturbations and the results are presented in Figure 2.4. The kernels ratios present an oscillatory shape for all the cases that gets more complicated for high radial orders giving the hint that these can be related with the autofunction of the frequencies. Therefore, due to their high variability with the temperature, it is difficult to predict how these ratios will change for a given opacity perturbation. For both r_{02} and r_{13}, the corresponding kernels are more shifted to negative values and that gives the hint that these ratios would increase if the opacity globally decreases. Ultimately, the final values of the ratios would depend on the magnitude of the opacity variations but more importantly on the shape of the chosen function, because the perturbations can be canceled out due to the shape of the kernels. Therefore, it is necessary to integrate all over the solar profile to be able to understand the effects of these perturbations on the small separation ratios. Some examples can be found in Chapter 3, where different radiative opacity tables are tested.

Comparing the results with the ones presented in Tripathy and Christensen-Dalsgaard (1998) and Villante (2010), is possible to find a very good agreement with the present calculations, even though in Villante (2010) an alternative approach in which the solar structure equations are first linearized and then solved and gives the opacity kernels as function of the solar radius. The only noticeable difference with Tripathy and Christensen-Dalsgaard (1998) is found for the kernel of the hydrogen abundance. Note, however, that this SSMs are calculated using diffusion while it was not taken into account in Tripathy and Christensen-Dalsgaard (1998). In Figure 2.5, the relative changes for the hydrogen abundance profile when the opacity is perturbed at $\log_{10} T_0 = 7$ with and without diffusion included are presented.

Finally, it is important to remark that once the opacity kernels are calculated, it is possible, in a very flexible way, to simulate perturbations in the solar quantities for different relative variations of the opacity functions. Therefore, for the purpose of this work, the next step is to parametrize the opacity uncertainty function, a key

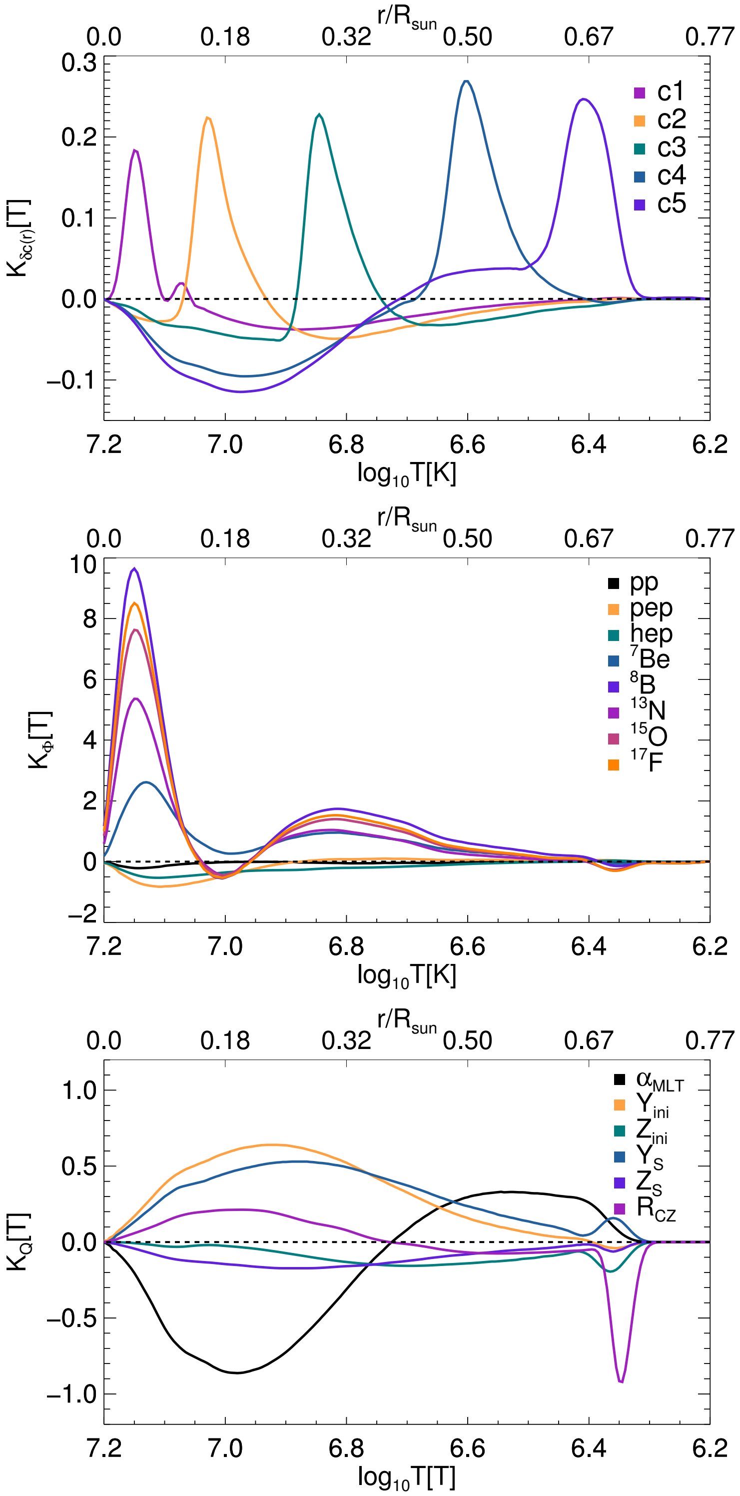

Figure 2.3: Opacity kernels for different quantities as a function of the solar temperature. Top-left panel: Five points of the sound speed at different solar radius; $c1 = c(0.06R_\odot)$, $c2 = c(0.15R_\odot)$, $c3 = c(0.28R_\odot)$, $c4 = c(0.48R_\odot)$ and $c5 = c(0.66R_\odot)$. Top-right panel: Neutrino fluxes. Low panel: Initial and surface metallicity and helium, α_{MLT} and radius at the base of the convective envelope.

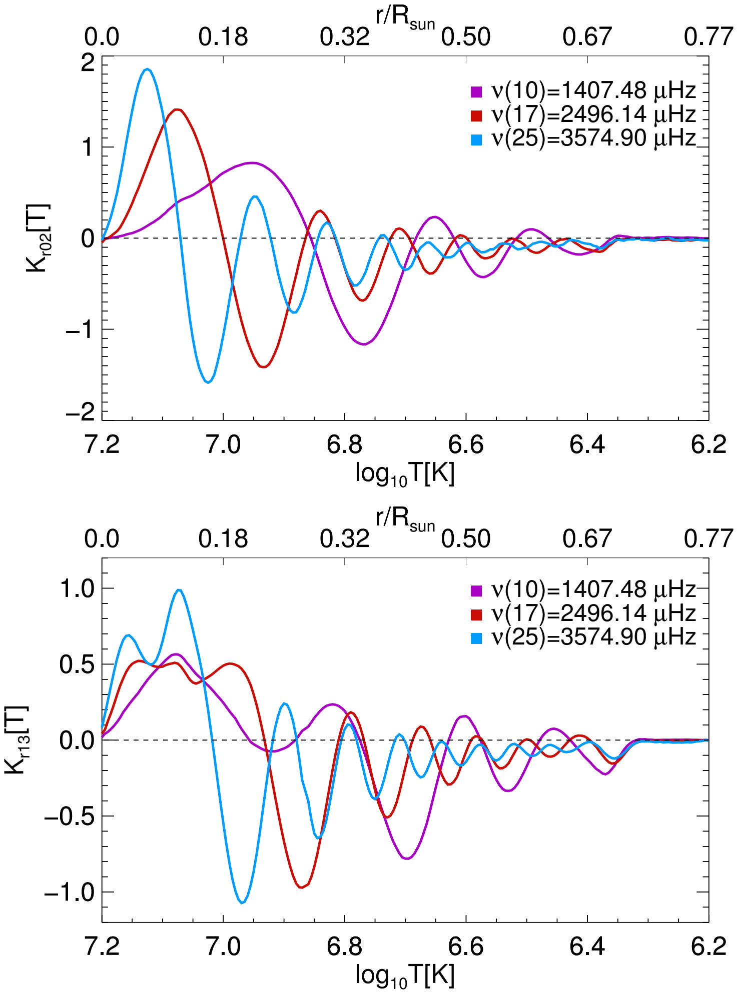

Figure 2.4: Opacity kernels for the small separation ratios. Upper panel: r_{02}, Lower panel: r_{13}. For each of the cases, three different ratios with radial order n=10,17,25 are presented.

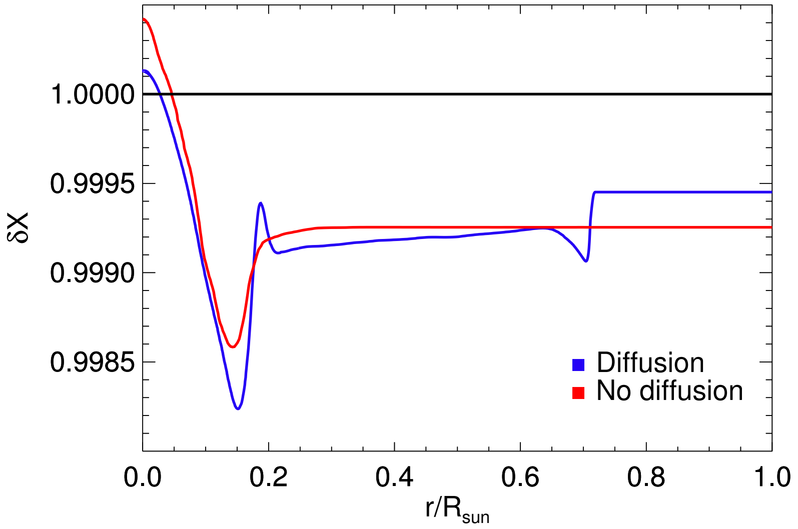

Figure 2.5: Relative changes for the hydrogen abundance profile when an opacity perturbation at $\log T_0 = 7.0$ (corresponding to $r = 0.18R_\odot$) is introduced. The solid red line corresponds to a SSM model with diffusion and the solid blue line to a SSM without diffusion.

---

part to account for the final errors of the models. The discussion and the final choice of the opacity uncertainties can be found in the next section (Section 2.2.2.2).

2.2.2.2 Opacity uncertainty parametrization

The evaluation of δQ is subject to the choice that is made for $\delta\kappa(T)$. In Haxton and Serenelli (2008) and Serenelli et al. (2013) the opacity error was modelled as a 2.5% constant factor at 1σ level, comparable to the maximum difference between the OP and OPAL (Iglesias and Rogers, 1996) opacities in the solar radiative region. Villante (2010) showed that this prescription underestimates the contribution of opacity uncertainty to the sound speed and convective radius error budgets because the opacity kernels for these quantities are not positive definite and integrate to zero for $\delta\kappa(T) = \text{const}$. Later on, Villante et al. (2014) considered the temperature-dependent difference between OP and OPAL opacities as 1σ opacity uncertainty. However, it is by no means clear that this difference is a sensible measure of the actual level of uncertainty in current opacity calculations.

Based on the previous reasons, here, a different approach is used, inspired by the most recent experimental and theoretical results and some simple assumptions. The contribution of metals to the radiative opacity is larger at the bottom of the convective envelope ($\sim 70\%$) than at the solar core ($\sim 30\%$). Also, Krief et al. (2016a) in a recent theoretical analysis of line broadening modelling in opacity calculations have found that uncertainties linked to this are larger at the base of the convective envelope than in the core. These arguments suggest that opacity calculations are more accurate at the solar core than in the region around the base of the convective envelope. It is thus natural to consider error parameterizations that allow opacity to fluctuate by a larger amount in the external radiative region than in the center of the Sun.

Taking all this into account, the following parameterization for the opacity change $\delta\kappa(T)$ is considered:

$$\delta\kappa(T) = a + b\,\frac{\log_{10}(T_{\mathrm{C}}/T)}{\Delta} \tag{2.7}$$

where $\Delta = \log_{10}(T_{\mathrm{C}}/T_{\mathrm{CZ}}) = 0.9$. T_{C} and T_{CZ} are the temperatures at the solar center and at the bottom of the convective zone respectively. This equation is applied only up to the lower regions of the convective envelope, where convection is adiabatic and changes in the opacity are irrelevant. Changes in the opacity in the uppermost part of the convective envelope and atmosphere are absorbed in the solar calibration by changes in the mixing length parameter and in sound speed inversions by the surface term and, in the context of SSMs, will not produce changes in the solar properties considered here. By changing the parameters a and b, one is able to rescale and tilt the solar opacity profile by arbitrary amounts. These parameters are considered as independent random variables with mean equal to zero and dispersions σ_a and σ_b, respectively. This corresponds to assuming that the opacity error at the solar center is $\sigma_{\mathrm{in}} = \sigma_a$, while it is given by $\sigma_{\mathrm{out}} \simeq \sqrt{\sigma_a^2 + \sigma_b^2}$ at the base of the convective zone. $\sigma_{\mathrm{in}} = \sigma_a = 2\%$ is fixed, which is the average difference of the OP and OPAL opacity tables. For σ_{out} the choice is 7% (i.e. $\sigma_b = 6.7\%$), motivated by the recent experimental results of Bailey et al. (2015) that have measured the iron opacity at conditions similar to those at the base of the solar convective envelope and have found a $7\% \pm 4\%$ increase with respect to the theoretical expectations. It is possible to note that the adopted functional form, see Equation 2.7, for the opacity error function is a simplified parametric description of a more complex (and unknown) behaviour. This choice is motivated by practical reasons and by the important fact that Christensen-Dalsgaard et al. (2009) and Villante (2010) have shown that an opacity solution to the solar abundance problem requires a tilt of opacity profile of the Sun by increasing opacity by a few percent at the solar center and a much larger increase (up to 15 to 20%) at the base of the convective region, i.e. the kind of behaviour for $\delta\kappa(T)$ described by Equation 2.7 when $b \neq 0$. The adopted functional form can mimic, moreover, the uncertainty in theoretical calculations introduced by line broadening modelling discussed by Krief et al. (2016a).

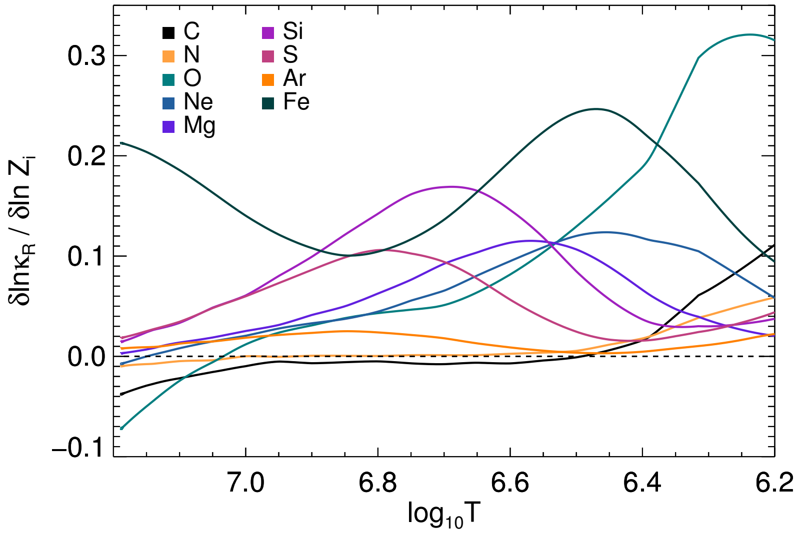

Figure 2.6: Logarithmic derivatives of the opacity with respect to individual metal abundances as function of the solar temperature.

2.2.2.3 Metal contributon to radiative opacities

Although the choice in this chapter is to use a lineal function to account for the radiative opacities, a more complicated function could be considered in future works. Therefore, in order to implement it, it is important to understand how the changes on the composition modify the radiative opacities. For that reason, it is illustrative to calculate the individual contribution of metals to the final values of the opacity as function of the solar temperature profile. For that purpose, on Figure 2.6 the Rosseland mean opacity derivative with respect to the different metal abundances considered is plotted against the temperature of the solar interior.

It is possible to see that at the center of the Sun, the opacity highly depends on the iron abundance variations, more moderately on the oxygen and carbon, while the other elements would introduce small variations if changes on their abundances occur. In the intermediate region changes on refractory elements would produce relevant effects while in the outer part, oxygen clearly dominates over the other elements.

2.3 Results

In this section, the main results of the B16 SSMs for GS98 and AGSS09met compositions are presented and differences with respect to previous SFII models discussed. Table 2.4 presents a summary of the most relevant quantities related to the calibration of SSMs and helioseismic quantities: mixing length parameter ($\alpha_{\rm MLT}$), initial helium

Qnt.	B16-GS98	B16-AGSS09met	Solar
$\mathrm{Y_S}$	0.2426 ± 0.0059	0.2317 ± 0.0059	0.2485 ± 0.0035
$\mathrm{R_{CZ}/R_\odot}$	0.7116 ± 0.0048	0.7223 ± 0.0053	0.713 ± 0.001
$\langle \delta c/c \rangle$	$0.0005^{+0.0006}_{-0.0002}$	0.0021 ± 0.001	0^a
α_{MLT}	2.18 ± 0.05	2.11 ± 0.05	-
$\mathrm{Y_{ini}}$	0.2718 ± 0.0056	0.2613 ± 0.0055	-
$\mathrm{Z_{ini}}$	0.0187 ± 0.0013	0.0149 ± 0.0009	-
$\mathrm{Z_S}$	0.0170 ± 0.0012	0.0134 ± 0.0008	-
$\mathrm{Y_C}$	0.6328 ± 0.0053	0.6217 ± 0.0062	-
$\mathrm{Z_C}$	0.0200 ± 0.0014	0.0159 ± 0.0010	-

Table 2.4: Main characteristics for the different SSMs with the corresponding model errors and the values for the observational values (when available) and their error. The observational values of $\mathrm{Y_S}$ is taken from Basu and Antia (2004) and $\mathrm{R_{CZ}}$ from Basu et al. (1997). ^{a}The solar value is zero, by construction of $\delta c/c = c_{obs} - c_{mod}/c_{mod}$.

$\mathrm{Y_{ini}}$ and metallicity $\mathrm{Z_{ini}}$ and the corresponding surface ($\mathrm{Y_S}$ and $\mathrm{Z_S}$) and central $\mathrm{Y_C}$ and $\mathrm{Z_C}$ quantities, $\mathrm{R_{CZ}}$ and the average rms difference of the relative sound speed difference shown in Figure 2.7. Notice that this rms value is only indicative of the quality of the models because it neglects correlations in the models. Table 2.5 gives results for solar neutrino fluxes and in Table 2.6 there is a quantification of the agreement between SSMs and solar data. Model errors and theoretical correlations among observable quantities have been obtained from MC simulations that are discussed later on in Section 2.4.1.2.

2.3.1 Helioseismology

2.3.1.1 Surface helium and radius of the convective envelope

Two helioseismic quantities widely used to estimate the quality of SSMs are the surface helium abundance $\mathrm{Y_S}$ and the location of the bottom of the convective envelope $\mathrm{R_{CZ}}$. Both are listed in Table 2.4 together with the corresponding seismic values. The model errors associated to these quantities are larger in B16 models than previously computed Bahcall et al. (2006) generations of SSMs because of the different treatment of uncertainties in radiative opacities (see Section 2.4 for details). Compared to SFII models, it is possible to find a small decrease in the predicted $\mathrm{Y_S}$ by 0.0003 for both compositions and a decrease in the theoretical $\mathrm{R_{CZ}}$ by 0.0007 $\mathrm{R_\odot}$, also for both compositions. A comparison of models and data for these two quantities yields $\chi^2 = 0.91$ and $\chi^2 = 6.45$ for GS98 and AGSS09met compositions that translate into 0.5σ and 2.1σ differences between models and data. This is summarised in Table 2.6.

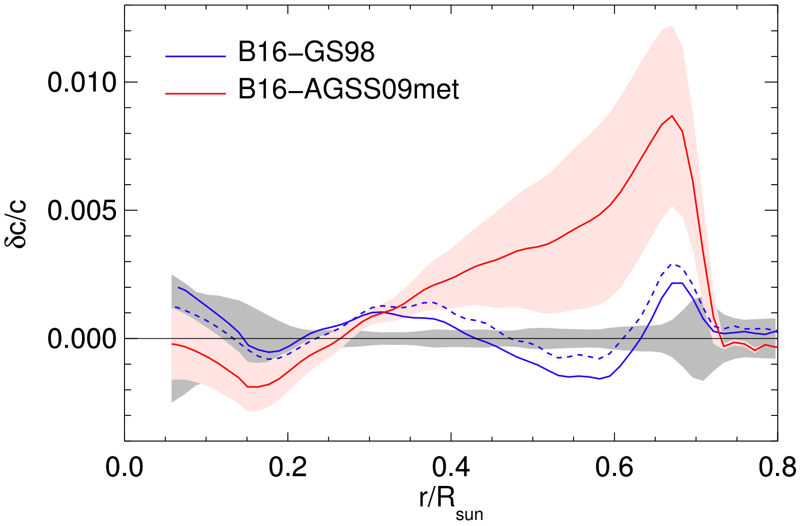

Figure 2.7: Fractional sound speed difference in the sense $\delta c/c = (c_{\odot} - c_{\mathrm{mod}})/c_{\mathrm{mod}}$. Grey shaded regions corresponds to errors from the inversion procedure (see text for details). Red shaded region corresponds to errors from the model variation which are plotted around the AGSS09met central value (solid red line). An equivalent relative error band holds around the central value of the GS98 central value (solid blue line) which is not plotted for the sake of clarity. Dashed line shows, for comparison, results for the older SFII-GS98 SSM.

2.3.1.2 Sound Speed profile

Figure 2.7 shows the fractional sound speed difference as a function of solar radius. The solar sound speed differences have been obtained for each of the two SSMs by performing new sound speed inversions, using the appropriate reference solar model, based on the BiSON-13 dataset (a combination of BiSON+MDI data) as described in Basu et al. (2009). The resulting $\delta c/c$ curves are not too different with respect to SFII models. This is expected because the differences between the two generations of models are mostly due to changes in the nuclear reaction rates. All rates have a negligible impact on the solar sound speed profile except for the $\mathrm{p(p, e^{+}\nu_e)d}$ rate, changes on it produces modification on the temperature profile and consequently to the solar sound speed. It is the newly adopted rate for this reaction that introduces the small differences with respect to the older generation of SSMs. This is shown in Figure 2.7 by including the sound speed difference for the previous SFII-GS98 SSM in dashed line.

A quantitative assessment of the agreement between model and solar sound speed is not straightforward. It requires a proper evaluation of model errors and correlations. Also, given a set of observed frequencies, extraction of the sound speed profile is sensitive to uncertainties in the measured frequencies, numerical parameters inherent to the inversion procedure and the solar model used as a reference model for performing the inversion. Such detailed analysis was carried out in Villante et al. (2014), in which the SSM response to varying input parameters was modelled using power-law expansions and the three uncertainties related to the extraction of $\delta c/c$ from observed data were taken directly from Degl'Innoccenti et al. (1997).

In this work, large MC sets of SSMs are used (see Section 2.4) to account for model errors and correlations. The total error from all input parameters in SSMs is illustrated in Figure 2.7 as the shaded area embracing the B16-AGSS09met curve. Note that in comparison to previous estimates, (e.g. Villante et al., 2014), errors are larger due to the adoption of the larger opacity uncertainty.

The total error due to the three error sources linked to $\delta c/c$ inversion is shown in Figure 2.7 as the grey shaded area around 0. The calculation of two of these error sources have been improved in comparison to results in Degl'Innoccenti et al. (1997). The first one is the error in $\delta c/c$ resulting from propagating the errors in the observed frequencies. This is now done on the basis of the BiSON-13 dataset, a much more modern dataset with smaller frequency errors. This is not a dominant error source at any location in the Sun. More importantly, however, is the dependence of the solar sound speed on the reference model employed for the inversion (see Section 1.2.5.3). Previously, in Degl'Innoccenti et al. (1997) and Basu et al. (2000), this dependence was estimated by performing sound speed inversions for a few solar models with different input physics, but with fixed solar composition. Here, instead, two sets of 1000 SSMs originally computed by Bahcall et al. (2006) are used, with one set based on GS98 and the other one on AGS05 (Asplund et al., 2005) solar compositions. In both cases, conservative composition uncertainties that are about twice as large, or more, as those quoted in the corresponding spectroscopic results are considered. In addition, all other input parameters in SSM calculations have been varied. For these 2000 models, inversions have been carried out to determine the solar sound speed profiles. The dispersion of the results, as a function of radius, have been used to derive the dependence of inferred solar sound speed on the inversion reference model.

An alternative, and more consistent approach, would be to perform inversions for all the models in the MC simulations, as was done in Bahcall et al. (2006). This is a very time consuming procedure because it is not fully automated and it was decided to not repeat it. In that case, the errors of the reference models would be included as

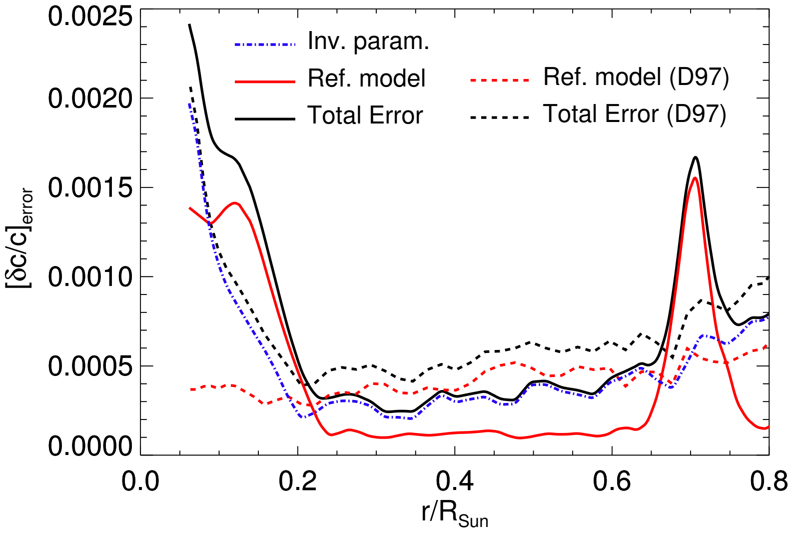

Figure 2.8: Relevant sources of error for solar sound speed inversions. Solid and dashed lines show respectively the new and the older (Degl'Innoccenti et al., 1997) estimates of total (black) and reference model (red) errors. The dashed-dotted line shows the error associated to numerical parameters in the inversion procedure from (Degl'Innoccenti et al., 1997).

model errors. But the current approach, just described, makes use of a broad range of SSMs and ensures a conservative estimate of this error source.

Finally, a comparison of the current estimates of uncertainties with respect to previous estimates is shown in Figure 2.8, where solid and dashed lines depict currently adopted and older errors respectively.

Using model and inversion uncertainties as described above, it is possible to compare how well the predicted sound speed profiles of B16-GS98 and B16-AGSS09met agree with helioseismic inferences. For this, 30 radial points representative of the sound speed profile up to $r \sim 0.8R_\odot$ are used. The sound speed profile for $r/\mathrm{R}_\odot > 0.80$ is excluded because the transport is convective in that region, the temperature gradient is adiabatic and then, the sound speed profiles of the models are not affected by changes in the solar interior and are in good agreement with helioseismic results. For values close to $r/\mathrm{R}_\odot \approx 1.0$, the predicted sound speed deviates from the observations due to surface effects that are not properly accounted for in the models. These points are the same ones used in Villante et al. (2014).

The models in the MC simulations are used to obtain the covariance matrix for these 30 points and assume inversion uncertainties at different radii as uncorrelated. The latter is an assumption and improvements on it in the future are expected.

Results are shown in the second row of Table 2.6. For 30 degrees-of-freedom (dof), B16-GS98 gives $\chi^2 = 58$, or a 3.2σ agreement with data. For B16-AGSS09met results are $\chi^2 = 76.1$, or 4.5σ. Below the significance of these results is analyzed in detail.

It is apparent from Figure 2.7 that, at almost all radii, the sound speed profile of B16-GS98 fits well within the 1σ uncertainties, even the peak right below the CZ at $r/\mathrm{R}_\odot \approx 0.6 - 0.7$. Also notice that the difference between B16-GS98 and the Sun is dominated by wiggles of relatively small amplitude. However, changes in input quantities, including radiative opacities, do not lead to variations in SSM sound speeds on small radial scales, so values of the sound speed at different radii in solar models are strongly correlated (see Section 2.4.1.2 for details). Including these correlations by means of a covariance matrix in the calculation of χ^2 explains why the large value $\chi^2 = 58$ is obtained for the B16-GS98 which, apparently, fits well within 1σ contours. This result reflects the fact that, within the framework of SSMs and the new treatment of uncertainties, particularly of opacities, it is not possible to find a combination of input parameters that would make the wiggles go away. To confirm this, the correlations have been neglected, obtaining a result of $\chi^2 = 23.6$ for the sound speed profile of B16-GS98, well within a 1σ result as expected by a looking at Figure 2.7.

For B16-AGSS09met, the discrepancy with the solar sound speed is dominated by the large and broad peak in $0.35 < r/\mathrm{R}_\odot < 0.72$. In this case, correlations in the model sound speed decrease the level of disagreement with the data. Variations in the model leading to improvements in the sound speed profile will do so at a global scale. If, as a test, sound speed correlations are neglected for this model, a larger $\chi^2 = 100.4$ is obtained, i.e. the opposite behavior than for B16-GS98.

It is important to notice that in the case of B16-GS98, the largest contribution to the sound speed χ^2 comes from the narrow region $0.65 < r/\mathrm{R}_\odot < 0.70$ that comprises 2 out of all the 30 points. If these two points are removed from the analysis χ^2 is reduced from 58 to 34.7, equivalent to a 1.4σ agreement with the solar sound speed (entry identified as $\delta c/c$ no-peak in Table 2.6). For B16-AGSS09met this test leads to a 2.7σ result. This exercise highlights the qualitative difference between SSMs with different compositions; it shows that for GS98 the problem is highly localized whereas for AGSS09met the disagreement between SSMs and solar data occurs at a global scale giving rise to the *solar abundance problem*.

The result of removing two points from the sound speed analysis is showing that the GS98 composition leads to a SSMs that is in quite good agreement with solar data. But it also highlights limitations of SSMs in providing an accurate description of the solar region just below the convective envelope as has been widely discussed in previous works (Antia and Chitre, 1998; Christensen-Dalsgaard et al., 2011).

2.3.1.3 Frequency separation ratios

As introduced in Section 1.2.5.4, frequency separation ratios give very valuable information about the solar core independently of the surface effects and actually, previous works as Serenelli et al. (2011) have already used them to test the performance of SSMs when compared with the observations.

Figure 2.9 shows the results for B16-SSMs with GS98 (blue) and AGSS09met (red) compositions. The model errors calculated using MC simulations (see Section 2.4.1), are represented with the grey shadow. The observational values taken from BiSON (Broomhall et al., 2009; Hale et al., 2016) are represented as black points with the corresponding error bars.

The updated B16-SSM do not show changes with respect to the agreement of the models with the observations when looking at r_{02} and r_{13} ratios. As shown in Serenelli et al. (2011), GS98 models are in good agreement with the observations for both r_{02} and r_{13} frequency combinations while AGSS09met results are much further away from the observations.

That could be understood by analysing the kernels of these quantities (see Figure 2.4). Globally, for r_{02} and r_{13} the kernels are slightly shifted toward negative values, meaning that an overall decrease on the opacity is translated to higher values of the ratios. Then, as for fixed radiative opacities changes of the composition translate into changes of the opacity profile, for AGSS09met an increase of the ratios with respect to GS98 is observed, related to the lower metallicity of the first. Then, it is possible to safely conclude that r_{02} and r_{13} are sensitive to models with different compositions.

Frequency separation ratios with different radial order n are completely correlated between each other and with the sound speed profile, and as the observational correlation is not currently available, they are not included to the statistical approach.

2.3.2 Neutrino fluxes

The most relevant updates in the B16 SSMs are related to updates in several key nuclear reaction rates (see Section 2.1.2) that have a direct effect on the predicted solar neutrino fluxes. The detailed results for all the neutrino fluxes are summarized in Table 2.5 with the solar values from Bergström et al. (2016) and the model errors calculated using MC simulation (see Section 2.4.1).

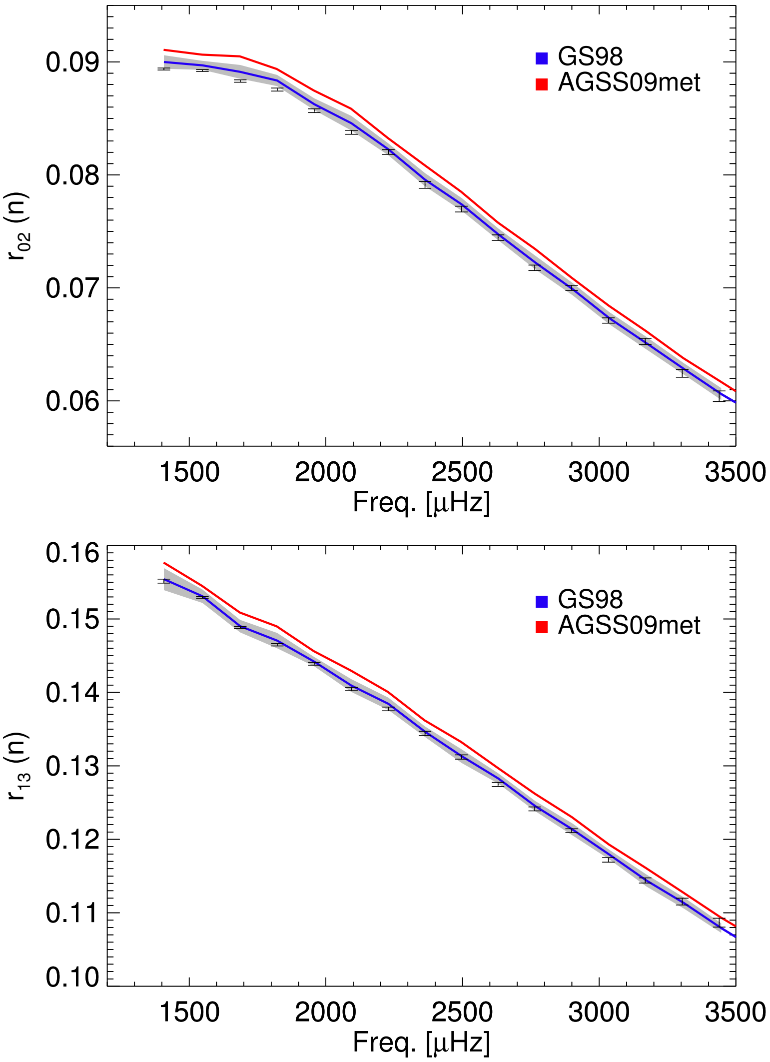

Figure 2.9: Frequency separation ratios for B16-SSMs using GS98 (blue) and AGSS09met (red) solar mixtures. The black points are the observational values from BiSON (Broomhall et al., 2009; Hale et al., 2016) with the corresponding observational errors. The grey shaded region shows the errors from the model. Top: r_{02}; Bottom: r_{13}.

Flux	B16-GS98	B16-AGSS09met	Solar^a	Chg.
$\Phi(\mathrm{pp})$	$5.98(1 \pm 0.006)$	$6.03(1 \pm 0.005)$	$5.97^{(1+0.006)}_{(1-0.005)}$	0.0
$\Phi(\mathrm{pep})$	$1.44(1 \pm 0.01)$	$1.46(1 \pm 0.009)$	$1.45^{(1+0.009)}_{(1-0.009)}$	0.0
$\Phi(\mathrm{hep})$	$7.98(1 \pm 0.30)$	$8.25(1 \pm 0.30)$	$19^{(1+0.63)}_{(1-0.47)}$	-0.7
$\Phi(^7\mathrm{Be})$	$4.93(1 \pm 0.06)$	$4.50(1 \pm 0.06)$	$4.80^{(1+0.050)}_{(1-0.046)}$	-1.4
$\Phi(^8\mathrm{B})$	$5.46(1 \pm 0.12)$	$4.50(1 \pm 0.12)$	$5.16^{(1+0.025)}_{(1-0.017)}$	-2.2
$\Phi(^{13}\mathrm{N})$	$2.78(1 \pm 0.15)$	$2.04(1 \pm 0.14)$	≤ 13.7	-6.1
$\Phi(^{15}\mathrm{O})$	$2.05(1 \pm 0.17)$	$1.44(1 \pm 0.16)$	≤ 2.8	-8.1
$\Phi(^{17}\mathrm{F})$	$5.29(1 \pm 0.20)$	$3.26(1 \pm 0.18)$	≤ 85	-4.2

Table 2.5: Model and solar neutrino fluxes. Units are: 10^{10} (pp), 10^9 (^{7}Be), 10^8 (pep, ^{13}N, ^{15}O), 10^6 (^{8}B,^{17}F) and 10^3(hep) cm^{-2}s^{-1}. ^{a}Solar values from Bergström et al. (2016). Last column corresponds to the relative changes (in %) with respect to SSMs based on SFII nuclear rates, which are almost independent of the reference composition.

2.3.2.1 ^{7}Be and ^{8}B fluxes

Currently, $\Phi(^8\mathrm{B})$ and $\Phi(^7\mathrm{Be})$ are the fluxes most precisely determined experimentally, and can be used to perform a simple test of the models. Furthermore, these are also the two fluxes from the pp-chains that are most sensitive to temperature and thus, to the conditions in the solar core and the inputs in solar models. In Serenelli et al. (2011), the agreement between SFII-GS98 and SFII-AGSS09met with solar fluxes was practically the same. The solar values determined from experimental data in that work were $\Phi(^8\mathrm{B}) = 5 \times 10^6\,\mathrm{cm^{-2}s^{-1}}$ and $\Phi(^7\mathrm{Be}) = 4.82 \times 10^9\,\mathrm{cm^{-2}s^{-1}}$ with 3% and 4.5% uncertainties respectively. SFII-GS98 yields $\Phi(^8\mathrm{B}) = 5.58(1 \pm 0.14) \times 10^6\,\mathrm{cm^{-2}s^{-1}}$ and $\Phi(^7\mathrm{Be}) = 5.00(1 \pm 0.07) \times 10^9\,\mathrm{cm^{-2}s^{-1}}$, while SFII-AGSS09met gives $\Phi(^8\mathrm{B}) = 4.59 \times 10^6\,\mathrm{cm^{-2}s^{-1}}$ and $\Phi(^7\mathrm{Be}) = 4.56 \times 10^9\,\mathrm{cm^{-2}s^{-1}}$ with same fractional errors as SFII-GS98. Experimental results for both $\Phi(^8\mathrm{B})$ and $\Phi(^7\mathrm{Be})$ were right in between the predictions for the two SSMs.

The new B16 generation of solar models, together with the recent determination of solar fluxes by Bergström et al. (2016) included in Table 2.5, leads to some changes in this stalemate. On one hand, SSM predictions for $\Phi(^8\mathrm{B})$ and $\Phi(^7\mathrm{Be})$ are reduced for both GS98 and AGSS09met compositions by about 2% with respect to previous SFII SSM due to the larger $\mathrm{p(p, e^+\nu_e)d}$ rate (for $\Phi(^8\mathrm{B})$ this is partially compensated by the increase in the $^7\mathrm{Be(p,\gamma)^8B}$ rate). This is illustrated in the left panel of Figure 2.11 where the relative changes with respect to SFII models of $\Phi(^8\mathrm{B})$ and $\Phi(^7\mathrm{Be})$ when the nuclear rates are updated individually are shown. On the other hand, solar

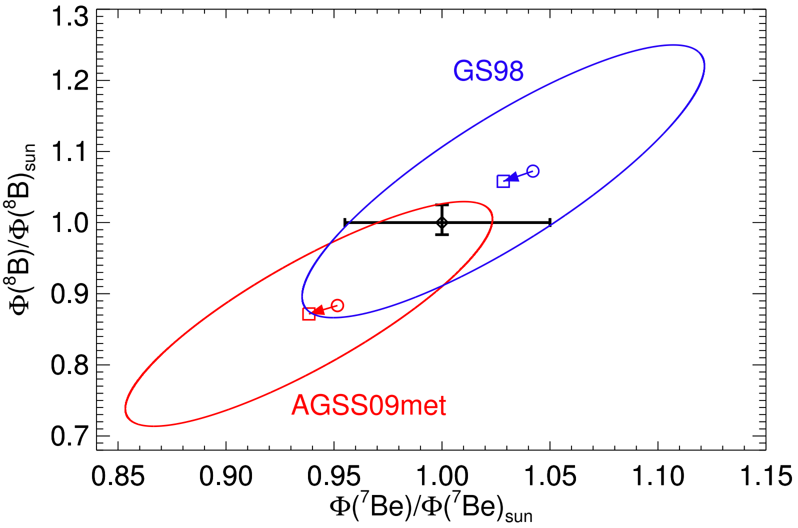

Figure 2.10: $\Phi(^8\mathrm{B})$ and $\Phi(^7\mathrm{Be})$ fluxes normalized to solar values (Bergström et al., 2016). Black circle and error bars: solar values. Squares and circles: results for B16 (current) and SFII (older) generation of SSMs respectively. Ellipses denote theoretical 1σ C.L. for 2 dof.

---

fluxes determined by Bergström et al. (2016) results in a solar $\Phi(^8\mathrm{B})$ that is about 3% higher than the value used in Serenelli et al. (2011). Figure 2.10 reflects the updated state and shows model and experimental results normalized to the newly determined solar values. Central values of B16-GS98 are closer to the solar values, both for $\Phi(^8\mathrm{B})$ and $\Phi(^7\mathrm{Be})$, than B16-AGSS09met fluxes. Both solar compositions lead to SSMs, however, that are consistent with solar neutrino fluxes within 1σ. A comparison between models and solar data for these two fluxes yields $\chi^2(\mathrm{GS98}) = 0.2$ and $\chi^2(\mathrm{AGSS09met}) = 1.45$ (see Table 2.6). This calculation includes model correlations obtained from the MC simulations (see Section 2.4.1) and the distribution of solar fluxes from Bergström et al. (2016).

Effect of updated S34 As discussed in Section 2.1.2, recent determinations of $S_{34}(0)$ range between 5.42×10^{-4} MeV b to 5.72×10^{-4} MeV b. It is interesting to speculate here on the impact of adopting the slightly lower $S_{34}(0)$ value such as determined by deBoer et al. (2014). A 3.2% reduction in $S_{34}(0)$ leads to a decrease in $\Phi(^8\mathrm{B})$ and $\Phi(^7\mathrm{Be})$ of about 2.7% and 2.8% respectively. This change leads to $\chi^2(\mathrm{GS98}) = 0.13$ (0.1σ) and $\chi^2(\mathrm{AGSS09met}) = 2.4$ (1.0σ). In this hypothetical scenario agreement between B16-AGSS09met and data is slightly larger than 1σ. Although this would still be far from being too useful as a discrimination test between

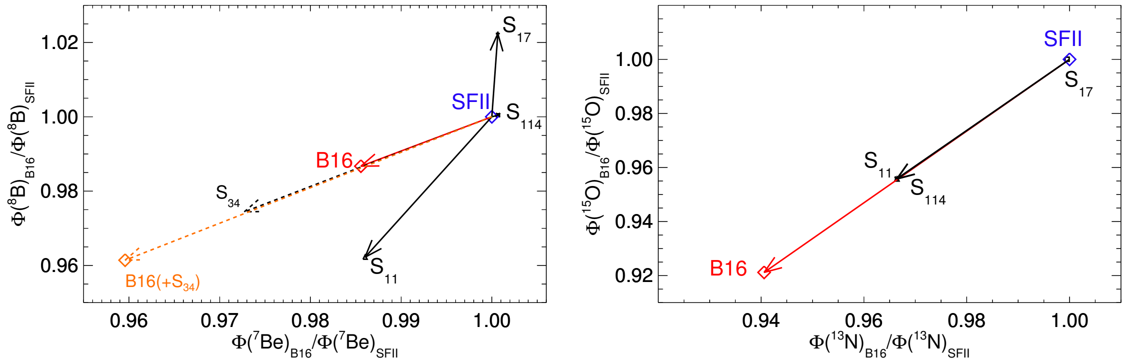

Figure 2.11: Relative changes of B16 (red) neutrino fluxes with respect to SFII models (blue). The individual contribution to the relative changes coming from the different updated nuclear rates (S_{11}, S_{17}, S_{114}) are plotted in black solid arrows. The total variation is represented with a red solid arrows for $\Phi(^7\text{Be})$ and $\Phi(^8\text{B})$ (left panel) and $\Phi(^{13}\text{N})$ and $\Phi(^{15}\text{O})$ (right panel). In the left panel the effect of an hypothetical change on S_{34} is represented with a black dashed arrow (individual) and orange dashed arrow (final B16) (see the text for more information).

solar models, this exercise helps in showing that the few percent systematics present in the determination of nuclear reaction rates can still be a relevant source of difficulty in using neutrino fluxes as constraints to solar model properties. In the left panel of Figure 2.11 the relative changes $\Phi(^8\text{B})$ and $\Phi(^7\text{Be})$ due to the individual update of S_{34} as well as the corresponding hypothetically final values are shown in dashed lines.

2.3.2.2 ^{13}N and ^{15} O fluxes

The most important changes in the neutrino fluxes occur for $\Phi(^{13}\text{N})$ and $\Phi(^{15}\text{O})$, in the CN-cycle. These fluxes are potentially excellent diagnostics of properties of the solar core. In particular, their dependence on the metallicty is two-fold: through opacities much in the same manner as pp-chain fluxes, and also through the influence of the added C+N abundance in the solar core. This latter dependence makes these fluxes a unique probe of the metal composition of the solar core. The expectation values in the B16 SSMs are about 6% and 8% lower than for the previous SFII models for $\Phi(^{13}\text{N})$ and $\Phi(^{15}\text{O})$ respectively. This results come from the combined changes in the p+p and ^{14}N+p reaction rates (see right panel of Figure 2.11). These neutrinos are not affected by the $^3\text{He}(^4\text{He},\gamma)^7\text{Be}$ reaction and therefore, their results would not change if the S_{34} rate is adopted from deBoer et al. (2014).

CN fluxes have not yet been determined experimentally. The global analysis of solar neutrino data performed by Bergström et al. (2016) yields the upper limits

		GS98		AGSS09met	
Case	dof	χ^2	p-value (σ)	χ^2	p-value (σ)
$\mathrm{Y_S} + \mathrm{R_{CZ}}$ only	2	0.9	0.5	6.5	2.1
$\delta c/c$ only	30	58.0	3.2	76.1	4.5
$\delta c/c$ no-peak	28	34.7	1.4	50.0	2.7
$\Phi(^7\mathrm{Be}) + \Phi(^8\mathrm{B})$	2	0.2	0.3	1.5	0.6
all ν-fluxes	8	6.0	0.5	7.0	0.6
global	40	65.0	2.7	94.2	4.7
global no-peak	38	40.5	0.9	67.2	3.0

Table 2.6: Comparison of B16 SSMs against different ensembles of solar observables.

that are included in Table 2.5. The Borexino collaboration, based on a different analysis of Borexino data alone, has reported an upper limit for the added fluxes $\Phi(^{13}\mathrm{N}) + \Phi(^{15}\mathrm{O}) < 7.7 \times 10^8 \mathrm{cm}^{-2}\mathrm{s}^{-1}$ (Bellini et al., 2012).

This section is closed with a comparison of models and solar data for all neutrino fluxes. χ^2 values are 6.01 and 7.05 for B16-GS98 and B16-AGSS09met models respectively and are also included in Table 2.6. This global comparison is clearly dominated by the $\Phi(^8\mathrm{B})$ and $\Phi(^7\mathrm{Be})$ fluxes. It is evident that current determination of solar neutrino fluxes are well described by models with any of the two solar compositions.

2.3.3 Global analysis

In this section all the observables are used to test the performance of both B16 SSMs globally. Results are summarized in the last two rows of Table 2.6 when all the sound speed profile is used or the two points in the region $0.65 < r/\mathrm{R}_\odot < 0.70$ are excluded. Global χ^2 is not strictly the sum of the individual contributions because of correlations between observables. Deviations are however small.

Final χ^2 values are dominated by the sound speed for both models, although $\mathrm{Y_S}$ and $\mathrm{R_{CZ}}$ are also relevant for B16-AGSS09met. The global analysis yields a not too good 2.7σ result for B16-GS98. However, this is strongly linked to the behaviour of the sound speed profile right below the convective zone, as explained in Section 2.3.1. Excluding two points in the sound speed lead to an overall 0.9σ agreement of this model with solar data. In the case of B16-AGSS09met, the overall agreement with the data is quite poor, at 4.7σ, which improves to only 3.0σ if the critical points in the sound speed profile are excluded. This is still a poor agreement with data.

It is interesting here to consider the impact of radiative opacity in the results obtained. It has been assumed a 7% uncertainty for the opacity at the base of the convective zone. Different authors have estimated that changes between 15 and 20% at that location are required to solve the solar abundance problem. Therefore, it may seem somewhat surprising that AGSS09met yields a much larger, 4.7σ, disagreement. At a first glance, a disagreement at approximately 3σ or smaller would be expected provided the level of uncertainty adopted for opacity. It should be noted, however, that the linear behavior for the opacity error function (Equation 2.7) permits to compensate the differences between the AGSS09met and GS98 SSMs but it is not flexible enough (for both compositions) to accommodate a better fitting sound speed profile, as it is further discussed in Chapter 3 and in Chapter 4.

Then, it is possible to conclude that a more complicated function than the linear one in this approach is necessary. Therefore, as the shape of the error function is itself unknown, a non-parametric approach, where no a priori assumptions are made about this shape, would be the next step related to the opacity uncertainties study. This is out of the scope of this thesis and left for future work.

2.4 Errors in SSMs

After presenting the results of both B16-SSMs, the following sections are dedicated to the model errors of this new generation of SSMs. First, the MC simulations and its corresponding results are described. Later on, the individual contributions of each of the input parameters (including the radiative opacity) to the final outputs of the SSMs are studied.

2.4.1 Monte Carlo Simulations

In order to estimate the errors coming from the input parameters, Monte Carlo simulations are done in a similar way than in Bahcall et al. (2006). This is done for GS98 and AGSS09met and for each of the compositions a large set of 10000 SSMs is constructed where, for each model, the values of the input quantities $\{I\}$ are chosen randomly from their respective distributions. Here, $\{I\}$ is the set of input parameters including composition of chemical elements, diffusion rate, $L_\odot$, $\tau_\odot$ and nuclear cross section parameters. The central values and the corresponding 1σ errors can be found in Table 2.1 and in Table 2.3. The opacity is treated a posteriori using the kerenels described previously in Section 2.2.2. In the following sections the inputs and the their distribution are described.

2.4.1.1 Treatment of uncertainties

Composition parameters For each of the computed MC sets, a reference composition is used, GS98 and AGSS09met. In each set, the j-th SSM is calculated by assuming:

$$\epsilon_{i,j} = \overline{\epsilon}_i + C_{i,j} \cdot \sigma_i, \tag{2.8}$$

where $\overline{\epsilon}_i$ and σ_i are the central value and error for each of the 9 elements i (different for each reference composition) and the factors $C_{i,j}$ are sampled from independent univariate gaussian random distributions. Note that $\overline{\epsilon}_i$ is a logarithmic measure of abundance.

Other input parameters For the other 11 non-composition input parameters (see Table 2.3), the j-th SSM is calculated by adopting

$$I_j = \overline{I}\,(1 + A_{I,j} \cdot \sigma_I)\,, \tag{2.9}$$

where the factors $A_{I,j}$ are sampled from independent univariate gaussian random distributions. For the case of diffusion, the central value “1” in Table 2.3 refers to the standard coefficients used in `GARSTEC`, computed following the method of Thoul et al. (1994).

Opacities As described in Section 2.2.2, the contribution of opacity uncertainty to all quantities Q are included *a posteriori* by using Equation 2.7. The linear response of solar models to opacity variations ensures that this procedure is sufficiently accurate. Therefore, this set of MC calculations can be used to test other opacity error functions, e.g. the OP-OPAL difference (Table 2.9 and Figure 2.15) or others motivated by other theoretical or experimental work on opacities.

With the opacity kernels in hand the implementation of opacity uncertainties is very simple. After the j-th SSM is calculated, a change of the opacity profile $\delta\kappa(T)$ is modelled using Equation 2.7, with the coefficients a_j and b_j being extracted from independent gaussian distributions with zero means and dispersions $\sigma_a = 2\%$ and $\sigma_b = 6.7\%$, respectively, values that reflect the estimates of the magnitude of opacity uncertainties. The effect of the opacity variation on the various SSM predictions Q is then calculated by using the kernels $K_Q(T)$ and the estimated change δQ then added to the SSM prediction.

2.4.1.2 Monte-Carlo Results

In this section the results of the MC simulations are presented for both compositions.

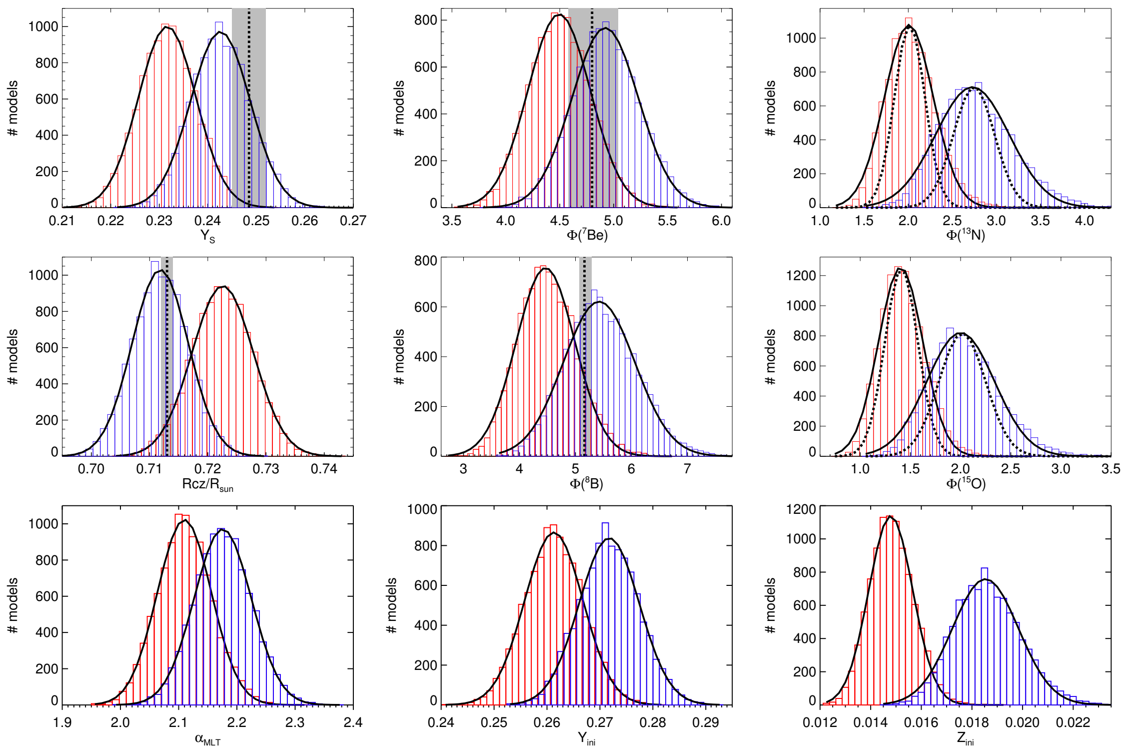

Figure 2.12: Monte-Carlo results for neutrino fluxes and main properties of SSMs. Blue shows results for GS98 and red for AGSS09met. Black solid lines shows the associated Gaussian distributions and the dashed lines, for $\Phi(^{13}\mathrm{N})$ and $\Phi(^{15}\mathrm{O})$, the distributions neglecting errors from solar composition. Vertical black dotted lines show the observational results when available and the grey shaded region the associated errors. Units for neutrino fluxes are as in Table 2.5.

Important solar quantities The distributions of important quantities resulting from the MC simulations are presented in Figure 2.12 for GS98 and AGSS09met compositions. These distributions have been used to compute the uncertainties σ_Q (68.3% C.L.) for model predictions of all quantities Q given in this work, in particular results reported in Table 2.4 and Table 2.5. Plots for $\mathrm{Y_S}$, $\mathrm{R_{CZ}}$, $\Phi(^{7}\mathrm{Be})$, and $\Phi(^{8}\mathrm{B})$ show the solar values as determined from helioseismology and solar neutrino experiments.

Overall, distributions are well described by Gaussian distributions, also included in Figure 2.12 as thick solid lines. The distributions are slightly skewed for $\Phi(^{13}\mathrm{N})$ and $\Phi(^{15}\mathrm{O})$, with a longer tail towards higher values. This is because for chemical elements the distribution is assumed Gaussian for their logarithmic abundance, and these fluxes depend linearly on the added C+N abundance. The dependence of Z_{ini} on this abundances results in a similar distribution shape than the mentioned neutrino fluxes. Then, at least formally, the resulting distributions for these fluxes are described better

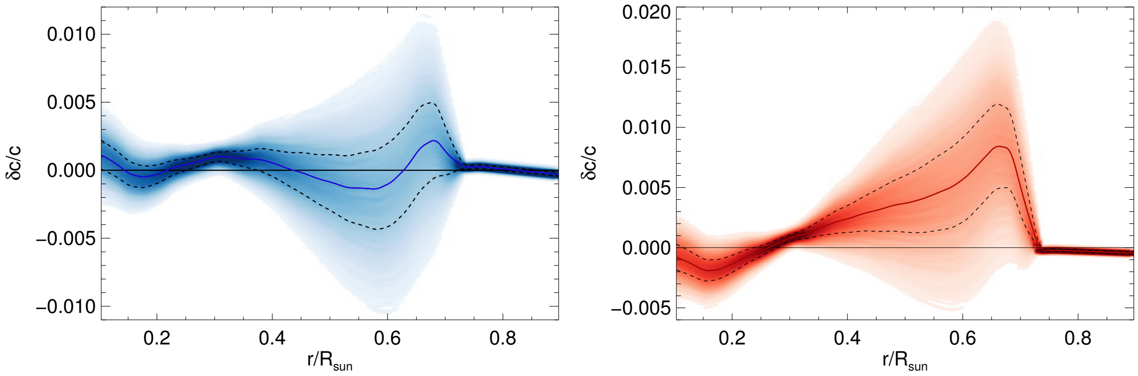

Figure 2.13: Results of 10,000 simulations from MC for the sound speed profile. In the left panel GS98 results are presented and in the right panel AGSS09met. The solid line corresponds to the median values and the dashed the models within 1σ.

---

by log-normal functions. Deviations are small, however, and it is preferred to ignore them by quoting symmetric uncertainties (Table 2.5). The Gaussian distribution resulting when composition errors are neglected are also shown for these neutrino fluxes. Therefore, this represent the power that CN fluxes have for discriminating between different sets of solar composition if no other information is used. This can be largely improved, however, using the method developed in Haxton and Serenelli (2008) and Serenelli et al. (2013), in which an appropriate ratio of $\Phi(^8\mathrm{B})$ and the CN fluxes is used to cancel out the effect of environmental uncertainties, i.e. those affecting fluxes by inducing temperature changes in the solar core, that affect similarly the $\Phi(^8\mathrm{B})$ and CN fluxes in solar models.

Sound speed profile The sound speed difference profile for each of the MC models has been obtained as $\delta c/c = (c_{\odot,C} - c_{\mathrm{mod}})/c_{\mathrm{mod}}$. Here $c_{\odot,C}$ is the solar sound speed profile and C identifies the composition of the reference SSM used in the inversion. Specifically, B16-GS98 or B16-AGSS09met are used depending on whether the MC model belongs to the GS98 or AGSS09met set. This is not a self-consistent procedure because the inferred solar sound speed has a formal dependence on the reference model used for the inversion. That is related to the fact that at inversion procedures, the oscillation equation is linearized around a theoretical reference model of the Sun. That introduce a dependence of the final solar sound speed upon the reference model of choice (Basu et al., 2000). This source of uncertainty then has to be taken into account in an explicit manner, as it has been described in Section 2.3.1. The results for the sound speed can be found in Figure 2.13 for both compositions.

Correlations By using the sets of MC models it is possible to study the correlations among different quantities of the SSMs. This is done by calculating the Pearson correlation (Equation 2.10) for each pair of quantites studied. Given the behavior of the different SSMs predictions, ρ is a good measure of the correlation. Thus, a value of $\rho_{i,j} = 1$ corresponds to two perfectly correlated quantities, $\rho_{i,j} = -1$ when perfectly anticorrelated and $\rho_{i,j} = 0$ when the points are totally uncorrelated between each other.

$$\rho_{i,j} = \frac{cov(i,j)}{\sigma_i \sigma_j} \tag{2.10}$$

In Table 2.7, the correlations among neutrino fluxes and the other relevant quantities are presented. To facilitate the lecture of it, correlations with $\rho_{i,j} > 0.5$ are highlighted in boldface.

As it is well known, the high correlation between $\Phi(\mathrm{pp})$ and $\Phi(\mathrm{pep})$ is because the pp and pep rates are proportional with a factor that is function of the temperature. This is related to the fact that they share the same nuclear matrix element (see Bahcall and May, 1969 for details). The high correlation between $\Phi(^7\mathrm{Be})$ and $\Phi(^8\mathrm{B})$ comes from the fact that they both are initiated by the same reaction and the strong correlation between $\Phi(^{13}\mathrm{N})$ and $\Phi(^{15}\mathrm{O})$ is because they both are part of the CN cycle. The correlations among $\Phi(^7\mathrm{Be})$ and $\Phi(^8\mathrm{B})$ and the CN neutrinos come from the fact that they are produced in high temperatures, and then, changes on the temperature will affect the production in a correlated manner.

The correlations of the other input parameters can be understood as follows. $\mathrm{Y_{ini}}$ and $\mathrm{Y_S}$ are strong correlated as it is the case of $\mathrm{Z_{ini}}$ and $\mathrm{Z_S}$. If diffusion would not be considered, the correlation among these quantities would be perfect, as the present day surface values would be exactly the same as the initial ones. The anticorrelation between the metal abundances and the $\mathrm{R_{CZ}}$ is related to the raise of the radiative opacities with increasing Z that will produce that the transition between the radiative and convective region occurs deeper in the Sun.

To understand the correlations of α_{MLT} with the other quantities it is important to keep in mind that when performing a solar calibration, α_{MLT} is adjusted in order to keep $L_\odot$ and $R_\odot$ constant. Therefore, the correlations of α_{MLT} with the metallicity are related to the fact that an increase of $\mathrm{Z_S}$ (and consequently $\mathrm{Z_{ini}}$) is associated to an increase of the opacities at the external part of the Sun deriving in a less efficient radiative transport. Therefore, in order to account for the required solar luminosity, an increase of α_{MLT} is necessary to increment the convective transport and compensate

	Φ(pp)	Φ(pep)	Φ(hep)	$\Phi(^7$Be)	$\Phi(^8$B)	$\Phi(^{13}$N)	$\Phi(^{15}$O)	$\Phi(^{17}$F)	α_{MLT}	$\mathrm{Y_{ini}}$	$\mathrm{Z_{ini}}$	$\mathrm{Y_S}$	$\mathrm{Z_S}$	$\mathrm{R_{CZ}}$
Φ(pp)	1.00	**0.83**	0.04	**-0.62**	-0.49	-0.29	-0.32	-0.26	-0.08	-0.44	-0.21	-0.19	-0.15	0.36
Φ(pep)	**0.83**	1.00	0.05	**-0.56**	-0.45	-0.28	-0.30	-0.24	0.02	-0.47	-0.18	-0.24	-0.13	0.19
Φ(hep)	0.04	0.05	1.00	-0.05	-0.05	-0.04	-0.04	-0.04	-0.03	-0.05	-0.03	-0.02	-0.02	0.04
$\Phi(^7$Be)	**-0.62**	**-0.56**	-0.05	1.00	**0.85**	0.35	0.42	0.45	0.22	**0.71**	0.16	0.43	0.10	**-0.50**
$\Phi(^8$B)	-0.49	-0.45	-0.05	**0.85**	1.00	0.40	0.47	**0.50**	0.22	**0.74**	0.18	0.43	0.11	-0.49
$\Phi(^{13}$N)	-0.29	-0.28	-0.04	0.35	0.40	1.00	**0.98**	0.31	0.36	0.34	0.40	0.07	0.33	-0.34
$\Phi(^{15}$O)	-0.32	-0.30	-0.04	0.42	0.47	**0.98**	1.00	0.36	0.34	0.42	0.37	0.14	0.30	-0.37
$\Phi(^{17}$F)	-0.26	-0.24	-0.04	0.45	**0.50**	0.31	0.36	1.00	**0.55**	0.46	**0.66**	0.22	**0.61**	**-0.59**
α_{MLT}	-0.08	0.02	-0.03	0.22	0.22	0.36	0.34	**0.55**	1.00	0.08	**0.84**	-0.22	**0.75**	**-0.71**
$\mathrm{Y_{ini}}$	-0.44	-0.47	-0.05	**0.71**	**0.74**	0.34	0.42	0.46	0.08	1.00	0.07	**0.77**	0.05	**-0.65**
$\mathrm{Z_{ini}}$	-0.21	-0.18	-0.03	0.16	0.18	0.40	0.37	**0.66**	**0.84**	0.07	1.00	-0.07	**0.97**	**-0.56**
$\mathrm{Y_S}$	-0.19	-0.24	-0.02	0.43	0.43	0.07	0.14	0.22	-0.22	**0.77**	-0.07	1.00	0.06	-0.41
$\mathrm{Z_S}$	-0.15	-0.13	-0.02	0.10	0.11	0.33	0.30	**0.61**	**0.75**	0.05	**0.97**	0.06	1.00	**-0.52**
$\mathrm{R_{CZ}}$	0.36	0.19	0.04	**-0.50**	-0.49	-0.34	-0.37	**-0.59**	**-0.71**	**-0.65**	**-0.56**	-0.41	**-0.52**	1.00

Table 2.7: Pearson correlations for neutrino fluxes and the main output and calibration parameters of the SSMs. The correlations that fullfill $\rho_{ij} > 0.5$ are highlighted in boldface for a better understanding.

---

the increase of opacities. The quantities α_{MLT} and $\mathrm{R_{CZ}}$ and their anticorrelation are related through the metals and the respective dependence to variation of them.

About the correlations between $\Phi(^7$Be) and $\Phi(^8$B) and the initial helium, if there is an increase of $\mathrm{Y_{ini}}$, it goes at expenses of hydrogen abundance, slowing the *pp* reaction rate. As the total energy trough pp reactions have to be maintained nearly constant to account for the observed solar luminosity, the temperature will have to increase, and therefore the other reaction rates will be accelerated implying an increase of the neutrino fluxes.

Finally, it is worth mentioning that the correlations among different solar quantities depend on the overall effects of the different inputs and outputs. Therefore, to study the correlation in pairs as it has been done is a first approximation in understanding the relationship among different quantities but more complicated dependences should be taken into account

In Figure 2.14 the correlations among different points of the sound speed profile are shown. Basically, this plot illustrates what has been discussed previously, that the sound speed profile is highly correlated along all the solar profile. Also, by looking at the correlations, it is possible to separate the sound speed profile in three different regions, the inner part ($r < 0.3R_\odot$) where the points are highly correlated among each other, the intermediate region ($0.3R\odot < r < \mathrm{R_{CZ}}$), that is perfectly anticorrelated with the inner part, and the outer region (convective envelope) $r > \mathrm{R_{CZ}}$ where the points are perfectly correlated between each other but there is only a weak correlation with the inner part. The region with $r \sim 0.3R_\odot$ shows null correlation with any other

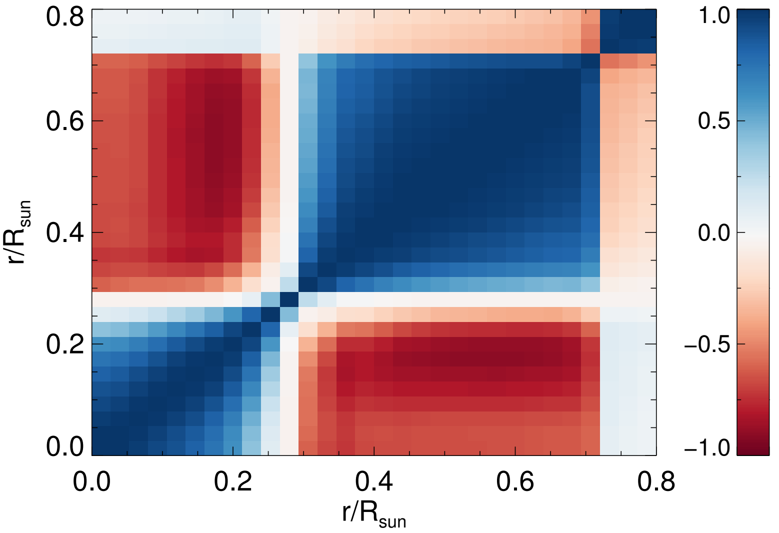

Figure 2.14: Pearson correlations among sound speed profile points at different solar radii. Blue color represents correlation among points while red corresponds to anticorrelation. In white, the points with no correlations are represented.

---

region because, as it is shown in Figure 2.13, is a fixed point not affected by changes on any of the input parameters.

2.4.2 Dominant error sources

As is has been previously presented in Serenelli et al. (2013) the log-derivatives $\alpha_{Q,I}$ are a very good tool to understand the individual contribution of uncertainties on the input parameter to the relevant quantities of the SSMs. In this work, using the B16-SSMs, the derivatives have been updated with respect to the previous ones (see Serenelli et al., 2013). This factors are used later to study which are the dominant error sources for each of the SSMs outputs.

Summarizing, the different contributions of the input parameters I to the total error of a given quantity Q can be described as:

$$\delta Q_I = \alpha_{Q,I}\, \sigma_I \tag{2.11}$$

where σ_I is the 1σ fractional uncertainty of the I input parameter and $\alpha_{Q,I}$ is defined by:

$$\alpha_{Q,I} \equiv \frac{\partial \ln Q}{\partial \ln I} \tag{2.12}$$

As it was done in Serenelli et al. (2013), the derivatives $\alpha_{Q,I}$ are calculated numerically by varying the input parameters individually in a range within their respective

Quant.	Dominant theoretical error sources in %			
$\Phi(\mathrm{pp})$	$\mathrm{L}_\odot$: 0.3	S_{34}: 0.3	κ: 0.2	Diff: 0.2
$\Phi(\mathrm{pep})$	κ: 0.5	$\mathrm{L}_\odot$: 0.4	S_{34}: 0.4	S_{11}: 0.2
$\Phi(\mathrm{hep})$	S_{hep}: 30.2	S_{33}: 2.4	κ: 1.1	Diff: 0.5
$\Phi(^{7}\mathrm{Be})$	S_{34}: 4.1	κ: 3.8	S_{33}: 2.3	Diff: 1.9
$\Phi(^{8}\mathrm{B})$	κ: 7.3	S_{17}: 4.8	Diff: 4.0	S_{34}: 3.9
$\Phi(^{13}\mathrm{N})$	C: 10.0	S_{114}: 5.4	Diff: 4.8	κ: 3.9
$\Phi(^{15}\mathrm{O})$	C: 9.4	S_{114}: 7.9	Diff: 5.6	κ: 5.5
$\Phi(^{17}\mathrm{F})$	O: 12.6	S_{116}: 8.8	κ: 6.0	Diff: 6.0
α_{MLT}	O: 1.3	Diff: 1.2	κ: 0.7	Ne: 0.7
$\mathrm{Y}_{\mathrm{ini}}$	κ: 1.9	Ne: 0.5	Diff: 0.4	Ar: 0.3
$\mathrm{Z}_{\mathrm{ini}}$	O: 4.7	C: 2.0	Ne: 1.7	Diff: 1.6
Y_{S}	κ: 2.2	Diff: 1.1	Ne: 0.6	O: 0.3
Z_{S}	O: 4.8	C: 2.0	Ne: 1.8	κ: 0.7
R_{CZ}	κ: 0.6	O: 0.3	Diff: 0.3	Ne: 0.2

Table 2.8: Dominant theoretical error sources for neutrino fluxes and the main characteristics of the SSM.

3σ uncertainties.

In this work the log-derivatives for the opacity error are also included. The opacity error is described in terms of the two independent parameters a and b, (Equation 2.7), that fix the scale and the tilt of the opacity profile. The derivative of a given quantity Q with respect to these parameters can be calculated from Equation 2.3 as:

$$\begin{aligned} \alpha_{Q,a} &\equiv \frac{\partial \ln Q}{\partial a} = \int \frac{dT}{T} K_Q(T) \\ \alpha_{Q,b} &\equiv \frac{\partial \ln Q}{\partial b} = \int \frac{dT}{T} K_Q(T) \frac{\log_{10}(T/T_0)}{\Delta} \end{aligned} \tag{2.13}$$

Finally, the total error due to opacity is estimated by combining the two contributions in quadrature:

$$\delta Q_\kappa = \sqrt{(\alpha_{Q,a}\,\sigma_a)^2 + (\alpha_{Q,b}\,\sigma_b)^2} \tag{2.14}$$

The updated log-derivatives $\alpha_{Q,I}$ can be found in Appendix A.

Equation 2.11, Equation 2.14 and σ_I are used to estimate the dominant error sources for each of the relevant solar quantities. These dominant sources are presented in Table 2.8 and in Figure 2.15 for the sound speed profile.

Dominant error sources can be grouped as: composition, nuclear, and stellar physics, the latter dominated by opacity and microscopic diffusion and are discussed in detail in the following sections:

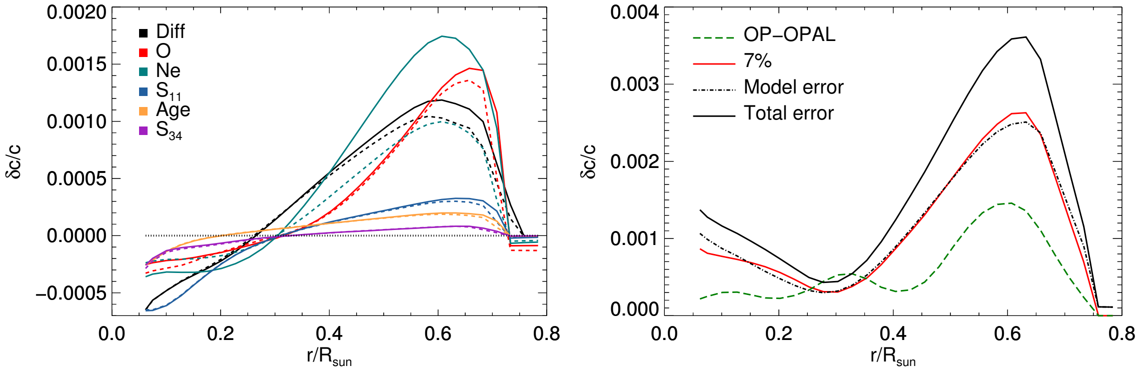

Figure 2.15: Dominant errors sources for the sound speed profile. *Left panel*: Dominant Uncertainty contributions to the sound speed profile. Both results from GS98 (dashed lines) and AGSS09met (solid lines) are presented. *Right panel*: Fractional sound speed variation resulting from different assumptions for the opacity error, (linear function and OP-OPAL). For comparison, the uncertainty due to all other model inputs and the total uncertainty (opacity + other model sources) are also shown.

Composition Errors from composition are dominated by C, O and Ne. This is not related to the solar composition problem, however, but just to the fact that even the most optimistic spectroscopic determinations of solar abundances have a level of uncertainty of about 10-12% that is very difficult to beat. Refractories, on the other hand, are more precisely measured from meteorites so their contribution to uncertainties in solar quantities is currently minimal. Clearly, CNO neutrino fluxes are directly affected by these uncertainties which are, in fact, the dominant error sources. For the same reason, $Z_{\rm ini}$ (and $Z_{\rm S}$) error is also dominated by uncertainties in these elements. For helioseismic quantities, O affects $R_{\rm CZ}$ because it is a dominant contributor to opacity at the base of the convective envelope (see Figure 2.6). On the other hand, $Y_{\rm ini}$ and $Y_{\rm S}$ depend more strongly on Ne due to a combination of its large abundance, impact on opacity at deeper layers and larger error. For the sound speed profile, Ne and O are again dominant sources and the regions more affected are the intermediate and outer regions where Ne and O have a greater impact on the opacity profile.

Nuclear reactions Nuclear rates are still an important uncertainty source for neutrino fluxes despite big progress in the field. In particular, errors in S_{34} and S_{17} are still comparable or larger than the uncertainties in the experimental determinations of $\Phi(^8\mathrm{B})$ and $\Phi(^7\mathrm{Be})$. As discussed in Section 2.3.2, the ability of solar neutrinos linked to pp-chains to play a significant role in placing constraints to the properties of the solar interior depends, although it is not the only factor, on reducing the errors of nuclear reaction rates to just $\sim 2\%$. For CN fluxes, S_{114} is the dominant error source if composition is left aside. Assuming a precise measurement of CN fluxes becomes available in the future, right now S_{114} is the limiting factor in using such measurement as a probe of the solar core C+N abundance (Serenelli et al., 2013). For the sound speed profile, the dominant error in the inner part comes from S_{11}, changes on it will also have an impact along the solar profile. That is related to the fact that changes on S_{11} require changes on the temperature profile in order to maintain the observed solar luminosity.

Microscopic diffusion Microscopic diffusion is typically a smaller source of uncertainty than radiative opacities. However, for CN neutrino fluxes its contribution is larger, only after S_{114} and C. The reason is that accumulation of metals in the solar core due to gravitational settling increases CN fluxes both because it leads to a larger opacity in the solar core, and therefore a higher temperature, but also because the increase in the C+N abundance directly affects the efficiency of the CN-cycle. For the sound speed profile, microscopic diffusion is one of the dominant error sources related to the fact that changes on the diffusion rate will produce changes on the opacity profile that will lead the variations on the sound speed profile.

Opacity For solar neutrinos, the estimated contribution of opacity to the total error is similar to previous calculations (Serenelli et al., 2013) despite the different treatment given to opacity errors. In this work a 2% uncertainty in the center that increases linearly outwards is assumed. Because neutrinos are produced in a localized region, the results are not too different from assuming a constant 2.5% fractional opacity variation, which was the previous choice. Opacity is the dominant error source for $\Phi(^{8}\mathrm{B})$, and the second one for $\Phi(^{7}\mathrm{Be})$. For these fluxes, it is important that opacities in the solar core be known to a 1% level of uncertainty. Current theoretical work shows variations of about 2% (Krief et al., 2016a) and experimental measurements are notoriously difficult due to the combination of high temperatures and densities involved.

Opacity is a dominant error source for helioseismic quantities, most notably $\mathrm{R_{CZ}}$ and $\mathrm{Y_S}$, with the new treatment of uncertainties. A 7% opacity uncertainty at the base of the convective envelope implies a 0.6% change in $\mathrm{R_{CZ}}$. This is larger than all other uncertainty sources combined and explains the substantially larger error in $\mathrm{R_{CZ}}$ given in this work, 0.7% (Table 2.4), compared to 0.5% previously determined

(Bahcall et al., 2006). A similar impact on $\mathrm{Y_S}$ is observed, for which a total 2.5% uncertainty is estimated now compared to 1.5% from previous estimations.

At first glance, the change in uncertainties for $\mathrm{R_{CZ}}$ and $\mathrm{Y_S}$ might seem not too large but in fact model uncertainties are now substantially larger than helioseismically inferred ones (0.14% for $\mathrm{R_{CZ}}$ and 1.4% for $\mathrm{Y_S}$). Moreover, the larger uncertainties lead to a formally better agreement between solar data and SSMs based on AGSS09met composition, which is now placed at about 2.1σ level when $\mathrm{R_{CZ}}$ and $\mathrm{Y_S}$ are considered, whereas before this was closer to 3.5σ.

For the sound speed profile the opacity is clearly the dominant source of errors. In the right panel of Figure 2.15, the contribution of the radiative opacity considering a 2% error in the center an a 7% error at the base of the convective envelope, is presented with the red line. For comparision, in black dashed lines the total contribution of all the other input parameters (the ones represented in the left panel) is compared to the opacity error showing that the opacity contribution to the total sound speed error matches that of all other uncertainty sources combined, including those from composition errors. This emphasizes the importance of the accurate determination of the radiative opacities to solve the *solar abundance problem*.

As discussed before, there is a certain level of arbitrariness in the choice of the error function for opacity. The standard choice arises from a comparison of available opacity data from both theoretical and experimental sources but also from an attempt of not being too aggressive (optimistic) in this choice. An other alternative used in the past is to the OP-OPAL difference as a 1σ measure of the opacity error (Bahcall et al., 2006; Villante, 2010). Using the opacity kernels, it is straightforward to evaluate the error in solar quantities Q if this opacity error function is used. In Table 2.9 the fractional errors of solar quantities Q are compared for the linear and the OP-OPAL error functions and in the right panel of Figure 2.15 the OP-OPAL contribution (dashed green line) can be compared with the lineal one (red line) for the sound speed profile. This comparison highlights the enhanced impact of opacity errors on solar quantities following the new approach, which better reflects the current level of uncertainty in stellar opacities.

2.5 Summary and Conclusions

In this chapter, a new generation of SSMs, B16-GS98 and B16-AGSS09met, has been presented. They have been computed using the new release of `GARSTEC` that includes the possibility of using an equation of state consistent with the composition used in

Quant.	$\sigma_{\mathrm{OP-OPAL}}$	$\sigma_{\mathrm{out}} = 7\%$
$\Phi(\mathrm{pp})$	0.001	0.002
$\Phi(\mathrm{pep})$	0.001	0.005
$\Phi(\mathrm{hep})$	0.002	0.011
$\Phi(^7\mathrm{Be})$	0.009	0.038
$\Phi(^8\mathrm{B})$	0.021	0.074
$\Phi(^{13}\mathrm{N})$	0.012	0.039
$\Phi(^{15}\mathrm{O})$	0.017	0.055
$\Phi(^{17}\mathrm{F})$	0.019	0.061
α_{MLT}	0.005	0.007
$\mathrm{Y}_{\mathrm{ini}}$	0.005	0.019
$\mathrm{Z}_{\mathrm{ini}}$	0.001	0.009
Y_{S}	0.004	0.021
Z_{S}	0.001	0.007
R_{CZ}	0.001	0.005

Table 2.9: Fractional error contribution of opacity to the neutrino fluxes and helioseismic quantities SSMs for different choices of opacity variations, as described in the text.

the SSM calibration. The most recent values for the nuclear reactions $\mathrm{p(p, e^+\nu_e)d}$, $^3\mathrm{He}(^4\mathrm{He},\gamma)^7\mathrm{Be}$ and $^{14}\mathrm{N}(\mathrm{p},\gamma)^{15}\mathrm{O}$ have also been incorporated. With respect to previous works, a new flexible treatment of opacity uncertainties has been implemented. This treatment is based on opacity kernels that allows testing any arbitrary modification to, or error function of, the radiative opacity profile. Based on current theoretical and experimental results on solar opacities, it has been adopted an opacity error that increases linearly from the solar core, where it is 2%, towards the base of the convective envelope where a 7% uncertainty is assumed. However, the difference between OP and OPAL as the opacity error function has also been tested. The estimation of central values of solar observables, their uncertainties and model correlations have been obtained from large MC sets of simulations of SSMs that comprise 10000 SSMs per reference composition (either GS98 or AGSS09met). SSMs have been compared against different ensembles of solar observables: $\mathrm{Y_S}$ and $\mathrm{R_{CZ}}$, sound speed profile, solar neutrinos, and a global comparison that includes the three classes of observables.

The most important findings are summarized in the following list:

1. Central values for $\Phi(^7\mathrm{Be})$ and $\Phi(^8\mathrm{B})$ in B16 SSMs are reduced by about 2% with respect to the previous generation of models that were based completely on the A11 nuclear reaction rates. $\Phi(^{13}\mathrm{N})$ and $\Phi(^{15}\mathrm{O})$, the CN-cycle fluxes, are reduced by 6% and 8% respectively.

2. Solar neutrino fluxes (Bergström et al., 2016) are reproduced almost equally well by both B16-GS98 and B16-AGSS09met, with only a very minor preference for B16-GS98 ($\chi^2 = 6.01$ versus 7.05). If only $\Phi(^7\mathrm{Be})$ and $\Phi(^8\mathrm{B})$ are considered, then $\chi^2 = 0.21$ and 1.50 for B16-GS98 and B16-AGSS09met models respectively.

3. Helioseismic properties of B16 models are almost unchanged with respect to SFII models. However, the estimation of errors is larger due to the more pessimistic assumption of a 7% uncertainty in the radiative opacity at the base of the convective envelope. Comparison of models against $\mathrm{Y_S}$ and $\mathrm{R_{CZ}}$ yields a very good agreement for B16-GS98 (0.5σ) and a poor one (2.1σ) for B16-AGSS09met.

4. The new B16-SSMs do not modify the picture of r_{02} and r_{13} with respect to the previous SFII models. B16-GS98 reproduces the observed small separation ratios while with B16-AGSS09met the agreement is lost.

5. Some of the sources of uncertainty associated with solar sound speed inversion have been reevaluated. This, together with the new adoption of larger opacity uncertainties lead to B16-GS98 and B16-AGSS09met to an agreement with data at the level of 3.16 and 4.5σ respectively.

6. The seemingly, and surprising, bad performance of the sound speed profile of B16-GS98 is caused almost exclusively by the large sound speed difference in the region $0.65 < r/\mathrm{R}_\odot < 0.70$. It is well known that the structure of the Sun in this narrow range of radius is not well reproduced by standard models. There is a long list of possibilities suggested to explain this deficit in SSMs: a smoother chemical profile as claimed by (Antia and Chitre, 1998) due to, e.g. turbulent mixing (Christensen-Dalsgaard and Di Mauro, 2007; Proffitt and Michaud, 1991), a smoother transition between an adiabatic and radiative temperature gradient (Christensen-Dalsgaard et al., 2011) due to overshooting, dynamic effects at the tachocline (Brun et al., 2011), among others. Removing this region from the analysis brings the agreement of B16-GS98 and the solar sound speed to a comforting 1.4σ. However, this discrepancy cannot be ignored and deserves further work.

7. For B16-AGSS09met, the mismatch with the solar sound speed profile is global. Removing the region $0.65 < r/\mathrm{R}_\odot < 0.70$ leads to a 2.7σ discrepancy with the solar sound speed profile.

8. The comparison of models with all data yields $\chi^2 = 65$ for B16-GS98 (40 dof) but only 40.5 (38 dof) when the region $0.65 < r/\mathrm{R}_\odot < 0.70$ is removed. This is equivalent to a very good 0.9σ result. For B16-AGSS09met results are $\chi^2 = 94$, i.e. 4.7σ (or $\chi^2 = 67$ and 3σ without the problematic region). B16-GS98 is a better model than B16-AGSS09met at a statistically significant level.

9. The estimated increase in opacity required to solve the *solar abundance problem* is 15 to 20% at the base of the convective envelope. By assuming a 7% opacity uncertainty in that region, it would be naively expected that B16-AGSS09met is discrepant with solar data at a 2-3σ level. The much larger, 4.7σ discrepancy is due to the fact that the adopted opacity error function Equation 2.7 allows to compensate the differences between AGSS09met and GS98 SSMs but is not flexible enough (for both compositions) to accommodate a better fitting sound speed profile. This is in qualitative agreement with Villante et al. (2014).

10. In order to evaluate the model errors a new MC simulation with 10,000 models for each of the compositions studied have been calculated. The results of these simulations are also useful to study correlations among the different outputs of the models. The contribution of the opacity uncertainties is added a posteriori by using the opacity kernels calculated in this work, providing a flexible method to test different hypothesis for the opacity uncertainties.

11. The dominant uncertainty sources for neutrino fluxes have been identified. Radiative opacity is one of the dominant source followed by the microscopic diffusion rates. Among nuclear reaction rates, the astrophysical factors S_{34}, S_{17} and S_{114} should have their uncertainties reduced to allow more precise tests of solar physics based on solar neutrino experiments. A smaller uncertainty for S_{114} will be crucial in determining the abundance of C+N in the solar core when a precision measurement of the $\Phi(^{13}\mathrm{N})$ and $\Phi(^{15}\mathrm{O})$ fluxes becomes available.

12. For helioseismic quantities, opacity and diffusion are the dominant *stellar* uncertainty sources. Volatile elements, particularly O and Ne, also play an important role.

Chapter 3

State-of-the-art of radiative opacities in SSMs

In the previous chapter it has been proven the importance of the uncertainties of radiative opacities, the role that they have on the final SSMs results and the impact on the unsolved *solar abundance problem*. Moreover, the efforts during the last years on theoretical calculation of radiative opacities have resulted in new releases and updated previous opacity tables as is the case of OPAS (Blancard et al., 2012; Mondet et al., 2015), STAR (Krief et al., 2016b) or the new OPLIB release (Colgan et al., 2016). Because of this context, in this chapter, a study of how these tables affect the SSMs results by using different solar composition mixtures is done. The corresponding SSMs are calculated for each of the cases and the corresponding results are compared among each other. This is a necessary step to help understanding to which level the most recent radiative opacity calculations go in the right direction for mitigating the *solar abundance problem*.

3.1 Opacity tables

In this section the different opacity tables studied in this chapter are presented and compared. Previously, different works have already compared different opacity tables considered here (e.g. Colgan et al., 2013, 2015; Seaton and Badnell, 2004) and also in the solar models context (e.g. Colgan et al. 2016; Le Pennec et al. 2015; Neuforge-Verheecke et al. 2001), but there is a lacking of a consistent comparision of all the radiative opacities tables and the calculation of SSMs using these tables for a different range of compositions. For that purpose, in this work, different opacity tables are calculated and compared using different solar compositions. The ones studied in this chapter are OP (Badnell et al., 2005), OPAL(Iglesias and Rogers, 1996), OPAS

(Mondet et al., 2015) and OPLIB (Colgan et al., 2016). For each of them, an opacity table has been calculated for different compositions, GS98, AGSS09ph, AGSS09met and AGSS15ph, when available. After comparing the opacity characteristics for each of the compositions, the resulting SSMs are consistenly calibrated and the results compared.

Below, there is a brief description of the main characteristics for each of the tables considered in this chapter:

- **OPAL:** The opacity calculations presented in Iglesias and Rogers (1996) are updated from the previous tables from Rogers and Iglesias (1992). In this release 21 elements from H to Ni are included to the calculations and the tables are available online in (`http://opalopacity.llnl.gov/`) for any given composition.

- **OP:** The last release of opacitites from the Opacity Project (OP) are the ones described in Badnell et al. (2005) that follows the previous works from Seaton et al. (1994) and Badnell and Seaton (2003). In this new release 17 elements from H to Ni are included. OP opacity tables can be calculated for any composition. In this chapter, the OP opacities are considered the reference.

- **OPAS:** Mondet et al. (2015) provides opacity tables useful for the solar radiative zone. They considered 22 different elements, from H to Ni, to the calculations. The only available table is for AGSS09ph solar mixture.

- **OPLIB:** In Colgan et al. (2016) a new opacity table is presented as the new generation of Los Alamos National Laboratory (LANL) OPLIB opacity tables described in Magee et al. (1995). In these tables, calculations of monochromatinc opacities and Rosseland mean for 30 elements from H through Zn for a range of densities and temperatures is done. The opacity tables are available online (`http://aphysics2.lanl.gov/cgi-bin/opacrun/tops.pl`) for any required composition.

In Figure 3.1, κ_{ross} provided by the different tables are compared along T-ρ profile from B16-SSMs. This shows the intrinsic differences among different opacity sources, as they have been computed for the same T-ρ and composition profile. The solid lines represent the case where the AGSS09ph is used while the dashed lines to GS98. The tables OPLIB, OPAL and OPAS are compared against OP table. It is important to take into account that in the convective envelope (represented as the grey shadow),

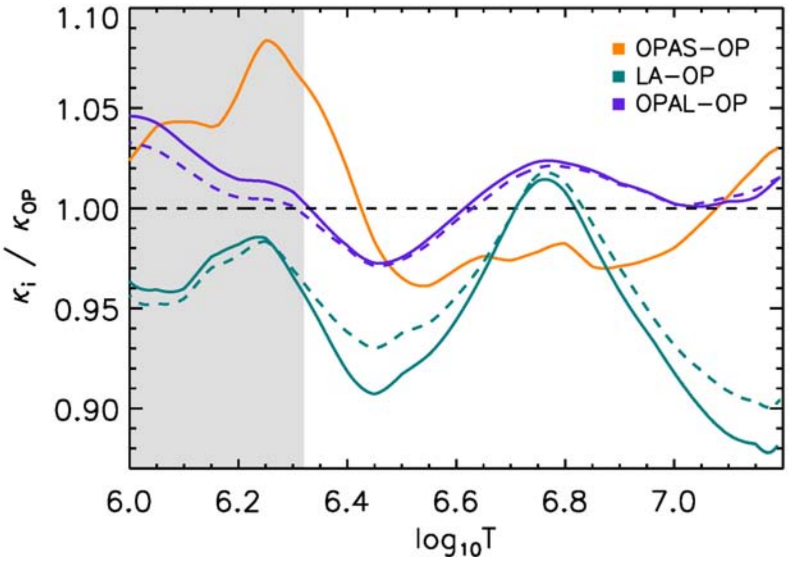

Figure 3.1: Comparision among the different opacity tables. The resulting κ_{ross} from OPAS, OPAL and OPLIB tables are compared with the ones resulting from OP for solar conditions (in temperature and density). The comparision is done for GS98 (dashed line) and AGSS09ph (solid line). Notice that for OPAS table the only opacity table available is AGSS09ph.

---

the transport is almost perfectly adiabatic and the radiative opacities have a negligible role. Consequently, opacity differences in this region will not affect the final SSMs. In purple, the OPAL/OP differences are plotted. For solar conditions, the variations oscillate around zero and reach values of about 2-3% maximum. At the center the variation is only of 1.5% while at the base of the convective envelope is of the order of 1%. Although the differences are moderate with respect to OP, the shape of the profile would derive in changes on the agreement with the observations as it is discussed later in this section. For OPAS table (orange) the changes are more notable along the solar profile. The maximum difference (∼ 8%) is reached inside the convective envelope reaching values of about 5% at the base of the convective envelope. As an example, these variations will move the R_{CZ} deeper in the interior. Finally, the comparison of OPLIB (green) show a large reduction of the opacity for solar conditions when compared with OP tables. This differences reach a 10% decrease at the solar core and about a 5-6% at the base of the convective envelope. These differences will translate in large differences on the neutrino fluxes and to the helioseismic quantities. Next sections present an in depth discussion of the consequences of changes on opacities tables on the solar model outputs.

3.2 The pull approach

In order to study and compare the different SSMs when different radiative opacities are used, it is necessary to describe a statistical approach that allows to quantify the agreement with the observations. In Chapter 2, this study was done by calculating the χ^2 function through a covariance matrix calculated using the results from MC simulations. Another equivalent method is to calculate this χ^2 by using a method called the *pull approach* presented in Fogli et al. (2002). This method, that only can be used in a linear regime, has the advantage that, for a given χ^2, it is possible to have the information of how central values of the input parameters have been modified to reach the value of χ^2. This is the method used in this chapter and its details are described in the following paragraphs.

Consider the fractional difference δQ between theoretical predictions and observational data defined as

$$\delta Q = 1 - \frac{Q_{\rm th}}{Q_{\rm obs}} \tag{3.1}$$

where $Q_{\rm th}$ and $Q_{\rm obs}$ denote the predicted and observed values respectively for the quantity Q. The differences δQ are affected by uncorrelated experimental errors U_Q and by correlated theoretical uncertainties $C_{Q,I}$.

This correlated theoretical uncertainties are calculated using the partial derivatives of the observables (Q) with respect to the different input parameters I as $C_{Q,I} = B_{Q,I}\delta I$ where $B_{Q,I} = \partial {\rm lnQ}/\partial {\rm lnI}$ (power-laws) and δI is the fractional error associated to the input parameter. The input parameters considered are the ones listed in Table 2.1 and Table 2.3. Further details about the determination of $B_{Q,I}$ have been discussed previously Section 2.4.2.

Following the formulation of Fogli et al. (2002), χ^2 can be calculated as:

$$\chi^2 = \min_{\{\xi_I\}} \left[\sum_Q \left(\frac{\delta Q - \sum_I \xi_I C_{Q,I}}{U_Q} \right)^2 + \sum_I \xi_I^2 \right] . \tag{3.2}$$

where the shifts $-\xi_I C_{Q,I}$ describe the effects of correlated errors. They gives the corrections of theoretical predictions $Q_{\rm th}$ when the input parameters I are varied by the fractional amount $\xi_I \delta I$. To normalize the effect of these corrections, a penalty $\sum_I \xi_I^2$ is introduced to the χ^2. This penalty assures that the input parameters does not get values far away from their expected values and take unrealistic values in terms of solar evolution. The values $\tilde{\xi}_I$ that minimize the χ^2 are referred to as pulls of correlated error sources. The quadratic sum $\chi^2_{\text{syst}} = \sum_I \tilde{\xi}^2_I$ give the systematic error contribution to the χ^2.

One of the main advantages of using the *pull approach* is that, apart from the information of the goodness of fit given by the χ^2 function, it provides information of how the input parameters should be modified in order to obtain a model with the best possible χ^2. This information is given by the pulls ξ_I, that represent the number of σ that each input I has to vary from its central value in order to find the best agreement (within realistic input values) with the observations. Also, because the total χ^2 is $\chi^2 = \chi^2_{\text{obs}} + \chi^2_{\text{syst}}$, it is straightforward to separate the contributions from the discrepancy with observations and from systematics (given by the pulls).

3.3 SSMs with different opacity tables

In order to compare the effects of using different opacity tables on the outputs of the SSMs, SSMs with different compositions (GS98, AGSS09ph, AGSS09met and AGSS15ph) and opacity tables (OP, OPAL, OPLIB, OPAS) have been calculated. The solar models are calculated as described in Chapter 2. As the effects of the radiative opacities on the models is the case study, in contrast with what is done in the previous chapter, the model errors presented here do not include uncertainties on the radiative opacities.

3.3.1 Helioseismology

3.3.1.1 Sound speed profile

In Figure 3.2 the sound speed profile for all the calibrated SSMs are presented. Each panel corresponds to a different composition where SSMs have been calculated using the different opacity options. The observational solar sound speed used to calculate $\delta c/c$ is the resulting from the inversions of the B16-SSMs and thus, calculated using OP radiative opacitites. For SSMs with AGSS09ph, AGSS09met and AGSS15ph the solar sound speed from B16-AGSS09met is used while for GS98 is B16-GS98. The fact that the inversions are not performed consistently is a safe option because, as it has been explained in the previous section, the corresponding error is considered as a term in the inversion uncertainties (see Figure 2.8).

As it has been discussed in the previous chapter, the correct quantification of the level of agreement between the sound speed of models and observations requires a proper account of the strong correlations in model predictions. This is done by including the correlations in the model sound speed predictions among different locations

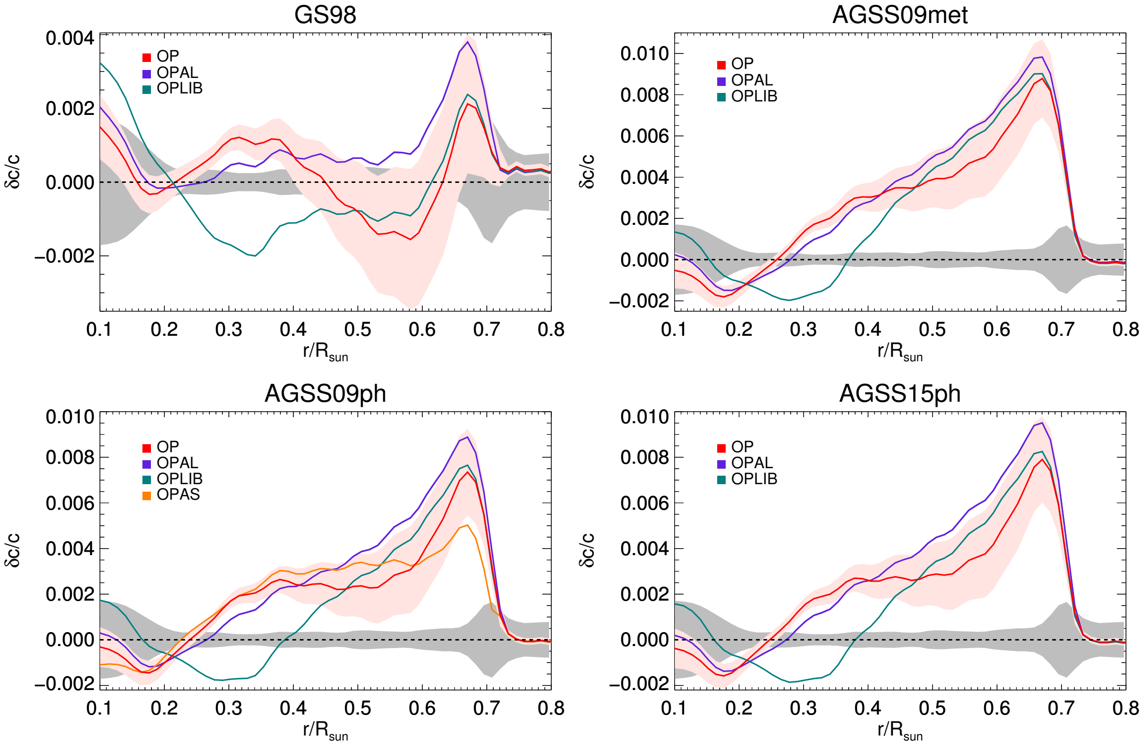

Figure 3.2: Sound speed profiles using the different compositions (GS98, AGSS09ph, AGSS09met and AGSS15ph) and the different opacity tables available (OP, OPAL, OPLIB and OPAS). The pink band corresponds to the model error (without uncertainties on the radiative opacities) and the grey band corresponds to the observational and inversion procedure errors.

through the power-laws, as described the previous sections. Table 3.1 summarizes the χ^2 for each of the SSMs with the corresponding p-values. These results are presented when 30 different points are used and when two points (25th and 26th) from the bump below the convective envelope are excluded, as it was previously done in Chapter 2.

When AGSS09met is used as solar composition, for all the cases, the final χ^2 is higher than the cases with low-Z where photospheric abundances are used (AGSS09ph and AGSS15ph). The reason for that is that meteoritic abundances have smaller errors associated and that for photospheric composition the Fe abundance is slightly higher ($\sim$ 0.05dex) and the model reproduces a bit better the observations. If the same errors were used for all the cases, the final results would be similar and the same conclusions for the three cases would apply. For that, the following discussion is focused on AGSS09ph (for which OPAS is available) and GS98.

As a first sight, when OPAL and OP models are compared in Figure 3.2, it is

	Compo	OP	OPAL	OPLIB	OPAS
δc/c	GS98	60.3 (3.3)	37.1 (1.4)	56.4 (3.0)	-
	AGSS09met	93.6 (5.6)	49.5 (2.5)	89.6 (5.4)	-
	AGSS09ph	72.3 (4.2)	46.5 (2.2)	54.5 (2.9)	32.6 (1.0)
	AGSS15ph	69.0 (4.0)	46.2 (2.2)	56.4 (3.0)	-
δc/c-peak	GS98	35.0 (1.4)	20.0 (0.2)	28.7 (1.7)	-
	AGSS09met	62.4 (3.7)	30.8 (1.0)	81.1 (5.0)	-
	AGSS09ph	47.1 (2.5)	28.8 (0.8)	37.9 (1.6)	25.4 (0.5)
	AGSS15ph	44.5 (2.2)	28.8 (0.8)	40.1 (1.8)	-

Table 3.1: Comparision of the SSMs with different opacity tables (OP, OPAL, OPLIB and OPAS) and compositions (GS98, AGSS09met, AGSS09ph and AGSS15ph). The χ^2 and the corresponding p-values in parenthesis for the complete sound speed profile (δ_c/c) are presented, as well as the sound speed including two points from the bump below the convective envelope ($\delta c/c$-peak).

possible to conclude that the agreement with the observations seems to be at the same level for both cases. The important difference is that for OPAL, the oscillatory behavior of the sound speed has smaller amplitude than when OP is used. This behavior can be seen by the local maximum and minimum at $0.35R_\odot$ and $0.55R_\odot$ respectively seen in the $\delta c/c$ profile with OP opacities and GS98 composition. That is the reason why, although the apparently similar disagreement with the observations, the value of χ^2 (see Table 3.1) is lower for OPAL than for OP. That is because for the first, there is a combination of pulls (ξ_I), associated to changes on the central values of the input parameters, that brings the SSM to an agreement at 1.4σ level for GS98 and 2.2σ for AGSS09ph. For OP models, it does not exist a combination of changes on the input parameters that can improve the 3.3σ agreement for GS98 and 4.2σ for AGSS09ph. Focusing on the OPAL case, and using the "pull approach" it is possible to study which are the contributions to the χ^2 and the different changes on the input parameters required to obtain the χ^2 for GS98 and AGSS09ph. The main differences between both compositions are that for GS98, the resulting model for the calibration is already close to the best agreement possible with only a small contribution from the pulls of $\chi^2_{SYS} = 5.3$, while for AGSS09ph this term is $\chi^2_{SYS} = 17.6$, meaning that larger changes on the input parameter are required. For this second case, the main contributions to this pull term are the changes on diffusion $\xi_{\rm diff} = 1$ and more importantly, on the composition. The latter is dominated by the oxygen pull $\xi_O = 3.2$, that would bring the oxygen to values similar (or even higher) than GS98, a result that is in consistency with the *solar abundance problem*.

The agreement of SSMs calculated using OPLIB is improved for both GS98 and AGSS09ph compositions when they are compared with the OP results. The reason is similar than for the previous case, for OPLIB models, there is a combination of pulls that change the central values of the inputs that results in a better agreement than for OP. By analyzing the resulting pulls, again, it is possible to see that the main required changes are for the composition and diffusion for both GS98 and AGSS09met. The contribution of the pulls to the final χ^2 is similar for both compositions, meaning that, by only studying the sound speed profile, it is not possible to determine which solar composition is favored by the observations. Also, by studying the individual pulls, it is possible to see that the pulls for the diffusion are $\xi_{\text{diff}} = -2$ that would imply a high decrease of a 30% for the diffusion coefficients.

Finally, the best agreement of sound speed with the observations is obtained when the OPAS opacity table is used. By looking at Figure 3.2, a notable improvement on the peak below the convective envelope can already be appreciated. The final agreement is at 1σ level with the main contribution of the pull term coming from changes on the composition (e.g. $\xi_O = 1$ and $\xi_{Fe} = -2.5$) and from the diffusion coefficients ($\xi_{\text{diff}} = 1.9$). While the agreement is good for OPAS, the pulls close to 2 are large, in particular for the case of diffusion, a corresponding decrease of a 30% it is not realistic. In fact, there are some evidences that give the hint that the considered standard diffusion is too high. For example any additional mechanism added at the base of the convective envelope to lower the bump on the sound speed profile lead to a reduction of the standard diffusion (Delahaye and Pinsonneault, 2006). Moreover, the study of solar-like stars in M67 cluster give the idea that standard diffusion should not be further increased (Önehag et al., 2014). To lower the iron about -2.5σ is also too high considering the associated photospheric error, that would bring the Fe abundance to unrealistic low values. For OPAS, the only table available corresponds to the AGSS09ph composition, and in order to have a complete picture of the performance of OPAS radiative opacities on SSMs, the tables for GS98 are required.

Finally, and to conclude this section, the results when two points from the bump below the convective region are excluded are summarized in Table 3.1. Consistently with the results presented in Chapter 2, the agreement is notably improved for all the cases but for models with OPAS. That is because, as it can be seen in Figure 3.2, the peak is already partially mitigated by the initial choice of radiative opacities.

	Opac.	GS98	AGSS09ph	AGSS09met	AGSS15ph
R_{CZ}	OP	0.7116 ± 0.0034	0.7207	0.7223 ± 0.0038	0.7213
	OPAL	0.7132	0.7217	0.7227	0.7227
	OPLIB	0.7113	0.7200	0.7214	0.7205
	OPAS	-	0.7162	-	-
Y_S	OP	0.2426 ± 0.0035	0.2353	0.2317 ± 0.0035	0.2332
	OPAL	0.2438	0.2367	0.2342	0.2346
	OPLIB	0.2368	0.2278	0.2241	0.2258
	OPAS	-	0.2324	-	-

Table 3.2: Y_S and R_{CZ} values from the different SSMs. Model errors do not include errors for the radiative opacities.

3.3.1.2 Depth of convective envelope and surface helium

Changes on the radiative opacities have a direct impact on the final values of the surface helium and the depth of the convective envelope. Globally and as a first sight, changes on these quantities can be related as follows. If the radiative opacities increase at the base of the convective envelope a deeper R_{CZ} is expected, due to an increase of the radiative gradient ∇_{rad}, that will lead the criteria for convective transport, $\nabla_{rad} > \nabla_{ad}$ to be fullfilled deeper in the Sun. For Y_S, the main changes come from modifications of the radiative opacities at the solar core. If the opacities are reduced at the center, the temperature in the solar interior decreases and that implies that the nuclear reaction rates slow down. As the constant total nuclear energy is required to account for the solar luminosity, the hydrogen abundance has to be higher to compensate the lower temperatures, at expense of the helium abundance. When the radiative opacities increase, the opposite situation applies.

In Table 3.2 the resulting Y_S and R_{CZ} values for the SSMs using different opacity tables are summarized for each of the compositions considered. To understand how each opacity table modifies these quantities, the opacity kernels presented in the previous chapter are a good mechanism. In Figure 2.3 the kernels show how the different quantities can be affected when there are changes on the opacitites in different regions of the solar interior. For example, R_{CZ} is mostly affected by changes at the base of the convective envelope, although it is also modified when changes on the opacity take place on the central part of the Sun. Therefore, the final value of R_{CZ} and Y_S have to be understood as the integrated contribution of opacity modifications all over the solar profile. In Figure 3.3, the product of the kernel ($K_Q(T)$) and the

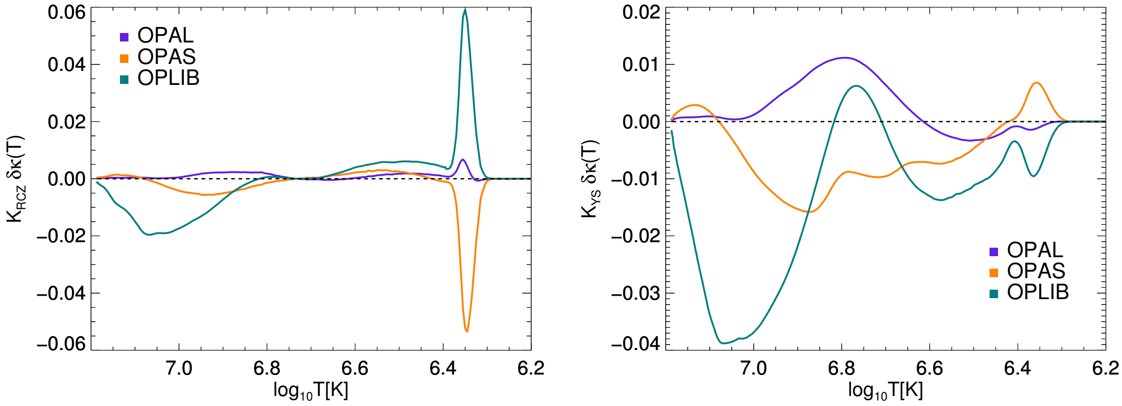

Figure 3.3: $K_Q(T) \cdot \delta\kappa(T)$ profile for $\mathrm{R_{CZ}}$ (left panel) and $\mathrm{Y_S}$ (right panel). $\delta\kappa(T)$ is the relative difference with respect to OP opacities for OPAL (purple), OPLIB (green) and OPAS (orange). The results correspond to tables calculated for AGSS09ph composition.

relative opacity change with respect to OP tables ($\delta\kappa(T)$) is plotted as a function of the temperature for $\mathrm{R_{CZ}}$ (left panel) and $\mathrm{Y_S}$ (right panel).

Focusing in $\mathrm{R_{CZ}}$, when the OPAL/OP difference is considered, it is possible to observe that the final result is slightly larger than the reference OP value (Table 3.2), explained by the fact that the opacity at the base at the convective envelope is reduced about 1%. In Figure 3.3, it can be seen that opacity changes along the solar profile only have a marginal effect and the main contribution comes from a perturbation at the base of the convective envelope. For OPAS, $\mathrm{R_{CZ}}$ experiments a notable decrease with respect to the reference value due to a 5% increase of the opacity at the base of the convective envelope. As in the more inner part OPAL opacities are lower than OP, that will also contribute to lower the final $\mathrm{R_{CZ}}$ value. Finally, the OPLIB/OP relative change for the opacity is considered. For this case, $\mathrm{R_{CZ}}$ slightly decreases with respect to the reference value although there is about a 5% decrease of the opacity at the base of the convective envelope. That is a consequence of the 10% opacity decrease at the center. As it has been already mentioned, $\mathrm{R_{CZ}}$ is not only affected by the opacities near its radius, but also for changes along the solar profile. Therefore, in this case, the large variation at the interior compensates the large increase of $\mathrm{R_{CZ}}$ that would take place if only the 5% decrease at the base of the convective envelope is considered. This can be better understood by looking at the $K_{\mathrm{R_{CZ}}} \cdot \delta\kappa$ profile illustrated in Figure 3.3.

	Compo	OP	OPAL	OPLIB	OPAS
Y_S	GS98	1.3 (0.6)	0.8 (0.9)	5.0 (2.2)	-
	AGSS09met	10.1 (3.2)	7.3 (2.7)	21.3(4.6)	-
	AGSS09ph	5.0 (2.2)	4.0 (2.0)	12.3 (3.5)	7.4 (2.7)
	AGSS15ph	2.6 (2.6)	5.5 (2.3)	14.7 (3.8)	-
R_{CZ}	GS98	0.2 (0.4)	0.01 (0.1)	0.2 (0.4)	-
	AGSS09met	5.3 (2.3)	5.6 (2.4)	4.3(2.1)	-
	AGSS09ph	3.4 (1.8)	4.4 (2.1)	2.7 (1.6)	0.6 (0.8)
	AGSS15ph	2.0 (2.0)	5.2 (2.3)	3.3 (1.8)	-
Y_S+R_{CZ}	GS98	1.3 (0.6)	0.9 (0.5)	5.1 (1.8)	-
	AGSS09met	14.8 (3.4)	12.4 (3.1)	24.8(4.6)	-
	AGSS09ph	7.7 (2.3)	7.7 (2.3)	14.0 (3.3)	7.7 (2.3)
	AGSS15ph	9.8 (2.7)	9.9 (2.7)	16.8 (3.7)	-

Table 3.3: Same than Table 3.1 but for Y_S, R_{CZ} and both quantities combined.

Y_S final results depend on the temperature profile and are a direct proof of variations of the opacities. For OPAL, Y_S values are higher than OP because radiative opacities are higher in the interior region where Y_S depends more on opacities. OPAS results are much lower, related to the fact that radiative opacities decrease in a dominant part of the solar interior. Finally, the lower OPLIB Y_S result is consequence of the lower values of the opacity at the main region of the Sun, although the Y_S decrease is partially compensated by the small region around $\log_{10} T = 6.8$ where the opacity takes values higher than OP. All this effects are illustrated and can be better understood in the right panel of Figure 3.3.

In Table 3.3, the results of χ^2 and the corresponding values are summarized for Y_S, R_{CZ} and for both quantities combined. For GS98, the good agreement obtained for Y_S when OP (0.6σ) or OPAL (0.9σ) are used is lost when OPLIB opacities are considered reaching a 2.2σ level of agreement. The situation is similar when AGSS09ph is used, OPLIB opacities worsens the fit (3.5σ) from OP (2.2σ) and OPAL(2σ). Finally, OPAS opacities bring Y_S abundance far away (2.7σ) from the observations with respect to OP and OPAL cases.

For the case of R_{CZ} the situation is similar when OP, OPAL or OPLIB are used, that is because the final R_{CZ} does not change with respect to the reference values (OP) because of the integrated effect of the opacity perturbation. The big difference comes from OPAS models, were for AGSS09ph a very good agreement (0.8σ) is reached.

The combination of both helioseismic parameters results in a convergence of the agreement for all the compositions when OP, OPAL and OPAS opacity tables are used. However, this is not the case for the models calculated with OPLIB, that the very low value of $\mathrm{Y_S}$ results in $\chi^2_{GS98} = 5.1$ and $\chi^2_{AGSS09ph} = 14.0$ for only two degrees of freedom.

Finally, it is worth commenting the low values of $\mathrm{Y_S}$ resulting from models with OPLIB tables. Before discarding these models one could argue that the low surface helium (and corresponding $\mathrm{Y_{ini}}$) resulting from models calculated with OPLIB opacity tables could be enhanced if an additional mixing process is introduced to the SSMs. An extra mixing process would inhibit partially the microscopic diffusion and thus, if assuming that $\mathrm{Y_{ini}}$ is uncorrelated with microscopic diffusion, that would indeed result in an increase of $\mathrm{Y_S}$ that could recover (at least partially) the agreement with the observations and make room to have also higher initial helium. But this argument is not valid because $\mathrm{Y_{ini}}$ is not independent of the microscopic diffusion. As it has already been commented in Serenelli (2010), a decrease of the microscopic diffusion would lead to a reduction of the gravitational settling of metals in the core resulting in a decrease of the radiative opacities at this region. That would reduce the temperature in the nuclear production region, and therefore, to maintain the integrated nuclear energy to account for the solar luminosity, a higher abundance of hydrogen is necessary lowering the initial abundance of helium. Therefore, an additional mixing process would decrease the values of $\mathrm{Y_S}$, but would even lower the initial value of $\mathrm{Y_{ini}}$ that is already too low and thus, the models would be even more unrealistic. To discuss why there is no room for lower $\mathrm{Y_{ini}}$, in Table 3.4 the results of $\mathrm{Y_{ini}}$ and $\mathrm{Z_{ini}}$ are summarized for the different models. For this discussion, the focus is on the model with AGSS09ph[1]. The $\mathrm{Y_{ini}}$ of the model have very low values, equal to $\mathrm{Y_{ini}} = 0.2564 \pm 0.002$, very close to the values of the primordial $\mathrm{Y_P} = 0.2482 \pm 0.0007$ (Steigman, 2010). This would imply that almost not chemical enrichment took place in the solar neighborhood. One measure of the enrichment and production of helium with respect to the metallicity is $\Delta Y/\Delta Z$ with $\Delta Y = \mathrm{Y_{ini}} - \mathrm{Y_{BBN}}$. Different authors and methods (see Section 9 of Gennaro et al. 2010 and references therein) have determined that the $\Delta Y/\Delta Z$ for the solar neighborhood should be in the range of approximately 1.5 - 2.5. This quantity is presented for each model in the last panel of Table 3.4 and it is possible to observe that when OPLIB is used, and even for GS98, these values are much lower than the predicted values. Therefore, it is difficult to find a way to justify such low values for $\mathrm{Y_{ini}}$ and $\mathrm{Y_S}$ and so, the radiative opacities for OPLIB tables should be increased at the core in order to have values consistent with the

---

[1] The discussion that follows can be extrapolated to the other SSMs with different compositions.

	Opac.	GS98	AGSS09ph	AGSS09met	AGSS15ph
$\mathbf{Y_{ini}}$	OP	0.2718 ± 0.0024	0.2650	0.2614 ± 0.0024	0.2629
	OPAL	0.2734	0.2669	0.2644	0.2647
	OPLIB	0.2650	0.2564	0.2524	0.2560
	OPAS	-	0.2615	-	-
$\mathbf{Z_{ini}}$	OP	0.0187 ± 0.0013	0.0150	0.0149 ± 0.0010	0.0149
	OPAL	0.0187	0.0150	0.0151	0.0149
	OPLIB	0.0188	0.0152	0.0150	0.0151
	OPAS	-	0.0151	-	-
$\mathbf{\Delta Y/\Delta Z}$	OP	1.25 ± 0.30	1.10	0.87 ± 0.37	0.97
	OPAL	1.33	1.23	1.05	0.97
	OPLIB	0.88	0.52	0.26	0.50
	OPAS	-	0.86	-	-

Table 3.4: $\mathrm{Y_{ini}}$, $\mathrm{Z_{ini}}$ and helium total enrichement ratio $\Delta\mathrm{Y}/\Delta\mathrm{Z}$ values from the different SSMs. Model errors do not include errors for the radiative opacities.

---

current observations. This result is in accord with the neutrino fluxes conclusions as it is discussed in Section 3.3.2.

3.3.1.3 Frequency separation ratios

This section analyses how the small separation ratios change with different opacity tables. The ratios presented are the ones described in Section 2.3.1.3, r_{02} and r_{13}. The results are plotted in Figure 3.6 where the left panel corresponds to SSMs calculated using GS98 mixture while the right panel correspons to AGSS09ph. The behavior of r_{02} and r_{13} with changes on the opacities is similar and it goes on the same direction. For GS98, if OPAL table is used, the ratios will slightly decrease with respect to OP while if OPLIB is used the good agreement obtained is lost with resulting ratios with much lower values than the observational ones. For AGSS09ph, the situation is similar, and interestingly, when OPLIB tables are used, AGSS09ph ratios agree with the observations. This the opposite situation of what happens when OP, OPAL or OPAS are used.

To understand the different behaviors of the ratios the opacity kernels are a good tool. In Figure 3.5, the product of $K_Q \cdot \delta\kappa$ for the two different ratios considered are shown as function of the solar temperature. Starting with r_{02}, is possible to see that for OPAL, $K_{r02} \cdot \delta\kappa_{OPAL}$ oscillates around zero with some small peak at

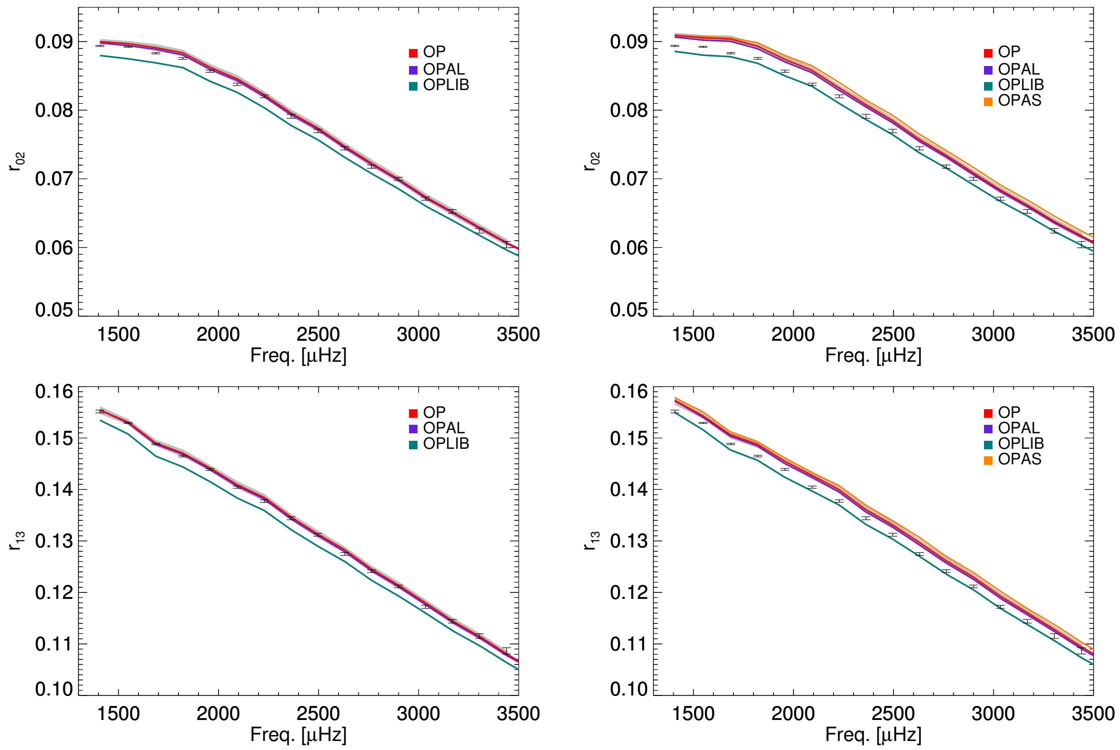

Figure 3.4: Small separation ratios for SSMs with OP (red), OPAL(purple), OPAS(yellow) and OPLIB(green). The black dots are the observational solar values with the corresponding errors (Broomhall et al., 2009; Hale et al., 2016). The shadowed grey band determines the model errors (without opacity uncertainties). Upper panel: r_{02}, Lower panel: r_{13}. The panels on the left correspond to models with GS98 and the ones in the right to models calculated with AGSS09ph.

$\log_{10} T(K) \sim 6.85$ that brings the final values to slightly lower values than for OP. For OPAS, the increase of the ratios is evident because all over the solar profile, the product $K_{r02} \cdot \delta\kappa_{OPAS}$ is dominantly positive. For OPLIB, the changes of the ratios are clearly dominated by the two peaks in the inner part, and more in particular, the one at $\log_{10} T(K) \sim 7.1$ that is a factor two larger than the second one. Then, it is that region that will dominate over the rest of the solar profile and it explains the lower values of the ratios obtained by OPLIB models. r_{13} have a very similar behavior than r_{02} and the same discussion and conclusions apply.

3.3.2 Neutrino Fluxes

The resulting neutrino fluxes from the different SSMs are presented in Table 3.5 for GS98, AGSS09met, AGSS09ph and AGSS15ph solar mixtures. The errors included are calculated using MC simulation presented in Section 2.4.1 without including the

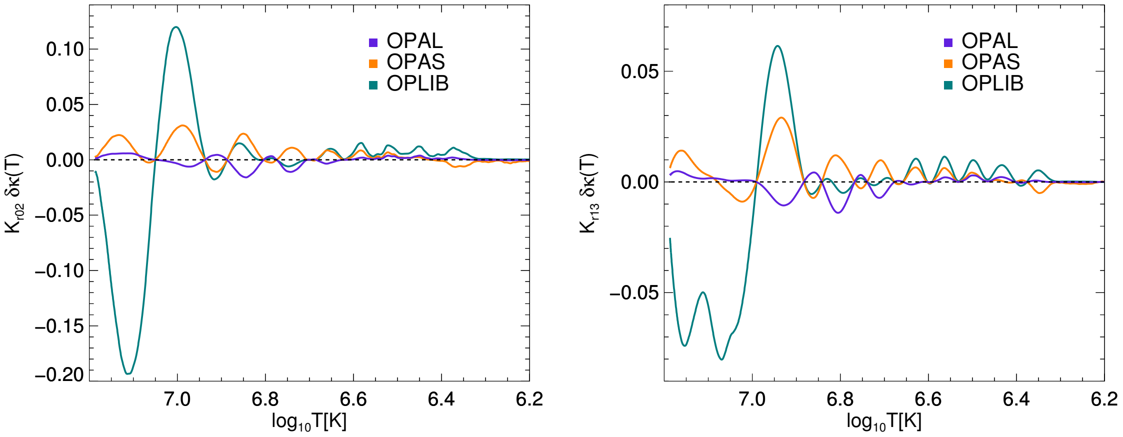

Figure 3.5: Same than Figure 3.3 but for small separation ratios. Left panel: r_{02}, Right panel r_{13}.

errors for the radiative opacities.

The effects of changes on the opacity profile on the final neutrino fluxes can be understood much straightforwardly than for the previous quantities because they are a direct consequence of changes on the temperature in the solar interior. In Chapter 1 it was shown that neutrino fluxes are proportional to the solar central temperature as using $\phi \propto T^m$. The exponents m are specified for each of the fluxes in Table 1.1. Neutrino fluxes are very sensitive to the temperature e.g. $m = 10$ for $\Phi(^7\mathrm{Be})$ or $m = 24$ for $\Phi(^8\mathrm{B})$. For OPAL, the relative central temperature changes with respect OP is of about 0.1%, that translate to an increase of $\sim 3\%$ for $\Phi(^8\mathrm{B})$ and $\sim 1.3\%$ for $\Phi(^7\mathrm{Be})$. For OPAS, the relative change of the opacities at the central part is slightly larger than for OPAL, deriving in an increase of 3.5% and 1.4% for $\Phi(^8\mathrm{B})$ and $\Phi(^7\mathrm{Be})$. The opacities for OPLIB decrease about a 10% in the center that translates in a central temperature that is a 1.25% lower than for OP and that result in a high decrease of a $\sim 20-25\%$ and $\sim 10-12\%$ for $\Phi(^8\mathrm{B})$ and $\Phi(^7\mathrm{Be})$. The changes of the rest of neutrino fluxes can be understood in the similar way, using the corresponding dependence on changes on the central temperature. Another way to approximately predict these changes on the solar neutrino fluxes is using the power-laws of the opacities as described in Section 2.4.2 by using the relative changes of the opacity on the nuclear production region (e.g. the central part of the Sun). It is important to keep in mind that, for this case study, the previous relations to predict the changes on neutrino fluxes are a first approximation, and changes on other parameters of the SSMs should be considered to obtain the final value from the solar calibrations.

	GS98				**AGSS09met**		
Flux	OP	OPAL	OPLIB	OPAS	OP	OPAL	OPLIB
$\Phi(pp)$	$5.98(1\pm0.005)$	5.97	6.02	-	$6.03(1\pm0.005)$	6.02	6.07
$\Phi(pep)$	$1.44(1\pm0.008)$	1.43	1.48	-	$1.46(1\pm0.007)$	1.46	1.51
$\Phi(hep)$	$7.98(1\pm0.30)$	7.94	8.16	-	$8.25(1\pm0.30)$	8.18	8.47
$\Phi(^7Be)$	$4.93(1\pm0.05)$	4.98	4.62	-	$4.50(1\pm0.05)$	4.59	4.13
$\Phi(^8B)$	$5.46(1\pm0.09)$	5.57	4.58	-	$4.50(1\pm0.09)$	4.67	3.60
$\Phi(^{13}N)$	$2.78(1\pm0.15)$	2.81	2.52	-	$2.04(1\pm0.13)$	2.12	1.82
$\Phi(^{15}O)$	$2.05(1\pm0.16)$	2.08	1.79	-	$1.44(1\pm0.15)$	1.50	1.21
$\Phi(^{17}F)$	$5.29(1\pm0.19)$	5.47	4.55	-	$3.26(1\pm0.17)$	3.41	2.69
	AGSS09ph				**AGSS15ph**		
Flux	OP	OPAL	OPLIB	OPAS	OP	OPAL	OPLIB
$\Phi(pp)$	6.01	6.01	6.06	6.02	6.02	6.02	6.06
$\Phi(pep)$	1.45	1.45	1.51	1.45	1.46	1.45	1.51
$\Phi(hep)$	8.17	8.13	8.40	8.21	8.21	8.17	8.44
$\Phi(^7Be)$	4.65	4.69	4.26	4.62	4.56	4.60	4.19
$\Phi(^8B)$	4.84	4.92	3.85	4.88	4.63	4.71	3.71
$\Phi(^{13}N)$	2.12	2.14	1.88	2.13	2.07	2.09	1.85
$\Phi(^{15}O)$	1.52	1.53	1.27	1.53	1.47	1.48	1.24
$\Phi(^{17}F)$	3.46	3.50	2.85	3.49	3.34	3.37	2.76

Table 3.5: Neutrino fluxes for SSMs using GS98, AGSS09ph, AGSS09met and AGSS15ph compositions and different opacity tables. Units are: 10^{10} (pp), 10^9 (^{7}Be), 10^8 (pep, ^{13}N, ^{15}O), 10^6 (^{8}B,^{17}F) and 10^3(hep) $cm^{-2}s^{-1}$.

To illustrate the changes on the neutrino fluxes, Figure 3.7 shows the product of the neutrino kernels with the opacity perturbation for $\Phi(^7Be)$ and $\Phi(^8B)$. Similar results can be extrapolated for the other neutrino fluxes because the shape of the kernels (see Figure 2.3) are very similar.

Figure 3.7 shows the probability distributions of $\Phi(^8B)$ (upper panels) and $\Phi(^7Be)$ (lower panels) when OP (right panel) and OPLIB (left panel) are used for the four different composition mixtures considered. It is possible to see how for all the compositions the use of OPLIB opacities results in neutrino fluxes much far away from the observations. To quantify this agreement with observations, in Table 3.6 the χ^2 and the corresponding p-values for $\Phi(^7Be)$, $\Phi(^8B)$ are presented, as well as the results when both fluxes are considered at the same time. For the discussion that follows, the results when both neutrino fluxes are considered at the same time are used. Unlike

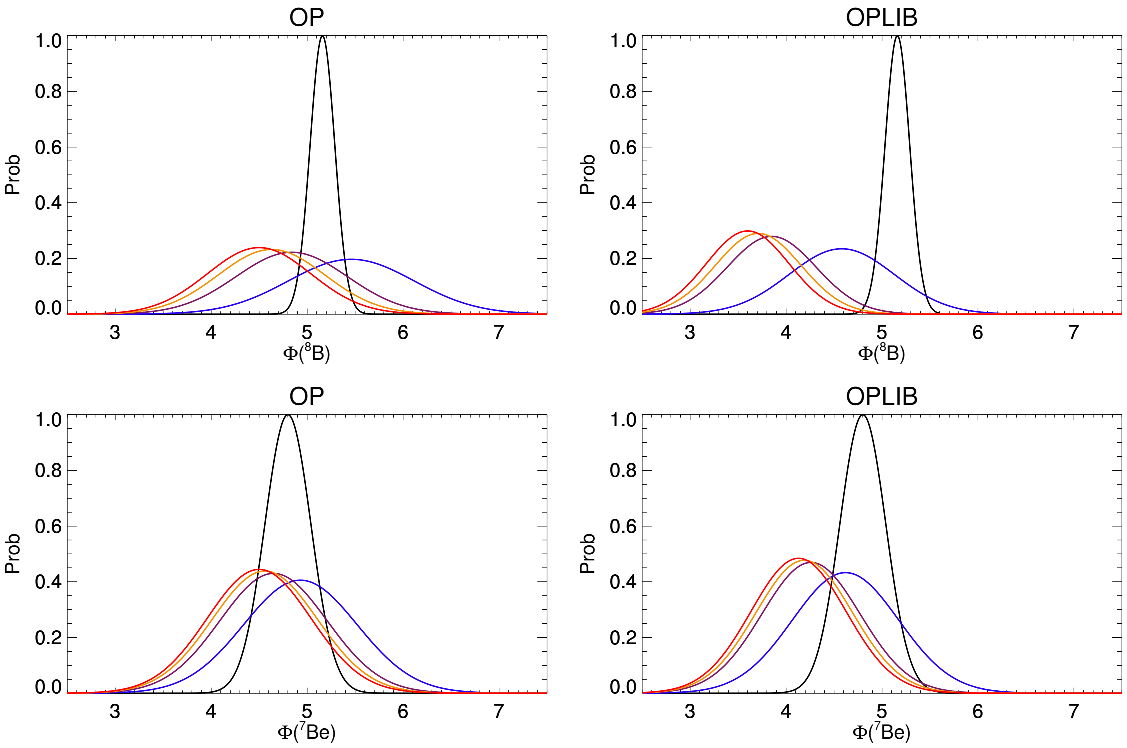

Figure 3.6: Normalized probability distribution for $\Phi(^7\mathrm{Be})$ and $\Phi(^8\mathrm{B})$. Red: AGSS09met, Orange: AGSS15ph, Purple: AGSS09ph, Blue: GS98 and Black: Solar values. Left panels corresponds to SSMs with OP and right panel with OPLIB.

---

the sound speed case, OPAL and OPAS opacities do not improve the agreement with the observations when compared with OP models, although the performance is at similar levels and below 1σ. The situation is different when OPLIB is considered. As commented in the paragraphs above, the 10% decrease of the opacities at the solar core notably lower the neutrino fluxes and the agreement obtained when OP, OPAL or OPAS opacity tables are used is lost for AGSS09ph and, although still compatible with the observations, is worst for GS98 models. This shows that the decrease of the radiative opacities at the interior is too high to be compatible with the current solar observations (Bergström et al., 2016).

3.3.3 Global results

Similarly than what was done in Section 2.3.3, and in order to test the global performance of the different SSMs considered in this chapter, the χ^2 are calculated using all the observables. This includes 30 points of the sound speed profile, $\mathrm{Y_S}$, $\mathrm{R_{CZ}}$, $\Phi(^8\mathrm{B})$ and $\Phi(^7\mathrm{Be})$. The results are summarized in Table 3.7 and for completeness, the re-

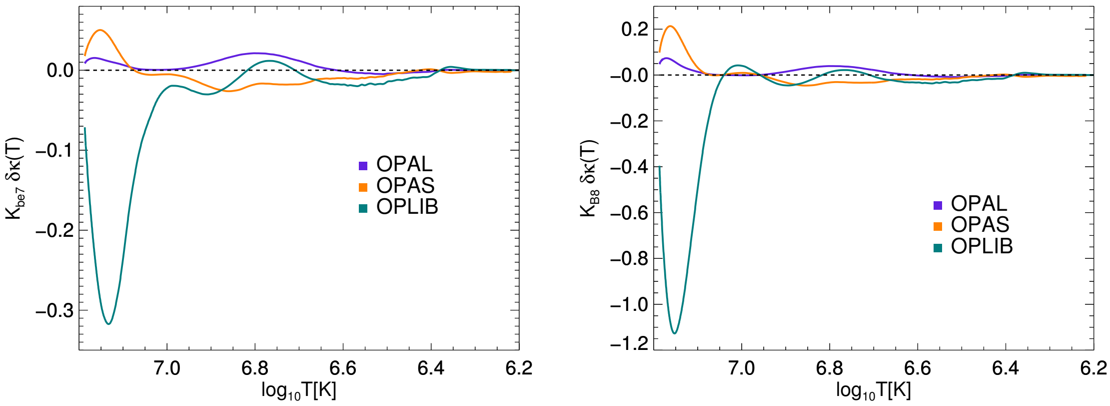

Figure 3.7: Same than Figure 3.3 but for $\Phi(^{7}\mathrm{Be})$ (left panel) and $\Phi(^{8}\mathrm{B})$ (right panel).

	Compo	OP	OPAL	OPLIB	OPAS
$\Phi(^{7}\mathrm{Be})$	GS98	0.1 (0.3)	0.2 (0.4)	0.2 (0.4)	-
	AGSS09met	0.6 (0.8)	0.3(0.5)	3.1 (1.8)	-
	AGSS09ph	0.1 (0.3)	0.1 (0.3)	1.8 (1.3)	0.2 (0.4)
	AGSS15ph	0.4 (0.6)	0.2 (0.4)	2.4 (1.5)	-
$\Phi(^{8}\mathrm{B})$	GS98	0.2 (0.5)	0.5 (0.7)	0.9 (0.9)	-
	A09m	1.2 (1.1)	0.6 (0.8)	6.5 (2.5)	-
	AGSS09ph	0.2 (0.4)	0.1 (0.3)	3.8 (1.9)	0.2 (0.4)
	AGSS15ph	0.6 (0.8)	0.5 (0.7)	4.7 (2.2)	-
$\Phi(^{7}\mathrm{Be})+\Phi(^{8}\mathrm{B})$	GS98	0.3 (0.2)	0.5 (0.3)	0.9 (0.5)	-
	AGSS09met	1.2 (0.6)	0.7 (0.4)	6.8 (2.1)	
	AGSS09ph	0.2 (0.1)	0.1 (0.1)	3.9 (1.5)	0.25 (0.2)
	AGSS15ph	0.7 (0.4)	0.5 (0.1)	4.9 (1.7)	-

Table 3.6: χ^2 (p-values) for $\Phi(^{7}\mathrm{Be})$, $\Phi(^{8}\mathrm{B})$ and $\Phi(^{7}\mathrm{Be}) + \Phi(^{8}\mathrm{B})$.

sults when the two points at the bump of the sound speed are removed have been added.

For OP, even though the linear opacity uncertainties are not considered, the same conclusions than in the previous chapter are obtained. For GS98 the best, although poor, agreement with the observations is obtained at a 3.3σ level. As it has already been discussed in Chapter 2, this bad performance of GS98 model is a result of the inaccurate modeling of the region below the convective envelope. For AGSS09ph a worst agreement at a 4.6σ level is obtained, and this time, this is a result of a global discrepancy of the sound speed along the solar profile.

The final χ^2 for SSMs that use OPLIB is lower than for OP, at 3.5σ for GS98 and

	Compo	OP	OPAL	OPLIB	OPAS
Global	GS98	66.0 (3.3)	47.1 (1.8)	68.1 (3.5)	-
	A09m	119.3 (6.7)	62.9 (3.0)	104.2 (5.9)	-
	A09ph	83.4 (4.6)	54.8 (2.5)	62.5 (3.1)	50.4 (2.1)
	A15ph	81.7 (4.5)	55.5 (2.5)	65.6 (3.3)	-
Global-peak	GS98	37.5 (1.2)	24.6 (0.9)	51.7 (2.4)	-
	A09m	88.9 (5.1)	41.3 (1.5)	95.9 (5.6)	-
	A09ph	57.8 (2.9)	34.2 (0.9)	45.8 (1.9)	40.2 (1.4)
	A15ph	56.5 (2.8)	35.1 (1.4)	49.1 (2.6) -	

Table 3.7: Global analysis of the agreement of the SSMs with the observations. The χ^2 (p-values) are presented when all the outputs (30 points of the sound speed profile, $\mathrm{Y_S}$, $\mathrm{R_{CZ}}$, $\Phi(^7\mathrm{Be})$ and $\Phi(^8\mathrm{B})$ are considered (*Global*) and when 2 points of the sound speed profile are excluded from the analysis (*Global-peak*).

3.1 for AGSS09ph, even though the unrealistic values obtained for the neutrino fluxes and the surface helium $\mathrm{Y_S}$. That is because a slightly improvement of the sound speed profile is obtained, and as 30 points of the sound speed are used, the contribution of the two neutrinos fluxes, the $\mathrm{R_{CZ}}$ and $\mathrm{Y_S}$ is diluted in front of the sound speed that dominates. However, the unrealistic values of the neutrino fluxes, $\mathrm{Y_S}$ and $\mathrm{R_{CZ}}$ allow to safely discard these models.

In general, OPAL performs a better job in bringing the models closer to the observations obtaining an agreement at 1.8σ level for GS98 and at 2.5σ for AGSS09ph. Still, the best agreement is found when GS98 is used.

Finally, there is the case where OPAS table is used that results in the best agreement, obtaining a 2.1σ for AGSS09ph. This improvement is mainly a result of the reduction of the peak below the convective envelope and a value of $\mathrm{R_{CZ}}$ closer to the helioseismic value.

To conclude, it is possible to say that SSMs that use OPAS and OPAL opacity tables have a better agreement with the observations than the achieved with OP or OPLIB. That does not mean that they are the correct radiative opacities, but it gives a hint on how the uncertainties of the radiative opacities could be better represented.

3.4 Summary and conclusions

Motivated by the *solar abundance problem* and the current uncertainties on the opacity radiative tables discussed in Chapter 2, different SSMs using the available opacity tables (OP, OPAL, OPAS and OPLIB) have been calculated. The purpose of it was to compare the results and test which radiative opacity tables could provide the best agreement considering different solar compositions (GS98, AGSS09met, AGSS09ph and AGSS15ph). The main results are summarized in the following list:

1. As it was expected, results of SSMs highly depend on the radiative opacities as it can be seen by the dispersion on the outputs quantities for each of the models.
2. For OPLIB opacities and for all the compositions, the agreement of the sound speed is only marginally improved with respect to the OP results while the neutrino fluxes are going further away from the observational results up to a 3σ difference for $\Phi(^8\mathrm{B})$ when using AGSS09ph. s $\mathrm{Y_S}$ also reach much lower values than other models with a $\mathrm{Y_{ini}}$ close to the primordial helium for some cases in contradiction with chemical evolution models of the galaxy. For $\mathrm{R_{CZ}}$ the agreement is not worst than OP but it does not improve it either. When using the AGSS09ph, a very good agreement is found for the small separation ratios r_{02} and r_{13}. In conclusion, the results show that the radiative opacities are too low at the solar interior resulting in models with outputs much further away from the observations than previous results.
3. With OPAL tables an improvement of the agreement with respect to the OP calculations is obtained. That may be surprising given that OPAL is the oldest release of all the tables considered in this chapter. But this good performance does not necessarily assures that the radiatives opacities considered are more correct than OP, but that the shape of the opacity profile along the solar interior is able to mitigate the discrepancies with the observations when combined with the variations of the input parameters (as for example the composition) within their errors.
4. The use of OPAS tables results, for AGSS09ph, in a better agreement with the observations when compared with OP. This improvement mainly comes from a better agreement of the sound speed profile where the bump at the base of the convective envelope is notably reduced. The value of $\mathrm{R_{CZ}}$ is much closer to the observations while $\mathrm{Y_S}$ and neutrino fluxes have similar results than for OP. Therefore, it is possible to say that OPAS tables are partially mitigating the discrepancies for high-Z compositions. OPAS tables are only available for the AGSS09ph composition, and it would be desirable that they become available for other solar compositions as well to allow for broader tests on their impact in solar and stellar modeling.

5. When only the old opacity tables were used (OP and OPAL), the results were more robust in determining which were the solar composition favored by the observations. That is because the agreement of both neutrino fluxes and helioseismology were better for GS98 than AGSS09. With the new release of opacity tables (OPAS and OPLIB) this picture is not that clear anymore. For example, the use of OPLIB tables results in a similar agreement with the observation of both GS98 and AGSS09 composition, specially for the sound speed profile and the frequency separation ratios, while the use of AGSS09ph and OPAS results in a big improvement of both sound speed profiles and $\mathrm{R_{CZ}}$ predictions.

6. The new releases of opacity tables (OPAS and OPLIB), do not converge to the same values for the opacities with large differences up to 13% in the central part of the Sun and about 10% at the base of the convective envelope. Unfortunately, these large differences seen in opacity calculations of ”new generation” cast doubts on the robustness of such calculations.

7. By analyzing the results obtained by each of the opacity tables, two main conclusions can be extracted in concordance with previous works as Christensen-Dalsgaard et al. (2009) and Villante (2010). The sound speed profile is mostly sensitive to changes on the tilt of the radiative opacity profile, while the neutrino fluxes are more affected by the absolute values of the opacities, mainly in the innermost region of the Sun. Therefore, in order to have a good agreement with all the observations (neutrino fluxes and helioseismology) a combination of changes on the shape of the radiative opacity profile and its absolute value is required.

8. Overall, the dispersion between opacity tables is of about 10%-15%, deriving in large changes between SSMs and their properties. Therefore, while this dispersion is not reduced, it is important to have a good representation of the radiative uncertainties in order to test the agreement of the SSMs with the observations. This is a necessary step because, as it has been shown, changes on the radiative opacities are required to go on the direction of solving the *solar abundance problem*. These changes are not only about increasing the values of the radiative opacities as mentioned it in Christensen-Dalsgaard et al. (2009) and Krief et al. (2016b) and supported by the experimental results of Bailey et al. (2015), but also to modify the tilt and the shape of the profile as it was already pointed out in Villante (2010) and supported by the good performance

of OPAL and OPAS and the poor agreement when a linear function for the opacities is taken into account.

Chapter 4

The Best Fit Model

Since there is evidence of discrepancies between SSMs and helioseismic observations and motivated by the *solar abundance problem* (see Section 1.2.6.1), different approaches have been used to build a solar model that reproduces the observations the best way possible within realistic evolutionary parameters. An example of this kind of models are the *seismic models*, models that are constructed such a way that the structure agrees with the helioseismic observations. In Turck-Chièze et al. (2001) and Couvidat et al. (2003) they calibrated the SSM adjusting some initial quantities within their errors bars which the sound speed profile is sensitive to (p-p rate, composition or radiative opacitites) and used the resulting model to have predictions for the neutrino fluxes. Other *seismic models* are constructed by solving the stellar structure equations to have a model that reproduces the helioseismic observations. This kind of model is a present-day seismic model and do not have information about its evolutionary history (see Kosovichev and Fedorova, 1991 and section 7 from Basu, 2016 and references therein). In Villante et al. (2014), a different approach is presented where, again, the discrepancy of the SSMs with the observation is minimized, but this time using both helioseismic observations and solar neutrino fluxes. The procedure is to change the input parameters within their errors bars at the same time that the composition is varied in order to obtain the best possible agreement with all solar observations available. From now on, this SSM modified in order to reproduce the observation is what is called the Best Fit Model (hereafter BFM). This chapter is focused on the construction and results of BFMs.

Seismic models and BFMs can be useful to give information about the input parameters, as for example opacities or composition, to obtain neutrino predictions consistent with the helioseismic observations, study extra-mixing in the radiative region or even to be used as a reference model to study non-standard physics. The last is one the main motivations of this thesis for studying and building a Best Fit

Model. In Chapter 5 the effect of different kinds of exotic particles in the Sun is studied using a BFM as derived in this chapter.

In this chapter the statistical method used to construct this BFM with a given SSM as a reference model is introduced. Then, the results when a linear approximation is used to construct the model and the results when a fully consistent solar calibration is done are compared. This comparison is done for the first time here and is needed to validate the assumptions used in the construction of the BFMs.

4.1 Statistical method

The goal of this work is to have a solar model that better reproduces the observations using realistic evolutionary input parameters. Therefore, it is necessary to find the combination of input parameters that produces a model with its properties as close as possible to the solar observations (neutrino fluxes and helioseismology) independently of the solar model used as reference. To do so, a statistical approach based on the *pull approach* previously presented in Section 3.2 is used to obtain the BFM. As it has been widely discussed previously (see Section 1.2.6.1), the solar composition is still under debate. Hence, to construct the BFM, the composition is considered as a free parameter and the χ^2 is minimized using an arbitrary composition and a combination of the pulls of the system that brings the solar model as close as possible to the observations. To minimize for the composition, the relevant elements are separated into two different groups in order to reduce the number of free parameters of the problem. These are the *volatiles* (C,N,O and Ne) and the *refrectaries* (Mg, Si, S and Fe).

The abundances vary by a constant multiplicative factor for each of the groups, $(1{+}\delta z_{\rm vol})$ and $(1{+}\delta z_{\rm ref})$ where $z_j \equiv {\rm Z}_{j,{\rm S}}/{\rm X}_{\rm S}$. $Z_{j,{\rm S}}$ is the surface abundance of the j-element, ${\rm X}_{\rm S}$ is that of hydrogen, and the index j runs over metals. The $\delta z_{\rm vol}$ and $\delta z_{\rm ref}$ are defined with respect to the adopted reference solar composition (GS98 or AGSS09met).

When arbitrary variations on the composition are added to the problem, Equation 3.2 is modified the following way:

$$\chi^2 = \min_{\{\xi_I,\delta z_{vol},\delta z_{ref}\}} \left[\sum_Q \left(\frac{\delta Q - \sum_I \xi_I C_{Q,I} - B_{Q,I}\delta z_{\rm ref} - B_{Q,I}\delta z_{\rm vol}}{U_Q} \right)^2 + \sum_I \xi_I^2 \right]. \tag{4.1}$$

Finally, the BFM is constructed using the pulls of the system ξ_I and the shifts for the element abundances ($\delta z_{\rm vol}$, $\delta z_{\rm ref}$) resulting from the minimization.

The input parameters of the system are: the age of the Sun, diffusion coefficients, luminosity, opacity and astrophysical factors of relevant nuclear reactions ($\rm S_{11}$, $\rm S_{33}$, $\rm S_{34}$, $\rm S_{17}$, $\rm S_{e7}$, $\rm S_{1,14}$). The chemical composition uncertainty is not included because the abundances of volatile and refractory elements are considered as free parameters in this problem and thus, changes on them will not contribute to the penalty term (ξ^2_{SYS}). The central values and their corresponding errors (U_Q) can be found in Table 2.3. The choice of the opacities uncertainties is a topic on its own and has been previously discussed in Section 2.2.2 and later on in Section 4.3.1 for this specific problem.

4.2 Observables

In this work the observables used to determine the BFM are the same 34 different observable quantities employed in Chapter 3 to test the agreement of the different SSMs with the observations. These are: the neutrino fluxes $\Phi(^8\rm B)$ and $\Phi(^7\rm Be)$; the convective envelope properties $\rm Y_S$ and $\rm R_{CZ}$ and the sound speed determinations $\rm c_\mathit{i} \equiv c(r_i)$ for 30 different values of $r/\rm R_\odot$ where $r/\rm R_\odot < 0.80$. The observational values for $\Phi(^8\rm B)$, $\Phi(^7\rm Be)$, $\rm Y_S$ and $\rm R_{CZ}$ can be found in Table 2.5 and in Table 2.4. The observational sound speed is obtained from the results of the inversion of the B16-SSMs and the corresponding experimental error can be found in Figure 2.8. More about the inversion procedure and the associated errors to it can be found in Section 2.3.1.2 and Section 1.2.5.3.

4.3 Power-laws

To describe the relation between input parameters and the properties of the model the partial derivatives of this observables with respect to the input parameters are used as described in Section 2.4.2. This derivatives are also used to calculate the χ^2 by giving information about the theoretical errors and correlations of the system. In Section 4.1 they are defined as $B_{Q,I}$, and therefore, this derivatives (hereafter power-laws) can be defined as,

$$B_{Q,I} = \frac{\partial \rm lnQ}{\partial \rm lnI}, \tag{4.2}$$

where Q corresponds to the output of the model (or observable) and I the input that is varied.

The power-laws of the system are a measure of how the model changes with variations of given input parameters. The power-laws described in Chapter 2 (see Appendix A) are calculated assuming a linear approximation and are a good description of the models if the changes are local to the reference model. Therefore, the power-laws of the composition when GS98 or AGSS09met are used present some differences. That is because the differences between compositions are large enough for the second order effects to be non negligible. These differences are illustrated in Figure 4.1. Thus, a solution adopted here to minimize the non linear effects is to recalculate the power-laws according to the new composition resulting from the minimization procedure. To do so, an iteration process is used to determine the power-laws that actually describe the changes of the system consistently with the composition. What it has been done is, for a given initial reference model and using the standard power-laws, the BFM is obtained with the corresponding new composition. After that, using linear interpolation the new power-laws that describe the new system are calculated. This step is repeated until a convergence on the BFM composition is reached using the new interpolated power-laws for each of the steps. In Figure 4.1 the resulting power-laws for the composition after using this iterative approach when AGSS09met is used as a reference model is plotted in green (see Section 4.5.1.1). It is possible to observe noticeable differences of the final power-laws with respect to the standard ones.

The power-laws (or $B_{Q,I}$ coefficients) used are the ones updated in Chapter 2 and summarized in Appendix A. The exceptions are the power-laws for the composition (interpolated for the studied composition) and the power-laws for the opacities, described in detail in the following section.

4.3.1 Opacities

The coefficients $B_{Q,I}$ related to the opacitiy are calculated using a different method. The reason for this is that its associated error is not a constant parameter but it is a function of temperature. Then, the same method presented in Chapter 2 is used in order to quantify the effects of its uncertainties. This is done through opacity kernels as has been described and widely discussed in Section 2.2.2.1.

The BFM obtained depends on the input parameters and the uncertainties associated with them. Therefore, the final results will be conditioned by the choice of the opacity uncertainties. This is crucial for the final BFM because depending on the

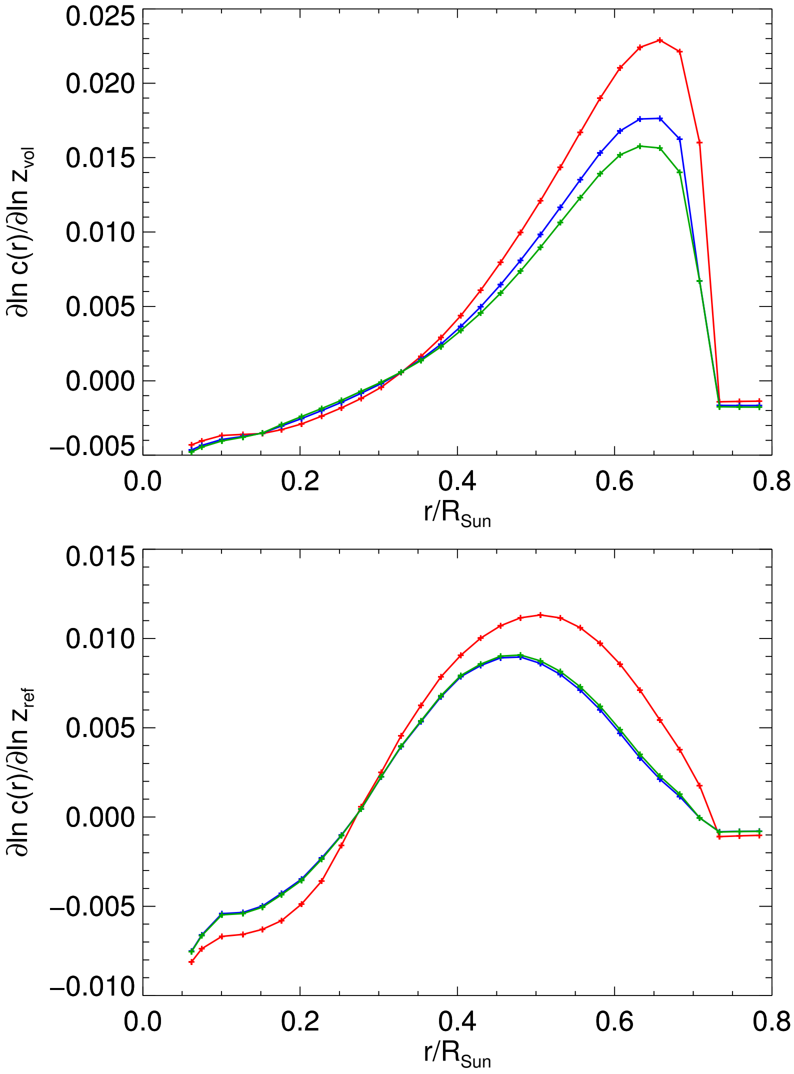

Figure 4.1: Partial derivatives for 30 points of the sound speed for the two different compositions. These are presented as a function of the solar radius. The red line corresponds to AGSS09met, the blue to GS98 and the green to the BFM when OP-OPAL differences are used as opacity error (see text). Top panel: Volatiles (C,N,O and Ne) Bottom panel: Refrectaries (Mg, Si, S and Fe)

---

shape of the chosen uncertainty function the final agreement with the observation can change significantly, as it has been discussed in Chapter 3.

To study this effect, and how the results depend on this choice, the BFM has been calculated using two different functions for the opacity uncertainties. First, the differences between OP and OPAL (OP1 from now on) are used as the 1σ error motivated by the results presented Chapter 3. The second choice (OP2) is the linear function presented in (Section 2.2.2), where the function is described by two parameters to obtain $\sigma = 0.02$ in the center and $\sigma = 0.07$ at the base of the convective envelope (see Equation 2.7). In the left panel of Figure 4.2 the differences between the two options are represented.

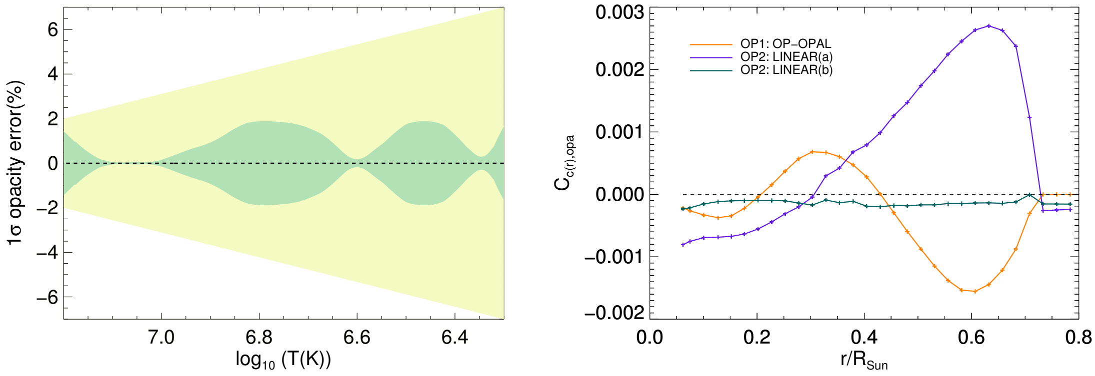

Figure 4.2: Left panel: Comparision of $1-\sigma$ error region as a function of the solar temperature for OP1 (green) and OP2 (yellow). Right panel: $C_{c,opa}$ for the opacity. Orange line corresponds to OP1, green to the parameter a of OP2 and purple to b of OP2.

For the case where the differences between OP and OPAL tables are considered as 1-σ error, the error of the opacity is represented by one input parameter *opa* the theoretical error of it is calculated as follows,

$$C_{Q,opa} = \int \frac{dT}{T} K_Q(T) \delta\kappa(T), \tag{4.3}$$

where $\delta\kappa(T) = \kappa_{OP}(T)/\kappa_{OPAL}(T)$ and K_Q are the opacity kernels.

For the second case, two different inputs parameters, a and b, are used to describe the opacity uncertainty function (see Equation 2.7) and the corresponding $C_{Q,I}$ are calculated as described in the following equations,

$$\begin{aligned} C_{Q,a} = B_{Q,a} \cdot \delta_a = \int \frac{dT}{T} K_Q(T) \cdot \delta_a, \\ C_{Q,b} = B_{Q,b} \cdot \delta_b = \int \frac{dT}{T} K_Q(T) \frac{\log(T/T_0)}{\Delta} \cdot \delta_b. \end{aligned} \tag{4.4}$$

For this particular case, $\delta_a = 0.02$ and $\delta_b = 0.067$ (see Section 2.2.2 for more details about this choice).

For the case of the opacity kernels, these are effectively constant for the composition and therefore, there is no need to perform the iteration process to find the right kernels for a given composition.

4.4 The Best fit model

Using the previously described method (see Section 4.1), a set of pulls for a given reference model are obtained. These pulls represent the changes that should be applied to the input parameters in order to obtain the BFM. In this section two approaches that can be used to construct this BFM are presented. The BFM is obtained from the minimization procedure and then it is validated by a full SSM calculation using input parameters as determined by the pulls.

4.4.1 Linear approximation

In this work the linear approximation is done by following the paper of Serenelli et al. (2013), that uses the power-laws ($B_{Q,I}$) to relate the changes to the properties of the model with the variations on the input parameters. The variations of the inputs are determined by the resulting pulls ξ_I from the minimization of Equation 4.1. Therefore, the properties of the BFM can be described relative to the SSM using the following expression:

$$\frac{Q_{\mathrm{BFM}}}{Q_{\mathrm{SSM}}} = \prod_I \left(\xi_I \cdot \delta I\right)^{B_{Q,I}}, \tag{4.5}$$

where Q_{BFM} are the different observable of the BFM, Q_{SSM} the ones from the standard reference models, $\xi_I \cdot \delta I$ is the product of the pull of an input and the corresponding error and $B_{Q,I}$ the power-law used to minimize Equation 4.1 (see Appendix A).

4.4.2 Solar calibration

This method is used to check the validity of the linear approximation. The calibrations have been done following the prescriptions and input parameters of Chapter 2 (B16) but with the inputs varied according to the pulls resulting from the minimization. The composition is given by the values of δz_{vol} and δz_{ref} that minimize the χ^2. The opacity tables have been recalculated to be consistent with the new composition. The detailed results and the comparison between BFMs calculated using the linear approximation and solar calibrations is shown in Section 4.5. This comparison is important because the linear expansion do not require to have an stellar evolution code and all the information necessary to construct the BFM (e.g. power laws) can be obtained from the literature. Another advantage of using the linear expansion is that is much less time consuming than a complete solar calibration and therefore, if equivalent to the solar calibrations, a powerful tool to calculate the BFMs.

4.5 Results

In this section the results for different BFMs are presented. The BFMs are calculated using as a reference model SSMs with GS98 composition ($\mathrm{BFM_G}$) and with AGSS09met composition ($\mathrm{BFM_A}$); ideally, they should be equal to each other. First the pulls are calculated for each of the reference models and then the corresponding BFM is constructed using linear expansion and solar calibrations. The results for the two methods are compared as well as the differences among BFMs coming from the choice of the reference model. All these cases are calculated by assuming the two different opacity uncertainties discussed in the previous Section 4.3.1 and again, the resulting models are compared and discussed.

4.5.1 Minimization

Table 4.1 lists the pulls of the BFM calculated using different reference models and uncertainty assumptions for the opacities. The values represent the number of σ that the input should vary from its central value in order to obtain the BFM. The errors associated to the inputs as well as the corresponding central values can be found in Table 2.3. In the last rows of the same table, the results for the minimization of the composition (δz_{ref} and δz_{vol}) are presented as well as with the resulting χ^2 (total, observational and systematics).

4.5.1.1 Composition

As in this problem the composition is considered as free parameter, the first step is to study the changes on the composition that lead to the best agreement with the observations. For OP1, taking AGSS09met as a reference model, the changes required on the volatiles is an increase of 61% and 12% for the refrectaries. If GS98 is used as starting point, the changes are much smaller with an increase of 17% for volatiles and a decrease of 2% for refrectaries. For both cases, the changes on the composition are bringing the final BFMs to the same values for the metallicity, higher than GS98, specially for the volatiles. For OP2 models the changes for AGSS09met are about 25% for the volatiles and 19% for the refrectaries while for GS98 the changes are just -6% and 7% respectively, meaning that the final composition is close to the standard GS98. As it has already been discussed in previous chapters, the fact that the changes

ξ_I	A_{OP1}	G_{OP1}	A_{OP2}	G_{OP2}
Opa 1	1.64	1.74	0.47	0.14
Opa 2	–	–	-1.68	-1.62
Age	0.34	0.23	0.97	0.94
Lumi	0.35	0.17	1.33	1.24
Diff	-1.02	-0.95	-0.81	-0.81
S_{11}	-0.65	-0.34	-0.42	-0.19
S_{33}	0.50	0.35	0.28	0.21
S_{34}	-1.11	-0.79	-0.51	-0.38
S_{17}	-1.04	-0.73	-0.23	-0.13
S_{be7}	0.26	0.18	0.05	0.02
S_{n14}	-0.10	-0.07	-0.10	-0.09
δ_{vol}	0.61	0.20	0.25	-0.06
δ_{ref}	0.12	-0.007	0.19	0.07
χ^2	58.2	42.2	107.7	108.8
χ^2_{obs}	51.2	36.8	100.7	102.82
χ^2_{sys}	7.0	5.4	7.0	6.0

Table 4.1: Results from the statistical procedure for the resulting BFM. Each column represents one BFM for a given composition (A(AGSS09met) or G(GS98)) with a given option for the opacity error (OP1 or OP2). The resulting pulls, the composition variation and the final χ^2 are included for each of the models. For OP2, OPA 1 corresponds to the parameter b and OPA 2 to a in Equation 2.7.

---

required are higher for AGSS09met than for GS98, does not necessarily imply that GS98 composition is preferred, but rather the thermal structure that is a result of composition and radiative opacities. Current probes (helioseismology and $\Phi(^8\mathrm{B})$ and $\Phi(^7\mathrm{Be})$ fluxes) are strongly degenerate to opacity composition change; they do not depend directly on the solar metallicity.

For different reference models, if the same input parameters and errors are used, the same final BFM and consequently the same final composition are expected. In Table 4.2 the detailed composition for the reference models using GS98 and AGSS09met is presented as well as the resulting composition of both BFM using OP1 and OP2. This composition is obtained by applying the corresponding changes (δz_{vol} and δz_{ref}) to the reference composition. For both OP1 and OP2 cases, the individual abundances for BFM_G and BFM_A are not exactly the same, although they are very similar. This is because the use of a two parameters problem for the composition. If the standard abundances for both composition are compared, it is possible to see that the differences between the modified refractory elements (Mg, Si, S and Fe) are constant for all the cases (0.05dex) while for the volatiles the situation is different.

Element	GS98	AGSS09met	BFM_G	BFM_A	BFM_G	BFM_A
C	8.52 ± 0.06	8.43 ± 0.05	8.60	8.64	8.49	8.54
N	7.92 ± 0.06	7.83 ± 0.05	8.00	8.04	7.89	7.94
O	8.83 ± 0.06	8.69 ± 0.05	8.91	8.90	8.80	8.80
Ne	8.08 ± 0.06	7.93 ± 0.10	8.16	8.14	8.05	8.04
Mg	7.58 ± 0.01	7.53 ± 0.01	7.58	7.59	7.61	7.61
Si	7.56 ± 0.01	7.51 ± 0.01	7.56	7.56	7.59	7.59
S	7.20 ± 0.06	7.15 ± 0.02	7.20	7.20	7.23	7.23
Fe	7.50 ± 0.01	7.45 ± 0.01	7.50	7.50	7.53	7.53
$(\text{Z/X})_\odot$	0.02292	0.01780	0.02646	0.02655	0.02221	0.02237

Table 4.2: Element abundances of the reference models and the resulting BFMs given as $\log \epsilon_i \equiv \log N_i/N_H + 12$. The two first columns corresponds to the standard composition of GS98 Grevesse and Sauval (1998) and AGSS09met Asplund et al. (2009). The next two columns corresponds to the BFM when OP1 option is used and the last two when OP2 is used.

While for C and N the changes between compositions are 0.09dex, for N the difference is 0.15dex and 0.15dex for Ne. Therefore, to change the abundances with the two-parameters process will force the final results to present slight differences between BFMs depending on the reference starting model. It is possible in principle to perform a 3-parameter analysis for the composition, grouping C,N separately than O and Ne. The complication would be that the contribution of C and N is subdominant with respect O and Ne, and therefore, if this 3 parameter analysis is performed, the values of C and N could take an unrealistic value for the BFM. In order to obtain some valid results some restriction for this third parameter would be needed, e.g. some observational constraint for CN coming from the observation of CN neutrino fluxes. Meanwhile, the two parameters problem is used, with the penalty that the same exact results are not obtained for both BFMs although very close.

4.5.1.2 "Godness of fit"

The better agreement with the observations of the studied BFMs can be quantified using the resulting values of χ^2 and comparing them with the χ^2 of the SSMs when these are computed using the reference compositions without any changes to the central values. Starting with the OP1 case, where OP-OPAL differences are used as uncertainties for the radiative opacitites, the results for GS98 are $\chi^2_{SSM} = 60$ and $\chi^2_{BFM} = 42.2$ while for AGSS09met the results are $\chi^2_{SSM} = 84$ and $\chi^2_{BFM} = 58.2$, showing a clear improvement of the agreement.

In theory, independently of the reference model used to construct the BFM, if the initial evolutionary parameters and the corresponding errors are the same, the resulting model should be equivalent. That is not the situation for this case, where $\mathrm{BFM_A}$ and $\mathrm{BFM_G}$ present large differences. This difference comes mainly from the observational part ($\chi^2_{obs}(GS98) = 36.8$ and $\chi^2_{obs}(AGSS09met) = 51.2$), meaning that the differences come from the final discrepancies between BFMs and not from the differences in the pulls. The reason for that could be that as for AGSS09met case, the changes on composition are much larger than for GS98 case, the interpolation procedure to calculate the power-laws could introduce some errors because there are deviations from the linear behavior. The higher discrepancies come mainly from the outer region of the Sun where there is the bump and the interpolation can get even more complicated. Therefore, the pulls would represent changes that are not exactly the ones for the composition considered, dragging some errors to the final models. This hypothesis is reinforced when the calibration and the linear approximation are compared, as it is discussed later on in Section 4.5.1, because when the solar calibration is done $\mathrm{BFM_G}$ and $\mathrm{BFM_A}$ are equivalent. Then, it is possible to conclude that the discrepancy between both χ^2 comes from the approximations done to the power-law system at the base of the convective envelope. This is going to be further discussed in Section 4.5.2 where the results using the linear approximations and the calibration are further compared and thus, the validity of the power-laws tested.

For the OP2 models, the results are $\chi^2_{SSM} = 65$ and $\chi^2_{BFM} = 107.7$ for GS98 and $\chi^2_{SSM} = 94.2$ and $\chi^2_{BFM} = 108.8$ for AGSS09met. In this situation, the final BFMs are clearly worsening the agreement with the observations with respect the standard model. The reason for that is the use of a two-parameters minimization of the composition combined with the linear function used for the opacities. To calculate the χ^2 of the SSM (as it is done in Section 5.5.4), Equation 3.2 is used, and thus, each of the element abundances considered is varied within its corresponding error. By looking at the resulting pulls of the composition, is possible find that, for GS98 composition, $\xi_O = 1.15$ and $\xi_{Ne} = -0.9$ while when minimizing for the composition, both elements are forced to move together in the same direction. It is possible to see then, that a two-parameter analysis for the composition in combination with a linear function for the opacities is not able to improve the SSM fit. As mentioned before, moving to a 3-parameter analysis is in principle possible but degeneracies among different elements appear and results are not robust; available solar data does not justify going beyond a 2-parameter analysis for the composition.

On the contrary, the two-parameter analysis yields a good improvement of the BFM with respect to the SSM when OP-OPAL differences are used as the opacity error function. That is because of the combination of the opacity and composition power-laws, able to mitigate the discrepancies of the sound speed.

In conclusion, OP1 option is used to construct the BFM that later on in Chapter 5 will be used to give constraints on exotic particles. As already discussed in Chapter 3, that does not mean that OP-OPAL differences are more realistic but that the resulting BFM is closer to the observations. It also gives the idea, already discussed in Chapter 2, that the shape of the opacity uncertainties has to be more complicated than a linear function in order to mitigate the discrepancy with the observed sound speed profile.

4.5.1.3 Pulls of the system

Now the focus is on the resulting pulls and their effects over the different observables considered here. It is important to not understand the effects of the pulls individually but as a combination of all the input variations that will result on the best agreement possible with the observations when combined with the minimization of the composition. To visualize the contribution of each of the pulls (and the composition minimization) on the observables, each of the inputs have been individually varied by using the values of the pulls obtained from the minimization. In Figure 4.3 and Figure 4.4, the results for GS98op1 and AGSS09op1 are plotted in different panels. Each panel contains the sound speed profile and the neutrino fluxes, $\mathrm{Y_S}$ and $\mathrm{R_{CZ}}$ resulting from the variation of one of the inputs. For comparison, the sound speed for the reference model (GS98 and AGSS09met) and the corresponding BFM ($\mathrm{BFM_G}$ and $\mathrm{BFM_A}$), are also included. Complete results and details about the final BFMs can be found later on Section 4.5.2.

Starting with the sound speed profile, it is most sensitive to changes in age, luminosity, opacity, diffusion, the final composition and the S_{11} cross section, according to the power-laws (see Appendix A)). Errors in age and luminosity are quite small so they cannot vary by much without introducing a large penalty in the χ^2. For this reason, they have a minor role in the BFM. Then, the changes in input parameters that can bring the sound speed from the reference close to observations are mainly the radiative opacities, diffusion and composition, while S_{11} will have a marginal effect (for similar reasons than the age and luminosity). Diffusion is relevant partly because of its large 15% uncertainty. In Figure 4.2 the $C_{Q,I}$ for the sound speed coming from the opacity is represented for both OP1. In order to have better agreement with

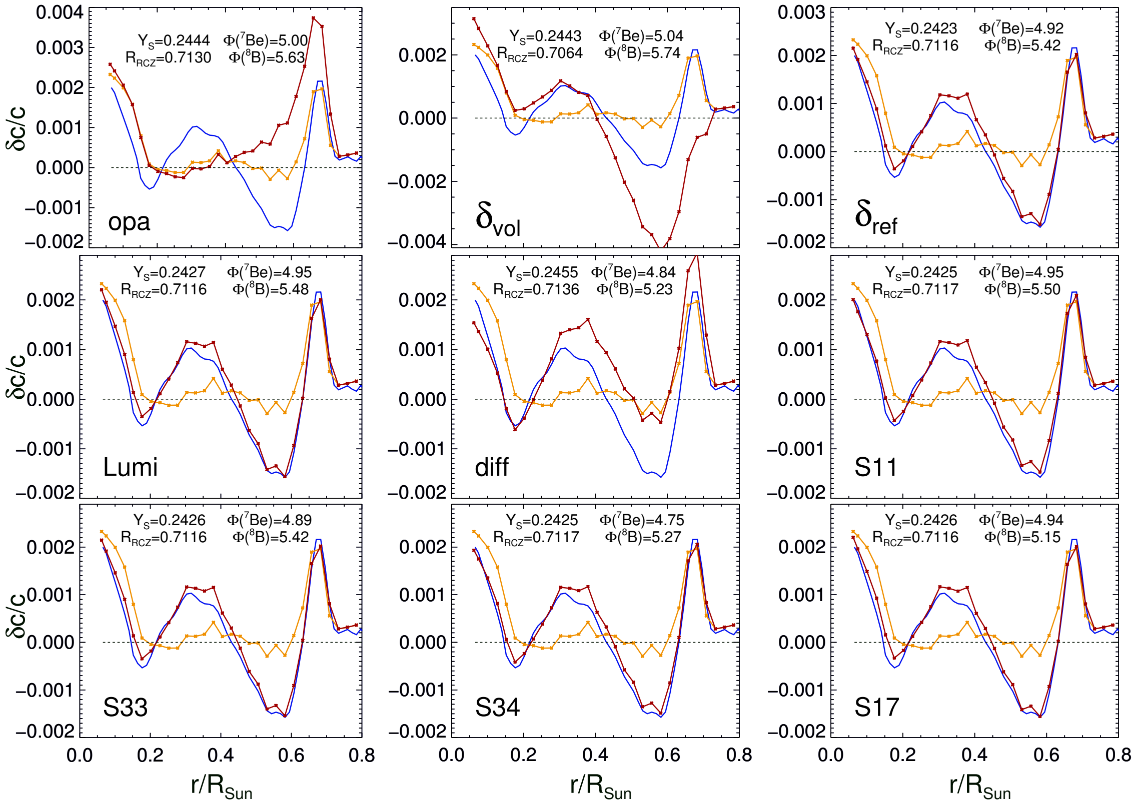

Figure 4.3: Effects of the individual variations of the inputs over the observables (sound speed profile, Y_S, R_{CZ}, $\Phi(^7Be)$ and $\Phi(^8B)$) when GS98 reference model is used with the corresponding pulls of Table 4.1. The blue sound speed profile correspond to the GS98 B16-SSM, the orange correspond to the final BFM when all the inputs are varied and the red one when only one input is varied. The standard values of neutrino fluxes and convective properties can be found in Chapter 2.

---

observations, is necessary to reduce $\delta c = (c_{obs} - c_{mod})/c_{obs}$ (see Figure 2.7). Hence, a negative opacity pull for OP1 would be expected, although results show that is not what happens with a pull for the opacity that goes on the other direction with $\xi_{opa} \sim 1.7$. The reason is that the final BFM is a result of the combination of changes on the input parameters, and for this case, the agreement with the observations is compensated by changes on the composition.

For Y_S, the quantities with more influence are the composition, diffusion and opacity, in this order. The changes on R_{CZ} observable come mainly from the changes on the volatiles, where the major contribution would come from changes on oxygen and neon. Finally, there are the neutrino fluxes. Both ($\Phi(^8B)$ and $\Phi(^7Be)$) are affected by variations on the composition, opacity and diffusion and for some of the cross sections considered here. S_{11} (because its small error and value of the pulls) has

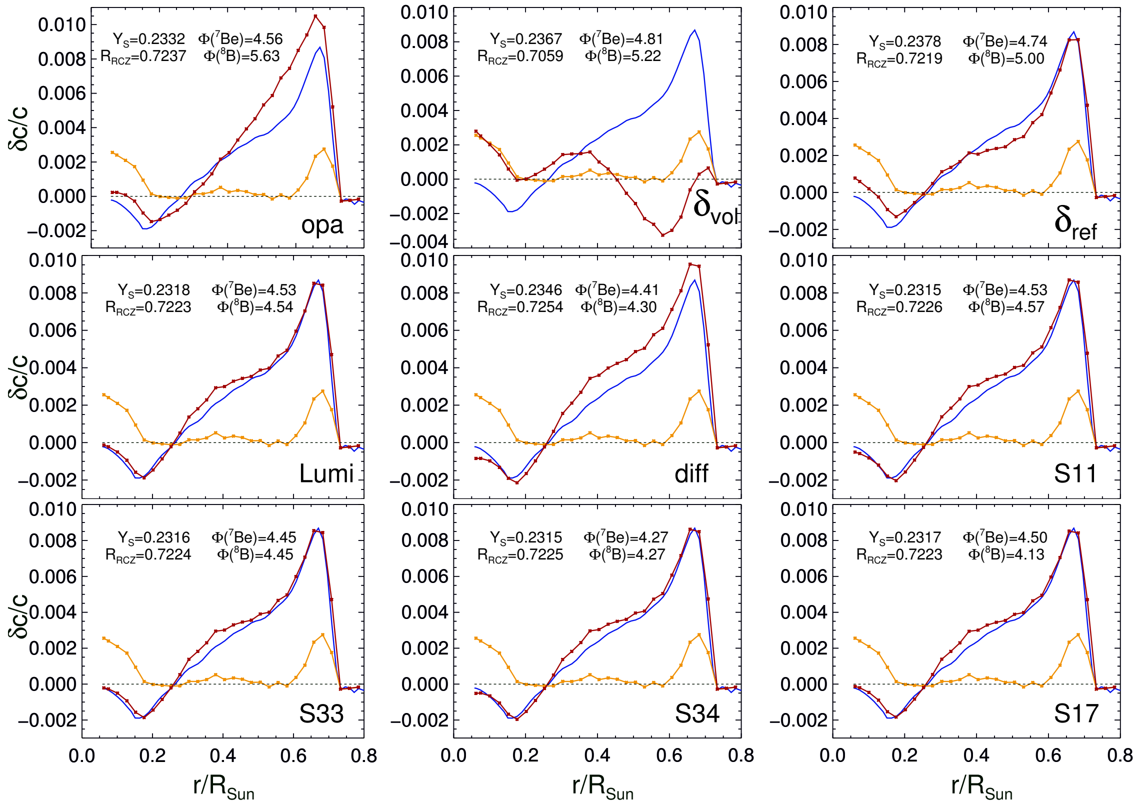

Figure 4.4: Same than Figure 4.3 but when AGSS09met B16-SSM is used as a reference model.

little effect on the neutrino fluxes while changes on S_{34} have a direct effect on both neutrino fluxes examined. For $\Phi(^8B)$, the more important changes come from the variation of S_{17} while $\Phi(^7Be)$ remains unaffected by this quantity. Clearly, the major variations are found when AGSS09met is used as a reference model, because is where the larger changes are required to improve the agreement with the observations.

4.5.2 Best Fit Models

Once the pulls of the system and the new composition are obtained, it is possible to construct the BFM starting from the reference models. In Table 4.3, the main outputs of the different BFM are presented. Summarizing, the BFMs presented in this table have been calculated using two different reference models (GS98 and AGSS09met), using two different approaches for the opacity uncertainties and using the linear expansion and calibrating the new solar models. The resulting sound speed profiles are presented and compared within each other and with the reference standard model in Figure 4.5.

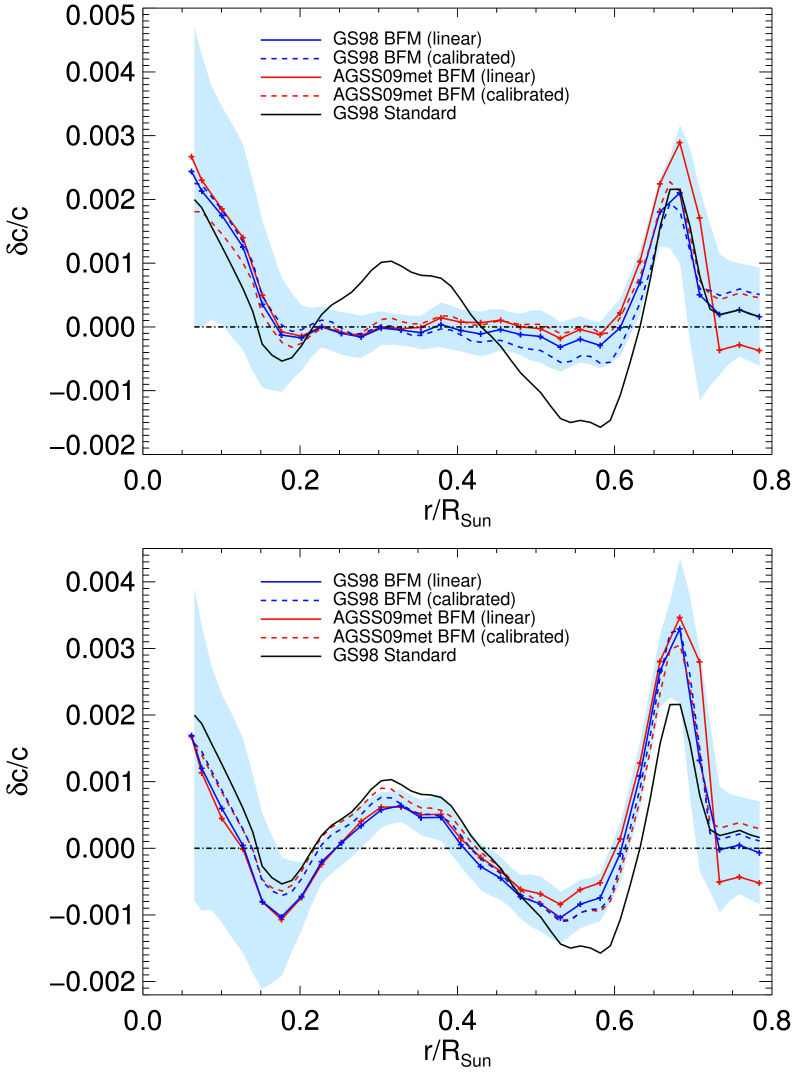

Figure 4.5: This plot shows the comparision of the sound speed profiles resulting from BFM constructed using linear approximation (solid line) solar calibration (dashed lines) with GS98 (blue) and AGSS09met (red) reference models. The blue shaded region represents the errors on the sound speed profile. In black, the sound speed profile for GS98 B16-SSM is plotted for comparision. Top panel: Using OP1. Bottom panel: Using OP2.

	Qnt.	SSM	**OP1** BFM lin.	**OP1** BFM cal	**OP2** BFM lin	**OP2** BFM cal
GS98	$\mathrm{Y_S}$	0.2426	0.2484	0.2484	0.2440	0.2443
	$\mathrm{R_{CZ}}$	0.7116	0.7100	0.7100	0.7140	0.7140
	$\Phi(^8\mathrm{B})$	5.46	5.14	5.13	5.11	5.18
	$\Phi(^7\mathrm{Be})$	4.93	4.80	4.79	4.77	4.80
	$\langle \delta c/c \rangle$	0.0007	0.00040	0.00040	0.00054	0.00056
AGSS09met	$\mathrm{Y_S}$	0.2317	0.2473	0.2471	0.2433	0.2433
	$\mathrm{R_{CZ}}$	0.7223	0.7093	0.7106	0.7137	0.7134
	$\Phi(^8\mathrm{B})$	4.5	5.03	4.89	5.01	5.03
	$\Phi(^7\mathrm{Be})$	4.5	4.75	4.69	4.74	4.73
	$\langle \delta c/c \rangle$	0.00216	0.00049	0.00039	0.00058	0.00055

Table 4.3: Outputs of the BFMs using different composition as a reference, distinct opacity errors and using a linear approximation of the solar calibration.

First the focus is on the BFMs constructed using the OP-OPAL difference as opacity uncertainty. For GS98 it is possible to see that the BFM calculated using the linear expansion is in complete agreement with the corresponding solar calibration for all observables ($\mathrm{Y_S}$, $\mathrm{R_{CZ}}$, $\Phi(^8\mathrm{B})$ and $\Phi(^7\mathrm{Be})$). In the top panel of Figure 4.5 the resulting sound speed profiles using both methods are represented in blue. In the center the results completely agree between both methods while some differences can be found in the region with $r = 0.4 - 0.6R_\odot$, and in the bump the agreement is recovered. Some differences for the three points in the convective region can also be appreciated, and that is because the treatment of the power-laws in this region. For points in the convective region, the results from the inversion converge to zero independently to the value of the sound speed of the model. As in this work the power-laws are calculated by using the same solar sound speed as reference for the inversions, the power-laws of these three points will only represent variations resulting from the fact that the inversions are not done consistently. For that reason, in this work, they are considered zero.

Overall, all the differences found are well within the sound speed error, and therefore, it can be concluded that the results are completely equivalent. The situation is a bit different when AGSS09met composition is used as a reference model, where some bigger differences between methods arise. In the top panel of Figure 4.5 the corresponding sound speed profiles are shown in red. For this case, there is a good agreement all over the inner region and the discrepancies arise in the outer part where the bump is higher when the linear approximation is used. As discussed in previous sections, that discrepancy comes from the approximation of the power-laws, that are not perfect in describing accurately the region below the convective envelope, and this is the reason why $\mathrm{BFM_A}$ agreement with observations is worst than for $\mathrm{BFM_G}$. This is also the source of the discrepancies of about 1σ on the other observables as $\mathrm{R_{CZ}}$ and $\Phi(^8\mathrm{B})$. However, as all the differences lay within the errors considered for all observables, it is possible to conclude that both methods are equivalent, and therefore, that the linear approximation is a good tool to construct BFMs. The same conclusions apply when OP2 option is used.

Now, the final properties of the resulting BFMs are analyzed. To start the focus is on the sound speed profile represented in Figure 4.5. When OP1 is used (top panel) is possible to see that the final BFM both for AGSS09met and GS98 reference models improve the agreement of GS98 SSM. This improvement is mainly in the inner part of the sun, where the oscillatory behavior in 0.2-0.6 $R_\odot$ region disappears. The discrepancies at the inner region ($r < 0.2R_\odot$) and the bump at the base of the convective envelope remain similar to those in the SSM. For OP2 the situation is completely different, as it has been already commented, there is no a combination of composition and opacity changes that improves the agreement of the SSM, resulting in a final sound speed of the BFM similar than the one SSM. These results are consistent with Chapter 2, where it was argued that the use of linear opacity error could bring AGSS09met to an agreement similar than GS98, but that this assumption for the error function is not able to improve the agreement for the GS98 case. Finally, is worth mentioning that in both cases (OP1 and OP2) the resulting sound speed profiles are equivalent independently of the reference model used.

Now, the neutrino fluxes and the convective envelope properties are analyzed (see Table 4.3). Focusing on OP1, a good agreement is found for $\mathrm{Y_S}$, $\Phi(^7\mathrm{Be})$ and $\Phi(^8\mathrm{B})$ (for AGSS09met, this last neutrino flux is exactly 1σ away from the observational value). The larger discrepancy with observations is found for $\mathrm{R_{CZ}}$. For $\mathrm{BFM_G}$, the discrepancy with the observational value is higher than for the corresponding SSM (from 1.4σ to 3σ). For AGSS09met, the agreement is better although the final value is still away from the observation value (from 9.3σ to 3σ). This can be explained because of tensions between the sound speed profile at the base of the convective envelope and the value of $\mathrm{R_{CZ}}$. In order to find a good agreement for both observables, changes on the opacity and composition in different directions should take place, therefore, using the current input parameters, is not possible to find a perfect agreement for all the observables considered. To show this tensions, BFMs without including the $\mathrm{R_{CZ}}$ observables have been calculated. It results in models with a sound speed profile much closer to the observations, mainly in the outer region where the tensions take place. The resulting godness of fit is much better then, going from $\chi^2_{\mathrm{BFM_G}} = 42.2$ to $\chi^2_{\mathrm{BFM_G - R_{CZ}}} = 25.7$ and from $\chi^2_{\mathrm{BFM_A}} = 58.2$ to $\chi^2_{\mathrm{BFM_A - R_{CZ}}} = 34.8$. The problem comes from the $\mathrm{R_{CZ}}$ final value, that as there is no constraints imposed to it, it takes values much further away from its observation: $\mathrm{R_{CZ(GS98)}} = 7.081$ (5σ) and $\mathrm{R_{CZ(AGSS09met)}} = 7.068$ (6.2σ).

Globally, it is possible to conclude that, although some discrepancies found in some of the parameters of the BFMs, this method is valid to construct BFMs independently of the reference model used and that the linear approximation is equivalent than performing all the calibrations consistently.

4.6 Summary and conclusions

In this chapter the properties and the procedure to obtain a Best Fit Model has been presented and the main results and conclusions are summarized:

1. The final BFM is independent of the reference model used, and then, very useful to test non-standard physics without depending on the composition and the solar abundance problem.

2. It has been shown that to construct the final BFM using linear approximations (power-laws) or solar calibrations is equivalent, and therefore, the validity of the linear approach is proven. This is important because this last method is much more flexible and does not requires to recalculate the solar model.

3. BFM is the result of the combination of variations in different input parameters and it depends on the input parameters and the corresponding errors. Therefore, as the uncertainties related to the opacity are still unknown, the choice of them can dramatically change the results and it explains the differences between models calculated using OP1 or OP2.

4. The best agreement with observations is reached when OP-OPAL differences are used as opacity uncertainties. This is consistent with the results of previous chapters, and therefore, this is the choice used later on in Chapter 5 when BFMs are used to place limits on the properties of exotic particles.

5. Some discrepancies appear between BFM with same input parameters and errors when the required change on composition is very large ($\sim 60\%$). That is related to the fact that the power-laws depend on the composition and then,

linear interpolation is needed to obtain the right parameters. Consequently, if large changes are required, the power-laws can deviate from the linear regime. This is the case at the base of the convective envelope when AGSS09met is used as a reference model.

6. This method is not intended to be used in order to test the correct physics or discard certain options (as compositions or opacity uncertainties), but to find a good tool capable of providing solar models that match well the available solar observations and that is rather detached and independent of the solar abundance problems.

Chapter 5

Constraints on exotic particles using solar models

Many studies have focused on using the Sun for setting limits on the properties of different types of particles. The Sun is by far the best-known star. The solar structure, revealed by helioseismology and solar neutrinos, is well determined, and accurate solar models give valuable information about the past, present and the future of the Sun (e.g. Bahcall et al., 2001; Christensen-Dalsgaard et al., 1996; Serenelli et al., 2011; Vinyoles et al., 2017). While in some cases (e.g. axions) the most restrictive bounds on the particle properties are not inferred from solar studies, the Sun remains the most useful benchmark for testing and validating different statistical approaches to constrain particle properties. Also, it is important to keep in mind that CAST (Zioutas et al., 1999), SUMICO (Moriyama et al., 1998) and the planned IAXO (Armengaud et al., 2014) are experiments specifically designed to detect exotic particles directly from the Sun, so having predictions of expected solar fluxes for exotic particles remains an important aspect to consider. The new upper limits for the axion coupling constant with electrons from LUX presented in Akerib et al. (2017) reinforces the importance of a detailed knowledge of the solar emission of non-standard particles.

Solar constraints on particle properties have been generally derived from applying limits to variations of either neutrino fluxes (Gondolo and Raffelt, 2009) or the sound speed profile derived from helioseismology (Schlattl et al., 1999). However, a systematic approach aimed at combining different sources of data accounting in detail for observation and theoretical errors has been badly missing in the literature. Here, a method to supply such a tool is presented.

The main goal of this chapter is to extend the general statistical approach presented in Villante et al. (2014) and in Chapter 4 to constrain properties of particles (e.g. mass, coupling constant, charge) making the best possible use of the available information on the Sun, both observational and theoretical. To do so, helioseismic data combined with the neutrino fluxes are used in a statistical approach that includes the theoretical and observational uncertainties and takes into account possible tensions among data and solar model input parameters. The analysis is based on the BFM concept, so results will be quite independent on the solar composition and the *solar abundance problem*. Then, solar bounds are placed for the well-studied hadronic axions, used to test the statistical approach, for the more novel cases as hidden photons for which the Sun sets the most restrictive limits on the kinetic mixing parameter for small hidden photon masses, $m \lesssim$eV and for minicharged particles where the parameter space (m_f, ϵ) is explored.

5.1 Cases of study

In these sections the different particles that have been studied are presented together with the previously existing solar limits. The results for the first two cases (axions and hidden photons) have been published in Vinyoles et al. (2015) while the results for minicharged particles case in a second paper (Vinyoles and Vogel, 2016).

5.1.1 Axions

Axions are light pseudoscalar particles that were introduced by the Peccei-Quinn (Peccei and Quinn, 1977) solution to the strong CP problem. Axions are very light and interact with ordinary particles much like neutral mesons $(\pi^0, \eta,...)$ but with coupling strengths vastly weaker. The most relevant interaction for astrophysics is the coupling of axions with electrons with similar strength than to nucleons, because this coupling tends to be very efficient to produce axions in stellar environments. The DFSZ model (Dine et al., 1981), as any axion model embedded in a GUT, is an example of axion model with tree-level axion coupling. Here, the main axion production mechanisms are the ABC proceses: axio-recombination, bremsstrahlung and Compton (Redondo, 2013). In the KSVZ model (hadronic axions) (Kim, 1979; Shifman et al., 1980) this coupling is absent at tree level and the relevant axion coupling is to two photons. Here, the Primakoff effect is the mechanism that converts photons into axions in the presence of electric or magnetic fields. The inverse Primakoff effect is used in helioscopes like CAST and SUMICO (and the proposed IAXO) to convert solar axions into detectable X-rays and to constraint the solar axion flux. The phenomenology of axions is extended to axion-like particles (ALPs) in a completely straight-forward way. ALPs are also bosons with a two-photon coupling, but their mass and interaction strength are in principle unrelated, unlike the axion case. Here the primary interest is the case of hadronic axions because the Sun is one of the most sensitive environments to look for their effects. Solar constraints are even more important for the case of ALPs, where the SN1987A constraint is absent in generic models (ALPs do not generically have large couplings to nucleons but axions do). It is not necessary trying to constrain the axion-electron coupling because limits from white dwarves and red-giant stars are much stronger than the bounds obtained from the Sun.

Until now, several works have provided constraints to the axion-photon coupling constant $g_{a\gamma}$ using the variations that axions produce on helioseismologic quantities or neutrino fluxes. An upper limit for $g_{a\gamma} = 10 \cdot 10^{-10}\mathrm{GeV}^{-1}$ is found by setting a limit to the deviation that axions can impart to the solar model sound speed at a given depth in the Sun (Schlattl et al., 1999). This work also gives values for the solar neutrino fluxes depending on axion emission and (Gondolo and Raffelt, 2009) uses this relation to give a more restrictive constraint of $g_{a\gamma} = 7 \cdot 10^{-10}\mathrm{GeV}^{-1}$ at a 3σ confidence level using the observed $\Phi(^{8}\mathrm{B})$ solar neutrino flux measured by the SNO experiment (see Aharmim et al., 2013 for the global analysis of the three SNO phases). In (Maeda and Shibahashi, 2013) they construct the so-called seismic models (non-evolutionary solar models constructed in ad-hoc manner to reproduce the sound speed derived from helioseismology), with different values for the axion-coupling constant and obtain an upper limit of $g_{a\gamma} = 2.5 \cdot 10^{-10}\mathrm{GeV}^{-1}$ by comparing the predicted $\Phi(^{8}\mathrm{B})$ with the experimental result and using 1σ uncertainties. For the mass range $m_a \leqslant 0.02\,\mathrm{eV}$, the most restrictive limit comes from the helioscope CAST with $g_{a\gamma} < 0.88 \cdot 10^{-10}\mathrm{GeV}^{-1}$ (Andriamonje et al., 2007). The future helioscope IAXO should improve these results, as it is expected to reach sensitivities to the axion-coupling constant 1 to 1.5 orders of magnitude better than CAST (collaboration).

5.1.2 Hidden photons

Hidden photons (HP), the second case study, are vector bosons that couple weakly via kinetic mixing with standard photons. The kinetic mixing is represented by the parameter χ and together with the HP mass, m, are the parameters to be constrain (see Jaeckel (2013); Jaeckel and Ringwald (2010); Redondo (2008); Redondo and Raffelt (2013) and references therein). In fact, solar constraints are mostly sensitive to the product χm if $m \lesssim$ eV (see Section 5.2.2). Previous solar limits on this product have been provided in works as Redondo (2013), where they place a limit by

$\chi m < 4 \cdot 10^{-12}$ eV at 3σ CL using $\Phi(^8\mathrm{B})$ and the relation that describes the changes of the neutrino fluxes and the energy loss derived in Gondolo and Raffelt (2009).

HPs can only be produced from photon ↔ HP oscillations, which are affected by the photon refraction in the solar plasma. The oscillations are resonant when the HP and photon dispersion relation match and this happens differently for transversely polarized photons and longitudinal excitations (L-plasmons). Resonant emission in the Sun is possible for HP masses below ∼0.3 keV, the highest plasma frequency ω_p in the Sun, which is then also the highest produced photon effective mass. The emission of L-modes is more important for low HP masses (below m ∼eV) An et al. (2013); Redondo and Raffelt (2013), for which resonant conditions happen all through the solar interior (each region of the Sun emits L-HPs with energy equal to the local plasma frequency). This is the case of interest in this chapter. Resonant emission of T-modes dominates the energy loss in the HP mass range ∼ eV-0.3 keV and it is localized in a narrow spherical shell of the solar interior for which the HP mass matches the plasma frequency $m \simeq \omega_\mathrm{p}$. This case is very interesting too, but the strongly localized character of the HPs production in this case prevents their treatment as linear perturbations to SSMs, so they fall out of the scope of this thesis. For higher masses, arguments from horizontal branch stars can give better constraints because higher plasma frequencies allow the production of higher mass HPs.

5.1.3 Minicharged particles

The third case study is the minicharged particle (MCP). MCPs are fermions that have a small and unquantized fraction of the electron charge and arise from possible extensions of the SM that allow the addition of charged and massive particles. Other scenarios where the MCPs can be naturally obtained are when a local and unbroken gauge group $U(1)_h$ is added to SM groups or when hidden sectors with very massive degrees of freedom are an extension of SM Holdom (1986a,b). The charge of the MCP is parametrized as ϵe, where e is the charge of the electron and ϵ is the minicharge parameter that can be very small depending on the model assumptions. In this chapter, ϵ is considered as a free parameter.

The minicharge allows MCPs to couple to the electromagnetic plasma inside the Sun, which contains a thermal bath of collective excitation modes ('plasmons'). These plasmons can deexcite, thereby emitting a pair of MCPs. The rate of this decay depends on the minicharge but also on the plasma frequency ω_p of the Sun and the MCP mass m_f since the decay into MCPs becomes kinematically disfavored for large MCP masses, $2m_f > \omega_p$. Once produced, the small minicharges considered here allow the MCPs to escape the Sun unimpeded, giving rise to an additional energy loss channel.

Similarly to the HPs case, the Sun is sensitive to masses of $m_f \sim eV$ which there is resonant emission and therefore, restrictive limits can be placed. To study larger masses is necessary to go to denser objects as horizontal branch stars, red giants or white dwarfs (Davidson et al., 2000).

5.2 Models and data

In this work SSMs are used as reference models (see Chapter 1 and Chapter 2 for details about the SSMs). The models calculated for the work presented in this chapter are previous to the update of the SSMs described in Chapter 2, so the cross sections of SFII are used following Serenelli et al. (2011). This fact does not affect the results because the interest is on the relative changes of the models when a non-standard energy loss source is included in the models and because, as it is explained later on in Section 5.4, the use of BFMs guarantees that the final results do not depend on the initial reference model (see Chapter 4).

To include the effects of the exotic particles to the SSMs, an extra energy loss term have been added (see Equation 1.25 in Section 1.3.2.1) to the energy equation in `GARSTEC`. The energy loss rate used for each of the cases are described in the following sections.

5.2.1 Models with Axions

The production of axions in the Sun occurs via the Primakoff effect, i.e. axions are produced by the conversion of photons in the electric field of nuclei and electrons with the interaction Lagrangian $\mathcal{L}_{a\gamma} = g_{a\gamma}\mathbf{B}\cdot\mathbf{E}\,a$, where a is the axion field. Thus, constraints can be placed on axion-photon coupling constant $g_{a\gamma}$. The energy loss rate per unit mass $\epsilon_{a\gamma}$ is given by Schlattl et al. (1999):

$$\epsilon_{a\gamma} = \frac{g_{a\gamma}^2}{4\pi}\frac{T^7}{\rho}F(\kappa^2), \tag{5.1}$$

where T is the temperature, ρ the density and $F(\kappa^2)$ is a dimensionless function describing electron screening effects given by:

$$F(\kappa^2) = \frac{\kappa^2}{2\pi^2}\int_0^\infty dx \frac{x}{e^x - 1}\left[(x^2+\kappa^2)\ln\left(1+\frac{\mathrm{x}^2}{\kappa^2}\right) - \mathrm{x}^2\right]. \tag{5.2}$$

Here, the parameter κ is defined as:

$$\kappa^2 = \pi\alpha \frac{n_B}{T^3} \left(\mathrm{Y_e} + \sum_j \mathcal{Z}_j^2 \, \mathrm{Y}_j \right) . \tag{5.3}$$

where α is the fine structure constant, n_B the baryon density, $\mathrm{Y_e}$ the electrons per baryon, $\mathrm{Y}_j = \mathrm{X}_j/\mathcal{A}_j$ and X_j, $\mathcal{A}_j$ and $\mathcal{Z}_j$ represent, respectively, the mass fraction, atomic weight and atomic number of the nuclear species j. For solar conditions the function $F(\kappa^2)$ can be approximated by Schlattl et al. (1999),

$$F(\kappa^2) = 1.842(\kappa^2/12)^{0.31}. \tag{5.4}$$

Solar models have been computed for different $g_{a\gamma} = g_{10} \cdot 10^{-10}$ GeV^{-1} values, where g_{10} spans the range from 0 to 20 with an interval of $\Delta g_{10} = 1$. Two sets of models have been computed, using the reference compositions GS98 and AGSS09met. However the solar composition is treated as free parameters in the current analysis through the best fit model as it has been described in Chapter 4. Therefore, the results obtained using both compositions are equivalent (see Section 5.5) and results are robust with respect to the *solar abundance problem*. In Section 5.4, the statistical method is discussed in detail for this particular case.

5.2.2 Models with hidden photons

The production of HPs (γ') in the interior of the Sun can be seen as $\gamma - \gamma'$ oscillations, described by the Lagrangian

$$\mathcal{L} = -\frac{1}{4} A_{\mu\nu} A^{\mu\nu} - \frac{1}{4} B_{\mu\nu} B^{\mu\nu} + \frac{m^2}{2} B_\mu B^\mu - \frac{\chi}{2} A_{\mu\nu} B^{\mu\nu},$$

where $A_{\mu\nu}$ and $B_{\mu\nu}$ are the field strengths of the photon and HP field, A_μ and B_μ respectively. The energy loss rate per unit mass ϵ_{hp} is calculated by using the approximation presented in Redondo and Raffelt (2013). Only the dominant process of resonant emission of longitudinal HPs (details in (Redondo, 2008; Redondo and Raffelt, 2013)) is taken into account and the corresponding energy loss rate is given by

$$\epsilon_{hp} = \frac{\chi^2 m^2}{e^{\omega_P/T} - 1} \frac{\omega_P^3}{4\pi} \frac{1}{\rho} \tag{5.5}$$

where χ is the kinetic mixing parameter, m the mass of the HP and ω_P is the characteristic plasma frequency. Typical values in the solar center are $\omega_P \sim 0.3$ keV and $T \sim 1$ keV. By expanding the exponential, it can be seen that the temperature dependence of the energy loss rate is linear to first order in $\omega_P/T \sim 0.3$. In principle, a threshold factor $\sqrt{1-(m/\omega_P)^2}$ should be included in Equation 5.5, but this term is completely irrelevant for the range of masses considered in this chapter, i.e. $m \lesssim \text{eV}$. As a consequence, the energy loss rate ϵ_{hp} depends only on the product χm which is the quantity that can be constrained by solar data. For HPs, χm ranges from 0 to $8 \cdot 10^{-12}$ eV with an interval $\Delta\chi m = 1 \cdot 10^{-12}$ eV. As for the case of axions, models with both GS98 and AGSS09met composition as reference have been computed.

5.2.3 Models with minicharged particles

MCPs are dominantly produced through plasmon decay $\gamma^* \to f\bar{f}$ while other processes like e^+e^--annihilation ($e^+e^- \to f\bar{f}$) or vector boson fusion $\gamma\gamma' \to f\bar{f}$ are suppressed due to the small number of positrons and HPs. On the other hand, SM photon fusion $\gamma\gamma \to f\bar{f}$ is of higher order in the small parameter ϵ. Hence, in the remainder only plasmon decay is considered.

The energy emission rate per volume for plasmons decaying into MCPs is given by Raffelt (1996) as:

$$\epsilon_{MCP} = \frac{2}{2\pi^2}\int_0^\infty \mathrm{d}k k^2 \frac{\omega\Gamma_{\gamma^*}}{e^{\omega/T}-1} \tag{5.6}$$

where T is the temperature of the Sun and the plasmon's frequency ω is related to its momentum k through the dispersion relation $\omega^2 - k^2 = \omega_p^2$, which holds for a transverse plasmon in a non-relativistic, non-degenerate plasma (Raffelt, 1996).

The decay rate Γ_{γ^*} reads

$$\Gamma_{\gamma^*} = \frac{\alpha}{3}\frac{Z}{\omega}\left(\omega_p^2 + 2m_f^2\right)\sqrt{1-\frac{4m_f^2}{\omega_p^2}}\,, \tag{5.7}$$

where the renormalization factor Z is of order unity. Finally, a factor 2 in eq. (5.6) arises because of the two different polarization states of transversal plasmons.

Equation (5.6) is valid as long as $\omega_p \geq 2m_f$ so that plasmons that fulfill the dispersion relation ('on-shell' plasmons) can decay into MCPs. However, even when $\omega_p < 2m_f$, plasmonic excitations that are not on-shell ('off-shell' plasmons) produce MCPs. These off-shell plasmons are thermally distributed (Weldon, 1983) and their emission rate can be obtained (Vogel and Redondo, 2014),

$$\epsilon_{MCP} = 2\int_0^\infty \frac{k^2\mathrm{d}k}{2\pi^2}\int_{\sqrt{4m_f^2+k^2}}^\infty \frac{\omega\mathrm{d}\omega}{\pi}\frac{2\,\mathrm{Im}\,\Pi}{(K^2-\mathrm{Re}\,\Pi)^2+(\mathrm{Im}\,\Pi)^2}\frac{\omega\Gamma_{\gamma^*}(K^2)}{e^{\omega/T}-1}, \tag{5.8}$$

where $K^2 = \omega^2 - k^2$, the decay rate is given by eq. (5.7) with ω_p^2 replaced by K^2, and the self energy is $\Pi = \omega_p^2 + i\omega\Gamma_{\mathrm{Th}}$. The decay rate for plasmons with $\omega_p < 2m_f$, Γ_{Th}, is controlled by Thomson scattering $\Gamma_{\mathrm{Th}} = n_e \sigma_{\mathrm{Th}} = n_e (8\pi\alpha^2)/(3m_e^2)$, as can be seen by analyzing the two-loop self energies of the photons (Weldon, 1983).

Using Equation 5.6 and Equation 5.8, it is possible to compute the production of MCPs with non-zero masses in all areas of the Sun. On-shell decay Equation 5.6 is valid in high density regions while Equation 5.8 can be used in low-density areas of the Sun.

For this case, the constraints are given on the mass of the MCP (m_f) and the charge of the particle (ϵ), and thus, in contrast to the axions and HPs case, it is a two-parameter problem. For that reason, different solar models with MCPs have been computed for different masses; with on-shell emission ($m_f = 0 - 125\,\mathrm{eV}$) and with only off-shell emission ($m_f = 150 - 3160\,\mathrm{eV}$). For each of the masses, different solar models are calculated with charges of the order of $\epsilon = \ 10^{-14}$ when there is on-shell emission ($2m_f < \omega_P$) and about one order of magnitude higher $\epsilon = \ 10^{-14} - 10^{-13}$ when only off-shell emission takes place ($2m_f > \omega_P$). Only AGSS09met composition is presented for this case, because results are independent of the reference model as it is proven by the axions and HPs cases (see Section 5.5 and in Chapter 4).

5.3 Observations

The observable quantities used in this analysis are the same than the ones used in Chapter 3 and Chapter 4; boron and beryllium neutrino fluxes, the convective envelope properties inferred for helioseismology ($\mathrm{Y_S}$ and $\mathrm{R_{CZ}}$) and 30 points of the solar sound speed profile $\mathrm{c_s(r)}$.

The observational values and the corresponding errors are the ones used to construct the BFMs in the previous chapter (see Section 4.2). These observational values as well as the values of the SSMs used in this chapter are summarized in Table 5.1. About the solar sound speed profile, it has been derived using helioseismic data independently for each model considered in this work, i.e. using consistently each model for the helioseismic inversion. Inversion has been done using the SOLA inversion technique. The adopted frequencies are the BISON-13 dataset complemented with data of MDI, GOLF and IRIS. More details on both the frequency dataset and inversion technique are given in Basu et al. (2009).

5.4 Statistical Method

The energy losses from the particles do not depend on the detailed metal composition of the Sun and the allowed range of energy losses is quite limited. Therefore, BFMs

Q	AGSS09met	GS98	Observables	Ref.
$\mathrm{Y_S}$	$0.232(1 \pm 0.013)$	$0.243(1 \pm 0.013)$	0.2485 ± 0.0035	1
$\mathrm{R_{CZ}/R_\odot}$	$0.7238(1 \pm 0.0033)$	$0.7127(1 \pm 0.0033)$	0.713 ± 0.001	2
$\Phi(^7\mathrm{Be})$	$4.56(1 \pm 0.06)$	$5.00(1 \pm 0.06)$	$4.80(1^{+0.050}_{-0.04})$	3
$\Phi(^8\mathrm{B})$	$4.60(1 \pm 0.11)$	$5.58(1 \pm 0.11)$	$5.16(1 \pm 0.025)$	3

Table 5.1: The first two columns show the SSM predictions for GS98 and AGSS09met composition and the corresponding theoretical uncertainties Serenelli et al. (2011). Note that theoretical errors do not include uncertainties due to the solar composition. The third column summarizes the observational values and errors. Neutrino fluxes are in $10^9\mathrm{cm}^{-2}\mathrm{s}^{-1}$ for the $\Phi(^7\mathrm{Be})$ and $10^6\mathrm{cm}^{-2}\mathrm{s}^{-1}$ for $\Phi(^8\mathrm{B})$. References: 1 - Basu and Antia (2004); 2 - Basu et al. (1997); 3 - Bergström et al. (2016).

described in the previous chapter can be used in order to eliminate the composition contribution and disentangle the peculiar effects introduced by exotic particles.

In this particular approach, there are three free parameters in theoretical predictions: one (g_{10}, χm or ϵ) is related to axions, HP or MCPs[1] properties, and the other two are the volatile elements (δz_{vol}) and refractories (δz_{ref}) that are used to rescale the composition from the reference solar models to obtain the corresponding BFM for each of the models calculated. To do so, the procedure described in Chapter 4 is used and each of the models is minimized with respect to ($\delta z_{\mathrm{vol}}, \delta z_{\mathrm{ref}}$), i.e. for each value of g_{10}, χm or ϵ, the solar surface composition that leads to the best agreement with observational data is chosen (the Best Fit Model is calculated for each of the models). This can be summarized with the following function

$$\tilde{\chi}^2\left(f\right) = \min_{\{\delta z_{\mathrm{j}}\}} \left[\chi^2\left(f, \delta z_{\mathrm{vol}}, \delta z_{\mathrm{ref}}\right)\right] \tag{5.9}$$

where $f = g_{10}$, χm, ϵ, that can be used to constrain axion, HP and MCP properties. The best fit values for g_{10} and χm are found by minimizing this function and the obtained value $\tilde{\chi}^2_{\mathrm{min}}$ provides information on the goodness of the fit. The allowed regions for g_{10} and χm at 1, 2 and 3σ confidence level (CL) are determined by cutting at the values of the variable $\Delta\chi^2 \equiv \tilde{\chi}^2 - \tilde{\chi}^2_{\mathrm{min}}$ =1, 4, and 9 respectively, as it is prescribed for a chi-squared function with one degree of freedom. For the case of MCPs, the $\tilde{\chi}^2_{\mathrm{min}}$ is calculated for each of the m_f and as it is a two-degrees of freedom problem (m_f,ϵ), the allowed regions for ϵ are determined by cutting $\Delta\chi^2$ =2.3, 6.2, and 11.8 corresponding to a CL of 1, 2 and 3σ respectively.

---

[1] For MCPs this χ^2 function is calculated for different values of the mass m_f, and therefore there is one extra degree of freedom.

As described in Chapter 4, the BFM for each of the models considered is calculated by using the *pull approach*. Therefore, for the models with exotic particles, the effects of an extra energy loss channel are partially compensated by the pulls of the input parameters and then, the bounds are placed with those effects in the models that cannot be mitigated by modifying the inputs. Therefore, the bounds obtained are much more restrictive and clearly more robust than previous solar bound, as for example those obtained in analyses that consider one observable quantity at a time (e.g. the ^{8}B neutrino flux or one point of the sound speed profile, see e.g. Gondolo and Raffelt, 2009; Maeda and Shibahashi, 2013; Schlattl et al., 1999).

5.5 Results

In this section all the results for the three different studied cases are presented. First, the energy loss distribution are shown together with the differences among the cases, that will lead to differences in the final results. Then, the outputs of the solar models (sound speed profiles, $\mathrm{Y_S}$, $\mathrm{R_{CZ}}$, $\Phi(^7\mathrm{Be})$ and $\Phi(^8\mathrm{B})$) are shown as function of the different properties of the particle studied. Finally, the results of the statistical analysis are discussed and the upper limits for the different properties of the particles are placed.

Some of the axions and HPs results are presented together for simplicity. This is not done for the MCP case because it is a two parameters problem in contrast with the other two cases.

5.5.1 Energy distribution

5.5.1.1 Axions and Hidden photons

Equation 5.1 and 5.5 give the dependence of the energy loss rates induced by axions and HPs on temperature and density. Different dependences translate into different changes in the structure of the Sun. To facilitate discussion and interpretation of results Figure 5.1 shows the normalized production profile, i.e. the energy loss rate per unit mass multiplied by the mass contained in a spherical shell of radius r, as a function of the solar radius for axions (red - thin line) and HPs (blue - thick line). For comparison, the energy loss rate for MCPs with $m_f = 0$ eV is included (orange - dashed line). The differences can be easily seen. The production of axions induces energy losses in the inner region of the Sun ($r < 0.4\mathrm{R}_\odot$), whereas the energy loss distribution is much broader for the case of HPs. The difference is mostly due to the temperature dependence of the energy loss rates, see Equation 5.1 and Equation 5.5.

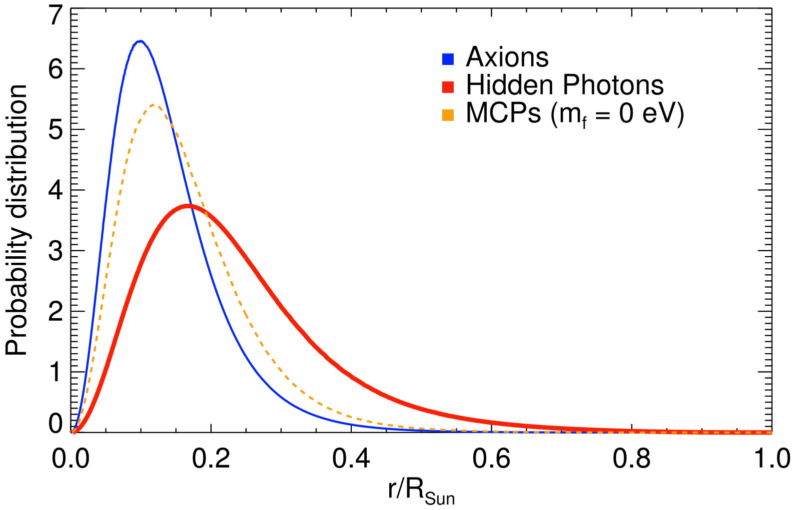

Figure 5.1: Normalized production distribution as a function of $r/R_{\odot}$. Solid red-thin and solid blue-thick lines correspond to axions and HPs respectively. For comparision, the normalized energy loss distribution for MCPs with $m_f = 0$ eV is plotted in orange dashed line. In Figure 5.2, the complete comparision for MCPs is presented.

For axions, the rate $\epsilon_{a\gamma}$ is roughly proportional to T^6, while for HPs the dependence of the rate ϵ_{hp} on the temperature is approximately linear under solar conditions. Based on the different emissivities, the observables are expected to be affected in a different way. For example, axions will have a major effect on the sound speed profile in the core regions while HPs can produce modifications of the sound speed profile in all regions. Notice, however, that although energy losses are localized in certain regions of the Sun, structural changes can be, to some degree, present all over the Sun. Indeed, local changes in certain quantities produce variations in the whole structure as it has been discussed in Section 2.2.2.1 and previously in Tripathy and Christensen-Dalsgaard (1998) and Villante (2010).

5.5.1.2 Minicharged Particles

In the top panels of Figure 5.2, the energy loss distribution is presented as a function of the solar radius for different m_f with a fixed value of the charge of $\epsilon = 2.2 \times 10^{-14}$. To understand better the on(off)-shell emission in the lower panel of the Figure 5.2 the plasma frequency ω_p is shown as a function of the solar radius. Differently from Figure 5.1, the absolute values of the energy for a fixed ϵ are presented because it is also important to understand how the energy loss distribution change with mass. For $m_f = 0$, on-shell plasmon decay is possible everywhere inside the Sun because

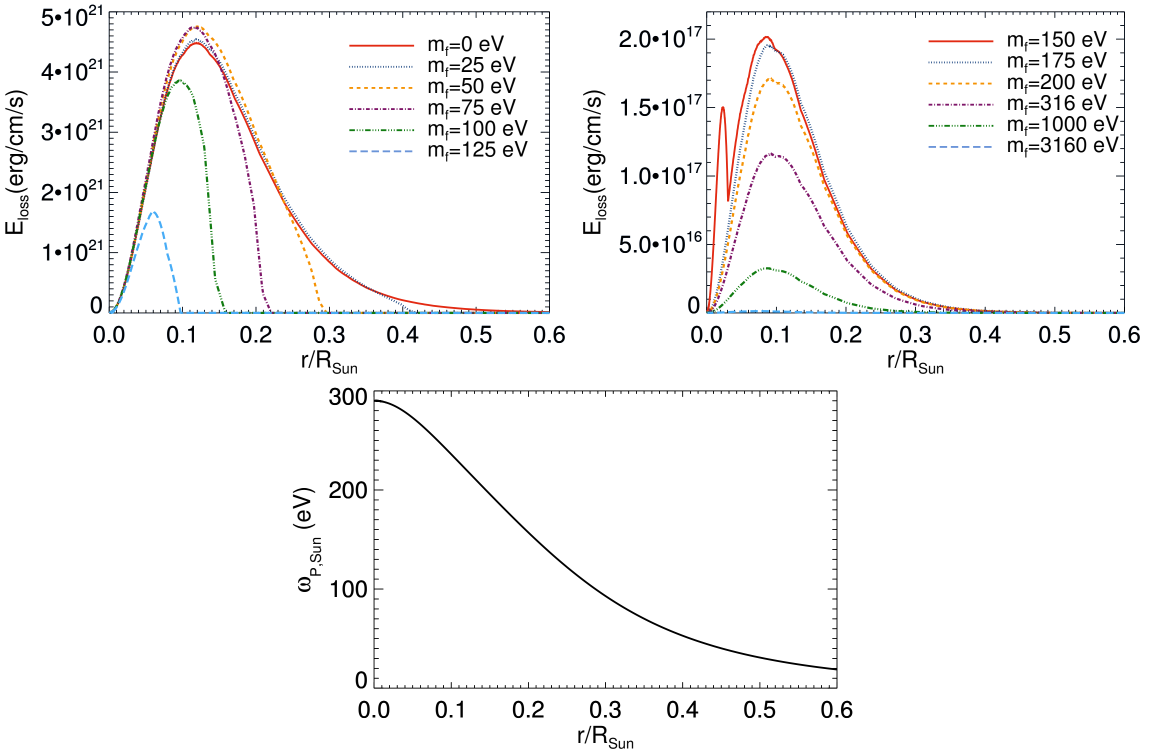

Figure 5.2: Energy loss distribution as a function of $r/R_\odot$ for different values of m_f. The top left panel corresponds to the case where $2m_f < \omega_p$ so that the emission is not suppressed at least somewhere inside the Sun. The top right panel corresponds to the suppressed emission $2m_f > \omega_p$. In the bottom panel, the plasma frequency ω_P is represented as a function of the solar radius.

$2m_f < \omega_p$ is always fulfilled. For $m_f > 0$, less dense regions do not allow for on-shell decay anymore and the weaker off-shell decay occurs. Hence, the emission rate is strongly suppressed for larger radii.

On-shell emission is completely suppressed when $2m_f > \omega_p$ everywhere inside the Sun. The maximum value for the plasma frequency of the SSMs is around $\omega_p \sim 290$ eV such that for $m_f \geq 145$ eV only off-shell decay is possible. For $m_f = 150$ eV, top-right panel of Figure 5.2 shows a two-peaked structure. The reason for this is that quasi on-shell emission occurs in a small sphere around the core of the Sun. Here, the emission rate is dominated by the flank of the quasi-particle Breit-Wigner profile which rises quickly when ω_p approaches $2m_f$.

As apparent from Figure 5.2, different values of m_f lead to different energy loss distributions, not only affecting the amount of the energy lost but also its shape. For that, different effects on the solar observables are expected depending on the mass m_f considered.

5.5.2 Solar neutrinos and convective envelope properties

5.5.2.1 Axions

Figure 5.3 shows the dependence of the solar neutrino fluxes $\Phi(^8\mathrm{B})$ and $\Phi(^7\mathrm{Be})$ and of the convective envelope properties $\mathrm{Y_S}$ and $\mathrm{R_{CZ}}$ on g_{10}. Red lines correspond to solar models implementing AGSS09met composition and blue ones to GS98. The shaded zones depict the 1σ theoretical errors calculated using the power-laws described in Section 2.4.2 but without the contribution of the composition errors and using OP-OPAL difference as opacity uncertainty (see Chapter 4 for the discussion about this choice). The black lines show the experimental values with 1σ errors, as given in Table 5.1. In the upper panels of Figure 5.3, it is possible to see how the observables $\mathrm{Y_S}$ and $\mathrm{R_{CZ}}$ change in the presence of axions. The surface helium abundance $\mathrm{Y_S}$ decreases with increasing values of the axion-coupling constant because it is almost perfectly correlated to the initial helium abundance $\mathrm{Y_{ini}}$. This quantity decreases with g_{10} because a higher initial amount of hydrogen is necessary to match the solar luminosity $\mathrm{L}_\odot$ in the presence of axion energy losses. The change in the convective radius $\mathrm{R_{CZ}}$ is quite small because energy losses are localized in the innermost regions of the Sun. The lower panels present results for the neutrino fluxes. $\Phi(^8\mathrm{B})$ and $\Phi(^7\mathrm{Be})$ increase with increasing g_{10} predominantly as a result of higher core temperatures and reach values well outside of the theoretical and experimental 1-σ errors already at relatively small values of g_{10}. The $\Phi(^8\mathrm{B})$ relative changes are larger than those of $\Phi(^7\mathrm{Be})$ due to its stronger sensitivity to temperature. As a consequence, it is expected that $^8\mathrm{B}$ neutrino measurements give stronger constraints on g_{10}. It is important to mention that the present experimental determinations of $\Phi(^8\mathrm{B})$ and $\Phi(^7\mathrm{Be})$ have very small uncertainties, 3% and 4.5% respectively. The constraining power of both fluxes, and particularly $\Phi(^8\mathrm{B})$, is currently limited by uncertainties in solar models.

Figure 5.3 also illustrates that the relative variations in the observables do not depend on the reference solar composition used, as expected because axion production does not depend directly on it. Differences between models with GS98 and AGSS09met compositions simply reflect the initial differences in the respective SSMs.

5.5.2.2 Hidden photons

In the case of HPs, the changes of the solar neutrino fluxes and convective envelope properties have the same qualitative behavior than for axions, as it is seen in Figure 5.4. The decrease of $\mathrm{Y_S}$ and the increase of $\Phi(^7\mathrm{Be})$ and $\Phi(^8\mathrm{B})$ are again a consequence of the solar luminosity constraint, i.e. of the fact that increased initial

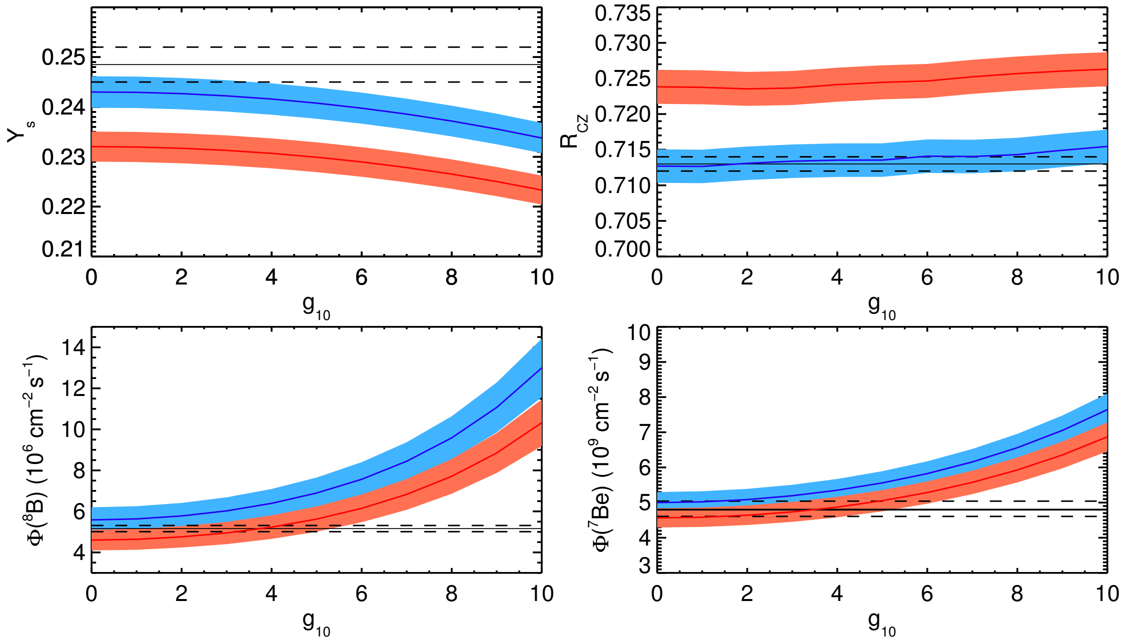

Figure 5.3: Evolution of the model parameters (Ys, R_{CZ}, $\Phi(^7Be)$, $\Phi(^8B)$) as a function of the axion-photon coupling constant. Red color correspond to AGSS09met abundances and the blue one to the GS98 abundances. Black lines represent the observational value with the errors and the shaded zones show model errors.

---

hydrogen abundance and increased core temperature are necessary to compensate energy losses. The behavior of R_{CZ} is instructive because it shows that different types of particles can induce different changes in the solar structure. Consider, e.g., models for axions and HPs for which the boron neutrino flux is comparable, say $\Phi(^8B) \sim 15 \cdot 10^6 cm^2 s^{-1}$. In the case of axions, this corresponds to solar models with an increase of the convective radius equal to $\Delta R_{CZ} \approx 0.003 R_\odot$. For HPs, the increase of R_{CZ} is a factor of two larger, i.e. $\Delta R_{CZ} \approx 0.006 R_\odot$. For a given change in the central conditions, as essentially determined by $\Phi(^8B)$, HPs lead to larger changes than axions in the outer layers as a consequence of the milder temperature dependence of their emission rate.

5.5.2.3 Minicharged Particles

Figure 5.5 and Figure 5.6 show the results for the MCP case. Each figure contains different panels corresponding to different masses m_f corresponding to cases where on-shell emission takes place in some of the regions of the Sun. The results for off-shell emission are expected to be similar but with values of ϵ one order of magnitude higher. Same conclusions than for previous cases apply for these cases where the

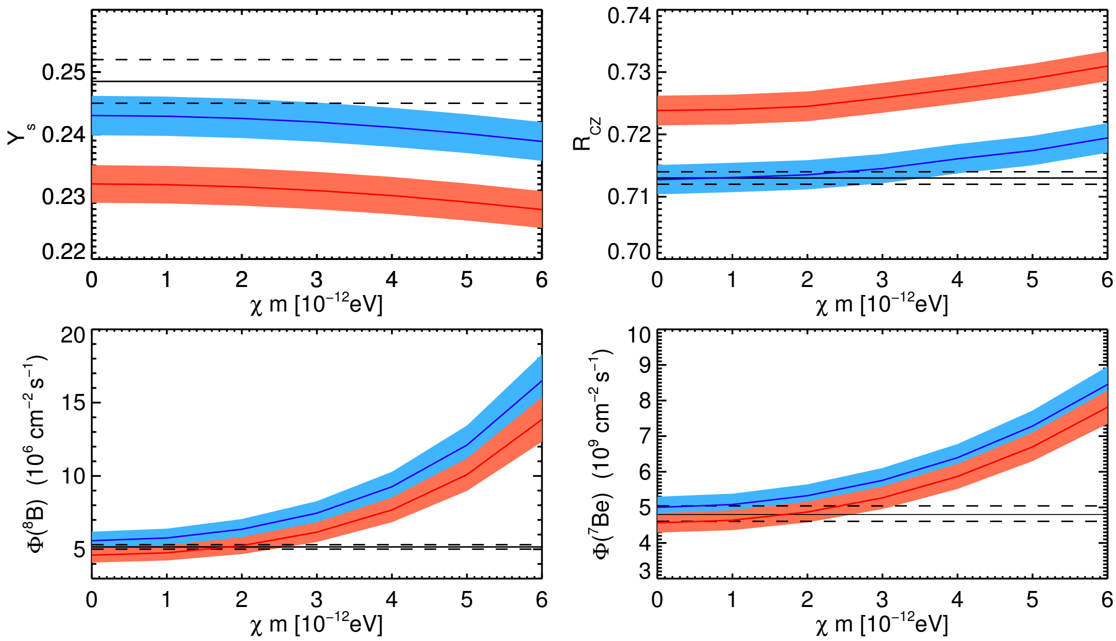

Figure 5.4: Same as Figure 5.3 but for the HPs case. The variable on the x-axis corresponds to the product of the kinetic mixing and the HP mass.

---

neutrino fluxes increase when the energy loss increases, while the surface helium decreases. The values of radius of the convective envelope are almost constant. For Y_S and neutrino fluxes, a clear correlation of the MCP mass with the changes of these quantities can be observed. For lower masses the increase of neutrinos fluxes (and helium decrease) is greater than for higher masses in consistency with the distribution of the energy loss rates presented in Figure 5.2, where the emission is suppressed for high masses. The results for the case where m_f = 125 eV is considered cannot be understood by the same arguments for the reasons explained in the following section.

- The particular case of $m_f = 125eV$ For all the cases, neutrino fluxes increase with increasing energy loss. As it has been previously discussed, that is related to the fact that when calculating solar models, one of the condition that have to be fullfilled is that total energy radiated by the Sun (solar luminosity + dark energy, if present) is produced by nuclear reactions and that the final luminosity matches the observed solar one. Therefore, if there is an extra-energy loss channel in the Sun, in order to obtain a model with the observed luminosity, an increase of the pp reaction is needed. To do so an increase of the temperature is necessary. That rise will have an impact on the Φ(^{8}B) and Φ(^{7}Be), very sensitive to changes on the temperature.

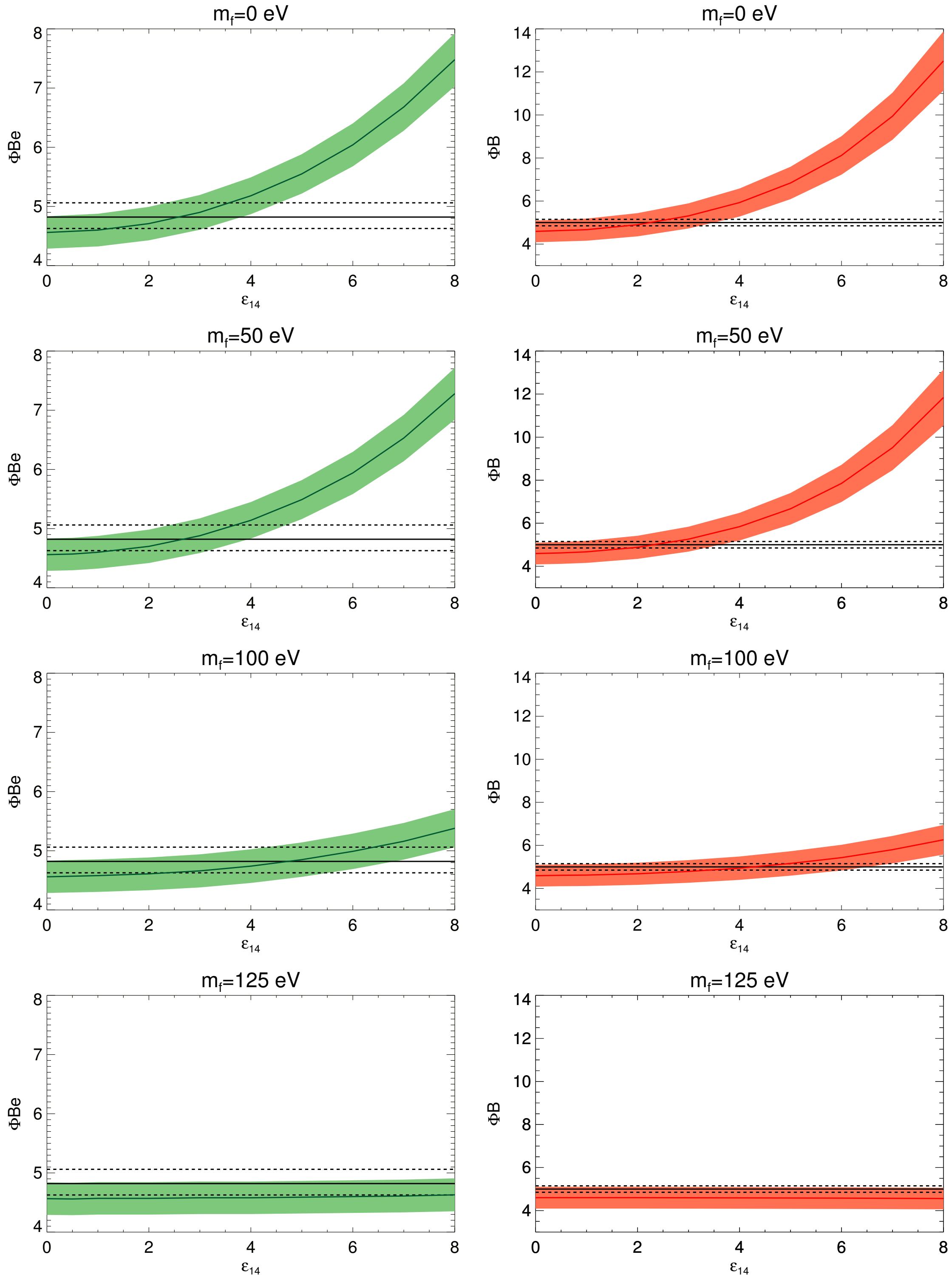

Figure 5.5: Evolution of $\Phi(^7\mathrm{Be})$ (left and green) and $\Phi(^8\mathrm{B})$ (right and red) as function of the parameter ϵ. The case for four different m_f are presented. Following Figure 5.3 the shadowed regions correspond to the model error and the black lines to the observational values (solid) and the corresponding errors (dashed.)

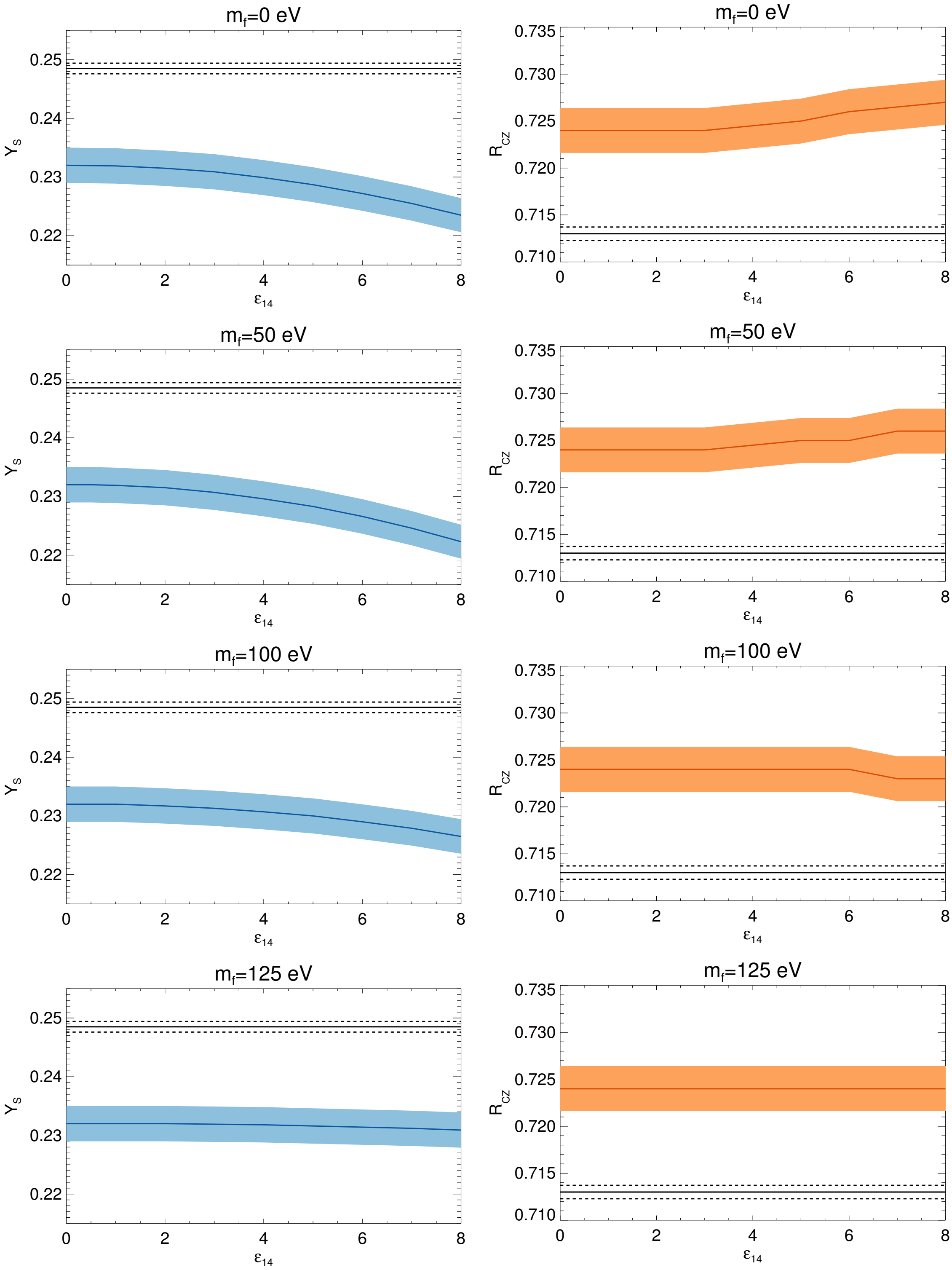

Figure 5.6: Same than Figure 5.5 but for Y_S (left and blue) and R_{CZ} (right and orange).

But that is not the situation when a deeper study is done to the results for $m_f = 125$ eV. At Figure 5.5 almost no changes can be observed for the parameter space studied. For that reason, at Figure 5.7 the ϵ range is increased in order to study the conditions where energy loss have an impact. In this figure, the $\Phi(^8\mathrm{B})$ and $\Phi(^7\mathrm{Be})$ are the relative values with respect of the standard ones, and it is possible to observe that the trend is not the same for both fluxes. $\Phi(^7\mathrm{Be})$ results are the expected but that is not the situation of $\Phi(^8\mathrm{B})$, where the flux initially decreases in contrary of what is expected.

This interesting behavior can be explained if the behavior of temperature profile in the interior is studied for cases with different ϵ. In the lower panel of Figure 5.7, this profile is shown for three different cases with $\epsilon = 0$, $\epsilon = 15 \times 10^{-14}$ (~ 0.1 $\mathrm{L}_\odot$) and $\epsilon = 20 \times 10^{-14}$ (~ 0.2 $\mathrm{L}_\odot$). In the interior ($r < 0.08$ R$\odot$), the temperature decreases with increasing extra energy loss, while in the rest of the Sun the temperature increases. The change in the temperature profile results in different flux variations depending on where the reactions take place. The lower panel of Figure 5.7 also shows the production probability distribution as a function of radius of the fluxes $\Phi(\mathrm{pp})$, $\Phi(^8\mathrm{B})$ and $\Phi(^7\mathrm{Be})$. It is possible to see that $\Phi(^8\mathrm{B})$ is localized in the region where the temperature decreases with increasing energy loss, which explains why the flux initially decreases with ϵ. On the other hand, the $\Phi(^7\mathrm{Be})$ flux lies in both (increasing and decreasing temperature) regions. The result is going to be a combination of the decrease of the ^{7}Be production rate in the inner part and the increase of the production of neutrinos in the more exterior part. In this particular situation, this results in an increase of the ^{7}Be neutrino production as a function of ϵ. In general, it is hard to predict the behavior of the neutrino fluxes for highly localized exotic emission since the variation depends on more factors than just the temperature profile (abundance of protons, ^{3}He equilibrium abundance, etc.).

Finally, it is interesting to mention that some works, as e.g. ref. Bahcall and Ulmer (1996) (see Section 1.2.4), show that the neutrino fluxes can be expressed as power-laws of the central temperature of the Sun ($\Phi_i \propto \mathrm{T}_\mathrm{c}^\mathrm{m}$). In contrast, the results of this work show that this relation should be used with great care because it does not apply to all situations and that one should take the whole temperature profile into consideration and not just focus on the central temperature of the Sun.

5.5.2.4 Neutrino fluxes comparison

A direct comparison between results of the three different particles studied (see Figure 5.3, 5.4 and 5.5) should not be done directly from the previous results because

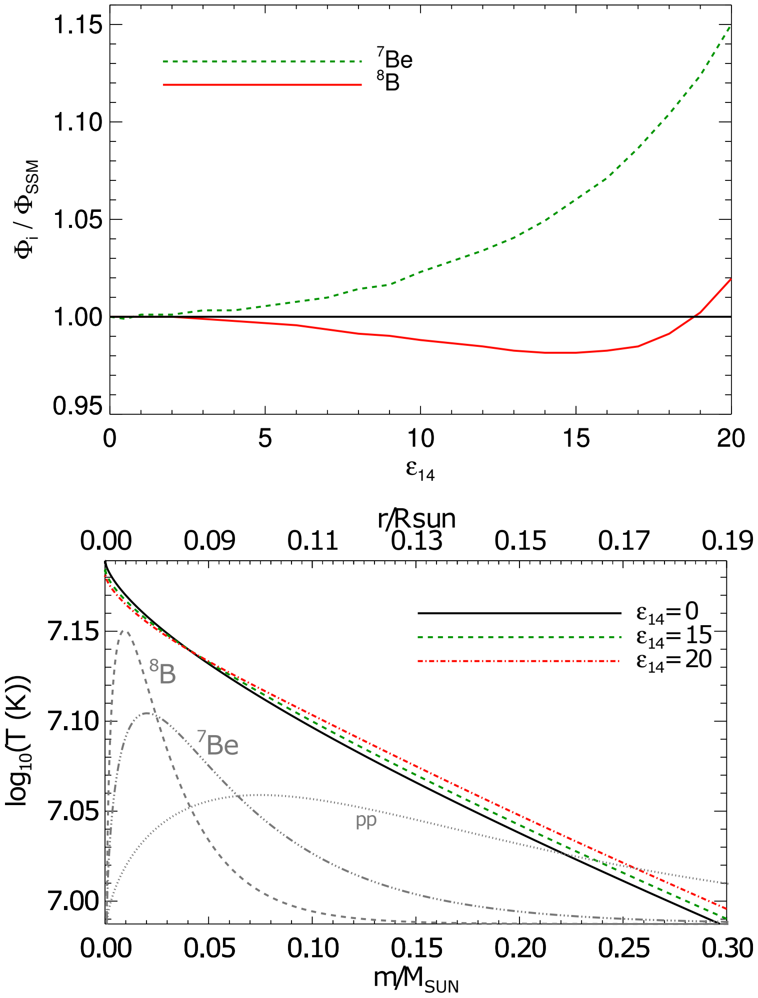

Figure 5.7: *Top panel:* Relative neutrino flux of the $m_f = 125$ eV model with respect to AGSS09met SSM as a function of $\epsilon_{14} = \epsilon \cdot 10^{14}$. The green dotted line corresponds to the ^{7}Be neutrino flux and the solid red line to the ^{8}B neutrino flux. *Low panel:* Temperature profile for the model with $m_f = 125\,\text{eV}$ for three different values of ϵ as a function of mass and radius. The normalized probability distribution of the production as a function of radius for the different neutrino fluxes are given by grey dotted, dashed and dash-dotted lines.

they are shown as functions of the parameters characteristic of each particles not related to each other in a direct way. In order to perform a consistent comparison, a common parameter for all the particles should be used, such as the luminosity contribution from the studied particle to the total solar luminosity ($L_i/L_\odot$). First, to compare the effects of axions and HPs, Figure 5.8 illustrates the fractional change of the neutrino fluxes with respect to the SSMs for axions (red lines) and HPs (blue lines) as a function of the luminosity $L_i/L_\odot$ carried away either by axions or HPs, i.e.

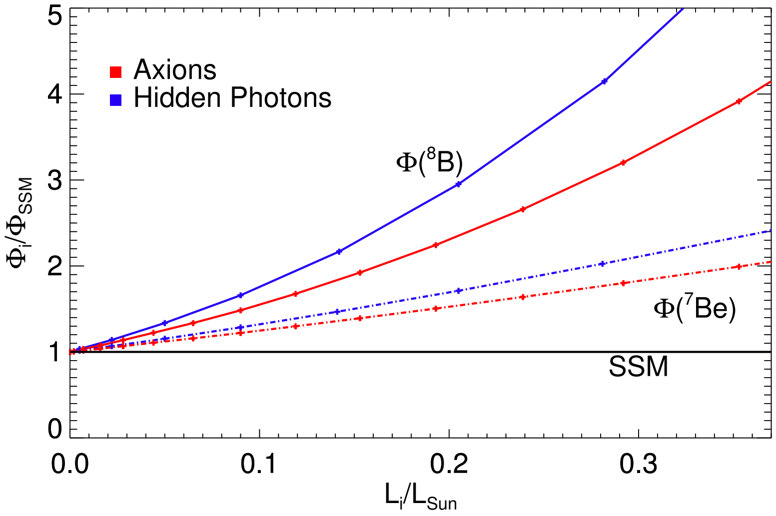

Figure 5.8: Relative changes of the neutrino fluxes with respect to SSM prediction as function of the luminosity contribution of axions (red line) and HPs (blue line).

$\mathrm{L_i} = \mathrm{L_a}$ or $\mathrm{L_{hp}}$.

For the same $L_i/\mathrm{L}_\odot$ value, changes in the neutrino fluxes are larger for the HPs models. It was shown by Gondolo and Raffelt (2009) that L_a and $\Phi(^8\mathrm{B})$ can be related by a simple analytic relation of the form

$$\frac{\Phi(^8\mathrm{B})}{\Phi_{\mathrm{SSM}}(^8\mathrm{B})} = \left(\frac{L_a + \mathrm{L}_\odot}{\mathrm{L}_\odot}\right)^\alpha, \tag{5.10}$$

where $\alpha = 4.6$, based on the older generation of SSMs computed by Schlattl et al. (1999). The present calculations yield $\alpha = 4.4$ for axions, very close to the previous result. Interestingly, for HPs the same functional form can be used but with a much steeper relation given by $\alpha = 5.7$.

In a similar way, for the case of MCPs, ϵ with different masses m_f lead to different energy loss rates. Figure 5.9 shows the relative changes of $\Phi(^8\mathrm{B})$ with respect to the SSM as a function of the MCP integrated energy loss rate. This is done for the different masses m_f with on-shell emission (excluding $m_f = 125$eV for its particular behavior). For comparison, the relative changes for axions and HPs are also plotted in dashed lines. The case of $\Phi(^7\mathrm{Be})$ is not shown because the same conclusions are deduced.

By looking at Figure 5.9 it is possible to see the differences among different masses. $m_f = 0$ eV and $m_f = 25$ eV are equivalent because for $m_f = 0$ eV there is on-shell emission in all regions of the Sun while for $m_f = 25$ eV this emission is supressed only in the outer region where this emission is not relevant. For $m_f = 50$ eV, the

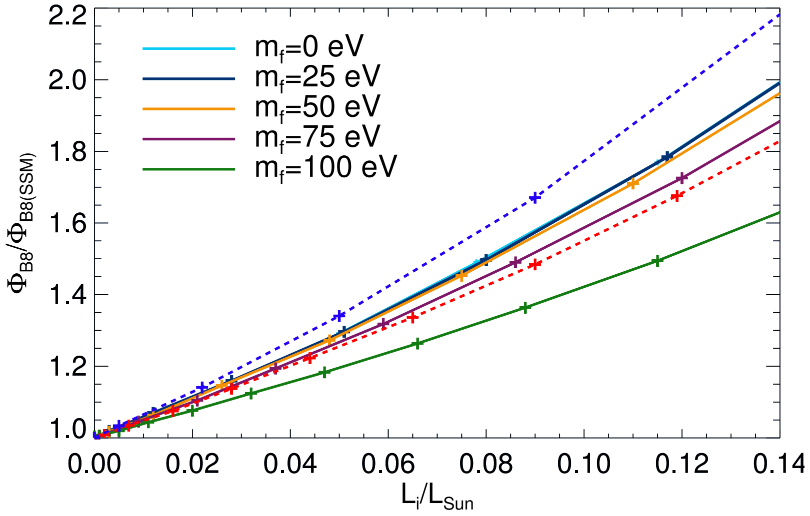

Figure 5.9: In solid lines, relative changes of $\Phi(^8\mathrm{B})$ with respect to SSM prediction as function of the luminosity contribution of minicharged with different masses. In dashed lines the $\Phi(^8\mathrm{B})$ relative changes of axions (blue) and HPs (red) are presented.

m_f(eV)	0	25	50	75	100
α	5.21	5.20	5.14	4.81	3.70

Table 5.2: α parameters that fit Equation 5.10 for MCP with different masses.

differences are small for the same reasons, although some changes start to arise. For larger masses, much larger differences occur, because on-shell emission is being reduced and consequently the corresponding effects on the neutrino fluxes. Then, for each of the cases, in order to use the relation of Equation 5.10, a different value of α is needed to describe their effects. These values are summarized in Table 5.2.

These results reinforce the importance of performing self-consistent solar model calculations to account for the effect of exotic particles. Also, they show that assuming a universality in the constraints that are imposed, e.g. a given $L_i/\mathrm{L}_\odot$ value, can lead to biased bounds on the properties of particles.

5.5.3 Solar sound speed profile

5.5.3.1 Axions and Hidden photons

In Figure 5.10 there is represented the sound speed profiles $\left(\delta c_s = \frac{c_{s,obs} - c_{s,th}}{c_{s,mod}}\right)$ of models including axions (top) and HPs (bottom panel). For each case, five different values of g_{10} and χm are considered. SSMs correspond to the null value of each parameter.

The solid lines are obtained for solar models implementing AGSS09met surface composition while the dotted lines correspond to GS98 surface admixture. The shaded zones show the theoretical uncertainties (blue and red colors; not including composition uncertainties) and the uncertainties coming from the inversion technique (grey color).

It is possible to see that axions produce effects on the sound speed in the inner region of the Sun. This is in line with the results obtained for the convective radius $\mathrm{R_{CZ}}$, which showed little variation in the presence of axion energy losses. This implies that the constraints on g_{10} would be obtained from the measurements of the sound speed at $r/R_\odot < 0.35$. On the other hand, HPs produce noticeable effect also in more external regions, meaning that the entire sound speed profile could potentially contribute to constrain the product χm. However, this is not so simple because in this statistical method composition is free to vary. Variations in the sound speed profile will be compensated, at least partially, by changes in the solar composition (see Section 5.4).

As it is seen from Figure 5.10, solar models implementing AGSS09met surface admixture provide a poor description of the sound speed profile inferred from helioseismic data. In particular, the sound speed prediction deviates at the bottom of the convective envelope by about $\sim 1\%$ with the helioseismic values. In this region, the modifications introduced either by axion or HP energy losses are generally small and cannot explain the observed discrepancy. On the contrary, for $r/\mathrm{R}_\odot < 0.35$, where axion or HPs effects are more relevant, the sound speed profiles of models with fixed reference surface composition deviate in the opposite direction as would be required to solve the *solar abundance problem*.

Although the composition is kept fixed in models shown in Figure 5.10, results suggest that the information encoded in the solar sound speed profile should be able to help constraining the axion and HP properties (see Section 5.5.4).

5.5.3.2 Minicharged Particles

In Figure 5.11, the results for the sound speed of models with MCPs are presented on different panels. Each panel corresponds to a given values of the mass m_f and several ϵ values.

The effects go on the same direction than the ones observed for axions and HPs, and same conclusions apply for these cases. More in particular, the smaller the m_f values, the larger the deviations from the SSM profile because on-shell emission still takes place in all (or relevant part) of the Sun interior. For larger masses m_f, the

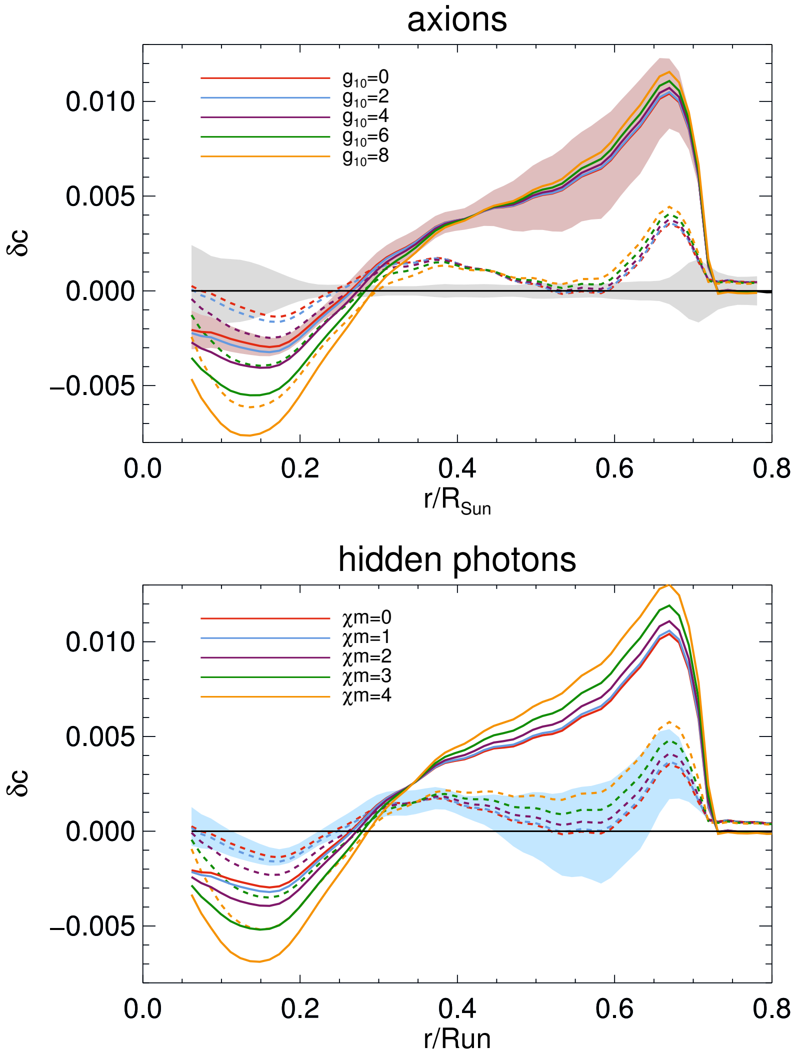

Figure 5.10: Sound speed profile of models with axions (left panel) and HPs (right panels) for different values of the axion-photon coupling constant g_{10} and of the product χm (expressed in 10^{-12}eV) for HPs. Models are calibrated to the reference solar compositions GS98 (dashed lines) and AGSS09met (solid lines). Red and blue shaded zone corresponds to the model errors and the grey one to errors in the helioseismic inversion.

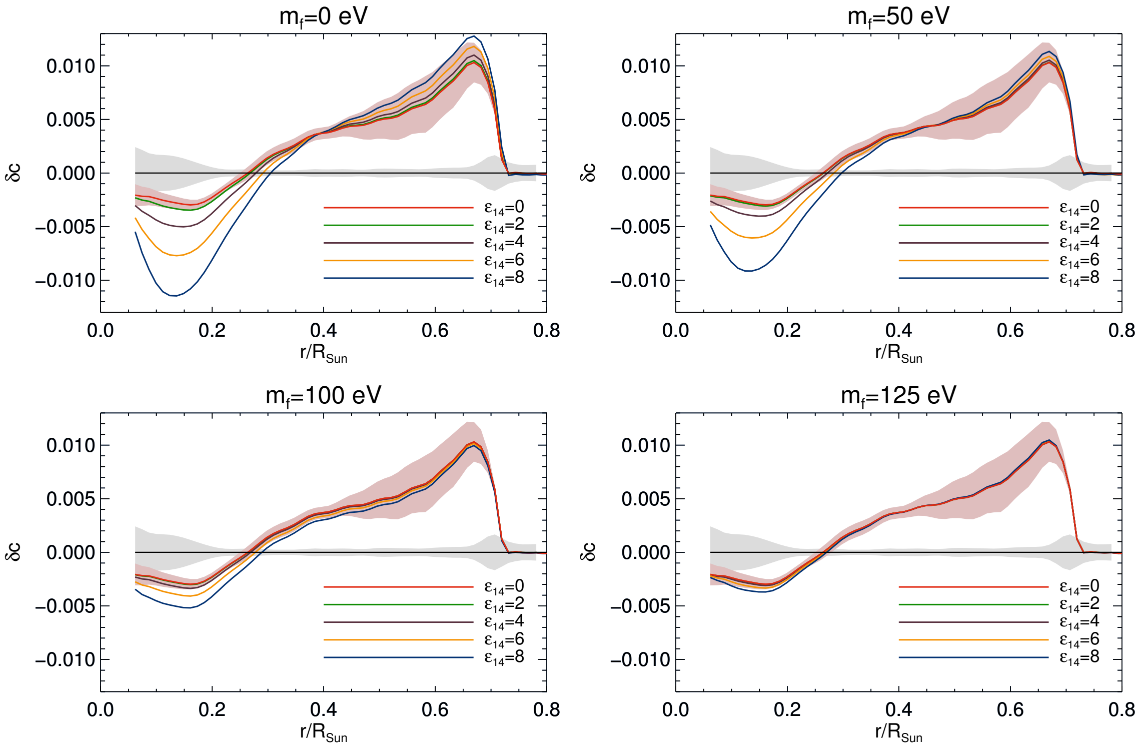

Figure 5.11: Same than Figure 5.10 for MCP case. Each panel corresponds to a given value of m_f and the results for different values of ϵ are presented for each of the cases.

total energy loss is reduced according to the reduction of the on-shell emission region and changes in the sound speed profile becomes less relevant. Moreover, the MCP emission is more localized in the inner part of the Sun where on-shell emission still takes place, so that the sound speed profile is altered more drastically in the inner region. For masses where only off-shell emission takes places, it would be necessary to go to ϵ values an order of magnitude higher than the ones studied here, and changes on the sound speed profile similar than for $m_f = 0$ eV are expected due to the fact that off-shell emission takes place all over the solar region.

5.5.4 Global results

This section presents the global results where all the information obtained from the solar models is used to place constraints to the different properties of the particles. As explained in Section 5.4, the χ^2 function is calculated by constructing a BFM for each of the solar models including different exotic emission. The same procedure than the described in Chapter 4 is used, and therefore, the SSM (model without energy loss) is the one described in the previous chapter with $\chi^2 = 58.2$, $\delta z_{vol} = 0.61$ and

$\delta z_{ref} = 0.12$ for AGSS09met while for GS98 the values are $\chi^2 = 42.2$, $\delta z_{vol} = 0.20$ and $\delta z_{ref} = -0.007$ (see Chapter 4 for details). As it is shown in the following sections, for all cases the minimum χ^2 corresponds to the model without extra energy loss showing that the presence of exotic particles in the Sun only worsens the agreement with the observations. By default, the results presented corresponds to the case where AGSS09met composition is used as reference model. As it has been previously discussed, the results are independent of the initial composition used as reference model.

5.5.4.1 Axions

There is no model including axions ($g_{10} \neq 0$) that improves the overall fit to the data with respect to the the best fit SSM. The variation of χ^2 and its equivalent $N\sigma = \sqrt{\Delta\chi^2}$ (for 1 d.o.f) as a function of g_{10} are shown with solid line in left panel of Figure 5.12. The right panel shows the values of the logarithmic abundances $\varepsilon_{\rm O}$ and $\varepsilon_{\rm Fe}$ that provides the best fit to the data as a function of g_{10}. These quantities are almost independent on g_{10} indicating that there are no degeneracies between composition and axion effects. In Figure 5.12 the results for GS98 have also been included in blue in order to show that results are completely independent than the composition choice for the reference model.

By setting a limit at $\Delta\chi^2 = 9$, the upper bound $g_{10} < 4.1$ is placed at a 3-σ CL. This is almost a factor of 2 lower than previous solar limits (Section 5.6).

One of the advantages on using Equation 4.1 to calculate χ^2 is the possibility to understand which are the contributions to the total value of χ^2. If the values for the SSM and for the model with $g_{10} = 4$ are compared, the following results are obtained; $\chi^2_{\rm obs} = 51.2$ and $\chi^2_{\rm sys} = 7.0$ for $g_{10} = 0$ while for the model with $g_{10} = 4$ the results are $\chi^2_{\rm obs} = 53.5$ and $\chi^2_{\rm sys} = 13$. The values for $\chi^2_{\rm obs}$ are similar for both cases. This is the result of letting the composition to adjust to provide a good fit the solar data. Also, the changes that axions induce in solar models (see Section 5.5.2 and 5.5.3) are partially compensated by the systematic pulls. This effect can be seen in Figure 5.13, where the resulting sound speed profiles of the BFMs are presented, and although some important differences are still evident, they have been compensated by the composition and by changes on the input parameters through the pulls. But changes to the input parameters come at the expense of increasing $\chi^2_{\rm sys}$, that thus provides the dominant contribution to $\Delta\chi^2$ and combined with the final BFMs, will restrict the parameter space of the particles properties. The dominant pulls that increase the value of the χ^2 with increasing g_{10} are the solar luminosity (decrease), S_{11} (increase)

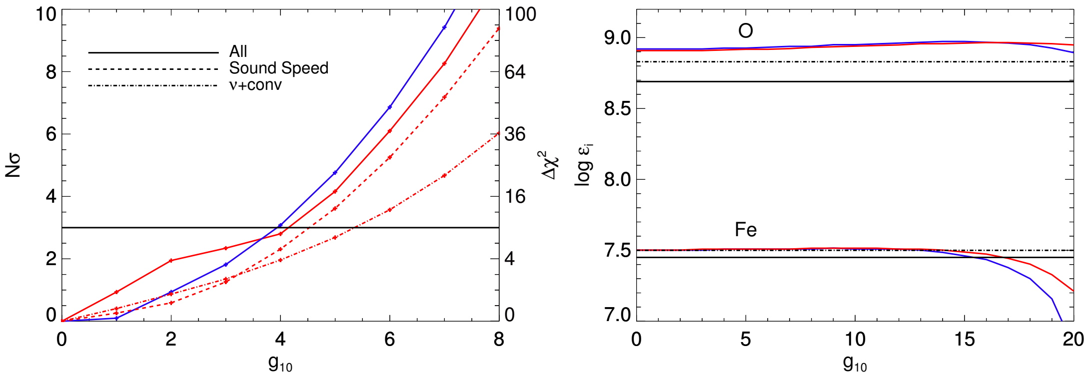

Figure 5.12: Left panel: values of $N\sigma$ and $\Delta\chi^2$ for models with axions. Solid line: using all observables $\Phi(^7\mathrm{Be})$, $\Phi(^8\mathrm{B})$, $\mathrm{Y_s}$, $\mathrm{R_{CZ}}$ and 30 points of the sound speed profile. Dashed line: using the sound speed. Dotted-dashed line: using the neutrinos and convective envelope properties. *Right panel*: best fit composition as a function of g_{10} presented as the logarithmic astronomical abundances (red solid lines). Black lines represent the standard GS98 (dashed) and AGSS09met (solid) values for ϵ_O and ϵ_{Fe}. The red line corresponds to the results with AGSS09met as reference models while blue are the results when GS98 is used.

and, to a lesser extent, $\mathrm{S_{17}}$ (decrease). The first two are mostly related to changes in the sound speed in the solar core. A lower solar luminosity and a larger $\mathrm{S_{11}}$ both contribute to decrease the theoretical sound speed in the solar core (see Schlattl et al. (1999) and Chapter 2), compensating the effect of axions. Changes in $\mathrm{S_{17}}$ occur in order to limit the increase in $\Phi(^8\mathrm{B})$ shown in Figure 5.3. The evolution of the pulls as function of g_{10} are represented in Figure 5.14 and it shows the increase with g_{10} related with the increase of the χ^2_{sys} term.

It is also instructive to discuss how much each piece of experimental information contributes to the bound on g_{10}. To this aim, the left panel of Figure 5.12 shows, with dotted lines, the $\Delta\chi^2$ functions obtained by considering separately the sound speed profile on one hand, and the neutrino fluxes $\Phi(^8\mathrm{B})$ and $\Phi(^7\mathrm{Be})$ and convective envelope properties $\mathrm{Y_S}$ and $\mathrm{R_{CZ}}$ on the other. This last dataset is referred with the label ν`+conv` in the following. The most restrictive limit comes from the sound speed profile that, alone, sets the limit $g_{10} < 4.6$ at 3σ CL. It can be noted, however, that also the ν`+conv` dataset provides a restrictive bound $g_{10} < 5.4$ at 3σ CL. The latter value is more restrictive than the found in Gondolo and Raffelt (2009) using only the $\Phi(^8\mathrm{B})$ even if composition is free in the fit. This result that may seem surprising can be explained from the results presented in Villante et al. (2014). It was shown in that paper that the two observable quantities $\mathrm{Y_S}$ and $\mathrm{R_{CZ}}$ permit to determine the surface

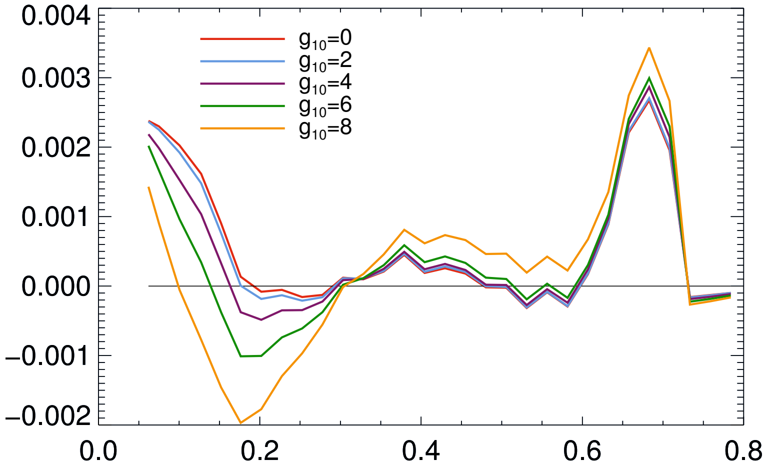

Figure 5.13: Sound speed profile for BFM with axions for different values of g_{10}.

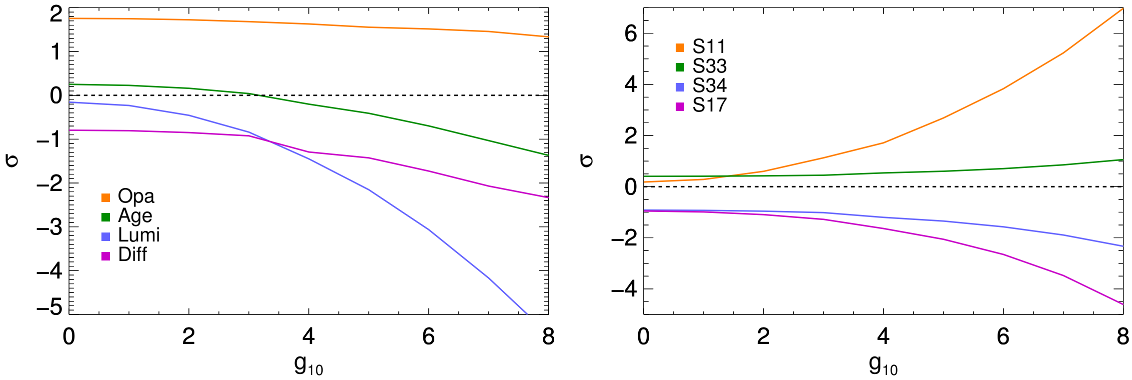

Figure 5.14: Dominant pulls for the input parameters (left) and cross sections (right) as a function of g_{10}.

composition of the Sun (in the two parameter analysis in terms of $\delta z_{\rm vol}$ and $\delta z_{\rm ref}$) with good accuracy. The experimental information on the neutrino fluxes, which are strongly dependent on g_{10}, can be then effectively translated into a bound on axion energy losses.

Finally, since the sound speed profile provide the most restrictive constraint, it is useful to check the bump of $c_s(r)$ observed in the tachocline, i.e. the region just below the convective boundary, does not affect the final results in a critical way. This bump is present even in models with optimized composition (e.g. the sound speed profile of the best fit SSM in Figure 4.5) and is due to the inadequacies of SSMs in modeling dynamic effects in that region that affect the composition gradient and the transition

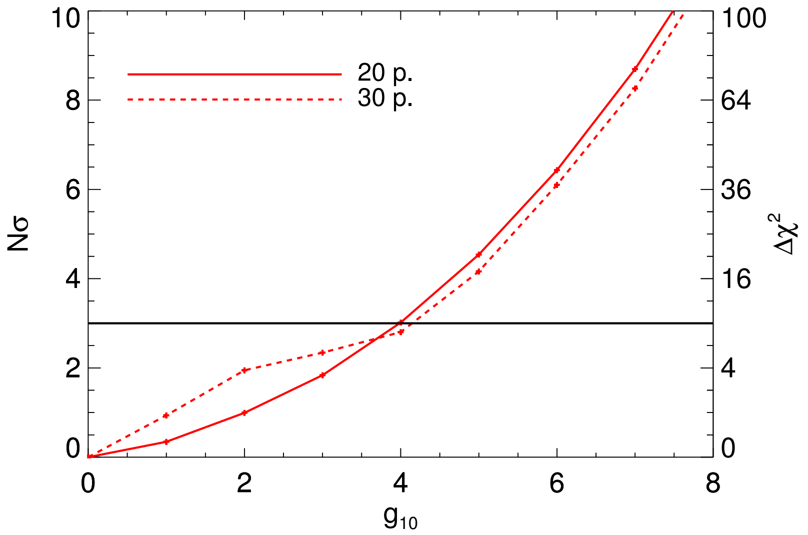

Figure 5.15: The values of $N\sigma$ and $\Delta\chi^2$ for models with axions using $\Phi(^7\mathrm{Be})$, $\Phi(^8\mathrm{B})$, $\mathrm{Y_s}$, $\mathrm{R_{CZ}}$ and 20 points of the sound speed profile as input observables.

between adiabatic and radiative gradient. (e.g. Basu et al. (1997); Christensen-Dalsgaard et al. (2011); Gough et al. (1996)). In Chapter 4 it has been shown that the existing tensions of the sound speed with the $\mathrm{R_{CZ}}$ can bring some discrepancies to the BFMs. For that reason, the global analysis is repeated, but this time excluding the sound speed data profile in the region $r/R_\odot > 0.6$, thus reducing the sound speed data set to 20 data points. The exclusion of the sound speed determinations in the external radiative region, as it expected, improves the quality of the fit being $\chi^2_{\mathrm{min}} = 11.8$ for 24 observational constraints. However, since the limits are derived from the $\Delta\chi^2$ distribution, the bound for g_{10} does not significantly change. In fact, by excluding this regions, as can be seen in Figure 5.15, $g_{10} < 3.9$ at 3σ CL which is an even more stringent limit than the case where the full sound speed profile (in combination with the other experimental informations) is used. The fact that axions mainly affect the sound speed in the inner region of the Sun (see Figure 5.10) explains why the results depend only weakly on the inclusion of the bump. And, using the full sound speed the bound of g_{10} is more conservative.

Considering results discussed in this section, the recommended upper limit is $g_{a\gamma} < 4.1 \cdot 10^{-10}\,\mathrm{GeV}^{-1}$ at 3-σ CL for the axion-photon coupling constant. Figure 5.16 summarizes the relevant astrophysical constraints for hadronic KSVZ axions and axion-like particles, including the newly derived limit, together with the prospects of the future IAXO.

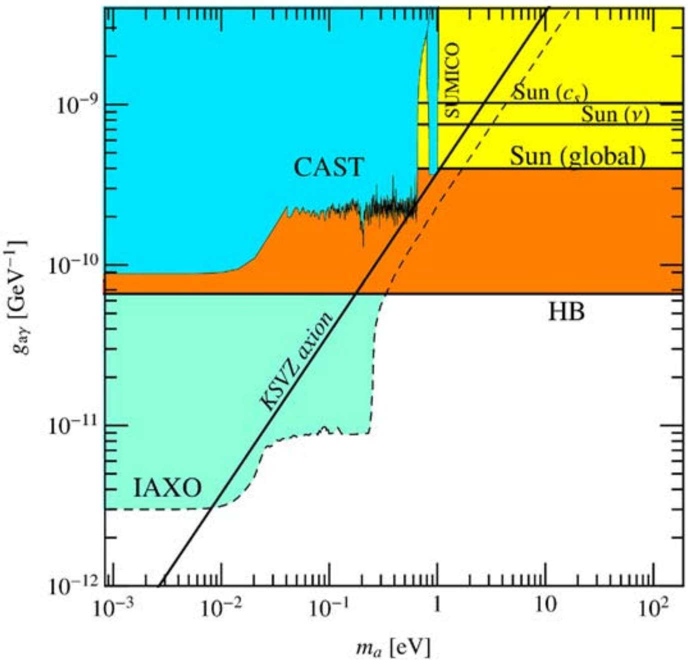

Figure 5.16: Constraints on axion-like particles with a two-photon coupling as a function of the mass. The hadronic axion would be a point in the KSVZ line. The global fit presented in this chapter provides a constraint (Sun (global)) that improves over the solar constraint obtained only with the solar neutrino argument (Sun ν) and previous seismology constraints (Sun c_s) by a significant factor. Still, more stringent bounds come from the lifetime of Horizontal Branch stars in globular clusters. For masses below ∼eV the axion heliosocopes CAST and SUMICO provide very competitive limits and the future International Axion Observatory (IAXO) has the potential of improving over them all. *This figure is courtesy of Javier Redondo.*

5.5.4.2 Hidden photons

In Figure 5.17, the results of this analysis for models including HPs are shown. The left panel shows the $\Delta\chi^2$ distribution and the corresponding $N\sigma$ values as a function of the product χm, as obtained by using all observational constraints. The right panel shows the values of $\varepsilon_{\rm O}$ and $\varepsilon_{\rm Fe}$ that minimize the χ^2 for each of the assumed values of χm. The bound at 3σ CL is given by $\chi m < 1.8 \cdot 10^{-12}$eV when the complete sound speed profile is used. If the region $r > 0.6\,{\rm R}_\odot$ is excluded, then the limit is only marginally different, $\chi m < 1.7 \cdot 10^{-12}$eV. Here again, using the full sound speed profile gives a slightly more conservative limit than excluding the sound speed bump at the base of the convective envelope.

The different observational data contributes to the final result as in the axion

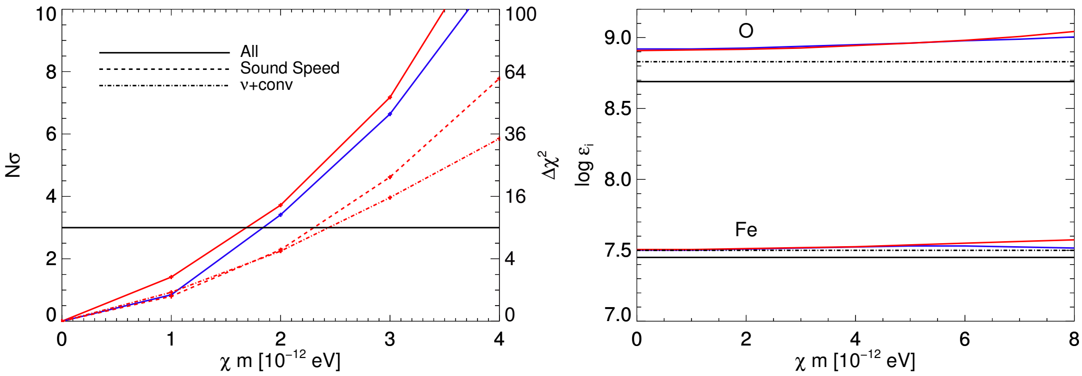

Figure 5.17: Same than Figure 5.12 but for models with HPs.

case. The sound speed is the most restrictive observable giving the constraint $\chi m < 2.3 \cdot 10^{-12}$eV at 3σ CL. In this case, the neutrinos fluxes and convective envelope properties also give a relevant constraint $\chi m < 2.5 \cdot 10^{-12}$eV at 3σ CL close to the one given by the sound speed profile.

As a final result of this analysis, the upper bound is placed at $\chi m \leq 1.8 \cdot 10^{-12}$eV at 3-$\sigma$ CL as an upper bound to product of the kinetic mixing parameter and mass of HPs. This limit does not depend on the assumed solar surface composition. Figure 5.18 shows the new constraint in the mass-mixing plane together with other concurrent limits. Notably, the constraint is the most stringent in the range from $3 \cdot 10^{-5}$ eV to 8 eV.

5.5.4.3 Minicharged particles

For this case, restrictions in the $(m_f,\ \epsilon)$ plane are placed, and therefore, this is a two-degrees problem and the confidence levels $N\sigma = 1, 2, 3, 4\,\sigma$ corresponds to $\Delta\chi^2 = 2.3, 6.2, 11.8, 19.3$. For consistency with previous works the current upper limit is placed at 2σ CL[2]. In Figure 5.19, the resulting values of $N\sigma$ are plotted as a function of ϵ (left panel). The bounds at 2σ and the corresponding MCP luminosity for a different range of masses are summarized in Table 5.3.

The result is that the 2σ bounds on ϵ become weaker for larger masses. That is because the MCP emission is reduced and more localized in the inner part as it was shown in Figure 5.2. When this bound is considered as a function of luminosity, 2σ bounds correspond to $L_{\rm MCP}/L_\odot = 1.5 - 2.7\%$. The dispersion in luminosity at 2σ is related to the fact that the distribution of energy loss in the Sun is different for each

---

[2] The limits of previous works were calculated using a 2σ CL, as well as the current limits for consistency. However, the results for a range of CL are presented in case a 3σ is preferred.

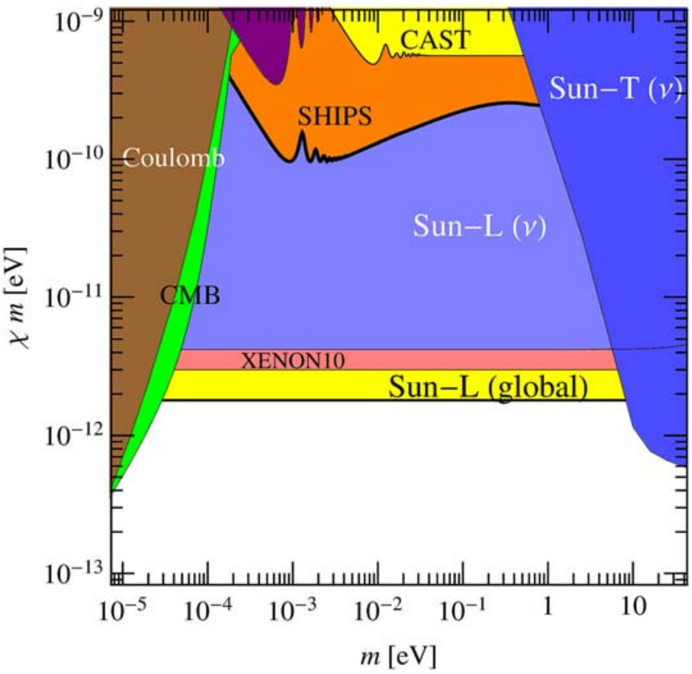

Figure 5.18: Constraints on HPs with mass m and kinetic mixing with photons χ. The global fit presented in this chapter, Sun-L (global), provides a constraint that improves over the solar constraint obtained only with the solar neutrino argument, Sun-L (ν), and the direct detection constraint from XENON10 data An et al. (2013). *This figure is courtesy of Javier Redondo.*

of the masses which will translate into different effects on the structure of the Sun. That means that it is not possible to use a general value for the MCP luminosity to constrain the MCPs parameter space because the luminosity depends on the specific $m_f - \epsilon$ combination.

Figure 5.19 shows the MCP models where $2m_f < \omega_p$ at least in some parts of the Sun so that stringent limits on ϵ can be achieved. For off-shell emission only, $2m_f > \omega_P$, much weaker bounds are obtained, as listed in Table 5.3.

Finally, it is necessary to make a comment about the model with $m_f = 150$ eV. This case is peculiar because of the two-peaked structure that is present in the center (see Figure 5.2). The first peak is very narrow which resulted into convergence problems of the solar models. In order to be conservative, for $m_f = 150$ eV the bound obtained for the model $m_f = 175$ eV is used, corresponding to a value of $\epsilon = 4.6 \times 10^{-12}$. This is justified because the emission rate of the $m_f = 150$ eV model is stronger than the emission rate for $m_f = 175$ eV (see Figure 5.2). The limit on ϵ would, hence, be stronger for $m_f = 150$ eV than the value adopted here.

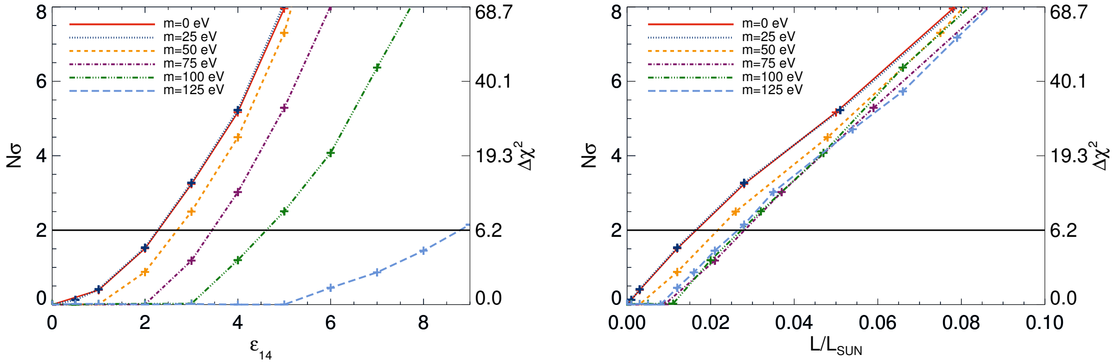

Figure 5.19: Left panel: Values of $N\sigma$ and $\Delta\chi^2$ for models with MCPs with different masses as function of the $\epsilon_{14} = \epsilon \cdot 10^14$ parameter. Right panel: Same than left panel but as function of the MCP luminosity.

On-shell emission			**Off-shell emission**		
m_f(eV)	$\epsilon \times 10^{14}$ at 2σ	$L_{\rm MCP}/L_\odot(\%)$	m_f(eV)	$\epsilon \times 10^{14}$ at 2σ	$L_{\rm MCP}/L_\odot(\%)$
0	2.2	1.5	150	460	-
25	2.2	1.5	175	460	2.3
50	2.6	2.0	200	500	2.4
75	3.4	2.7	316	600	2.3
100	4.5	2.6	1000	1090	2.3
125	8.7	2.6	3160	7720	2.8

Table 5.3: Bounds on ϵ at 2σ CL and the corresponding luminosity for different values of m_f. For $m_f = 150$ eV, the limit of $m_f = 175$ eV is taken (see the main text).

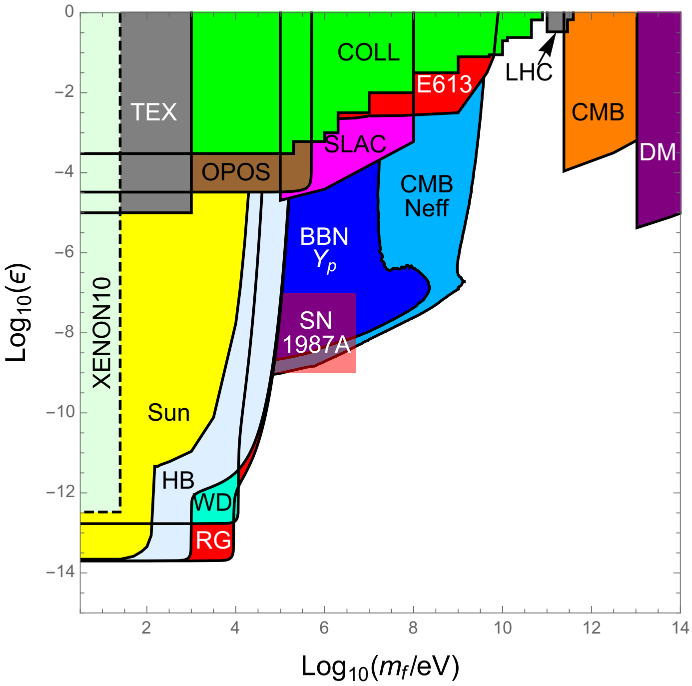

Figure 5.20: Summary of constraints on fermionic MCPs in the mass/minicharge plane. The result of this work is depicted in yellow. CMB and BBN bounds from Vogel and Redondo (2014) using 2015 Planck data Ade et al. (2015), the collider bounds (COLL) from Davidson et al. (1991); Davidson et al. (2000). The remaining bounds are from DM Davidson et al. (1991), CMB Dubovsky et al. (2004), LHC Jaeckel et al. (2013), SLAC Prinz et al. (1998), OPOS Badertscher et al. (2007), TEX Gninenko et al. (2007), E613 Soper et al. (2014), and HB, WD, RG Davidson et al. (2000); Vogel and Redondo (2014). *This figure is courtesy of Hendrik Vogel.*

5.6 Discussion

In this chapter, the solar limits on the axion-photon coupling constant, the product of the kinetic mixing and mass of the HPs and the charge and mass of the MCPs have been revised by combining different solar constraints. This have been done by using a statistical approach that accounts for both experimental and theoretical errors and uses the best fit model that lets the composition free in order that the solar abundance problem do not bias the final results. Previous works on the subject have often relied on setting an upper limit to the total energy loss carried away from the Sun expressed as a fraction of the solar photon luminosity $L_\odot$. Then it is useful to present the results as a function of $L_i/L_\odot$. Also, $L_i/L_\odot$ sets a natural scale for comparing the effects of the losses from different particles with each other.

In Figure 5.21, global results for axions, HPs and MCPs are presented again (only

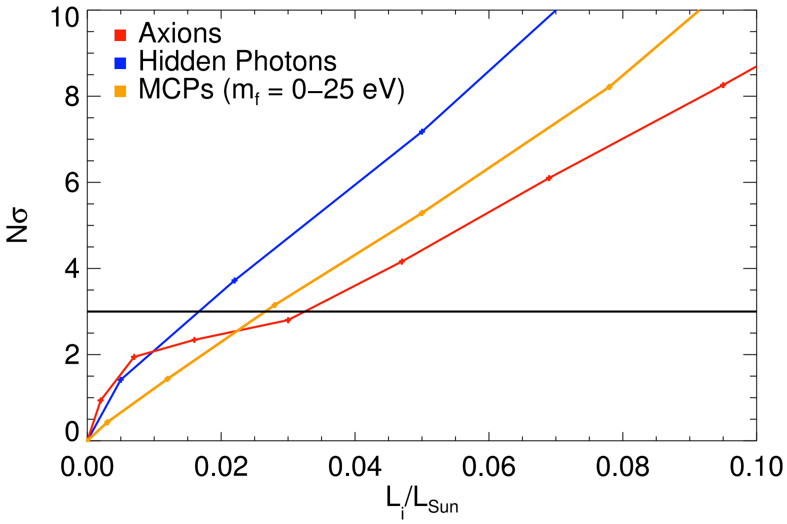

Figure 5.21: $\Delta\chi^2$ and $N\sigma$ as function of the luminosity contribution of axions (red line), HPs (blue line) and MCPs with a mass in the range $m_f = 0 - 25eV$ (orange).

---

for the AGSS09met sets of models) but now as a function of $L_i/L_\odot$. For the MCP case, the results from the case where the most restrictive limits are found ($m_f = 0-25$ eV) have been plotted. A comparison of the results at 3-σ is done and it is possible to observe that for HPs, the contribution on the solar luminosity is of only about 2%, for MCPs around 2.5% while for the axions this value is around 3%. For comparison, in Gondolo and Raffelt (2009) the upper limit to axions is set by demanding $L_a < 0.1\mathrm{L}_\odot$. Here it is shown that a much more restrictive limit can actually be imposed.

Comparing the results for axions and HPs, it is interesting to note that a smaller fraction of $\mathrm{L}_\odot$ is required for HPs than for axions to set a given confidence level. This can be explained by considering how the observables change in both cases. In Figure 5.10 it has been seen that the changes on the solar sound speed profile are localized towards the center for the axion case while for the HPs the whole profile is affected. Also, it is possible to find a steeper relation between the energy lost through HPs and the change in $\Phi(^8\mathrm{B})$ than in the case of axions. All this contributes to placing somewhat stronger constraints for HPs than for axions in terms of the fraction of energy that is lost through these channels. Same conclusions apply for the MCP case, where different values of the masses are related to different energy loss emissions distributions, and then, different luminosity limits for each of the cases (see right panel of Figure 5.19).

Solar bounds on the coupling of hadronic axions to photons are not the most restrictive ones. However, this is a well-studied subject and it allows testing the performance of the new global statistical approach by comparing this findings to results from previous investigations. The first work that placed a limit on the axion-photon coupling constant using helioseismology is Schlattl et al. (1999), where a set of solar models was calculated including effects of axions self-consistently. The bound $g_{10} < 10$ was found by restricting the axion luminosity at $L_a < 0.2L_\odot$. For this bound, the deviations of the sound speed profile are 0.8% at $R = 0.1R_\odot$. More recently, Gondolo and Raffelt (2009) found $g_{10} < 7$ by using the experimental $\Phi(^8\mathrm{B})$ determination and, based upon its agreement with SSMs values, assuming that the actual solar flux cannot exceed the SSM prediction by more than 50% (roughly equivalent to a limit of 3σ model uncertainty). As mentioned before, this is comparable to setting the limit $L_a < 0.1\mathrm{L}_\odot$. A different approach has been followed in Maeda and Shibahashi (2013), where a seismic model is used to determine the effect of the axions. Seismic models are static models of the Sun which, by construction, reproduce the sound speed profile. They do not account for the evolutionary history which determines the chemical composition profile of the present Sun. Axions were included in the seismic models by adding the energy loss in the energy equation and modifying the central temperature and the abundances with respect the standard case so that the sound speed and solar luminosity were recovered. The constraint on g_{10} is derived from the experimental value of $\Phi(^8\mathrm{B})$ and it is set to $g_{10} < 2.5$ at a 1σ CL. To compare, from Figure 5.15 it is possible to set limit at a 1σ CL around $g_{10} < 2.0$. In comparison to these works, the current result $g_{10} < 4.1$ to a 3-σ CL is much more restricting. This is a direct consequence of the global approach of combining consistently helioseismic and solar neutrino constraints. As discussed in the previous section, the sound speed profile is the most restrictive observational constraint. If the analysis is restricted in using ν+`conv`, a $g_{10} < 5.5$ upper limit is found and a corresponding $L_a < 0.06\,\mathrm{L}_\odot$ limit on the axion luminosity.

Using the limits on the parameters found for axions, the present upper limits are presented for the respective fluxes on Earth expected in direct detection experiments such as CAST or IAXO. Using Eq. 15 from Andriamonje et al. (2007) and the limit $g_{10} = 4.1$ obtaining $\Phi_a \sim 6.0 \cdot 10^{12}\mathrm{cm}^{-1} \cdot \mathrm{s}^{-1}$. During the CAST data taking, the limiting flux has been found to be more restrictive for a wide range of axion masses. Andriamonje et al. (2007) find a limit for the axion-photon coupling constant of $g_{10} = 0.88$ for $m_a \lesssim 0.2\mathrm{eV}$ corresponding to $\Phi_a \sim 2.9 \cdot 10^{11}\mathrm{cm}^{-2} \cdot \mathrm{s}^{-1}$ and in Arik et al. (2009) they find an upper limit of $g_{10} = 2.17$ for the mass range of $0.02 < m_a < 0.39\mathrm{eV}$ corresponding to a solar flux of $\Phi_a \sim 1.8 \cdot 10^{12}\mathrm{cm}^{-2} \cdot \mathrm{s}^{-1}$. As already stated in the introduction, the current bound does not improve the best limits on $g_{a\gamma}$ but it confirms that, at the CAST limits, it is not expected that axions would have a measurable effect on helioseismology and solar neutrinos.

HPs have a younger history than axions in the literature, and previous bounds on the kinetic mixing parameter based on solar models are limited to An et al. (2013) and Redondo and Raffelt (2013). In the first case, a very conservative limit was derived by assuming that $L_{hp} < \mathrm{L}_\odot$, leading to $\chi m < 1.4 \cdot 10^{-11}$eV. In the second, the more restrictive upper bound $\chi m < 4 \cdot 10^{-12}$eV for masses smaller than $m < 0.3$ keV was derived from the condition $L_{hp} < 0.1\,\mathrm{L}_\odot$ and Equation 5.10. This limit has been improved by including the sound speed profile in the analysis and a more consistent treatment of uncertainties in this global approach. As discussed above, the limit $\chi m < 1.8 \cdot 10^{-12}$eV is obtained from models for which $L_{hp} < 0.02\,\mathrm{L}_\odot$, a much smaller fraction than employed in previous works. Using Eqs 4.10 and 4.11 from Redondo and Raffelt (2013), the upper limit for the flux on the Earth is $\Phi_{\mathrm{HP}} \sim 3.2 \cdot 10^{14}\mathrm{cm}^{-2} \cdot \mathrm{s}^{-1}$ corresponding to $\chi m < 1.8 \cdot 10^{-12}$eV.

For MCPs this is the first time the the Sun is used to place constraints on their properties, with a restrictive bound of $\epsilon = 2.2 \cdot 10^{-14}$ at 2σ for $m_f = 0 - 25$ eV. For higher masses the derived bound is much weaker and not competitive with the constraints placed by other stellar objects and experiments. The expected flux on the Earth when using the limit at 3σ of $L_{MCP}/L_\odot = 0.026$ (see Figure 5.21) and $m_f = 0$ eV is $\Phi_{\mathrm{HP}} \sim 1 \cdot 10^{13}\mathrm{cm}^{-2} \cdot \mathrm{s}^{-1}$.

It is important to remark that the results presented in this chapter are not affected by the ongoing *solar abundance problem*. Indeed, in this work the role of the composition used in solar models have been systematically studied for the constraints on $g_{a\gamma}$, χm and $\epsilon(m_f)$ by constructing a BFM for each models, letting the composition and marginalizing it for each value of g_{10}, χm and ϵ. The results showed that the values for the composition are more or less constant with increasing g_{10} χm and ϵ and that the values are closer to the GS98, implying that models with this composition are a good representation of the actual thermal stratification of the Sun, as discussed in the previous chapters.

As shown in the literature (Christensen-Dalsgaard et al., 2009; Villante, 2010; Villante et al., 2014), and discussed in previous chapters, an equally good BFM could be achieved by letting the radiative opacity vary instead of the solar composition. Keeping this in mind one concludes then that the current limits are, to a good approximation, independent of the composition. This also indicates that exotic energy losses cannot be advocated as a possible explanation of the disagreement between solar models with AGSS09met composition and helioseismic data. There are different ways in which to move forward. This global approach represents a qualitative step forward in combining different sources of solar data for using the Sun as a laboratory for particle physics. But further data is available which have not been considered. For example, frequency separation ratios can enhance the constraining power of helioseismology. The difficulty is that correlations among different helioseismic observables have to be taken into account. It has already been acknowledged that even the radial profile of the sound speed presents correlations that have not yet been quantified in the literature. It is important to notice that current uncertainties are dominated by model uncertanties. Moreover, there is not a unique dominant error source. For example, the 12% error in the theoretical $\Phi(^8\mathrm{B})$ results from 5% error in S_{17} and 7% from radiative opacities. If one includes solar composition as a source of uncertainty, this contributes a further 9%. Thus, reducing modeling errors is a difficult task. A similar situation happens for the sound speed profile, where the solar composition and the radiative opacities play comparable roles. On the other hand, the $\Phi(pp)$ and $\Phi(pep)$ fluxes have the interesting property that their theoretical errors are small, 0.6% and 1.2% respectively and therefore experimental determinations would place constraints on non-standard energy losses almost completely independent on solar modeling uncertainties. Recently Bellini et al. (2014b), Borexino has directly measured the solar $\Phi(pp)$ for the first time, with an observational error of $\sim$ 10% and the solar $\Phi(pep)$ Bellini et al. (2012) with an observational error of $\sim$ 20%. Due to these large experimental errors, they have not been included as observational inputs because they would not contribute to the derived limits. In a future generation of experiments, reaching a 1% error in such measurements could provide a cross comparison between the solar photon and neutrino luminosities.

5.7 Summary and conclusions

In the previous sections the main results for the three cases study (axions, HPs and MCPs) have been presented and discussed . To summarize, the main conclusions of this chapter are enumerated.

1. The statistical approach presented in Villante et al. (2014) has been extended as described in Chapter 4, by combining in a consistent manner helioseismic and solar neutrino data for using the Sun for particle physics studies. In order to avoid that the *solar abundance problem* could bias the final result, the surface abundances of the Sun are considered as free parameters in the present analysis (BFMs).

2. As a test case the first application of the method have been to the well studied case of hadronic axions and showed that previous solar bounds on the axion-photon coupling can be improved with the methodology used. A strong upper limit of $g_{a\gamma} = 4.1 \cdot 10^{-10}$GeV have been derived at a 3σ CL, almost a factor of two better than previous results.

3. After testing the statistical method with axions, the same procedure have been used to place bounds on the properties of HPs. This case is particularly interesting because the Sun offers the most restrictive limits over a wide range of photon masses. A new upper limit have been derived for the product of the kinetic mixing parameter and mass $\chi m = 1.8 \cdot 10^{-12}$eV for a HP mass in the range $m \lesssim 0.3$ keV, more than a factor of 2 improvement over previous results (Redondo and Raffelt, 2013) and better than the direct detection constraint of XENON10 (An et al., 2013).

4. The third case study are the MCPs from which a bound of $\epsilon < 2.2{\times}10^{-14}$ (95% CL) for $m_f \lesssim 25$ eV have been obtained. This result is comparable to previous limits from the cooling of globular cluster stars (Davidson et al., 2000), while at the same time it is better understood and takes theoretical and observational errors into account.

5. By comparing in detail results from axions, HPs and MCPs it is possible to conclude that relations between *dark* luminosities and observables such as $\Phi(^8\mathrm{B})$, (see Equation 5.10), depend on the type of particle under consideration and should be employed consistently to avoid biasing results.

6. Finally, it has been proven that including an extra energy loss due to weakly interacting light particles in solar models with AGSS09met composition degrades the agreement between models and helioseismology, and thus does not help in mitigating the *solar abundance problem.*

7. The approach is of course general and will be extended to account for correlations among observables, a fact hitherto neglected in the literature, that will allow including additional helioseismic constraints as the small separation ratios among others. Another future goal is to include possible future observations as the Φ(pp), when the observational errors are reduced or g-modes if finally detected.

Chapter 6

Summary and conclusions

This thesis is focused on the study of the Standard Solar Models and how they can be used to test non standard physics. More in particular, the SSMs have been updated presenting a new generation o SSMs (B16) and this update has been complemented with a new error evaluation. This includes a new treatment for this errors in radiative opacities, which are a key ingredient for solving the *solar abundance problem*. An exhaustive study of how different available opacity calculations affect SSMs is also part of this thesis. Current uncertainties in the solar composition and opacities can be overcome for studies of particle physics that do not depend on a detailed knowledge of the solar interior composition. For this purpose, the Best Fit Model, a solar model that better reproduces the observations using realistic evolutionary inputs, is introduced. Later, the BFM has been used to place the most restrictive solar constraints on weakly interacting light particles (e.g axions, hidden photons and minicharged particles).

In this chapter the main conclusions and results obtained in each of the chapters are reviewed and summarized, as well as the future steps that will naturally follow this work.

6.1 Results

SSMs are useful models for describing the solar interior, and at the same time provide a deeper knowledge on other disciplines, as stellar evolution, particle physics and also to test non-standard physics. In Chapter 2 the previously existing SSMs have been updated. The models have been constructed using two different compositions, GS98 and AGSS09met. The updates are related to the use of EoS and to the update of some of the cross sections used as S_{11}, S_{17} and S_{114}. A possible update of S_{34} have also been studied and discussed, and although the new values are not finally used, the relevance of having accurate and precise (to better than a few percent) determinations of the key nuclear cross sections used in solar models has been discussed in some detail. The new generation, B16, of SSMs have values of $\Phi(^7\mathrm{Be})$ and $\Phi(^8\mathrm{B})$ reduced about 2% and CN fluxes of the order of 6% being compatible with models with both GS98 and AGSS09met compositions. If S_{34} value is reduced, as it is recommended by some recent work, the final neutrino fluxes would favor GS98 composition over AGSS09met. By using the helioseismic observations, exactly the same conclusions than for the old generations of solar models are obtained; the agreement is much better for the old GS98 than for AGSS09met (*solar abundance problem*).

The experimental errors of the sound speed have been also updated, including the most recent inversion, reference model and observational errors, as well as the errors of the models by performing new Monte-Carlo simulations. Finally, the main contribution sources to the error for each of the outputs of the SSMs has been exhaustively studied. The most relevant contribution of this part of the work is the new flexible method based on opacity kernels to study the effects of radiative opacities uncertainties. Basically, the radiative opacitites are in the spotlight as one of the most attractive and neat solution of the *solar abundance problems*. Therefore, opacity kernels have been used in order to include, in a flexible way, the contribution of opacities to the model errors. This is useful because the uncertainties associated to the opacities are still unknown, and therefore, it is important to have a method to test different models and to be able to include new opacity results that might become available in the future. For this particular case, the choice of opacity errors is motivated by several recent works that suggested an increase of the opacity at the base of the convective envelope and for previous works that recommended a tilt on the uncertainty opacity error in order to mitigate the helioseismic discrepancies. For all that, a linear function is used with an error of 2% at the solar center and a 7% at the base of the convective envelope.

Finally, with the new B16-SSMs models and the updated errors the agreement of the models with the observations have been studied in detail. The results are consistent with the existing *solar abundance problem*, the global agreement of GS98 with observations is at 2.7σ while for AGSS09met is 4.7σ. The fair performance of AGSS09met can be understood by terms of a global disagreement related to the *solar abundance problem* while it is found that the bad performance of GS98 is related to the poor modeling at the base of convective envelope, the high correlation between different sound speed points and the rigid choice of opacity uncertainties. Related to the last, it has been proven that the choice of a linear function is too rigid to accommodate a better fitting, giving the hint that a more complicated function for the opacity uncertainties could alleviate the discrepancy at a greater level.

Motivated by the fact that radiative opacitites could be a possible solution to the *solar abundance problem* and by the poor performance of a linear uncertainty function to bring the models back to an agreement with heliosesimology, in Chapter 3 SSMs computed with opacities from different sources have been studied. This is necessary to understand better the available radiative opacities and it is a previous step before studying more complicated functions for the radiative opacity uncertainties. In this work, the results are presented for models calculated by using OP, OPAL, OPAS and OPLIB opacity tables and different solar composition (GS98, AGSS09met, AGSS09ph and AGSS15ph). First, the resulting κ_{ross} with respect to OP (the opacities used in Chapter 2) are compared. It is possible to see that for OPAL, the maximum difference is of about 2%, for OPAS 5% and for OPLIB large reduction up to 10% is found in the center that lead to lower and unrealistic values of neutrino fluxes among other effects. Calibrating the SSMs with these different opacity tables it has been possible to extract the following conclusions. For OPAL the global agreement with respect to OP is improved, although the differences of the neutrino fluxes and heliosesimic quantities are small, and that, when looking it by eye, the shape of the sound speed profile is similar. Therefore, this improvement with respect to OP comes mainly to the fact that when using OPAL opacities, it is possible to find a combination of input parameters within their errors that brings the model closer to the observations. For OPAS a better agreement with respect to OP is obtained, with a notable improvement on $\mathrm{R_{CZ}}$ agreement and a reduction of the peak of the sound speed profile at the base of the convective envelope. Is worth mentioning that for OPAS, the only tables are available for AGSS09ph, and therefore, in order to exhaustively study and understand the effects of OPAS on SSMs, it is important to have the corresponding tables for all the other solar compositions. The last opacity table to mention is OPLIB, that have a final global agreement with the observations at levels of OP models. Although the similar global agreement, the low values of neutrino fluxes $(\Phi(^8\mathrm{B})_{OPLIB}/\Phi(^8\mathrm{B})_{OP} \sim 0.80)$ and the low and unrealistic values obtained for the surface helium $(\mathrm{Y_S}_{AGSS09ph} = 0.2278)$ allow to conclude that the radiative opacities, especially at the solar center, are too low to fit the current observations and by the moment, unreliable to construct solar models. With all that information, it is possible to conclude that in order to have a better agreement with the observations, radiative opacities at the center should not change much in order to keep the current agreement of the models with the observed solar fluxes. About the agreement with helioseismic observations, if they have to come from changes on the radiative opacities, changes on the shape of the opacity profile are necessary and results from OPAL and OPAS can give a hint of which is the direction to go.

One of the main goals of this thesis was to use the Sun and all the available information to study the effects of exotic particles and to be able to place limits on the properties of these particles. To this purpose, in Chapter 4 the Best Fit Model is presented. The BFM is a model that reproduces, in the best possible way, the solar observations using realistic input parameters and letting the composition free in order to obtain a model independent of the *solar abundance problem*. The final BFM does not depend on the reference model (e.g. GS98 or AGSS09met) and therefore is very useful to test non-standard physics, as long as it does not depend on the detailed metal content of the Sun. The process of letting the composition free is done by grouping the elements in two groups (refrectoris and volatiles). This choice have advantages and disadvantages. On one hand, to minimize for two parameters avoids unrealistic values for individual elements that are sub-dominant, because the solar data do not allow for a more detailed discrimination and the results could be degenerate. On the other hand, the use of only two parameters can bring tensions with the radiative opacities, mainly when a linear function for the uncertainties is used. For example, if the linear function is used, the final BFM does not improve the agreement of GS98 model, because as it has been mentioned previously it is too rigid to mitigate the oscillatory behavior seen in the sound speed profile. If the difference between OP-OPAL uncertainty is used as opacity errors, the combination with the two free composition parameters is able to mitigate the oscillatory behavior of the sound speed profile, although the bump at the base of the convective envelope remains practically the same. Therefore, the interest is on having a model independent of the composition of the reference that better reproduces the thermal stratification of the Sun, the BFM constructed with OP/OPAL differences for the opacity errors has been used. It is important to mention that the final BFM is close to GS98 SSMs, in consistency with the *solar standard model*. That does not mean that the composition of the BFM or the opacities are correct but the combination leads to a good representation of the thermal stratification of the Sun. We finally have shown that the two methods to calculate the BFMs (linear approximation and complete solar calibrations) are equivalent. Therefore, the linear approximation can be used with the advantage of the low computational time necessary and the flexibility of the method.

In Chapter 5 the previous results on standard solar models and best fit models have been used in order to provide bounds on different exotic particles, in particular axions, hidden photons and minicharged particles, using all the available information of the Sun. The bounds obtained are: for axions $g_{10} < 4.1$ at 3 C.L., for hidden photons $\chi m < 1.8 \cdot 10^{-12}$ eV at 3 C.L and for minicharged particles, $\epsilon = 2.2 \cdot 10^{-14}$ at 2 CL for $m_f = 0 - 25$ eV. For all of them the obtained bounds are the most restrictive solar bounds available. For HP and MCPs, these limits are the most overall restrictive bounds. For the case of the axions, the solar bounds are less restrictive than for other stellar sites and experiments. The fact that the well tested axions give the most restrictive solar limit up to now show the potential of the statistical method. As BFMs are used for each of the cases, it is possible to safely conclude that our results are independent on the *solar abundance problem*. Moreover, it is possible to conclude that the inclusion of weakly interacting light particles does not offer a solution to the *solar abundance problem* and, in fact, it worsens the agreement between solar models and data. Finally, the importance of studying each class of particles separately has been proven, because the final constraints depend not only on the total amount of energy lost by these particles, but also on the emissivity profile in the solar interior that can modify the structure differently.

Summarizing, in this thesis updated solar models have been constructed, the role of the radiative opacities on solar models has been studied and understood giving the motivation to find a method non-dependent of the *solar abundance problem* to finally use it to give constraints on exotic particles.

6.2 Future work

There are several possibilities to continue this work in the future. The principal topic to go further would be related to the radiative opacities. Associated to that, there is the possibility to explore more deeply different options of radiative opacities uncertainties that would go on the direction of solving the *solar abundance problem*. Motivated by the good performance of OPAL and OPAS opacity tables and the rigidness of the linear function, there is the idea that the changes on the opacities should be a more complicated function. The determination of this function could be done by using more complete statistical analysis, such as modeling the error function by means of a non-parametric Gaussian process. The final goal would be to be able to reconstruct an effective solar opacity profile from the helioseismic and solar neutrino data without imposing a prior functional form to it. To have a better understanding of how the radiative opacities should change in order to recover the agreement with the observations is important to give an idea of the direction that they should take.

Then, theoretical determinations of radiative opacities, could help understand if the changes required are plausible or if the radiative opacities are not the solution of *solar abundance problem*. Therefore, it is mandatory to not forget other non-standard solutions for the *solar abundance problem* and possible non-standard physics missing in solar models should be further explored and one should keep in mind that the solution could be related to a combination of several factors.

It is important to remark the importance of a better understanding of the *solar abundance problem*, that would have an impact on stellar physics but also on the study of particle physics, because even in the cases where the emissivity does not depend on the detailed composition, reliable solar models would imply more robust results. Also, a better understanding will have an impact on cases where the detailed composition of the Sun matters, e.g. capture of dark matter.

An improvement related to the Best Fit Model would be the inclusion of correlations among observational data, specially related with the frequencies and inversions. That would improve the reliability of the models and it would open the possibility to include some additional data in a combined statistical analysis, such as the frequency ratios, that are so far excluded because of unknown correlations among them and the sound speed profile.

It is important to be open to possible future experiments that could improve the present results. For example, the detection of CN fluxes would give extra observables to test the solar models while at the same time will give very valuable information about the solar composition of the Sun. Another potential future observations are the detection of g-modes, that will give very valuable information of the innermost solar core.

Finally, it is important to remark that the real future work is to be aware and open to future new experiments, observations, applications or new physics that could bring solar models as close to the reality as possible in order to keep them as a powerful tool for a broad range of topics in physics and astrophysics.

Appendix A

Power-laws

In this appendix the updated log-derivatives $\alpha_{Q,I}$ "power-laws" (see Section 2.4.2) are presented for the different neutrino fluxes and other relevant parameters in Table A.1 for AGSS09met and Table A.2 for GS98. In Figure A.1 the results for the sound speed profile are presented.

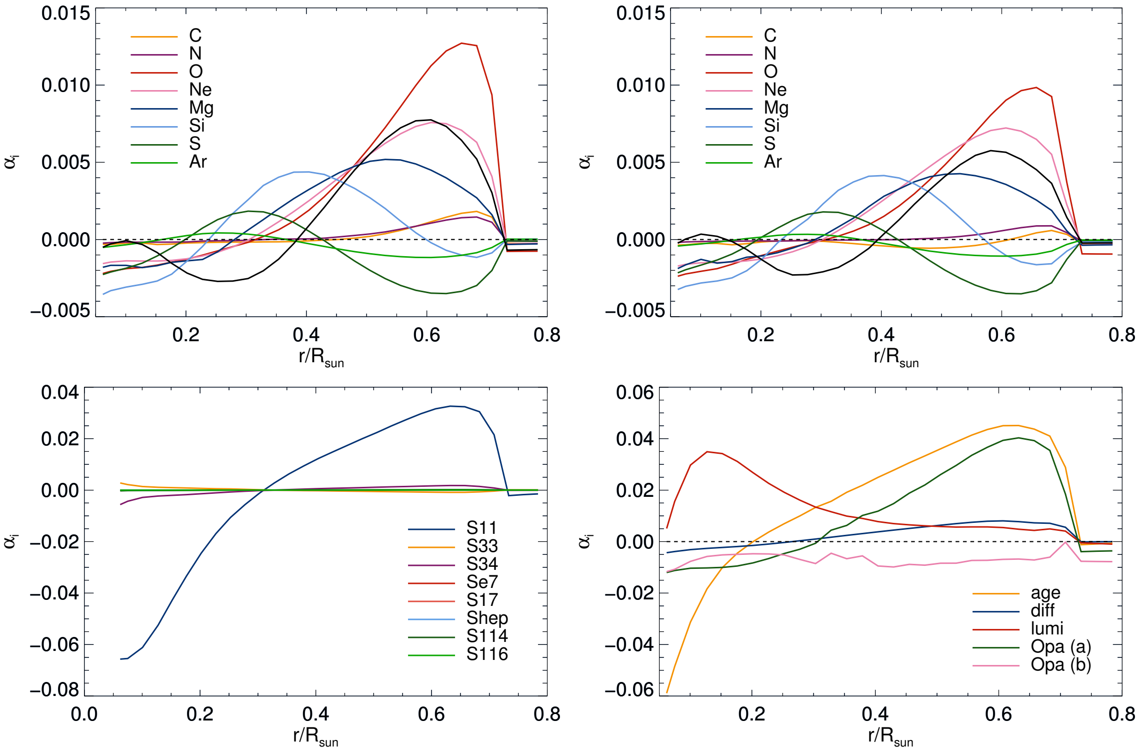

Figure A.1: Log-derivatives $\alpha_{Q,I}$. Top panels represent the power-laws of the composition for AGSS09met (left) and GS98 (right). The left bottom panel shows the parameters for the nuclear cross sections while in the right panel the power-laws for some relevant parameters as the age, diffusion, luminosity or opacity plotted. The results in the bottom panel are equivalent for both compositions.

	$\Phi(\mathrm{pp})$	$\Phi(\mathrm{pep})$	$\Phi(\mathrm{hep})$	$\Phi(^{7}\mathrm{Be})$	$\Phi(^{8}\mathrm{B})$	$\Phi(^{13}\mathrm{N})$	$\Phi(^{15}\mathrm{O})$	$\Phi(^{17}\mathrm{F})$	α_{MLT}	$\mathrm{Y_{ini}}$	$\mathrm{Z_{ini}}$	$\mathrm{Y_S}$	$\mathrm{Z_S}$	$\mathrm{R_{CZ}}$
$\mathrm{S_{11}}$	0.090	-0.236	-0.115	-1.069	-2.716	-2.037	-2.944	-3.114	0.249	0.064	-0.101	0.138	-0.042	-0.062
$\mathrm{S_{33}}$	0.030	0.043	-0.466	-0.446	-0.430	0.026	0.019	0.016	-0.007	-0.003	0.002	-0.004	0.001	0.002
$\mathrm{S_{34}}$	-0.059	-0.086	-0.073	0.892	0.859	-0.053	-0.040	-0.036	0.013	0.008	-0.004	0.009	-0.003	-0.003
$\mathrm{S_{e7}}$	0.000	0.000	0.000	0.001	-0.999	-0.000	-0.000	0.000	0.000	0.000	0.000	0.000	0.000	0.000
$\mathrm{S_{17}}$	0.000	0.000	0.000	-0.001	1.028	0.000	-0.000	-0.000	0.000	0.000	0.000	-0.000	0.000	0.000
$\mathrm{S_{hep}}$	0.000	-0.000	1.000	-0.000	-0.000	0.000	-0.000	-0.000	0.000	0.000	0.000	0.000	0.000	0.000
$\mathrm{S_{114}}$	-0.004	-0.007	-0.004	-0.002	0.003	0.714	1.051	0.003	0.001	0.000	-0.000	0.001	-0.000	0.000
$\mathrm{S_{116}}$	0.000	0.000	0.000	0.000	0.000	0.000	0.000	0.527	0.000	0.000	0.000	0.000	0.000	0.000
Age	-0.077	0.003	-0.119	0.795	1.386	0.809	1.334	1.438	0.345	-0.141	0.108	-0.198	0.058	-0.080
Lumi	-0.009	-0.013	-0.029	0.106	0.218	0.263	0.306	0.324	0.064	0.024	0.090	-0.061	0.019	-0.014
Diff	0.810	1.049	0.172	3.517	7.055	4.311	5.994	6.461	1.174	0.398	-0.088	0.373	-0.113	-0.016
C	-0.004	-0.009	-0.007	0.003	0.026	0.872	0.818	0.028	0.039	-0.005	0.176	-0.004	0.175	-0.005
N	-0.001	-0.002	-0.002	0.002	0.005	0.139	0.201	0.004	0.013	-0.001	0.050	0.001	0.050	-0.003
O	-0.004	-0.006	-0.020	0.053	0.112	0.054	0.083	1.092	0.110	0.014	0.409	0.027	0.415	-0.030
Ne	-0.004	-0.004	-0.014	0.043	0.082	0.035	0.056	0.062	0.029	0.022	0.073	0.028	0.078	-0.010
Mg	-0.003	-0.003	-0.017	0.055	0.106	0.049	0.076	0.083	0.014	0.030	0.030	0.035	0.034	-0.005
Si	-0.012	-0.017	-0.034	0.111	0.195	0.090	0.141	0.154	-0.009	0.063	0.029	0.064	0.029	0.005
S	-0.008	-0.016	-0.026	0.078	0.141	0.067	0.103	0.112	-0.024	0.048	0.010	0.045	0.010	0.007
Ar	-0.002	-0.004	-0.006	0.017	0.030	0.015	0.023	0.025	-0.006	0.010	0.002	0.009	0.002	0.001
Fe	-0.018	-0.054	-0.061	0.208	0.486	0.242	0.369	0.405	-0.006	0.082	0.055	0.087	0.058	-0.009
κ_{a}	-0.084	-0.270	-0.400	1.33	2.863	1.592	2.220	2.427	-0.345	0.614	-0.186	0.608	-0.201	0.008
κ_{b}	-0.019	-0.001	-0.061	-0.107	0.380	0.658	0.314	0.456	0.020	0.214	-0.114	0.255	-0.085	-0.079

Table A.1: Log-derivatives $\alpha_{Q,I}$ for AGSS09met.

	$\Phi(pp)$	$\Phi(pep)$	$\Phi(hep)$	$\Phi(^7Be)$	$\Phi(^8B)$	$\Phi(^{13}N)$	$\Phi(^{15}O)$	$\Phi(^{17}F)$	α_{MLT}	Y_{ini}	Z_{ini}	Y_S	Z_S	R_{CZ}
S_{11}	0.101	-0.223	-0.104	-1.034	-2.664	-2.115	-2.916	-3.071	0.238	0.065	-0.096	0.131	-0.042	-0.059
S_{33}	-0.000	0.000	-0.000	-0.000	-0.000	-0.000	-0.000	-0.000	0.000	0.000	0.000	0.000	0.000	0.000
S_{34}	-0.065	-0.094	-0.080	0.876	0.834	-0.060	-0.049	-0.045	0.013	0.008	-0.004	0.010	-0.003	-0.003
S_{e7}	-0.000	0.000	-0.000	0.001	-0.999	-0.000	-0.000	0.000	0.000	0.000	0.000	0.000	0.000	0.000
S_{17}	0.000	0.000	0.000	-0.001	1.029	0.000	0.000	0.000	0.000	0.000	0.000	-0.000	0.000	0.000
S_{hep}	0.000	0.000	1.000	0.000	0.000	0.000	0.000	0.000	0.000	0.000	0.000	0.000	0.000	0.000
S_{114}	-0.006	-0.010	-0.006	-0.002	0.005	0.752	1.053	0.005	0.001	0.001	-0.000	0.001	-0.000	0.001
S_{116}	0.000	0.000	-0.000	0.000	0.000	0.000	0.000	0.526	0.000	0.000	0.000	-0.000	0.000	0.000
Age	-0.080	0.000	-0.129	0.762	1.342	0.886	1.351	1.449	0.346	-0.137	0.113	-0.197	0.063	-0.092
Lumi	-0.010	-0.014	-0.031	0.104	0.218	0.269	0.309	0.326	0.063	0.021	0.088	-0.060	0.019	-0.014
Diff	0.771	0.998	0.149	3.462	6.961	4.440	5.955	6.395	1.166	0.375	-0.089	0.351	-0.113	-0.031
C	-0.006	-0.014	-0.008	0.002	0.026	0.862	0.816	0.028	0.036	-0.007	0.167	-0.006	0.166	-0.003
N	-0.001	-0.002	-0.002	0.002	0.008	0.148	0.202	0.008	0.012	-0.001	0.048	-0.000	0.049	-0.003
O	-0.005	-0.011	-0.023	0.056	0.126	0.072	0.102	1.110	0.106	0.010	0.438	0.019	0.442	-0.023
Ne	-0.004	-0.005	-0.018	0.051	0.099	0.050	0.073	0.080	0.029	0.024	0.085	0.031	0.090	-0.012
Mg	-0.002	-0.001	-0.016	0.055	0.097	0.050	0.072	0.079	0.010	0.028	0.027	0.032	0.031	0.000
Si	-0.010	-0.013	-0.035	0.105	0.199	0.110	0.155	0.168	-0.013	0.059	0.023	0.060	0.023	0.005
S	-0.006	-0.012	-0.025	0.071	0.129	0.072	0.100	0.108	-0.023	0.042	0.008	0.040	0.008	0.005
Ar	-0.001	-0.004	-0.006	0.017	0.033	0.019	0.026	0.028	-0.007	0.010	0.002	0.009	0.001	0.001
Fe	-0.018	-0.057	-0.064	0.201	0.475	0.259	0.369	0.403	-0.015	0.080	0.046	0.084	0.048	-0.009
κ_a	-0.084	-0.270	-0.400	1.33	2.863	1.592	2.220	2.427	-0.345	0.614	-0.186	0.608	-0.201	0.008
κ_b	-0.019	-0.001	-0.061	-0.107	0.380	0.658	0.314	0.456	0.020	0.214	-0.114	0.255	-0.085	-0.079

Table A.2: Log-derivatives $\alpha_{Q,I}$ for GS98.

Bibliography

J. N. Abdurashitov, V. N. Gavrin, S. V. Girin, et al. Measurement of the solar neutrino capture rate with gallium metal. *Phys. Rev. C*, 60(5):055801, November 1999. doi: 10.1103/PhysRevC.60.055801.

B. Acharya, B. D. Carlsson, A. Ekstrom, C. Forssen, and L. Platter. Uncertainty quantification for proton-proton fusion in chiral effective field theory. *Phys. Lett.*, B760:584–589, 2016. doi: 10.1016/j.physletb.2016.07.032.

P. A. R. Ade et al. Planck 2015 results. XIII. Cosmological parameters. 2015.

E. G. Adelberger, A. García, R. G. H. Robertson, et al. Solar fusion cross sections. II. The pp chain and CNO cycles. *Reviews of Modern Physics*, 83:195–246, January 2011. doi: 10.1103/RevModPhys.83.195.

C. Aerts, J. Christensen-Dalsgaard, and D. W. Kurtz. *Asteroseismology*. 2010.

B. Aharmim, S. N. Ahmed, A. E. Anthony, et al. Combined analysis of all three phases of solar neutrino data from the Sudbury Neutrino Observatory. *Phys. Rev. C*, 88(2):025501, August 2013. doi: 10.1103/PhysRevC.88.025501.

Q. R. Ahmad, R. C. Allen, T. C. Andersen, et al. Direct Evidence for Neutrino Flavor Transformation from Neutral-Current Interactions in the Sudbury Neutrino Observatory. *Physical Review Letters*, 89(1):011301, July 2002. doi: 10.1103/PhysRevLett.89.011301.

D. S. Akerib, S. Alsum, C. Aquino, et al. First searches for axions and axion-like particles with the LUX experiment. *ArXiv e-prints*, April 2017.

C. W. Allen. *Astrophysical quantities*. 1973.

H. An, M. Pospelov, and J. Pradler. Dark Matter Detectors as Dark Photon Helioscopes. *Phys. Rev. Lett.*, 111:041302, 2013. doi: 10.1103/PhysRevLett.111.041302.

H. An, M. Pospelov, and J. Pradler. New stellar constraints on dark photons. *Physics Letters B*, 725:190–195, October 2013. doi: 10.1016/j.physletb.2013.07.008.

S. Andriamonje, S. Aune, D. Autiero, et al. An improved limit on the axion photon coupling from the CAST experiment. *JCAP*, 4:010, April 2007. doi: 10.1088/1475-7516/2007/04/010.

S. Andriamonje et al. An Improved limit on the axion-photon coupling from the CAST experiment. *JCAP*, 0704:010, 2007. doi: 10.1088/1475-7516/2007/04/010.

J. Angle, E. Aprile, F. Arneodo, et al. Search for Light Dark Matter in XENON10 Data. *Physical Review Letters*, 107(5):051301, July 2011. doi: 10.1103/PhysRevLett.107.051301.

C. Angulo, M. Arnould, M. Rayet, et al. A compilation of charged-particle induced thermonuclear reaction rates. *Nuclear Physics A*, 656:3–183, August 1999. doi: 10.1016/S0375-9474(99)00030-5.

H. M. Antia. Estimate of solar radius from f-mode frequencies. *A& A*, 330:336–340, February 1998.

H. M. Antia and S. M. Chitre. Determination of temperature and chemical composition profiles in the solar interior from seismic models. *A& A*, 339:239–251, November 1998.

T. Appourchaux, K. Belkacem, A.-M. Broomhall, et al. The quest for the solar g modes. *Astron. Astrophys. Rev.*, 18:197–277, February 2010. doi: 10.1007/s00159-009-0027-z.

E. Arik, S. Aune, D. Autiero, et al. Probing eV-scale axions with CAST. *JCAP*, 2:008, February 2009. doi: 10.1088/1475-7516/2009/02/008.

E. Armengaud, F. T. Avignone, M. Betz, et al. Conceptual design of the International Axion Observatory (IAXO). *Journal of Instrumentation*, 9:T05002, May 2014. doi: 10.1088/1748-0221/9/05/T05002.

M. Asplund. New Light on Stellar Abundance Analyses: Departures from LTE and Homogeneity. *ARA&A*, 43:481–530, September 2005. doi: 10.1146/annurev.astro.42.053102.134001.

M. Asplund, N. Grevesse, and A. J. Sauval. The Solar Chemical Composition. In T. G. Barnes, III and F. N. Bash, editors, *Cosmic Abundances as Records of Stellar Evolution and Nucleosynthesis*, volume 336 of *Astronomical Society of the Pacific Conference Series*, page 25, September 2005.

M. Asplund, N. Grevesse, A. J. Sauval, and P. Scott. The Chemical Composition of the Sun. *ARA&A*, 47:481–522, September 2009. doi: 10.1146/annurev.astro.46.060407.145222.

S. Asztalos, E. Daw, H. Peng, et al. Large-scale microwave cavity search for dark-matter axions. *Phys. Rev. D*, 64(9):092003, November 2001. doi: 10.1103/PhysRevD.64.092003.

A. Ayala, I. Dominguez, M. Giannotti, A. Mirizzi, and O. Straniero. Revisiting the bound on axion-photon coupling from Globular Clusters. *ArXiv e-prints*, June 2014.

A. Badertscher, P. Crivelli, W. Fetscher, U. Gendotti, S. Gninenko, et al. An Improved Limit on Invisible Decays of Positronium. *Phys.Rev.*, D75:032004, 2007. doi: 10.1103/PhysRevD.75.032004.

N. R. Badnell and M. J. Seaton. On the importance of inner-shell transitions for opacity calculations. *Journal of Physics B Atomic Molecular Physics*, 36:4367–4385, November 2003. doi: 10.1088/0953-4075/36/21/015.

N. R. Badnell, M. A. Bautista, K. Butler, F. Delahaye, C. Mendoza, P. Palmeri, C. J. Zeippen, and M. J. Seaton. Updated opacities from the Opacity Project. *MNRAS*, 360:458–464, June 2005. doi: 10.1111/j.1365-2966.2005.08991.x.

J. N. Bahcall. *Neutrino astrophysics*. 1989.

J. N. Bahcall. The luminosity constraint on solar neutrino fluxes. *Phys. Rev. C*, 65(2):025801, February 2002. doi: 10.1103/PhysRevC.65.025801.

J. N. Bahcall and A. Loeb. Element diffusion in stellar interiors. *ApJ*, 360:267–274, September 1990. doi: 10.1086/169116.

J. N. Bahcall and R. M. May. The Rate of the Proton-Proton Reaction and Some Related Reactions. *ApJ*, 155:501, February 1969. doi: 10.1086/149886.

J. N. Bahcall and M. H. Pinsonneault. Standard solar models, with and without helium diffusion, and the solar neutrino problem. *Reviews of Modern Physics*, 64: 885–926, October 1992. doi: 10.1103/RevModPhys.64.885.

J. N. Bahcall and A. Ulmer. Temperature dependence of solar neutrino fluxes. *Phys. Rev. D*, 53:4202–4210, April 1996. doi: 10.1103/PhysRevD.53.4202.

J. N. Bahcall and R. K. Ulrich. Solar models, neutrino experiments, and helioseismology. *Reviews of Modern Physics*, 60:297–372, April 1988. doi: 10.1103/RevModPhys.60.297.

J. N. Bahcall, W. A. Fowler, I. Iben, Jr., and R. L. Sears. Solar Neutrino Flux. *ApJ*, 137:344–346, January 1963. doi: 10.1086/147513.

J. N. Bahcall, M. H. Pinsonneault, and G. J. Wasserburg. Solar models with helium and heavy-element diffusion. *Reviews of Modern Physics*, 67:781–808, October 1995. doi: 10.1103/RevModPhys.67.781.

J. N. Bahcall, M. H. Pinsonneault, and S. Basu. Solar Models: Current Epoch and Time Dependences, Neutrinos, and Helioseismological Properties. *ApJ*, 555:990–1012, July 2001. doi: 10.1086/321493.

J. N. Bahcall, A. M. Serenelli, and S. Basu. New Solar Opacities, Abundances, Helioseismology, and Neutrino Fluxes. *ApJL*, 621:L85–L88, March 2005. doi: 10.1086/428929.

J. N. Bahcall, A. M. Serenelli, and S. Basu. 10,000 Standard Solar Models: A Monte Carlo Simulation. *ApJS*, 165:400–431, July 2006. doi: 10.1086/504043.

J. E. Bailey, T. Nagayama, G. P. Loisel, et al. A higher-than-predicted measurement of iron opacity at solar interior temperatures. *Nature*, 517:56–59, January 2015. doi: 10.1038/nature14048.

S. Basu. Global seismology of the Sun. *Living Reviews in Solar Physics*, 13:2, December 2016. doi: 10.1007/s41116-016-0003-4.

S. Basu and H. M. Antia. Constraining Solar Abundances Using Helioseismology. *ApJL*, 606:L85–L88, May 2004. doi: 10.1086/421110.

S. Basu, J. Christensen-Dalsgaard, W. J. Chaplin, Y. Elsworth, G. R. Isaak, R. New, J. Schou, M. J. Thompson, and S. Tomczyk. Solar internal sound speed as inferred from combined BiSON and LOWL oscillation frequencies. *MNRAS*, 292: 243, December 1997.

S. Basu, M. H. Pinsonneault, and J. N. Bahcall. How Much Do Helioseismological Inferences Depend on the Assumed Reference Model? *ApJ*, 529:1084–1100, February 2000. doi: 10.1086/308302.

S. Basu, W. J. Chaplin, Y. Elsworth, R. New, and A. M. Serenelli. Fresh Insights on the Structure of the Solar Core. *ApJ*, 699:1403–1417, July 2009. doi: 10.1088/0004-637X/699/2/1403.

G. Bellini, J. Benziger, D. Bick, et al. First Evidence of pep Solar Neutrinos by Direct Detection in Borexino. *Physical Review Letters*, 108(5):051302, February 2012. doi: 10.1103/PhysRevLett.108.051302.

G. Bellini, J. Benziger, D. Bick, et al. Final results of Borexino Phase-I on low-energy solar neutrino spectroscopy. *Phys. Rev. D*, 89(11):112007, June 2014a. doi: 10.1103/PhysRevD.89.112007.

G. Bellini, J. Benziger, D. Bick, et al. Neutrinos from the primary proton-proton fusion process in the Sun. *Nature*, 512:383–386, August 2014b. doi: 10.1038/nature13702.

M. Bergemann and A. Serenelli. *Solar Abundance Problem*, pages 245–258. 2014. doi: 10.1007/978-3-319-06956-2_21.

J. Bergström, M. C. Gonzalez-Garcia, M. Maltoni, C. Peña-Garay, A. M. Serenelli, and N. Song. Updated determination of the solar neutrino fluxes from solar neutrino data. *Journal of High Energy Physics*, 3:132, March 2016. doi: 10.1007/JHEP03(2016)132.

C. Blancard, P. Cossé, and G. Faussurier. Solar Mixture Opacity Calculations Using Detailed Configuration and Level Accounting Treatments. *ApJ*, 745:10, January 2012. doi: 10.1088/0004-637X/745/1/10.

A.-M. Broomhall, W. J. Chaplin, G. R. Davies, Y. Elsworth, S. T. Fletcher, S. J. Hale, B. Miller, and R. New. Definitive Sun-as-a-star p-mode frequencies: 23 years of BiSON observations. *MNRAS*, 396:L100–L104, June 2009. doi: 10.1111/j.1745-3933.2009.00672.x.

T. M. Brown and J. Christensen-Dalsgaard. Accurate Determination of the Solar Photospheric Radius. *ApJL*, 500:L195–L198, June 1998. doi: 10.1086/311416.

A. S. Brun, M. S. Miesch, and J. Toomre. Modeling the Dynamical Coupling of Solar Convection with the Radiative Interior. *ApJ*, 742:79, December 2011. doi: 10.1088/0004-637X/742/2/79.

E. Caffau, H.-G. Ludwig, M. Steffen, B. Freytag, and P. Bonifacio. Solar Chemical Abundances Determined with a CO5BOLD 3D Model Atmosphere. *Sol. Phys.*, 268:255–269, February 2011. doi: 10.1007/s11207-010-9541-4.

M. E. Camisassa, L. G. Althaus, A. H. Córsico, N. Vinyoles, A. M. Serenelli, J. Isern, M. M. Miller Bertolami, and E. García-Berro. The Effect of ^{22}NE Diffusion in the Evolution and Pulsational Properties of White Dwarfs with Solar Metallicity Progenitors. *ApJ*, 823:158, June 2016. doi: 10.3847/0004-637X/823/2/158.

P. Candelas, G. T. Horowitz, A. Strominger, and E. Witten. Vacuum configurations for superstrings. *Nuclear Physics B*, 258:46–74, 1985. doi: 10.1016/0550-3213(85) 90602-9.

S. Cassisi, M. Salaris, and A. W. Irwin. The Initial Helium Content of Galactic Globular Cluster Stars from the R-Parameter: Comparison with the Cosmic Microwave Background Constraint. *ApJ*, 588:862–870, May 2003. doi: 10.1086/374218.

M. Castro, S. Vauclair, and O. Richard. Low abundances of heavy elements in the solar outer layers: comparisons of solar models with helioseismic inversions. *A& A*, 463:755–758, February 2007. doi: 10.1051/0004-6361:20066327.

J. Christensen-Dalsgaard. Helioseismology. *Reviews of Modern Physics*, 74:1073–1129, 2002. doi: 10.1103/RevModPhys.74.1073.

J. Christensen-Dalsgaard and M. P. Di Mauro. Diffusion and Helioseismology. In C. W. Straka, Y. Lebreton, and M. J. P. F. G. Monteiro, editors, *EAS Publications Series*, volume 26 of *EAS Publications Series*, pages 3–16, 2007. doi: 10.1051/eas: 2007121.

J. Christensen-Dalsgaard and D. O. Gough. Is the sun helium-deficient. *Nature*, 288: 544–547, December 1980. doi: 10.1038/288544a0.

J. Christensen-Dalsgaard and M. J. Thompson. On solar p-mode frequency shifts caused by near-surface model changes. *MNRAS*, 284:527–540, January 1997. doi: 10.1093/mnras/284.3.527.

J. Christensen-Dalsgaard, C. R. Proffitt, and M. J. Thompson. Effects of diffusion on solar models and their oscillation frequencies. *ApJL*, 403:L75–L78, February 1993. doi: 10.1086/186725.

J. Christensen-Dalsgaard, W. Dappen, S. V. Ajukov, et al. The Current State of Solar Modeling. *Science*, 272:1286–1292, May 1996. doi: 10.1126/science.272.5266.1286.

J. Christensen-Dalsgaard, M. P. di Mauro, G. Houdek, and F. Pijpers. On the opacity change required to compensate for the revised solar composition. *A& A*, 494:205–208, January 2009. doi: 10.1051/0004-6361:200810170.

J. Christensen-Dalsgaard, M. J. P. F. G. Monteiro, M. Rempel, and M. J. Thompson. A more realistic representation of overshoot at the base of the solar convective envelope as seen by helioseismology. *MNRAS*, 414:1158–1174, June 2011. doi: 10.1111/j.1365-2966.2011.18460.x.

D. D. Clayton. *Principles of stellar evolution and nucleosynthesis.* 1984.

B. T. Cleveland, T. Daily, R. Davis, Jr., J. R. Distel, K. Lande, C. K. Lee, P. S. Wildenhain, and J. Ullman. Measurement of the Solar Electron Neutrino Flux with the Homestake Chlorine Detector. *ApJ*, 496:505–526, March 1998. doi: 10.1086/305343.

E. R. Cohen and B. N. Taylor. The 1986 adjustment of the fundamental physical constants. *Reviews of Modern Physics*, 59:1121–1148, October 1987. doi: 10.1103/RevModPhys.59.1121.

J. Colgan, D. P. Kilcrease, N. H. Magee, Jr., G. S. J. Armstrong, J. Abdallah, Jr., M. E. Sherrill, C. J. Fontes, H. L. Zhang, and P. Hakel. Light element opacities of astrophysical interest from ATOMIC. In J. D. Gillaspy, W. L. Wiese, and Y. A. Podpaly, editors, *American Institute of Physics Conference Series*, volume 1545 of *American Institute of Physics Conference Series*, pages 17–26, July 2013. doi: 10.1063/1.4815837.

J. Colgan, D. P. Kilcrease, N. H. Magee, J. Abdallah, M. E. Sherrill, C. J. Fontes, P. Hakel, and H. L. Zhang. Light element opacities of astrophysical interest from

ATOMIC. *High Energy Density Physics*, 14:33–37, March 2015. doi: 10.1016/j.hedp.2015.02.006.

J. Colgan, D. P. Kilcrease, N. H. Magee, M. E. Sherrill, J. Abdallah, Jr., P. Hakel, C. J. Fontes, J. A. Guzik, and K. A. Mussack. A New Generation of Los Alamos Opacity Tables. *ApJ*, 817:116, February 2016. doi: 10.3847/0004-637X/817/2/116.

IAXO collaboration. *IAXO - The International Axion Observatory*. `http://iaxo.web.cern.ch/iaxo/`.

A. H. Córsico, L. G. Althaus, A. D. Romero, M. M. Miller Bertolami, E. García-Berro, and J. Isern. Constraining the Axion Mass through the Asteroseismology of the ZZ Ceti Star G117-B15A. In H. Shibahashi, M. Takata, and A. E. Lynas-Gray, editors, *Progress in Solar/Stellar Physics with Helio- and Asteroseismology*, volume 462 of *Astronomical Society of the Pacific Conference Series*, page 533, September 2012.

S. Couvidat, S. Turck-Chièze, and A. G. Kosovichev. Solar Seismic Models and the Neutrino Predictions. *ApJ*, 599:1434–1448, December 2003. doi: 10.1086/379604.

A. N. Cox, J. A. Guzik, and R. B. Kidman. Oscillations of solar models with internal element diffusion. *ApJ*, 342:1187–1206, July 1989. doi: 10.1086/167675.

S. Davidson, B. Campbell, and David C. Bailey. Limits on particles of small electric charge. *Phys. Rev.*, D43:2314–2321, 1991. doi: 10.1103/PhysRevD.43.2314.

S. Davidson, S. Hannestad, and G. Raffelt. Updated bounds on milli-charged particles. *Journal of High Energy Physics*, 5:003, May 2000. doi: 10.1088/1126-6708/2000/05/003.

R. J. deBoer, J. Görres, K. Smith, E. Uberseder, M. Wiescher, A. Kontos, G. Imbriani, A. Di Leva, and F. Strieder. Monte Carlo uncertainty of the He3(α,γ)Be7 reaction rate. *Phys. Rev. C*, 90(3):035804, September 2014. doi: 10.1103/PhysRevC.90.035804.

S. Degl'Innoccenti, W. A. Dziembowski, G. Fiorentini, and B. Ricci. Helioseismology and standard solar models. *Astroparticle Physics*, 7:77–95, June 1997. doi: 10.1016/S0927-6505(97)00004-2.

F. Delahaye and M. H. Pinsonneault. The Solar Heavy-Element Abundances. I. Constraints from Stellar Interiors. *ApJ*, 649:529–540, September 2006. doi: 10.1086/505260.

M. Dine, W. Fischler, and M. Srednicki. A simple solution to the strong CP problem with a harmless axion. *Physics Letters B*, 104:199–202, August 1981. doi: 10.1016/0370-2693(81)90590-6.

V. Domingo, B. Fleck, and A. I. Poland. The SOHO Mission: an Overview. *Sol. Phys.*, 162:1–37, December 1995. doi: 10.1007/BF00733425.

D. Dravins and A. Nordlund. Stellar Granulation - Part Four - Line Formation in Inhomogeneous Stellar Photospheres. *A& A*, 228:184, February 1990.

H. K. Dreiner, J. Fortin, J. Isern, and L. Ubaldi. White Dwarfs constrain Dark Forces. *Phys.Rev.*, D88:043517, 2013. doi: 10.1103/PhysRevD.88.043517.

S.L. Dubovsky, D.S. Gorbunov, and G.I. Rubtsov. Narrowing the window for millicharged particles by CMB anisotropy. *JETP Lett.*, 79:1–5, 2004. doi: 10.1134/1.1675909.

Y. Elsworth, R. Howe, G. R. Isaak, C. P. McLeod, and R. New. Low-l p-mode solar eigenfrequency measurements from the Birmingham Network. *MNRAS*, 251:7P–9P, July 1991. doi: 10.1093/mnras/251.1.7P.

R. Essig, J. A. Jaros, W. Wester, et al. Dark Sectors and New, Light, Weakly-Coupled Particles. *ArXiv e-prints*, October 2013.

J. W. Ferguson, D. R. Alexander, F. Allard, T. Barman, J. G. Bodnarik, P. H. Hauschildt, A. Heffner-Wong, and A. Tamanai. Low-Temperature Opacities. *ApJ*, 623:585–596, April 2005. doi: 10.1086/428642.

G. L. Fogli, E. Lisi, A. Marrone, D. Montanino, and A. Palazzo. Getting the most from the statistical analysis of solar neutrino oscillations. *Phys.Rev.*, 66(5):053010, September 2002. doi: 10.1103/PhysRevD.66.053010.

E. Fossat. The IRIS network for full disk helioseismology - Present status of the programme. *Sol. Phys.*, 133:1–12, May 1991. doi: 10.1007/BF00149818.

B. Freytag, H.-G. Ludwig, and M. Steffen. Hydrodynamical models of stellar convection. The role of overshoot in DA white dwarfs, A-type stars, and the Sun. *A& A*, 313:497–516, September 1996.

A. Friedland, M. Giannotti, and M. Wise. Constraining the Axion-Photon Coupling with Massive Stars. *Phys.Rev.Lett.*, 110:061101, 2013. doi: 10.1103/PhysRevLett.110.061101.

J. A. Frieman, S. Dimopoulos, and M. S. Turner. Axions and stars. *Phys. Rev. D*, 36:2201–2210, October 1987. doi: 10.1103/PhysRevD.36.2201.

C. Fröhlich and J. Lean. The Sun's total irradiance: Cycles, trends and related climate change uncertainties since 1976. *Geophys. Res. Lett*, 25:4377–4380, December 1998. doi: 10.1029/1998GL900157.

C. Fröhlich, J. Romero, H. Roth, et al. VIRGO: Experiment for Helioseismology and Solar Irradiance Monitoring. *Sol. Phys.*, 162:101–128, December 1995. doi: 10.1007/BF00733428.

S. Fukuda, Y. Fukuda, M. Ishitsuka, et al. Solar ^{8}B and hep Neutrino Measurements from 1258 Days of Super-Kamiokande Data. *Physical Review Letters*, 86:5651–5655, June 2001. doi: 10.1103/PhysRevLett.86.5651.

Y. Fukuda, T. Hayakawa, K. Inoue, et al. Solar Neutrino Data Covering Solar Cycle 22. *Physical Review Letters*, 77:1683–1686, August 1996. doi: 10.1103/PhysRevLett.77.1683.

A. H. Gabriel, G. Grec, J. Charra, et al. Global Oscillations at Low Frequency from the SOHO Mission (GOLF). *Sol. Phys.*, 162:61–99, December 1995. doi: 10.1007/BF00733427.

R. A. García. Detecting individual gravity modes in the Sun: Chimera or reality? *Highlights of Astronomy*, 15:345–346, November 2010. doi: 10.1017/S1743921310009695.

R. A. García, S. Turck-Chièze, S. J. Jiménez-Reyes, J. Ballot, P. L. Pallé, A. Eff-Darwich, S. Mathur, and J. Provost. Tracking Solar Gravity Modes: The Dynamics of the Solar Core. *Science*, 316:1591–, June 2007. doi: 10.1126/science.1140598.

M. Gennaro, P. G. Prada Moroni, and S. Degl'Innocenti. ΔY/ΔZ from the analysis of local K dwarfs. *A& A*, 518:A13, July 2010. doi: 10.1051/0004-6361/201014227.

S.N. Gninenko, N.V. Krasnikov, and A. Rubbia. Search for millicharged particles in reactor neutrino experiments: A Probe of the PVLAS anomaly. *Phys.Rev.*, D75: 075014, 2007. doi: 10.1103/PhysRevD.75.075014.

P. Gondolo and G. G. Raffelt. Solar neutrino limit on axions and keV-mass bosons. *Phys. Rev. D*, 79(10):107301, May 2009. doi: 10.1103/PhysRevD.79.107301.

D. O. Gough. Linear adiabatic stellar pulsation. In J.-P. Zahn and J. Zinn-Justin, editors, *Astrophysical Fluid Dynamics - Les Houches 1987*, pages 399–560, 1993.

D. O. Gough and M. J. Thompson. *The inversion problem*, pages 519–561. 1991.

D. O. Gough, A. G. Kosovichev, J. Toomre, et al. The Seismic Structure of the Sun. *Science*, 272:1296–1300, May 1996. doi: 10.1126/science.272.5266.1296.

N. Grevesse and A. J. Sauval. Standard Solar Composition. *Space Sci. Rev.*, 85: 161–174, May 1998. doi: 10.1023/A:1005161325181.

N. Grevesse, M. Asplund, A. J. Sauval, and P. Scott. The chemical composition of the Sun. *Ap&SS*, 328:179–183, July 2010. doi: 10.1007/s10509-010-0288-z.

N. Grevesse, P. Scott, M. Asplund, and A. J. Sauval. The elemental composition of the Sun. III. The heavy elements Cu to Th. *A& A*, 573:A27, January 2015. doi: 10.1051/0004-6361/201424111.

B. Gustafsson, B. Edvardsson, K. Eriksson, U. G. Jørgensen, Å. Nordlund, and B. Plez. A grid of MARCS model atmospheres for late-type stars. I. Methods and general properties. *A& A*, 486:951–970, August 2008. doi: 10.1051/0004-6361: 200809724.

J. A. Guzik and K. Mussack. Exploring Mass Loss, Low-Z Accretion, and Convective Overshoot in Solar Models to Mitigate the Solar Abundance Problem. *ApJ*, 713: 1108–1119, April 2010. doi: 10.1088/0004-637X/713/2/1108.

J. A. Guzik, L. S. Watson, and A. N. Cox. Can Enhanced Diffusion Improve Helioseismic Agreement for Solar Models with Revised Abundances? *ApJ*, 627:1049–1056, July 2005. doi: 10.1086/430438.

M. Haberreiter, W. Schmutz, and A. G. Kosovichev. Solving the Discrepancy between the Seismic and Photospheric Solar Radius. *ApJL*, 675:L53, March 2008. doi: 10.1086/529492.

M. Haft, G. Raffelt, and A. Weiss. Standard and nonstandard plasma neutrino emission revisited. *ApJ*, 425:222–230, April 1994. doi: 10.1086/173978.

S. J. Hale, R. Howe, W. J. Chaplin, G. R. Davies, and Y. P. Elsworth. Performance of the Birmingham Solar-Oscillations Network (BiSON). *Sol. Phys.*, 291: 1–28, January 2016. doi: 10.1007/s11207-015-0810-0.

W. Hampel, J. Handt, G. Heusser, et al. GALLEX solar neutrino observations: results for GALLEX IV. *Physics Letters B*, 447:127–133, February 1999. doi: 10.1016/S0370-2693(98)01579-2.

J. W. Harvey, F. Hill, R. P. Hubbard, et al. The Global Oscillation Network Group (GONG) Project. *Science*, 272:1284–1286, May 1996. doi: 10.1126/science.272.5266.1284.

W. C. Haxton and A. M. Serenelli. CN Cycle Solar Neutrinos and the Sun's Primordial Core Metallicity. *ApJ*, 687:678-691, November 2008. doi: 10.1086/591787.

W. C. Haxton, R. G. Hamish Robertson, and A. M. Serenelli. Solar Neutrinos: Status and Prospects. *ARA&A*, 51:21–61, August 2013. doi: 10.1146/annurev-astro-081811-125539.

L. G. Henyey, J. E. Forbes, and N. L. Gould. A New Method of Automatic Computation of Stellar Evolution. *ApJ*, 139:306, January 1964. doi: 10.1086/147754.

B. Holdom. Two U(1)'s and Epsilon Charge Shifts. *Phys. Lett.*, B166:196, 1986a. doi: 10.1016/0370-2693(86)91377-8.

B. Holdom. Searching for ϵ Charges and a New U(1). *Phys.Lett.*, B178:65, 1986b. doi: 10.1016/0370-2693(86)90470-3.

D. Horns, J. Jaeckel, A. Lindner, A. Lobanov, J. Redondo, and A. Ringwald. Searching for WISPy cold dark matter with a dish antenna. *JCAP*, 4:016, April 2013. doi: 10.1088/1475-7516/2013/04/016.

D. G. Hummer and D. Mihalas. The equation of state for stellar envelopes. I - an occupation probability formalism for the truncation of internal partition functions. *ApJ*, 331:794–814, August 1988. doi: 10.1086/166600.

C. A. Iglesias and F. J. Rogers. Updated Opal Opacities. *ApJ*, 464:943, June 1996. doi: 10.1086/177381.

C. Iliadis, K. Anderson, A. Coc, F. Timmes, and S. Starrfield. Bayesian Estimation of Thermonuclear Reaction Rates. *ArXiv e-prints*, August 2016.

I.G. Irastorza et al. The International Axion Observatory (IAXO). 2012. doi: 10.3204/DESY-PROC-2011-04/irastorza_igor.

J. Isern, M. Hernanz, and E. Garcia-Berro. Axion cooling of white dwarfs. *Astrophys.J.*, 392:L23, 1992. doi: 10.1086/186416.

J. Isern, E. García-Berro, S. Torres, and S. Catalán. Axions and the Cooling of White Dwarf Stars. *ApJL*, 682:L109–L112, August 2008. doi: 10.1086/591042.

J. Isern, E. Garcia-Berro, L.G. Althaus, and A.H. Corsico. Axions and the pulsation periods of variable white dwarfs revisited. *Astron.Astrophys.*, 512:A86, 2010. doi: 10.1051/0004-6361/200913716.

J. Jaeckel. A force beyond the Standard Model - Status of the quest for hidden photons. *ArXiv e-prints*, March 2013.

J. Jaeckel and A. Ringwald. The Low-Energy Frontier of Particle Physics. *Annual Review of Nuclear and Particle Science*, 60:405–437, November 2010. doi: 10.1146/annurev.nucl.012809.104433.

J. Jaeckel, M. Jankowiak, and M. Spannowsky. LHC probes the hidden sector. *Phys. Dark Univ.*, 2:111–117, 2013. doi: 10.1016/j.dark.2013.06.001.

J. Keller and A. Sedrakian. Axions from cooling compact stars. *Nucl.Phys.*, A897: 62–69, 2013. doi: 10.1016/j.nuclphysa.2012.11.004.

J. Khoury and A. Weltman. Chameleon Fields: Awaiting Surprises for Tests of Gravity in Space. *Physical Review Letters*, 93(17):171104, October 2004a. doi: 10.1103/PhysRevLett.93.171104.

J. Khoury and A. Weltman. Chameleon cosmology. *Phys. Rev. D*, 69(4):044026, February 2004b. doi: 10.1103/PhysRevD.69.044026.

J. E. Kim. Weak-interaction singlet and strong CP invariance. *Physical Review Letters*, 43:103–107, July 1979. doi: 10.1103/PhysRevLett.43.103.

R. Kippenhahn, A. Weigert, and E. Hofmeister. Methods for Calculating Stellar Evolution. *Methods in Computational Physics*, 7:129–190, 1967.

R. Kippenhahn, A. Weigert, and A. Weiss. *Stellar Structure and Evolution.* 2012. doi: 10.1007/978-3-642-30304-3.

H. Kjeldsen, T. R. Bedding, and J. Christensen-Dalsgaard. Correcting Stellar Oscillation Frequencies for Near-Surface Effects. *ApJL*, 683:L175, August 2008. doi: 10.1086/591667.

A. G. Kosovichev and A. V. Fedorova. Construction of a Seismic Model of the Sun. *Soviet Ast. Soviet Astronomy*, 35:507, October 1991.

M. Krief, A. Feigel, and D. Gazit. Line Broadening and the Solar Opacity Problem. *ApJ*, 824:98, June 2016a. doi: 10.3847/0004-637X/824/2/98.

M. Krief, A. Feigel, and D. Gazit. Solar Opacity Calculations Using the Super-transition-array Method. *ApJ*, 821:45, April 2016b. doi: 10.3847/0004-637X/821/1/45.

K. S. Krishna Swamy. Profiles of Strong Lines in K-Dwarfs. *ApJ*, 145:174, July 1966. doi: 10.1086/148752.

M. Le Pennec, S. Turck-Chièze, S. Salmon, C. Blancard, P. Cossé, G. Faussurier, and G. Mondet. First New Solar Models with OPAS Opacity Tables. *ApJL*, 813:L42, November 2015. doi: 10.1088/2041-8205/813/2/L42.

L.B. Leinson. Axion mass limit from observations of the neutron star in Cassiopeia A. *JCAP*, 1408:031, 2014. doi: 10.1088/1475-7516/2014/08/031.

C.-H. Lin, H. M. Antia, and S. Basu. Seismic Study of the Chemical Composition of the Solar Convection Zone. *ApJ*, 668:603–610, October 2007. doi: 10.1086/520916.

K. Lodders, H. Palme, and H.-P. Gail. Abundances of the Elements in the Solar System. *Landolt Börnstein*, 2009. doi: 10.1007/978-3-540-88055-4_34.

G. G. Luther and W. R. Towler. Redetermination of the Newtonian gravitational constant G. *Physical Review Letters*, 48:121–123, January 1982. doi: 10.1103/PhysRevLett.48.121.

K. Maeda and H. Shibahashi. Constraint on the Axion-Photon Coupling Constant from Helioseismic Solar Models. In H. Shibahashi and A. E. Lynas-Gray, editors, *Astronomical Society of the Pacific Conference Series*, volume 479 of *Astronomical Society of the Pacific Conference Series*, page 453, December 2013.

N. H. Magee, J. Abdallah, Jr., R. E. H. Clark, et al. Atomic Structure Calculations and New LOS Alamos Astrophysical Opacities. In S. J. Adelman and W. L. Wiese, editors, *Astrophysical Applications of Powerful New Databases*, volume 78 of *Astronomical Society of the Pacific Conference Series*, page 51, 1995.

M. Maltoni and A. Y. Smirnov. Solar neutrinos and neutrino physics. *European Physical Journal A*, 52:87, April 2016. doi: 10.1140/epja/i2016-16087-0.

L. E. Marcucci, R. Schiavilla, and M. Viviani. Proton-Proton Weak Capture in Chiral Effective Field Theory. *Physical Review Letters*, 110(19):192503, May 2013. doi: 10.1103/PhysRevLett.110.192503.

M. Marta, A. Formicola, D. Bemmerer, et al. The N14(p,γ)O15 reaction studied with a composite germanium detector. *Phys. Rev. C*, 83(4):045804, April 2011. doi: 10.1103/PhysRevC.83.045804.

R. Mayle, J. R. Wilson, J. R. Ellis, Keith A. Olive, D. N. Schramm, et al. Constraints on Axions from SN 1987a. *Phys.Lett.*, B203:188, 1988. doi: 10.1016/0370-2693(88)91595-X.

R. Mayle, J. R. Wilson, J. R. Ellis, Keith A. Olive, D. N. Schramm, et al. Updated Constraints on Axions from SN 1987a. *Phys.Lett.*, B219:515, 1989. doi: 10.1016/0370-2693(89)91104-0.

M. M. Miller Bertolami, B. E. Melendez, L. G. Althaus, and J. Isern. Testing Fundamental Particle Physics with the Galactic White Dwarf Luminosity Function. *ArXiv e-prints*, October 2014.

G. Mondet, C. Blancard, P. Cossé, and G. Faussurier. Opacity Calculations for Solar Mixtures. *ApJS*, 220:2, September 2015. doi: 10.1088/0067-0049/220/1/2.

S. Moriyama, M. Minowa, T. Namba, Y. Inoue, Y. Takasu, and A. Yamamoto. Direct search for solar axions by using strong magnetic field and X-ray detectors. *Physics Letters B*, 434:147–152, August 1998. doi: 10.1016/S0370-2693(98)00766-7.

H. Munakata, Y. Kohyama, and N. Itoh. Neutrino energy loss in stellar interiors. *ApJ*, 296:197–203, September 1985. doi: 10.1086/163436.

C. Neuforge-Verheecke, S. Goriely, J. A. Guzik, F. J. Swenson, and P. A. Bradley. Seismological Tests of Solar Models Calculated with the NACRE Reaction Rates and the Grevesse and Sauval 1998 Mixture. *ApJ*, 550:493–502, March 2001. doi: 10.1086/319708.

Å. Nordlund, R. F. Stein, and M. Asplund. Solar Surface Convection. *Living Reviews in Solar Physics*, 6:2, December 2009. doi: 10.12942/lrsp-2009-2.

A. Önehag, B. Gustafsson, and A. Korn. Abundances and possible diffusion of elements in M 67 stars. *A& A*, 562:A102, February 2014. doi: 10.1051/0004-6361/201322663.

A. Payez, C. Evoli, T. Fischer, M. Giannotti, A. Mirizzi, and A. Ringwald. Revisiting the SN1987A gamma-ray limit on ultralight axion-like particles. *JCAP*, 1502(02):006, 2015. doi: 10.1088/1475-7516/2015/02/006.

R. D. Peccei and H. R. Quinn. CP conservation in the presence of pseudoparticles. *Physical Review Letters*, 38:1440–1443, June 1977. doi: 10.1103/PhysRevLett.38.1440.

W. D. Pesnell, B. J. Thompson, and P. C. Chamberlin. The Solar Dynamics Observatory (SDO). *Sol. Phys.*, 275:3–15, January 2012. doi: 10.1007/s11207-011-9841-3.

M. Pinsonneault. Mixing in Stars. *ARA&A*, 35:557–605, 1997. doi: 10.1146/annurev.astro.35.1.557.

A.A. Prinz, R. Baggs, J. Ballam, S. Ecklund, C. Fertig, et al. Search for millicharged particles at SLAC. *Phys.Rev.Lett.*, 81:1175–1178, 1998. doi: 10.1103/PhysRevLett.81.1175.

C. R. Proffitt and G. Michaud. Gravitational settling in solar models. *ApJ*, 380:238–250, October 1991. doi: 10.1086/170580.

G. G. Raffelt. Axion Constraints From White Dwarf Cooling Times. *Phys.Lett.*, B166:402, 1986. doi: 10.1016/0370-2693(86)91588-1.

G. G. Raffelt. Axion bremsstrahlung in red giants. *Phys. Rev. D*, 41:1324–1326, February 1990. doi: 10.1103/PhysRevD.41.1324.

G. G. Raffelt. *Stars as laboratories for fundamental physics.* 1996. ISBN 9780226702728. URL `http://wwwth.mpp.mpg.de/members/raffelt/mypapers/199613.pdf`.

G. G. Raffelt. *Stars as laboratories for fundamental physics : the astrophysics of neutrinos, axions, and other weakly interacting particles.* University of Chicago Press, 1996.

G. G. Raffelt and D. S. P. Dearborn. Bounds on light, weakly interacting particles from observational lifetimes of helium-burning stars. *Phys. Rev. D*, 37:549–551, January 1988. doi: 10.1103/PhysRevD.37.549.

G. G. Raffelt and D. Seckel. Bounds on Exotic Particle Interactions from SN 1987a. *Phys.Rev.Lett.*, 60:1793, 1988. doi: 10.1103/PhysRevLett.60.1793.

G. G. Raffelt and A. Weiss. Red giant bound on the axion-electron coupling reexamined. *Phys. Rev. D*, 51:1495–1498, February 1995. doi: 10.1103/PhysRevD.51.1495.

J. Redondo. Helioscope bounds on hidden sector photons. *JCAP*, 7:008, July 2008. doi: 10.1088/1475-7516/2008/07/008.

J. Redondo. Solar axion flux from the axion-electron coupling. *JCAP*, 12:008, December 2013. doi: 10.1088/1475-7516/2013/12/008.

J. Redondo and G. Raffelt. Solar constraints on hidden photons re-visited. *JCAP*, 8: 034, August 2013. doi: 10.1088/1475-7516/2013/08/034.

D. Reimers. Circumstellar absorption lines and mass loss from red giants. *Memoires of the Societe Royale des Sciences de Liege*, 8:369–382, 1975.

F. J. Rogers and C. A. Iglesias. Rosseland mean opacities for variable compositions. *ApJ*, 401:361–366, December 1992. doi: 10.1086/172066.

F. J. Rogers and A. Nayfonov. Updated and Expanded OPAL Equation-of-State Tables: Implications for Helioseismology. *ApJ*, 576:1064–1074, September 2002a. doi: 10.1086/341894.

F. J. Rogers and A. Nayfonov. Updated and Expanded OPAL Equation-of-State Tables: Implications for Helioseismology. *ApJ*, 576:1064–1074, September 2002b. doi: 10.1086/341894.

I. W. Roxburgh and S. V. Vorontsov. The ratio of small to large separations of acoustic oscillations as a diagnostic of the interior of solar-like stars. *A& A*, 411: 215–220, November 2003. doi: 10.1051/0004-6361:20031318.

E. E. Salpeter. Electrons Screening and Thermonuclear Reactions. *Australian Journal of Physics*, 7:373, September 1954. doi: 10.1071/PH540373.

P. H. Scherrer, R. S. Bogart, R. I. Bush, et al. The Solar Oscillations Investigation - Michelson Doppler Imager. *Sol. Phys.*, 162:129–188, December 1995. doi: 10.1007/BF00733429.

P. H. Scherrer, J. Schou, R. I. Bush, et al. The Helioseismic and Magnetic Imager (HMI) Investigation for the Solar Dynamics Observatory (SDO). *Sol. Phys.*, 275: 207–227, January 2012. doi: 10.1007/s11207-011-9834-2.

H. Schlattl and M. Salaris. Quantum corrections to microscopic diffusion constants. *A& A*, 402:29–35, April 2003. doi: 10.1051/0004-6361:20030230.

H. Schlattl, A. Weiss, and G. Raffelt. Helioseismological constraint on solar axion emission. *Astroparticle Physics*, 10:353–359, May 1999. doi: 10.1016/S0927-6505(98)00063-2.

J. Schou, A. G. Kosovichev, P. R. Goode, and W. A. Dziembowski. Determination of the Sun's Seismic Radius from the SOHO Michelson Doppler Imager. *ApJL*, 489: L197, November 1997. doi: 10.1086/316782.

J. Schou, P. H. Scherrer, R. I. Bush, et al. Design and Ground Calibration of the Helioseismic and Magnetic Imager (HMI) Instrument on the Solar Dynamics Observatory (SDO). *Sol. Phys.*, 275:229–259, January 2012. doi: 10.1007/s11207-011-9842-2.

M. Schwarz. Solar Hidden Photon Search. In K. Zioutas and M. Schumann, editors, *7th Patras Workshop on Axions, WIMPs and WISPs (PATRAS 2011)*, page 129, January 2012.

P. Scott, M. Asplund, N. Grevesse, M. Bergemann, and A. J. Sauval. The elemental composition of the Sun. II. The iron group elements Sc to Ni. *A& A*, 573:A26, January 2015a. doi: 10.1051/0004-6361/201424110.

P. Scott, N. Grevesse, M. Asplund, A. J. Sauval, K. Lind, Y. Takeda, R. Collet, R. Trampedach, and W. Hayek. The elemental composition of the Sun. I. The intermediate mass elements Na to Ca. *A& A*, 573:A25, January 2015b. doi: 10.1051/0004-6361/201424109.

R. L. Sears. Helium Content and Neutrino Fluxes in Solar Models. *ApJ*, 140:477, August 1964. doi: 10.1086/147942.

M. J. Seaton and N. R. Badnell. A comparison of Rosseland-mean opacities from OP and OPAL. *MNRAS*, 354:457–465, October 2004. doi: 10.1111/j.1365-2966.2004.08205.x.

M. J. Seaton, Y. Yan, D. Mihalas, and A. K. Pradhan. Opacities for Stellar Envelopes. *MNRAS*, 266:805, February 1994. doi: 10.1093/mnras/266.4.805.

A. M. Serenelli. New results on standard solar models. *Ap&SS*, 328:13–21, July 2010. doi: 10.1007/s10509-009-0174-8.

A. M. Serenelli. Alive and well: A short review about standard solar models. *European Physical Journal A*, 52:78, April 2016. doi: 10.1140/epja/i2016-16078-1.

A. M. Serenelli, S. Basu, J. W. Ferguson, and M. Asplund. New Solar Composition: The Problem with Solar Models Revisited. *ApJL*, 705:L123–L127, November 2009. doi: 10.1088/0004-637X/705/2/L123.

A. M. Serenelli, W. C. Haxton, and C. Peña-Garay. Solar Models with Accretion. I. Application to the Solar Abundance Problem. *ApJ*, 743:24, December 2011. doi: 10.1088/0004-637X/743/1/24.

A.M. Serenelli, C. Peña-Garay, and W. C. Haxton. Using the standard solar model to constrain solar composition and nuclear reaction S factors. *Phys. Rev. D*, 87(4): 043001, February 2013. doi: 10.1103/PhysRevD.87.043001.

M. A. Shifman, A. I. Vainshtein, and V. I. Zakharov. Can confinement ensure natural CP invariance of strong interactions? *Nuclear Physics B*, 166:493–506, April 1980. doi: 10.1016/0550-3213(80)90209-6.

P. Sikivie. Experimental tests of the 'invisible' axion. *Physical Review Letters*, 51: 1415–1417, October 1983. doi: 10.1103/PhysRevLett.51.1415.

D. E. Soper, M. Spannowsky, C. J. Wallace, and T. M. P. Tait. Scattering of Dark Particles with Light Mediators. *Phys. Rev.*, D90(11):115005, 2014. doi: 10.1103/PhysRevD.90.115005.

D. N. Spergel and W. H. Press. Effect of hypothetical, weakly interacting, massive particles on energy transport in the solar interior. *ApJ*, 294:663–673, July 1985. doi: 10.1086/163336.

G. Steigman. Primordial helium and the cosmic background radiation. *JCAP*, 4:029, April 2010. doi: 10.1088/1475-7516/2010/04/029.

M. Tada, Y. Kishimoto, K. Kominato, M. Shibata, H. Funahashi, K. Yamamoto, A. Masaike, and S. Matsuki. CARRACK II - a new large-scale experiment to search for axions with Rydberg-atom cavity detector. *Nuclear Physics B Proceedings Supplements*, 72:164–168, March 1999. doi: 10.1016/S0920-5632(98)00519-2.

M. Taoso, F. Iocco, G. Meynet, G. Bertone, and P. Eggenberger. Effect of low mass dark matter particles on the Sun. *Phys. Rev. D*, 82(8):083509, October 2010. doi: 10.1103/PhysRevD.82.083509.

A. A. Thoul, J. N. Bahcall, and A. Loeb. Element diffusion in the solar interior. *ApJ*, 421:828–842, February 1994. doi: 10.1086/173695.

E. Tognelli, S. Degl'Innocenti, L. E. Marcucci, and P. G. Prada Moroni. Astrophysical implications of the proton-proton cross section updates. *Physics Letters B*, 742: 189–194, March 2015. doi: 10.1016/j.physletb.2015.01.033.

S. C. Tripathy and J. Christensen-Dalsgaard. Opacity effects on the solar interior. I. Solar structure. *A& A*, 337:579–590, September 1998.

S. Turck-Chieze, S. Cahen, M. Casse, and C. Doom. Revisiting the standard solar model. *ApJ*, 335:415–424, December 1988. doi: 10.1086/166936.

S. Turck-Chièze, S. Couvidat, A. G. Kosovichev, et al. Solar Neutrino Emission Deduced from a Seismic Model. *ApJL*, 555:L69–L73, July 2001. doi: 10.1086/321726.

S. Turck-Chièze, A. Palacios, J. P. Marques, and P. A. P. Nghiem. Seismic and Dynamical Solar Models. I. The Impact of the Solar Rotation History on Neutrinos and Seismic Indicators. *ApJ*, 715:1539–1555, June 2010. doi: 10.1088/0004-637X/715/2/1539.

S. Turcotte, J. Richer, G. Michaud, C. A. Iglesias, and F. J. Rogers. Consistent Solar Evolution Model Including Diffusion and Radiative Acceleration Effects. *ApJ*, 504: 539–558, September 1998. doi: 10.1086/306055.

M. S. Turner. Axions from SN 1987a. *Phys.Rev.Lett.*, 60:1797, 1988. doi: 10.1103/PhysRevLett.60.1797.

H. Umeda, N. Iwamoto, S. Tsuruta, L. Qin, and K. Nomoto. Axion mass limits from cooling neutron stars. 1997.

K. van Bibber, N. R. Dagdeviren, S. E. Koonin, A. K. Kerman, and H. N. Nelson. Proposed experiment to produce and detect light pseudoscalars. *Physical Review Letters*, 59:759–762, August 1987. doi: 10.1103/PhysRevLett.59.759.

N. Viaux, M. Catelan, P. B. Stetson, G. G. Raffelt, J. Redondo, A. A. R. Valcarce, and A. Weiss. Neutrino and Axion Bounds from the Globular Cluster M5 (NGC 5904). *Physical Review Letters*, 111(23):231301, December 2013. doi: 10.1103/PhysRevLett.111.231301.

F. L. Villante. Constraints on the Opacity Profile of the Sun from Helioseismic Observables and Solar Neutrino Flux Measurements. *ApJ*, 724:98–110, November 2010. doi: 10.1088/0004-637X/724/1/98.

F. L. Villante, A. M. Serenelli, F. Delahaye, and M. H. Pinsonneault. The Chemical Composition of the Sun from Helioseismic and Solar Neutrino Data. *ApJ*, 787:13, May 2014. doi: 10.1088/0004-637X/787/1/13.

A. C. Vincent and P. Scott. Thermal conduction by dark matter with velocity and momentum-dependent cross-sections. *JCAP*, 4:019, April 2014. doi: 10.1088/1475-7516/2014/04/019.

A. C. Vincent, A. Serenelli, and P. Scott. Generalised form factor dark matter in the Sun. *JCAP*, 8:040, August 2015. doi: 10.1088/1475-7516/2015/08/040.

A. C. Vincent, P. Scott, and A. Serenelli. Updated constraints on velocity and momentum-dependent asymmetric dark matter. *JCAP*, 11:007, November 2016. doi: 10.1088/1475-7516/2016/11/007.

N. Vinyoles and A. Serenelli. A sensitivity study of s-process: the impact of uncertainties from nuclear reaction rates. In *Journal of Physics Conference Series*, volume 665 of *Journal of Physics Conference Series*, page 012028, January 2016. doi: 10.1088/1742-6596/665/1/012028.

N. Vinyoles and H. Vogel. Minicharged particles from the Sun: a cutting-edge bound. *JCAP*, 3:002, March 2016. doi: 10.1088/1475-7516/2016/03/002.

N. Vinyoles, A. Serenelli, F. L. Villante, S. Basu, J. Redondo, and J. Isern. New axion and hidden photon constraints from a solar data global fit. *JCAP*, 10:015, October 2015. doi: 10.1088/1475-7516/2015/10/015.

N. Vinyoles, A. M. Serenelli, F. L. Villante, S. Basu, J. Bergström, M. C. Gonzalez-Garcia, M. Maltoni, C. Peña-Garay, and N. Song. A New Generation of Standard Solar Models. *ApJ*, 835:202, February 2017. doi: 10.3847/1538-4357/835/2/202.

H. Vogel and J. Redondo. Dark Radiation constraints on minicharged particles in models with a hidden photon. *JCAP*, 1402:029, 2014. doi: 10.1088/1475-7516/2014/02/029.

S. V. Vorontsov, V. A. Baturin, S. V. Ayukov, and V. K. Gryaznov. Helioseismic calibration of the equation of state and chemical composition in the solar convective envelope. *MNRAS*, 430:1636–1652, April 2013. doi: 10.1093/mnras/sts701.

A. Weiss and H. Schlattl. GARSTEC: the Garching Stellar Evolution Code. The direct descendant of the legendary Kippenhahn code. *Ap&SS*, 316:99–106, August 2008. doi: 10.1007/s10509-007-9606-5.

H. A. Weldon. Simple Rules for Discontinuities in Finite Temperature Field Theory. *Phys.Rev.*, D28:2007, 1983. doi: 10.1103/PhysRevD.28.2007.

X. Zhang, K. M. Nollett, and D. R. Phillips. Halo effective field theory constrains the solar ^{7}Be + p $\rightarrow$ ^{8}B + γ rate. *Physics Letters B*, 751:535–540, December 2015. doi: 10.1016/j.physletb.2015.11.005.

K. Zioutas, C. E. Aalseth, D. Abriola, et al. A decommissioned LHC model magnet as an axion telescope. *Nuclear Instruments and Methods in Physics Research A*, 425:480–487, April 1999. doi: 10.1016/S0168-9002(98)01442-9.

K. Zioutas et al. First results from the CERN Axion Solar Telescope (CAST). *Phys.Rev.Lett.*, 94:121301, 2005. doi: 10.1103/PhysRevLett.94.121301.